

DISS. ETH NO. 30108

Linear-Rotary Drive System for Novel Valveless Implantable Pulsatile Total Artificial Heart

A thesis submitted to attain the degree of

DOCTOR OF SCIENCES
(Dr. sc. ETH Zurich)

presented by

ROSARIO VINCENZO GIUFFRIDA

MSc ETH RSC, ETH Zurich
born on 27.08.1994

accepted on the recommendation of

Prof. Dr. Johann W. Kolar, examiner
Prof. Dr. Hans-Peter Nee, co-examiner

2024

ETH Zurich
Power Electronic Systems Laboratory
Physikstrasse 3 | ETL H23
8092 Zurich | Switzerland

<http://www.pes.ee.ethz.ch>

© 2024, Rosario V. Giuffrida

Chi ha tempo non aspetti tempo.
– Caterina da Siena

γνώθι σαυτόν (Conosci te stesso).
– Massima, Tempio di Apollo a Delfi

Prima di essere ingegner, voi siete persone.*
– F. De Sanctis, ma rivisitato per tutt*

Acknowledgments

WHEN I took my Power Electronic Systems II exam, I couldn't predict that moment would turn into a starting point, rather than a finish line. I sincerely thank Prof. Dr. Johann Kolar for offering me the unique opportunity of joining the PES team and continue my studies at ETH. The institute represents an extraordinary example of what can be achieved with the team effort of inspiring and motivated people: "*if you can dream it, you can do it*". Of Prof. Dr. Johann Kolar, I could appreciate not just his immense technical knowledge, but also his fine sense for understanding people. I also very much thank him for all the valuable advice on my project and articles, with a solution-oriented approach in front of both technical and non-technical challenges. Furthermore, I express my gratitude for the valuable opportunity to take over teaching responsibilities. Teaching has always been something that I've resonated with for a long time. Over the past years, I have had the pleasure of supervising the electric machines laboratory course and the exercise sessions of the lectures on electric machines.

I am honored to have Prof. Dr. Hans-Peter Nee from the KTH Royal Institute of Technology, Stockholm, as a co-examiner. Thank you very much for taking the time and attention to read my thesis and attending my examination. Moreover, I would like to thank Prof. Dr. Ulrike Grossner for chairing my doctoral examination.

I owe a particular thank you to my co-supervisor, Dr. Dominik Bortis. From him, I learned to be a sharper engineer, critically questioning assumptions and results with attention to details and consistency. His broad expertise and inner desire to multiply knowledge taught me a lot on the entire spectrum of power electronics and mechatronics, from the first principles to hardware commissioning. I also had the pleasure of assisting him with the lectures on electric machines and occasionally discussing the related teaching challenges.

A great thank you goes to the *ShuttlePump* project partners at the *Charité, Berlin* and the *Medical University of Vienna*, namely ap. Prof. Dr. Marcus Granegger, Tim Bierewirtz and Krishnaraj Narayanaswamy. I am grateful for the very constructive collaboration, the interdisciplinary exchange and the positive spirit in tackling exciting challenges to build a working system together.

A special thank you goes to my mentor and friend DDr. Prof. Ass. Spasoje Mirić. He was a guide and reference for me since when I started my master thesis at PES under his supervision. He introduced me to research and life at the institute with a high sense of commitment and always with a good

attitude. The many interesting discussions and experiences we shared make me wish our paths could cross again soon, both personally and professionally.

A big thank you goes to the PES team, embracing the good ‘PES Spirit’ and creating an enthusiastic and engaging atmosphere at the institute. I start with Dr. Yunni Li – with whom I had the pleasure of sharing office, conversations, and support, and continue with the doctoral students and graduates of ‘my generation’: Ivana Bagarić – we enjoyed teaming up to supervise the electric machines laboratory, Reto Bonetti – we shared many tips and insights on mechatronics projects, Emanuel Hubmann – a reference for patience and positive attitude, Neha Nain – talented, committed, and helpful for any power electronics question, Gwendolin Rohner – we did a lot of fun sports and traveling together, Dr. Marc Röthlisberger, and Dr. Daifei Zhang. Thanks also to the newer talents of PES: Elias Bürgisser, Saransh Chhawchharia – how quickly can you click with a person, Andreas Horat – of invaluable support in the last stage of the *ShuttlePump* commissioning, Luc Imperiali, Sven Weihe – a continuous discovery, and Patrick Ziegler. I wish them all success in tackling the challenges of the upcoming years. Furthermore, I thank the senior and post-doctoral researchers Dr. Jonas Huber, Dr. Florian Krismer, Dr. David Menzi, and Dr. Jannik Schäfer. Thanks also to the alumni of the ‘previous generation’ of PES that I had the pleasure to share some time with, namely Dr. Marcel Alexander-Schuck, Dr. Jon Azurza Anderson, Dr. Michael Antivachis, Dr. Pedro Bezerra, Dr. Julian Böhler, Dr. Piotr Czyż, Dr. Mattia Guacci, Dr. Thomas Guillod, Dr. Michael Haider, Dr. Morris Heller, Dr. Gustavo Knabben, Dr. Mario Mauerer, Dr. Dominik Neumayr, Dr. Pascal Niklaus, and Dr. Panteleimon Papamanolis. I would also like to thank the many academic guests that I met throughout my stay at PES, in particular Giacomo Andrioli, Dr. Davide Biadene, Dr. Rafał Kopacz, Dr. Thomas Langbauer, and Dr. Junzhong Xu.

I warmly thank Peter Seitz for his help and advice for any technical, soldering, and equipment-related issue, always provided with kindness, patience, and competence. Moreover, it goes without saying that the institute could not work as it does without the PES administrative team, so many thanks to Prisca Maurantonio, Yvonne Schnyder-Lieberherr, Nadine Wacha, and, formerly, Roswitha Coccia, and Monica Kohn-Müller for their valuable support, organization, patience, and friendliness. Many thanks also to the IT team around Marina Eisenstat and Edoardo Talotti.

I am very much indebted to the team of the D-ITET mechanical workshop. Their work was essential to realizing the motor prototype and test bench of the *ShuttlePump*, manufacturing extremely high-quality mechanical parts,

and performing the numerous further modifications on demand. A sincere thank you to Silvio Scherr – for the countless visits and discussions, Cyrill Béguin, Oliver Knecht, Urs Rohner, and, formerly, Stefan Brassel and Stephan Siegrist. Without their availability, expertise, and support neither this project, nor any other mechatronic project, could have been conducted.

I also thank all the motivated bachelor, semester, and master students that I had the pleasure to supervise during my doctoral studies for their contributions, namely Benjamin Weinhold, Wisnu Lang, Raffael Senti, Luca Dragomirovic, Jeroen Buitendijk, Micha Stulz, Pascal Schmid, Michael Lustenberger, and Iancu Radu. Additionally, I gladly include the teaching assistants of the electric machines laboratory, with whom we shared many interesting discussions, namely Christof Stäger, Luca Vogel, Renato Lazzarini, and Ali Doruk Bekatli.

A big thank you goes to Emilio Benenati, good friend, smart colleague, and passionate researcher with whom I started my long journey both in the world of engineering and in Zürich at ETH. Without him, many things would be certainly different today. Then, I can't miss to thank my everlasting friends Ciccio, Davide, Giulio, Andrea, Gianluca, and Bruno, last true romantics scattered across Europe. My life would be much less interesting without them, and I would have not discovered the wonders of music and art. A particular thank you goes to my friend Federico Roy, for the reciprocal support during lockdown days first and in life then. He was key to shape my personality, positive attitude towards others, and understanding what my needs and limits are. My friend Julian Förster deserves a special thank you for all his support throughout the entire duration of my doctoral studies. He is an inspiring model, from whom I always have something to learn, and which I admire for his balance, diligence, kindness, and optimism. A warm thank you certainly goes to Jan Speckien, always interested in my progress and well-being, and generous with advice since the time we were flat mates. Likewise, a big thank you to Varsha Behrunani for her loyal friendship, stemmed from hard working times we shared together.

Finally, I owe the biggest thank you to my parents Domenico and Anna Rosa and my sister Alessia for their unconditional love. With their commitment, sacrifice, vision, care, and constance, they allowed me to become who I am today, and to choose any path in life I could desire.

Thanks! Merci! Grazie a tutti!

Rosario V. Giuffrida

Zurich, February 2024

Abstract

CONCURRENTLY to the ageing society in industrial nations, the number of people suffering from severe heart failure has registered a steady increase over the last decades. At the end stage, a heart transplantation is often the only effective long-term treatment. However, the number of suitable donor hearts remains extremely limited. Total artificial hearts (TAHs) are a promising solution to completely replace a failing heart, but the currently available concepts still suffer from limited durability and relatively high complication rates, which can also be related to their complex design (with too many moving parts, such as valves or flexible membranes) and limited hemocompatibility (due to high velocities and shear rates within the pumps). At the *Deutsches Herzzentrum der Charité* in Berlin, a radically new low-complexity pumping concept was proposed that aims to overcome the current drawbacks of TAHs. The ‘*ShuttlePump*’ is an implantable TAH offering a pulsatile physiological blood flow with only one moving part. This requires a specially designed piston that follows a combined linear-rotary trajectory, supported radially by a hydrodynamic journal bearing. Such concept is for the first time implemented as a demonstrator system in the course of this research project. This is possible by bringing together experts from very diverse domains (actuators, power electronics, fluid dynamics, medicine, surgery, etc.) in the context of a collaboration between *Charité Berlin*, the *Medical University of Vienna* and *ETH Zurich*. The fluid-dynamic, clinical and physiological aspects of the pump were preliminarily investigated at *Charité Berlin* and the *Medical University of Vienna*. To enable the pumping operation, a *drive system* is needed, which consists of an electric machine serving as Linear-Rotary Actuator (LiRA) together with the corresponding position sensors and power electronics (inverter and control) unit. This essential part of the system is developed in the context of this thesis at the Power Electronic Systems Laboratory of ETH Zurich. From the feasibility studies of the project partners, the constraints and requirements for the electromechanical actuation design are defined, particularly in terms of spatial constraints, hydraulic load force/torque, bearing radial load, mission profile, power losses, and mass. As a result, the definition of an appropriate actuation concept and the subsequent design of the LiRA are very challenging and need to address several trade-offs. Due to the inherent unbalance in the required mechanical output power for linear and rotary actuation (3.6 W versus 0.1 W, respectively), the two building blocks of the LiRA are designed individually. The Linear Actuator (LA) has the largest power requirements, and it is therefore analyzed first. The chosen Permanent Magnet Synchronous Machine (PMSM)

topology is a tubular LA to maximize the active area for force generation. The Finite Element Method (FEM) optimization explores the crucial trade-off between ohmic power losses (10 W limit) and radial magnetic attraction force (to be sustained by the hydrodynamic bearing; 25 N limit) for a peak required axial force of 43 N. The selected design is realized as a hardware prototype and verified experimentally, attaining 7.9 W of average ohmic losses over a period of operation and 23.8 N of maximum radial attraction force. The Rotary Actuator (RA) is then integrated in the remaining volume closely to the designed LA. Due to the tight spatial constraints, the PMSM design features only a partial coverage of both the rotor PMs and the stators, which results in an irregular circumferential torque profile with pronounced cogging. This is investigated with FEM simulations, and the trade-off between cogging-induced speed ripple in the operational range of 90-300 rpm and ohmic losses for a fixed required torque of 3.1 mN m is highlighted. Importantly, the interactions of the proposed RA with the previously realized LA are investigated. The experimental measurements on the RA prototype indicate that the proposed concept can meet the continuous torque requirement with 324 mW of power losses. With the LiRA designed, the next step is to accurately measure and control the linear-rotary position of its moving part (mover), which is integrated in the piston. For this purpose, a Printed Circuit Board (PCB)-integrated linear-rotary Eddy-Current Sensor (ECS) is realized. The sensor is obtained by extending a commercially available rotary sensor with two post-processing options to extract also the linear position information. The realized ECS prototype offers position accuracies below 100 μm and around 5°, with adequately large bandwidth up to 10 kHz. The possibilities offered by eddy-current sensing are further explored with the analysis and design of an ECS capable of measuring through a conductive barrier. This ‘through-the-walls’ concept may be used for the *ShuttlePump* in case of a metallic enclosure, or more in general for any other high-purity application requiring a sealed actuator. The achievable sensitivity and bandwidth, as well as the temperature stability of the sensor, are investigated, and design rules are provided. A prototype of the sensor is realized, which offers a position resolution down to 1 μm and 10 kHz of bandwidth. All the building blocks are finally brought together for the closed-loop linear-rotary position control of the LiRA. An electromechanical dynamic model of the LiRA is derived and used to design the controller. Its hardware implementation includes the realization of a compact inverter and control unit. Synchronized linear-rotary position control is demonstrated on the complete prototype, with tracking of the specified motion profile within 1 mm and 5° of error. The control system

capabilities are tested even under heavy axial force disturbances, with a controllable load emulating the required hydraulic force. As a result, the realized drive system meets the provided specifications and requirements and can hence be used to enable the pumping operation of the *ShuttlePump*. This way, the feasibility of the device as a novel, reliable, durable, and implantable TAH can be demonstrated with the very next steps of *in vitro* and *in vivo* testing. Assuming a successfully completed test phase, the new device will represent a major step towards improved TAH systems and/or improved long-term prognosis for end-stage heart failure patients.

Sommario

IN concomitanza con il progressivo invecchiamento della popolazione nei paesi industrializzati, il numero di pazienti che soffrono di insufficienza cardiaca grave ha registrato un sostenuto aumento negli scorsi decenni. Allo stadio finale, un trapianto di cuore è di solito l'unica terapia efficace a lungo termine. Tuttavia, il numero di donatori di cuore idonei rimane estremamente limitato. I cuori artificiali totali (TAHs) rappresentano una soluzione promettente per sostituire completamente un cuore in difficoltà, ma i sistemi attualmente disponibili non sono ancora abbastanza durevoli e i tassi di complicazioni sono relativamente elevati, il che può essere anche legato al loro design spesso complesso (con troppe parti in movimento, come valvole o membrane flessibili) e alla scarsa emocompatibilità (a causa delle elevate velocità di taglio all'interno delle pompe). Al *Centro Cardiologico Tedesco della Charité (Deutsches Herzzentrum der Charité)* a Berlino è stato ideato un principio di pompaggio radicalmente nuovo e dalla bassa complessità, in modo da superare gli attuali limiti dei cuori artificiali. La *'ShuttlePump'* è un TAH impiantabile, che offre un flusso sanguigno pulsatile e fisiologico utilizzando una singola parte mobile. Ciò richiede un pistone dalla forma speciale, che segue una traiettoria combinata lineare e rotazionale, supportato radialmente da un cuscinetto idrodinamico. Tale sistema è implementato per la prima volta come prototipo dimostrativo nel corso di questo progetto di ricerca. Ciò è possibile unendo le forze di esperti in campi di ricerca molto diversi (attuatori, elettronica di potenza, fluidodinamica, medicina, chirurgia, ecc.) nel contesto di una collaborazione tra *Charité Berlin*, la *Università di Medicina di Vienna* e il *Politecnico Federale (ETH) di Zurigo*. Gli aspetti fluidodinamici, clinici e fisiologici della pompa sono stati preventivamente studiati a *Charité Berlin* e all'*Università di Medicina di Vienna*. Per avviare il pompaggio, è necessario un sistema di azionamento (driver) composto da un motore elettrico, che funge da Attuatore Lineare e Rotazionale (LiRA), e dai relativi sensori di posizione e unità elettronica di potenza (inverter e circuiti di controllo). Questa parte fondamentale del sistema è sviluppata nel contesto della presente tesi al Power Electronic Systems Laboratory del *Politecnico Federale di Zurigo*. A partire dagli studi di fattibilità dei partner del progetto, vengono definiti i vincoli e i requisiti tecnici per la progettazione dell'azionamento elettromeccanico, in particolare in termini di dimensioni, forza/coppia di carico idraulico, carico radiale sui cuscinetti, profilo di missione, potenza dissipata e massa. Di conseguenza, la definizione di un adeguato sistema di azionamento e la successiva progettazione del LiRA sono molto impegnative e non senza diversi compromessi. A causa dello squilibrio intrinseco tra la potenza meccanica richiesta

in uscita per l'attuatore lineare e quello rotazionale (rispettivamente 3.6 W e 0.1 W), le due parti del LiRA sono progettate separatamente. L'Attuatore Lineare (LA) ha requisiti di potenza più elevati ed è quindi analizzato per primo. La topologia della macchina sincrona a magneti permanenti (PMSM) scelta è un attuatore lineare tubolare, così da massimizzare l'area attiva, che contribuisce alla generazione di forza. L'ottimizzazione dell'attuatore è condotta con simulazioni FEM (Metodo degli Elementi Finiti) ed esplora il compromesso cruciale tra la potenza ohmica dissipata (limite di 10 W) e la forza di attrazione magnetica radiale (da sostenere dal cuscinetto idrodinamico, limite di 25 N) per una forza assiale massima richiesta di 43 N. Il design selezionato è realizzato come prototipo hardware e verificato con misure sperimentali, ottenendo 7.9 W di potenza ohmica dissipata media per un periodo di operazione e 23.8 N di forza massima di attrazione radiale. Successivamente, l'Attuatore Rotazionale (RA) viene integrato nel volume rimasto disponibile attorno al LA progettato. A causa degli stretti vincoli spaziali, la topologia della PMSM presenta solo una copertura parziale sia dei PMs su rotore che degli statori, ottenendo un profilo di coppia irregolare lungo la circonferenza e con marcato *cogging*. Tale aspetto è investigato con simulazioni FEM, evidenziando il compromesso tra la variazione di velocità indotta dalla coppia di *cogging* nell'intervallo operativo di 90-300 rpm e la potenza ohmica dissipata per una coppia richiesta fissa di 3.1 mN m. Per la loro particolare importanza, vengono esaminate le interazioni dell'RA scelto con l'LA precedentemente realizzato. Le misure sperimentali sul prototipo dell'RA indicano che la topologia proposta può soddisfare il requisito di coppia continua con 324 mW di potenza dissipata. Una volta progettato il LiRA, il passo successivo è misurare e controllare con precisione la posizione lineare e rotazionale della sua parte mobile (*mover*), integrata nel pistone. A questo scopo, viene realizzato un sensore di posizione lineare-rotazionale a correnti parassite (ECS), integrato su scheda con circuito stampato (PCB). Il sensore è ottenuto estendendo un sensore di posizione rotazionale già disponibile commercialmente, utilizzando due diverse opzioni per estrarre anche una misura della posizione lineare. Il prototipo di ECS realizzato offre precisioni di posizionamento inferiori a 100 μm e circa 5° , con una larghezza di banda adeguatamente ampia fino a 10 kHz. Le possibilità offerte dai sensori a correnti parassite sono esplorate ulteriormente con l'analisi e progettazione di un ECS in grado di misurare attraverso una barriera conduttiva. Tale sensore che misura 'attraverso le pareti' può essere utilizzato per la *ShuttlePump* qualora un involucro metallico fosse necessario, o più in generale per qualsiasi altra applicazione ad alta purezza che richieda un attuatore interamente sigillato. Vengono studiate la sensibilità e la larghezza

di banda ottenibili, nonché la stabilità termica del sensore, e vengono fornite regole di progettazione. Viene realizzato un prototipo del sensore, che offre una risoluzione della posizione fino a $1\ \mu\text{m}$ e una larghezza di banda di 10 kHz. Tutte le parti studiate sono infine combinate e interfacciate per il controllo di posizione lineare-rotazionale ad anello chiuso del LiRA. A tal fine, viene derivato un modello dinamico elettromeccanico del LiRA, utilizzato per progettare il controllore, la cui implementazione hardware richiede la realizzazione di un inverter compatto e di un'unità di controllo. Il controllo sincronizzato della posizione lineare-rotazionale è dimostrato utilizzando il prototipo completo, con un tracciamento della traiettoria specificata entro 1 mm e 5° di errore. Le capacità del sistema di controllo sono testate anche in presenza di elevati forze assiali di disturbo, con un carico controllabile che simula la forza idraulica richiesta. Il sistema di azionamento realizzato soddisfa le specifiche e i requisiti stabiliti e può quindi essere utilizzato per abilitare l'operazione di pompaggio della *ShuttlePump*. In questo modo, la fattibilità del dispositivo come TAH innovativo, affidabile, duraturo e impiantabile può essere dimostrata con le successive fasi di test *in vitro* e *in vivo*. Assumendo una fase di test completata con successo, il nuovo dispositivo rappresenterà un passo importante per migliorare i TAHs e/o migliorare la prognosi a lungo termine per i pazienti affetti da insufficienza cardiaca in fase terminale.

Abbreviations

AC	Alternating Current
ADC	Analog-to-Digital Converter
AGC	Automatic Gain Control
AMB	Active Magnetic Bearing
AO	Aorta
BW	Bandwidth
CFD	Computational Fluid Dynamics
CMRR	Common-Mode Rejection Ratio
CNC	Computer Numerical Control
DC	Direct Current
DDS	Direct Digital Synthesis
DOB	Disturbance Observer
DSB-AM	Double-Sideband Amplitude Modulation
ECS	Eddy-Current Sensor
FEM	Finite Element Method
FOC	Field-Oriented Control
FPGA	Field-Programmable Gate Array
IPM	Interior Permanent Magnet
LA	Linear Actuator
LiRA	Linear-Rotary Actuator
LPF	Low Pass Filter
LVAD	Left Ventricular Assist Device
MCS	Mechanical Circulatory Support
MCU	Microcontroller Unit
MFPA	Maximum Force per Ampere
MMF	Magnetomotive Force
MTPA	Maximum Torque per Ampere
NDT	Non-Destructive Testing
PA	Pulmonary Artery
PCB	Printed Circuit Board
PEEK	Polyether Ether Ketone
PID	Proportional-Integral-Derivative
PMSM	Permanent Magnet Synchronous Machine
POM	Polyoxymethylene
PTFE	Polytetrafluoroethylene
PV	Pulmonary Vein
PWM	Pulse Width Modulation

Abbreviations

RA	Rotary Actuator
RBP	Rotary Blood Pump
RX	Receive
SISO	Single Input Single Output
SPI	Serial Peripheral Interface
SPM	Surface Permanent Magnet
SRF	Self-Resonant Frequency
TAH	Total Artificial Heart
TET	Transcutaneous Energy Transfer
TLA	Tubular Linear Actuator
TX	Transmit
VAD	Ventricular Assist Device
VC	Vena Cava
VSD	Variable Speed Drive

Contents

Acknowledgments	v
Abstract	ix
Sommario	xiii
Abbreviations	xvii
1 Introduction	1
1.1 Mechanical Circulatory Support	1
1.2 State of the Art and Limitations of TAHs	4
1.3 The <i>ShuttlePump</i> TAH	5
1.4 Challenges	6
1.5 Aims and Contributions	7
1.6 List of Publications	8
1.6.1 Journal Papers	8
1.6.2 Conference Papers	9
1.6.3 Workshops and Seminars	10
1.7 Outline of the Thesis	10
2 The <i>ShuttlePump</i>: Pumping Principle and Requirements	13
2.1 Introduction	13
2.2 Mechanical Design and Geometry	13
2.3 Pumping Principle	15
2.4 Drive System Requirements	16
2.5 Summary	20
3 Linear Actuator Design and Verification	23
3.1 Introduction	23
3.2 Machine Analysis and Dimensioning	24
3.2.1 LiRA Concept: Independent Actuators	24
3.2.2 PMSM Topology Selection for the TLA	25
3.2.3 Variable Air Gap Reluctance Effects	27
3.2.4 Analysis and Dimensioning from First Principles	29
3.3 FEM Machine Optimization	32
3.3.1 2D FEM Model	33
3.3.2 Three-Steps Optimization Procedure	36
3.3.3 Optimization, Design Space and Selected Design	39
	xix

3.4	Hardware Prototype	42
3.4.1	Stator Realization	43
3.4.2	Mover Realization	45
3.4.3	Experimental Test Bench	46
3.5	Experimental Verification	48
3.5.1	Radial Attraction Force Measurements	48
3.5.2	Machine Constant - Axial Force Profile	48
3.6	Summary	51
4	Rotary Actuator Design and Verification	53
4.1	Introduction	54
4.2	Spatial Constraints and Requirements for the RA	54
4.3	Proposed Machine Concept	57
4.3.1	Placement of the RA PMs and Stators	57
4.3.2	PMSM Topology Selection	59
4.3.3	Main RA Design and Integration Aspects	61
4.4	FEM Machine Optimization	64
4.4.1	2D FEM Model of the RA	64
4.4.2	3D FEM Model of the Full LiRA	67
4.4.3	RA Optimization Procedure	68
4.4.4	Integration and Interactions with the LA	72
4.5	Hardware Prototype	75
4.5.1	Stator Realization	75
4.5.2	Rotor Realization	78
4.5.3	Effect of the Stator Assembly Tolerances	78
4.5.4	Experimental Test Bench	80
4.6	Experimental Verification	81
4.7	Summary	83
5	Integrated Linear-Rotary Eddy-Current Sensors	85
5.1	Introduction	86
5.2	Linear Sensor's Operating Principle	87
5.3	Extension to a Linear-Rotary Sensor	90
5.3.1	Option 1: Magnitude and Argument	90
5.3.2	Option 2: Frequency and Argument	93
5.4	Hardware Prototype	94
5.4.1	Measurement Requirements	94
5.4.2	PCB-Embedded Realization	95
5.5	Measurements and Results	96
5.5.1	Option 1: Magnitude and Argument	96

5.5.2	Option 2: Frequency and Argument	99
5.5.3	Comparison and Discussion	99
5.5.4	Real Mission Profile - Dynamic Operation	100
5.6	Summary	101
6	Linear-Rotary Position Control	103
6.1	Introduction	103
6.2	ShuttlePump LiRA and Motion Control Requirements	104
6.2.1	Parameters of the LiRA and Linear-Rotary Position Sensors	104
6.2.2	Motion Control Requirements for the LiRA	108
6.3	Electro-Mechanical System Modeling	111
6.3.1	Linear/Axial Position Dynamics	111
6.3.2	Rotary/Angular Position Dynamics	113
6.3.3	Electrical Dynamics in the Mover-Oriented Frame	113
6.4	Control System Design	116
6.4.1	Control Structure and Specifications	116
6.4.2	Current Controller Design	117
6.4.3	Linear/Axial Position Controller Design	119
6.4.4	Rotary/Angular Position Controller Design	123
6.4.5	Controller Discretization	123
6.5	Hardware Implementation	126
6.5.1	Inverter and Control Unit	126
6.5.2	Experimental Test Bench	128
6.6	Experimental Measurements and Verification	130
6.6.1	Linear-Rotary Position Control: Tracking with No Load	130
6.6.2	Linear-Rotary Position Control: Tracking with Axial Load	132
6.7	Summary	135
7	Eddy-Current Position Sensor Through Conductive Barriers	137
7.1	Introduction	138
7.2	Operating Principle of the Conventional ECS	140
7.2.1	Equivalent Transformer Model	141
7.2.2	Impedance Variations from FEM Simulations	143
7.3	Analysis of the ECS Measuring Through Walls	144
7.3.1	Impedance Variations from FEM Simulations and Op- timal Excitation Frequencies	146
7.3.2	General ECS Design Guidelines	149
7.3.3	Extended Equivalent Transformer Model	149

7.3.4	Optimal PCB-Embedded Coil Design Considerations	152
7.3.5	Experimental Impedance Measurements and Model Verification	154
7.4	Influence of the Temperature on the Sensor's Output	155
7.5	Sensor Interface and Signal Conditioning	159
7.5.1	Overview of the Proposed Measurement Circuit	159
7.5.2	Analysis and Selection of the AC Wheatstone Bridge Configuration	161
7.5.3	Amplification and Demodulation Stage	165
7.5.4	Realized Measurement/Evaluation Board	165
7.6	Measurements and Results	167
7.6.1	Measurement Circuit Verification	167
7.7	Summary	170
8	Conclusion and Outlook	173
8.1	Summary and Findings	173
8.2	Outlook and Future Research	175
	Appendices	179
A	Measurements of the Undesired Air Gaps in the RA	181
B	Post-Processing of the Linear-Rotary Measurement Signals	183
C	Input Impedance of the Excitation Coil for the ECS Through the Walls	185
	Bibliography	187
	Curriculum Vitae	201

1

Introduction

HEART failure is a serious disease currently affecting more than 26 million people worldwide, and the number of cases is expected to increase in the near future, also due to the progressive aging of the population [1–3]. Despite considerable progress in treatments and prevention, the rates of mortality and morbidity remain elevated, with a consequent impact on the patients' quality of life. A milestone in end-stage heart failure treatment was reached with the first heart transplantation, performed in 1967 [4]. Still today, this remains the gold standard long-term treatment for carefully selected end-stage heart failure patients, with a median survival of about 11 years, with 82% 1-year survival rate, and 69% after 5 years [5, 6]. However, the main limitation is the availability of organs from donors, which is extremely scarce [7]. As a result, up to 20% of the patients die while on the waiting list for heart transplantation [8]. Furthermore, there are still cases when transplantation is not even possible due to graft failure, rejection, or other systemic diseases. For these reasons, there is an urgent need for alternative, long-term solutions.

1.1 Mechanical Circulatory Support

Mechanical Circulatory Support (MCS) proved to be a very promising treatment option for end-stage heart failure patients who are not eligible for heart transplantation. It is possible to distinguish between two primary types of MCS devices, specifically Ventricular Assist Devices (VADs) and Total Artificial Hearts (TAHs). As illustrated in **Fig. 1.1 (a)**, VADs are designed to support a failing heart and restore physiological rates of blood flow. Since they mimic the pumping functionality of a single ventricle, they can be relatively simple and compact. This favored the development of implantable (Left)

VADs, which are already in use as destination therapy and demonstrated to be comparable to a full heart transplantation in terms of survival rates in the first years of implantation [9]. As the name suggests, and as shown in **Fig. 1.1 (b)**, TAHs completely replace a failing heart instead. These devices are especially needed in all those cases where VADs are not applicable, e.g., in the case of severe biventricular heart failure [10].

At the core of both types of devices there is blood pumps employing various pumping principles. One main discriminant is the type of blood flow provided by the pump. Positive displacement pumps generate a volume variation in a blood chamber in a fill-and-eject cycle to offer a pulsatile blood flow that emulates the physiological one. On the contrary, continuous flow blood pumps lack this feature, but can be very compactly and efficiently realized as Rotary Blood Pumps (RBPs). They typically exploit a fast spinning impeller, equipped with blades, to accelerate the blood. RBP can feature either an axial flow, i.e., with the blood meeting the impeller along its rotation axis and being accelerated along the same direction, or a centrifugal flow, for which the direction of propulsion is along the plane perpendicular to the rotation axis. The employed electrical motors are usually Permanent Magnet Synchronous Machines (PMSMs), which are key to the compactness and efficiency of RBPs. These lend themselves very well to the integration of magnetic bearings, which are used in the most advanced RBPs to support the spinning impeller without any contact.

The application of these pumping principles has been evident in the development of various (Left) VADs, facilitating their successful implantation.

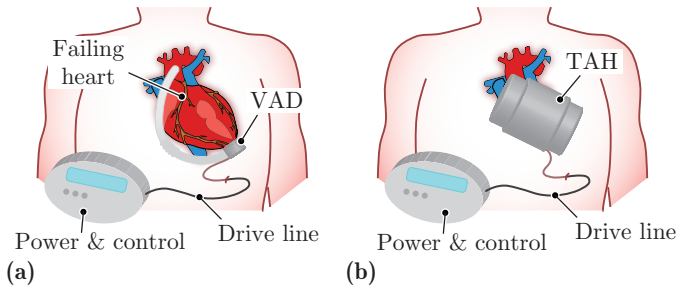


Fig. 1.1: Two main types of implantable MCS devices, connected to the extracorporeal power and control unit via percutaneous drive lines. **(a)** The VAD supports a failing heart in its pumping function to restore physiological rates of blood flow. **(b)** The TAH completely replaces the patient's heart instead.

Indeed, it is possible to distinguish up to three generations of clinically available devices according to their flow mechanics [11].

Irrespective of the specific pumping principle employed, MCS devices share common key requirements and characteristics, such as:

- ▶ *Compactness*: the smaller the volume occupied by the device, the easier its usage and/or implantation is;
- ▶ *Efficiency*: both from the hydraulic and electromechanical points of view. Especially for electrically actuated systems, high efficiency is beneficial not just because they are often battery-powered, but also to limit heat generation in the implant due to power losses. Excessively high temperatures can indeed result in blood damage;
- ▶ *Durability* and *reliability*: especially if implanted, the blood pump should ideally operate for as long time as possible to avoid any (inevitably surgical) replacement. Therefore, each and every other part of the device is simply not allowed to fail. In terms of reliability, especially challenging is the compromise between simplicity and redundancy;
- ▶ *Hemocompatibility*: elevated shear rates in the generated flow can lead to blood trauma, i.e., damage to the blood cells. This should clearly be minimized, also to reduce the risk of adverse events such as thromboembolism and related complications.

Each pumping principle scores differently in these aspects, with corresponding advantages and disadvantages. Therefore, the research and development of new MCS devices promising to meet most of the aforementioned requirements is definitely ongoing. A particularly determining aspect is the employed type of bearings (mechanical, magnetic, electromagnetic or hydrodynamic), with non-contact solutions performing the best in terms of both durability and hemocompatibility.

Finally, it should not be forgotten that a working blood pump is ultimately an electromechanical system consisting of not only the machine itself, but also of its power supply (the inverter feeding the machine with AC currents from a DC supply), measurement and control systems needed to guarantee stable operating conditions. Such Variable Speed Drive (VSD) systems need to be analyzed and designed in each of their components to reliably bring the blood pumps into operation.

1.2 State of the Art and Limitations of TAHs

As mentioned, TAHs represent a promising alternative solution to completely replacing a failing heart. Indeed, they have been the subject of continued interest and research in the last decades, with steady advancements and the development of numerous concepts [12–22]. From the very first pneumatic/hydraulic and electromechanical concepts conceived to provide pulsatile blood flow via a positive volume displacement [15–19], TAHs progressively incorporated RBPs in their design and turned into more compact, efficient, and reliable devices [20–22]. Some remarkable examples of pulsatile flow TAHs include the Cardiowest TAH (SynCardia Systems, Inc.) or the CARMAT TAH (Carmat SA), both pneumatically driven. Furthermore, the Abioco TAH (Abiomed, Inc.), Rein Heart TAH [6] and Realheart TAH [7] still offer a pulsatile flow, but based on an electrohydraulic actuator. The Cleveland continuous flow TAH [9], the BiVACOR TAH [10], and the OregonHeart TAH (OregonHeart, Inc.) are instead examples of electrohydraulic RBPs, the last one also featuring hydrodynamic bearings. Despite the blood pumps used for TAHs often share the same pumping principles as used for VADs, TAHs have not yet reached a mature stage as a viable alternative for implantation, and are more often used as a bridge to transplant.

This is clearly indicated by the number of MCS implantations from recent statistics, which is sixty times smaller for TAHs compared to VADs. The reason for this pronounced difference lies in the limitations of currently available TAHs. In fact, they suffer from limited durability and/or relatively high complication rates, which can be related to their complex design and limited hemocompatibility [23, 24]. For instance, positive displacement blood pumps with pneumatic/hydraulic actuation utilize diaphragms and valves to create the pulsatile flow, which constitute a risk for potential failure. Even when the volume displacement is generated directly via electromechanical actuation, size and technical complexity are still the main obstacles to long-term implantation [8]. On the other hand, TAHs based on RBPs cause high shear rates in the blood flow due to their fast-spinning impeller, with the risk of excessive hemolysis, which can lead to gastrointestinal bleeding and thromboembolic complications, among others [12]. It is therefore apparent that the need for fully implantable, reliable, and hemocompatible TAHs is still high: as a matter of fact, no TAH has been approved for long-term treatment so far.

1.3 The *ShuttlePump* TAH

With the ambitious target of overcoming the current limitations of TAHs, the *ShuttlePump* (cf. **Fig. 1.2**) was proposed at the *Deutsches Herzzentrum der Charité* in Berlin [25]. Its radically new, low-complexity pumping principle provides a pulsatile flow with only one moving part, removing the need for any prone-to-failure valve or flexible membrane. Furthermore, the *ShuttlePump* operates with low frequencies, and hence low velocities and shear rates within the pump, which cause very low blood trauma compared to a fast spinning impeller in RBPs.

The pumping principle of *ShuttlePump* relies on a specially designed piston following a combined linear-rotary motion. This is enclosed in a cylindrical housing and divides it into two chambers serving as left and right heart ventricles. Each chamber has an inlet and an outlet. With the linear motion, the shuttling piston pushes the blood into circulation out of one chamber, while the other one fills up. At the same time, the piston rotates continuously around its axis and its rotary position is synchronized to the linear one. This way, thanks to the special shape of its blades, the opening and closing of the

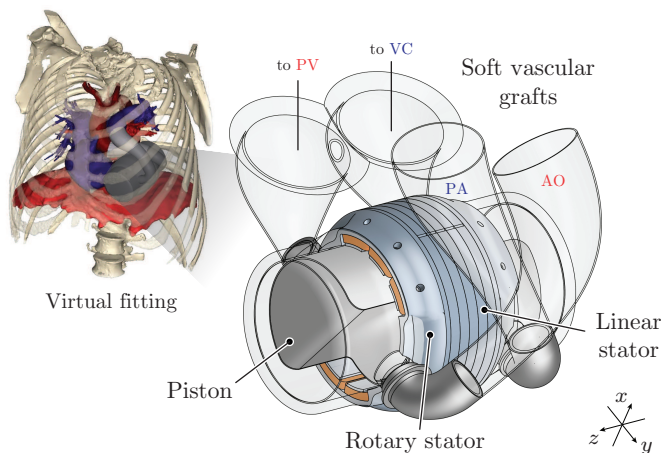


Fig. 1.2: The implantable TAH *ShuttlePump*, conceptual illustration with virtual fitting in a patient with biventricular failure (ethics approval obtained at *Medical University of Vienna*). The TAH is connected via soft vascular grafts to the Aorta (AO), the Vena Cava (VC) and the Pulmonary Artery (PA) and Vein (PV).

pump's inlets and outlets is controlled. Furthermore, continuous rotation of the blood-immersed piston establishes a hydrodynamic journal bearing, which supports it radially during pumping operation, avoiding contact with the pump enclosure. More comprehensive details on the operating principle, dimensions and requirements of the device are discussed in **Chapter 2**.

The *ShuttlePump* is currently under development in the context of a research collaboration between the Power Electronic Systems Laboratory of *ETH Zurich*, the *Deutsches Herzzentrum der Charité* and the *Medical University of Vienna* [25–28]. Concomitantly to the proposal of the new pumping concept, the fluid-dynamic, clinical, and physiological aspects of the *ShuttlePump* have been studied at *Charité* and the *Medical University of Vienna* [26]. To enable the pumping operation and finally assess the feasibility of the overall system, a suitable *drive system* is needed, which is the topic of this dissertation. The drive system consists of the electric motor serving as Linear-Rotary Actuator (LiRA), together with the corresponding position sensors and power electronics (inverter and control) unit. In order to guarantee the pump's functionality, it is necessary to provide about 45 N of peak force for the linear motion and about 3 mN m of continuous torque for the rotation. Force and torque generation should not exceed an average power loss limit of 10 W in a volume of about 0.4 dm³. The synchronized linear-rotary motion of the piston needs to be performed up to a frequency of 5 Hz with a positioning accuracy of 1 mm and 5°. If the employed actuation concept is kept as simple as possible, the *ShuttlePump* could represent a promising example of a next-generation implantable TAH for long-term treatment.

1.4 Challenges

The development of a linear-rotary drive system for the *ShuttlePump* comes with a number of challenges, as collected in the following list:

- ▶ *Simplicity*: for improved reliability, the actuation concept needs to remain simple. This is challenging for highly integrated LiRAs, as the number of required phases and sensors, and hence the overall complexity, can easily increase;
- ▶ *Tight spatial constraints*: compactness is a requirement of utmost importance for an implantable TAH. However, the geometry of the *ShuttlePump* imposes many constraints to the LiRA design, which highly restrict the possible placement options for the motors and position sensors;

- ▶ *Least power losses*: as with any MCS device, local temperature increases in the blood in the pump must be avoided. The *ShuttlePump* is especially sensitive due to the employed hydrodynamic bearing, consisting of a thin layer of blood, which can heat up rapidly. Limiting the power losses of the LiRA reveals fundamental trade-offs that appear during machine optimization;
- ▶ *Synchronized motion control*: the combined linear and rotary motion has to be precisely controlled and synchronized in order to achieve proper pumping operation. This requires not just an appropriate control system, but contactless sensors that also need to be fitted in the pump's volume;
- ▶ *System-level co-design*: the design of each part of the VSD system (motor, inverter, and sensors) is always highly interdependent. Moreover, the external requirements imposed by the application have to be considered and, in some cases, negotiated due to inevitable trade-offs. Frequently, what is favorable from a fluid dynamics or medical standpoint may not necessarily be favorable from a machine design standpoint;
- ▶ *Interdisciplinarity*: last but not least, the research collaboration of which this work is a part requires a high level of coordination and information sharing between three leading research institutions throughout Europe. The added value of the combined expertise in very different research fields comes at the cost of a more challenging decision-making process.

1.5 Aims and Contributions

This aim of this thesis is to propose a LiRA drive system with a high degree of integration for the novel TAH concept *ShuttlePump*, and demonstrate experimentally its functionality and suitability for the application. A summary of the most relevant contributions is provided in the following list:

- ▶ The novel TAH concept is for the first time implemented as a demonstrator system (cf. **Fig. 1.3 (a)**) in the course of this research project. The conceptualization and realization of the system was possible by bringing together experts of very diverse domains (actuators, power electronics, fluid dynamics, medicine, surgery, etc.) in the context of a collaboration between *Charité - Universitätsmedizin Berlin*, the *Medical University of Vienna*, and *ETH Zurich*. The developed knowledge is of

great help in accelerating the development of next-generation TAHs and MCS devices in general.

- ▶ For the LA part of the LiRA, a design procedure for Tubular Linear Actuators (TLAs) with non-stiff bearings (hydraulic, air, or magnetic) is provided. The insights on the emerging trade-offs between power losses and strong radial magnetic attraction forces can easily be extended and translated to similar systems.
- ▶ For the RA part of the LiRA, a spatially highly constrained PMSM design with partial stator and PMs coverage is proposed. This can serve as an example for future constrained designs.
- ▶ The PCB-integrated Eddy-Current Sensor (ECS) design proposed for the *ShuttlePump* represents a compact and accurate solution for highly dynamic and simultaneous linear-rotary position measurement of a moving target.
- ▶ Rule-of-thumbs, optimal coil design guidelines and a temperature sensitivity analysis for a special ECS measuring the position of a moving target behind a conductive barrier are provided. Such a ‘through-the-walls’ measurement concept has only been very partially explored in literature.

1.6 List of Publications

Key insights presented in this thesis have already been published in international scientific journals, conference proceedings, or presented at workshops. The publications created as part of this thesis, or also in the scope of other related projects, are listed below.

1.6.1 Journal Papers

- ▶ **R. V. Giuffrida**, A. Horat, D. Bortis, T. Bierewirtz, K. Narayanaswamy, M. Granegger, and J. W. Kolar, “Linear-Rotary Position Control System with Enhanced Disturbance Rejection for a Novel Total Artificial Heart,” *IEEE Open Journal of the Industrial Electronics Society*, vol. 5, pp. 359-375, 2024. DOI: [10.1109/OJIES.2024.3385865](https://doi.org/10.1109/OJIES.2024.3385865).

- ▶ **R. V. Giuffrida**, R. Senti, D. Bortis, T. Bierewirtz, K. Narayanaswamy, M. Granegger, and J. W. Kolar, “Spatially Highly-Constrained Auxiliary Rotary Actuator for a Novel Total Artificial Heart,” *IEEE Open Journal of the Industrial Electronics Society*, vol. 4, pp. 732-747, 2023. DOI: [10.1109/OJIES.2023.3339838](https://doi.org/10.1109/OJIES.2023.3339838).
- ▶ **R. V. Giuffrida**, R. Senti, J. W. Kolar, T. Bierewirtz, K. Narayanaswamy, M. Granegger, and D. Bortis, “Design and Realization of a Highly Compact Tubular Linear Actuator for a Novel Total Artificial Heart,” *IEEE Journal of Emerging and Selected Topics in Industrial Electronics (Pioneering Work)*, vol. 4, no. 4, pp. 1010-1023, October 2023. DOI: [10.1109/JESTIE.2023.3305939](https://doi.org/10.1109/JESTIE.2023.3305939).
- ▶ **R. V. Giuffrida**, S. Mirić, J. W. Kolar, and D. Bortis, “Highly Dynamic Eddy-Current-Based Sealed Magnetic Bearing Position Measurement with Temperature Drift Correction - “Seeing Through Conductive Walls”,” *IEEE Open Journal of the Industrial Electronics Society*, vol. 3, pp. 252-264, April 2022. DOI: [10.1109/OJIES.2022.3163014](https://doi.org/10.1109/OJIES.2022.3163014).

Moreover, the author had the pleasure to contribute to the following Journal papers:

- ▶ T. Bierewirtz, K. Narayanaswamy, **R. V. Giuffrida**, T. Rese, D. Bortis, D. Zimpfer, J. W. Kolar, U. Kertzscher, and M. Granegger, “A Novel Pumping Principle for a Total Artificial Heart,” *IEEE Transactions on Biomedical Engineering*, vol. 71, no. 2, pp. 446-455, February 2024. DOI: [10.1109/TBME.2023.3306888](https://doi.org/10.1109/TBME.2023.3306888).
- ▶ S. Mirić, **R. V. Giuffrida**, D. Bortis, and J. W. Kolar, “Dynamic Electromechanical Model and Position Controller Design of a New High-Precision Self-Bearing Linear Actuator,” *IEEE Transactions on Industrial Electronics*, vol. 68, no. 1, pp. 744-755, January 2021. DOI: [10.1109/TIE.2020.2992943](https://doi.org/10.1109/TIE.2020.2992943).
- ▶ S. M. Mirić, **R. V. Giuffrida**, D. Bortis, and J. W. Kolar, “Enhanced Complex Space Vector Modeling and Control System Design of Multi-phase Magnetically Levitated Rotary-Linear Machines,” *IEEE Journal of Emerging and Selected Topics in Power Electronics*, vol. 8, no. 2, pp. 1833-1849, June 2020. DOI: [10.1109/JESTPE.2019.2945625](https://doi.org/10.1109/JESTPE.2019.2945625).

1.6.2 Conference Papers

- ▶ **R. V. Giuffrida**, J. W. Kolar, and D. Bortis, “Eddy-Current Linear-Rotary Position Sensor for an Implantable Total Artificial Heart,”

in *Proc. of the 25th International Conference on Electrical Machines and Systems (ICEMS)*, Chiang Mai, Thailand, November 2022. DOI: [10.1109/ICEMS56177.2022.9982894](https://doi.org/10.1109/ICEMS56177.2022.9982894).

- ▶ **R. V. Giuffrida**, S. Mirić, A. Horat, D. Bortis, and J. W. Kolar, “Control System Design and Experimental Verification of a Self-Bearing Double-Stator Linear-Rotary Actuator,” in *Proc. of the 13th International Symposium on Linear Drives for Industry Applications (LDIA)*, Wuhan, China, July 2021. DOI: [10.1109/LDIA49489.2021.9505865](https://doi.org/10.1109/LDIA49489.2021.9505865).
- ▶ **R. V. Giuffrida**, S. Mirić, D. Bortis, and J. W. Kolar, “Looking Through Walls – Actuator Position Measurement Through a Conductive Wall,” in *Proc. of the 23rd International Conference on Electrical Machines and Systems (ICEMS)*, Hamamatsu, Japan, November 2020. DOI: [10.23919/ICEMS50442.2020.9291020](https://doi.org/10.23919/ICEMS50442.2020.9291020).

Furthermore, the author had the pleasure to contribute to the following conference publication:

- ▶ S. Mirić, **R. V. Giuffrida**, G. Rohner, D. Bortis, and J. W. Kolar, “Design and Experimental Analysis of a Selfbearing Double-Stator Linear-Rotary Actuator,” in *Proc. of the IEEE International Electric Machines & Drives Conference (IEMDC)*, Hartford, CT, USA, May 2021. DOI: [10.1109/IEMDC47953.2021.9449501](https://doi.org/10.1109/IEMDC47953.2021.9449501).

1.6.3 Workshops and Seminars

- ▶ S. Mirić, **R. V. Giuffrida**, D. Bortis, and J. W. Kolar, “Multifunctional Self-Bearing Linear-Rotary Actuators,” presented at the *25th International Conference on Electrical Machines (ICEM)*, Valencia, Spain, September 2022. DOI: not available.

1.7 Outline of the Thesis

According to the goals and contributions mentioned above, the content of the thesis is divided into seven main chapters and a conclusion. All the chapters can be read independently since the interdependencies have been reduced to the strict minimum.

- ▶ **Chapter 2** provides a more detailed overview of the *ShuttlePump* TAH. In particular, its novel pumping principle is explained, from which

the need for a linear-rotary actuation system is apparent. Further mechanical and hydraulic aspects of the pump that are relevant for the subsequent actuation design are reported. This way, a set of constraints and requirements for the LiRA is defined.

- **Chapter 3** presents the design, realization and experimental verification of the LA part of the LiRA (cf. **Fig. 1.3 (b)**). Based on the specified constraints and requirements of the *ShuttlePump*, the appropriate PMSM topology is selected and its design is optimized using FEM simulations. The corresponding hardware prototype is verified with experimental measurements. The measured machine constant indicates

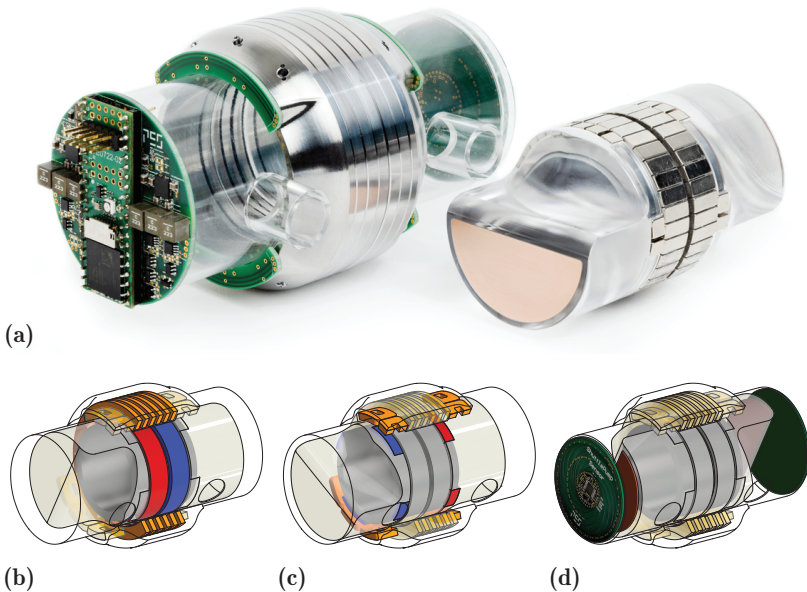


Fig. 1.3: (a) Hardware prototype of the *ShuttlePump* drive system, consisting of the drive and control unit, linear-rotary position sensors, and the LiRA (stator and mover). (b) LA part of the LiRA highlighted. As the LA needs to deliver most of the mechanical power, it occupies most of the available volume. (c) RA part of the LiRA highlighted. The RA is accommodated in the remaining volume after the LA is designed. (d) Linear-rotary ECSs highlighted. The semicircular measurement target is made of copper and embedded at the axial surfaces of the piston.

that the designed TLA can provide the required axial actuation force within the specified power losses.

- ▶ **Chapter 4** presents, analogously to **Chapter 3**, the design, realization and experimental verification of the RA part of the LiRA (cf. **Fig. 1.3 (c)**). After designing the LA, the RA is accommodated in the remaining available volume. Due to the stringent spatial constraints, the selected machine concept is very peculiar, as only a partial coverage of the stator and the PMs is allowed.
- ▶ **Chapter 5** discusses the design of the PCB-integrated linear-rotary eddy-current position sensor (cf. **Fig. 1.3 (d)**), needed to accurately control the motion of the piston of the *ShuttlePump*. The ECS is obtained by extending a commercial rotary ECS into a full linear-rotary one by appropriate post-processing with two linear position measurement options.
- ▶ **Chapter 6** describes the linear-rotary position control system that enables accurate tracking of the specified motion profile for the piston of the *ShuttlePump*. Based on a detailed electromechanical dynamical model of the LiRA, the controller is designed with special attention to its disturbance rejection capabilities. This is particularly important for the control of the axial/linear position, which is disturbed by strong hydraulic load forces. The experimental measurements demonstrate successfully synchronized linear-rotary position control within the allowed tracking tolerances.
- ▶ **Chapter 7** presents a detailed analysis and design of an eddy-current position sensor that extends the capabilities of standard ECSs to the case when a conductive barrier is interposed between the sensor head and the moving target. Furthermore, the influence of temperature variations on measurement accuracy is studied, and a drift-correcting technique is proposed. In the context of the *ShuttlePump*, this alternative sensing concept could be used in case a metallic enclosure is needed.
- ▶ **Chapter 8** concludes the thesis by recapitulating the results and contributions and putting them in perspective with an outlook on future work.

2

The *ShuttlePump*: Pumping Principle and Requirements

Chapter Abstract

This chapter provides an overview of the *ShuttlePump*, describing the device and its geometry, and explaining its operating pumping principle. The most important requirements that need to be considered to design a linear-rotary drive system are listed and commented on. These include, among others, the targeted motion profile, with force and torque requirements, and limits on the maximum allowed power losses, volume, and mass.

2.1 Introduction

As a necessary premise to the subsequent design of the Linear-Rotary Actuator (LiRA) drive system, in this chapter the *ShuttlePump* is presented more in detail. In particular, first the device is described with an overview on its parts and their mechanical design. Then, its novel, low-complexity operating principle providing a pulsatile blood flow without valves and only one moving part is explained. Finally, the requirements that will guide the design of the drive system are listed and discussed.

2.2 Mechanical Design and Geometry

The initial design of the proposed TAH concept was conducted at *Charité* [26], taking into account the main requirements for implantable TAHs, such as:

1. similar spatial dimensions as the native ventricles, to favour the device's implantability;
2. high durability for use as a long-term therapy;
3. use of hemocompatible materials in blood contact;
4. versatile anatomically oriented vascular connections to permit implantation in a large patient population.

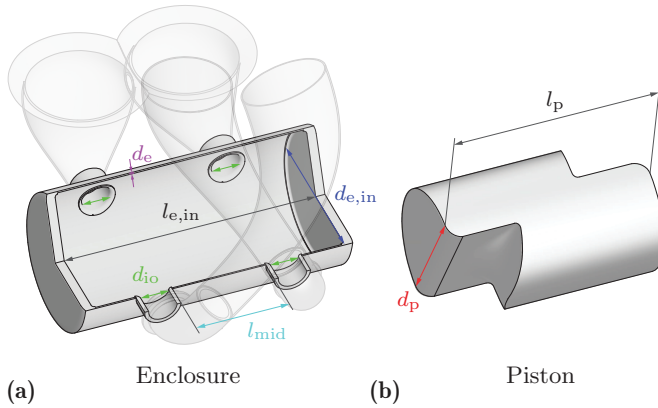


Fig. 2.1: Parts and geometry of the *ShuttlePump*, with annotated dimensions reported in **Tab. 2.1**. **(a)** Cylindrical enclosure with two round inlets and two round outlets on its lateral surface. **(b)** Cylindrical piston with specially-carved axial ends forming two opposite blades to control opening/closing of the inlets/outlets.

Tab. 2.1: Geometric parameters of the *ShuttlePump*.

Name	Symbol	Value	Unit
Enclosure inner axial length	$l_{e,in}$	100	mm
Enclosure inner diameter	$d_{e,in}$	49	mm
Enclosure thickness (lateral)	d_e	0.5	mm
In-/outlets diameter	$d_{i,o}$	12	mm
Inter- in-/outlets distance	l_{mid}	40	mm
Blood gap	d_{bg}	140	μm
Piston axial length	l_p	78	mm
Piston outer diameter	d_p	48.72	mm

As shown by **Fig. 2.1** and then in the yz -cut view of **Fig. 2.3 (a)**, the *ShuttlePump* consists of a cylindrical piston (diameter $d_p = 48.72$ mm; length $l_p = 78$ mm) with a special curved shape at its two axial ends and an enclosure (inner diameter $d_{e,in} = 49$ mm; inner length $l_{e,in} = 100$ mm; walls thickness $d_e = 0.5$ mm) with two inlets and two outlets (diameter $d_{io} = 12$ mm). All the dimensions are also reported in **Tab. 2.1**. The piston divides the volume within the enclosure into two chambers, serving as left and right heart ventricles, and has to simultaneously translate along and rotate about the axial direction z . The pump assembly is completed with titanium ducts at the in- and outlets, connected to soft vascular grafts. All in all, the construction of the device is relatively simple, and the specially shaped piston is the only moving part. Concerning materials, at an earlier stage of the project the use of medical grade titanium for the enclosure was considered. Finally, silicon carbide is used, as it features high thermal conductivity and good hemocompatibility [29]. The outer shell of the piston is instead made of polyether ether ketone (PEEK) which is also hemocompatible [30].

2.3 Pumping Principle

The operating principle of the *ShuttlePump* is illustrated in **Fig. 2.2**, showing four stages of the piston's linear-rotary motion. With the linear motion, the piston pushes the blood out of one chamber and new blood is collected in the other. The volume of blood displaced per stroke is 30.2 mL and the full axial stroke length is $2 \cdot z_{\text{strk}} = 16$ mm. The shuttling frequency can be adjusted from 1.5 - 5 Hz to reach sufficient cardiac outputs from 2.5 - 9 L/min against arterial pressures of 50 - 160 mmHg. As a result, the linear motion is the one with larger power requirements. The (continuous) rotary motion instead coordinates the opening and closing of the inlets and outlets, thanks to the special shape of the piston. This way, the blood flow is interrupted without the need for any valve, thus improving the durability and reliability of the device and reducing its complexity. Moreover, compared to rotary blood pumps with a fast spinning impeller, this physiological, pulsatile flow featuring low velocities may significantly reduce blood damage. The other important function of the rotary motion is to establish a hydrodynamic journal bearing [31]. In fact, between the piston and the enclosure's inner surface, there is a small gap allowing a thin layer of blood to be formed. By maintaining continuous rotation at a frequency of at least 1.5 Hz, this supports the piston radially during operation, avoiding contact with the pump's enclosure. This self-bearing feature not only extends the lifetime of the device, but also

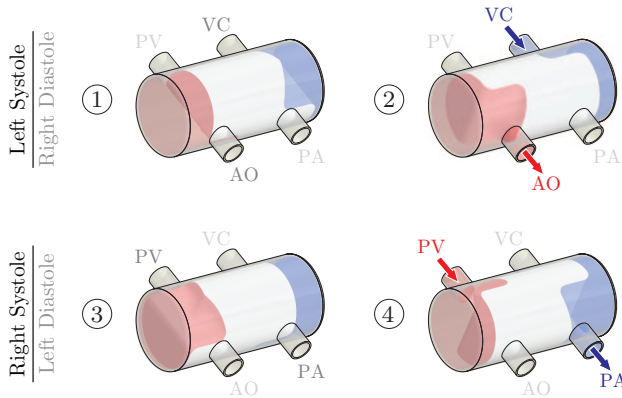


Fig. 2.2: Operating principle of the *ShuttlePump*. The piston continuously rotates around the z -axis, controlling the opening/closing of the inlets/outlets and establishing a hydrodynamic journal bearing. During the left systole (stages 1 and 2), the piston translates along the positive z -axis, pushing the blood in the left chamber out while the right chamber fills up. During the right systole (stages 3 and 4), the translation direction is reversed, as well as the chambers being emptied/filled up.

reduces the risk of thrombosis and similar adverse events that are usually related to the use of mechanical bearings in blood pumps [32, 33]. The length of the blood gap is a key parameter that plays an important role both for the hydrodynamic bearing, the shear stresses on the blood cells and the heating of the blood. Its value is optimized by means of Computational Fluid Dynamic (CFD) simulations at the *Medical University of Vienna* and selected to be $d_{bg} = 140 \mu\text{m}$ [26].

2.4 Drive System Requirements

The design of the drive system for the *ShuttlePump* needs to be carried out taking into account several important constraints and requirements. A complete list is available in **Tab. 2.2** and some of the most relevant ones are discussed in the following.

Tab. 2.2: Specifications of the *ShuttlePump*.

Name	Symbol	Value	Unit
Maximum axial dimensions	l_{ax}	105	mm
Maximum radial dimensions	d_{out}	70	mm
Inter- in-/outlets distance	l_{mid}	40	mm
Magnetic gap	$d_{ag,min}$	1	mm
Axial stroke amplitude	z_{strk}	8	mm
Maximum axial force	$F_{req,peak}$	≈ 43	N
Axial torque	M_{req}	3.1	mN m
Max. allowed radial force	$F_{rad,max}$	25	N
Maximum piston weight	$m_{mov,max}$	300	g
Piston frequency	f_{op}	1.5 - 5	Hz
Piston rotational speed	Ω_{op}	90 - 300	rpm
Operating conditions		2.5 - 9	L/min
		50 - 160	mmHg
Maximum av. cont. losses	$P_{tot,avg,max}$	10	W
Blood temperature increase	ΔT_{max}	2	K

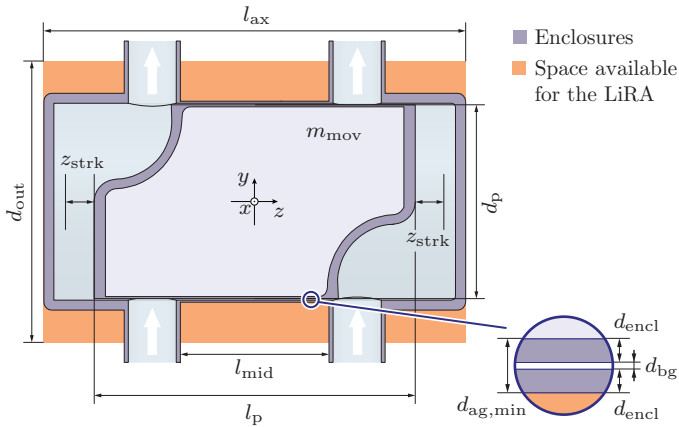


Fig. 2.3: *yz*- cut view of the *ShuttlePump*, showing its enclosure and specially-shaped piston with annotated dimensions, reported in **Tab. 2.2**. The orange area indicates the available space that can be used to fit the LiRA. A detailed view of the gap between enclosure and piston is shown on the right side.

Spatial Constraints

The first important set of requirements are the spatial constraints imposed by the pump's geometry and the maximum allowed external dimensions to guarantee that the final system is implantable. As annotated in **Fig. 2.3**, the available space that can be occupied by the stator(s) of the LiRA is limited axially to $l_{ax} = 105$ mm and radially to a maximum outer diameter of $d_{out} = 70$ mm. Furthermore, the presence of the inlets and outlets limits even further the available space on the lateral surface of the enclosure. To ensure the manufacturability and sufficient rigidity of the enclosure, the thickness of its lateral wall cannot be smaller than $d_{encl} = 0.5$ mm. The same constraint applies to the external shell of the piston that is needed to prevent direct contact of the bare mover with the blood, which is clearly not allowed. The resulting minimum magnetic gap is hence $d_{ag,min} = d_e + d_{shell} = 1$ mm. In addition, the thickness of the blood gap $d_{bg} = 140$ μ m between the enclosure and the piston shell has to be considered.

Motion Profile

One of the most important requirements for correct operation of the pump is that the piston tracks the specified motion profile in **Fig. 2.4**. The linear trajectory follows a quasi-sinusoidal profile shuttling axially around the center of the enclosure with a stroke amplitude of $z_{strk} = 8$ mm. The linear motion needs to be synchronized with the rotary motion, which happens at constant speed in the operational range. Further details on the motion profile are provided in **Sec. 6.2.2**, defining the linear and rotary positioning tolerances.

Force and Torque

Linear-rotary position tracking has to comply with the required axial force profile F_{req} and torque M_{req} . As the hydraulic resistance of the systemic circulation is higher than for the pulmonary circulation, the afterload pressure during the left systole is higher than during the right systole, which explains the asymmetric profile of F_{req} reported in **Fig. 2.4** and obtained from the CFD simulations. A higher linear force, with a peak of $F_{req,peak} \approx 43$ N is hence needed when shuttling from the right side towards the left one. The (continuous) torque requirement to keep the piston rotating in blood till $f_{op,max} = 5$ Hz is estimated by CFD simulations to be $M_{req} = 3.1$ mN m.

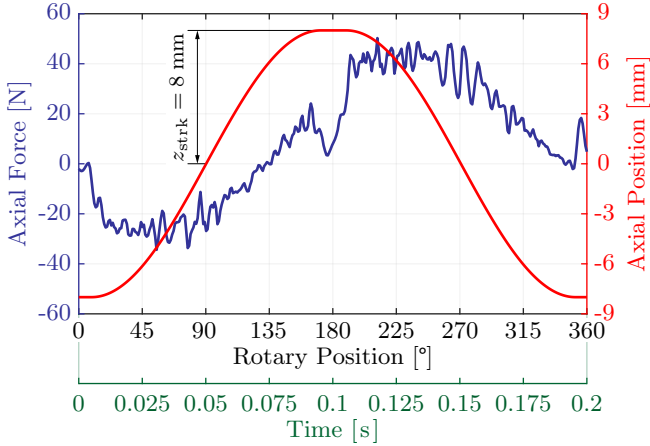


Fig. 2.4: Linear (axial) motion profile to be followed by the piston of the *ShuttlePump* during one operational cycle, synchronized to the rotary motion. Simultaneously, the required force profile F_{req} has to be provided to generate the necessary pressure at the cannula of the pump. The force profile is obtained by means of CFD simulations [26].

Power Losses

Another crucial constraint is on the maximum allowed total losses of the LiRA for continuous operation, since they cause heating of the blood in the pump. To comply with the regulations for active implantable devices, the local blood temperature increase in any part of the pump has to be limited to $\Delta T_{\text{max}} = 2 \text{ K}$ [26, 34]. The blood flow through the pump serves as forced convection cooling for the system. Nevertheless, the region between inlets and outlets, is the most critical. In fact, due to the thin blood gap for the hydrodynamic bearing, there is only a small volume of fluid between the piston and the enclosure, which can heat up rapidly. Considering the worst-case scenario that all the losses coming from the LiRA are concentrated in this region, and assuming that the heat is completely transferred to the blood, it is calculated that the average power losses over one period of operation should not exceed $P_{\text{tot,avg,max}} = 10 \text{ W}$.

Power Supply

Minimizing the power losses is also very important as the *ShuttlePump* is finally powered by a battery pack. This is typical for implantable blood pumps, with a system consisting, e.g., of two batteries, one supplying the device while the other one is being charged [35]. For the first trials, the battery pack is extracorporeal and connected to the implanted device via a percutaneous drive line (cf **Fig. 1.1**). In a second stage, this can potentially be replaced by a Transcutaneous Energy Transfer (TET) system [36].

Radial Forces

The hydrodynamic journal bearing of the *ShuttlePump* is designed according to the geometry of the piston, its eccentricity with respect to the enclosure and the blood gap length, with a maximum sustainable radial load of $F_{\text{bear,max}} = 42 \text{ N}$ [37]. The validity of the bearing design is further supported by the results of CFD simulations [26]. In order to ensure that the designed LiRA can be integrated in the final system without compromising the operation of the hydrodynamic bearing, it is decided to limit the radial forces it introduces to a maximum of $F_{\text{rad,max}} = 25 \text{ N}$. Furthermore, the design of the LiRA should preserve axial symmetry as much as possible. In fact, an asymmetric placement of the stator(s) could lead to excessive tilting of the piston during operation due to unbalanced reluctance forces between the PMs of the mover and the stator(s).

Piston's Mass

Finally, another aspect to consider is the total mass of the piston, which should be minimized. This reduces not only the inertial force required to accelerate it during axial motion but also the reaction forces on the stator. This way, the stress on the tissues surrounding the implant is also beneficially reduced. The mass of the piston mostly consists of the mass of the mover of the LiRA and will hence be indicated with m_{mov} in this work.

2.5 Summary

This chapter provided an overview on the *ShuttlePump* TAH. The geometry of the pump was described, and the dimensions of its parts were provided. Then, the most important requirements for the drive system to be designed were discussed. The maximum outer dimensions of the system are limited to

a diameter of $d_{\text{out}} = 70$ mm and a length of $l_{\text{ax}} = 105$ mm. The synchronized linear-rotary motion profile was provided, together with the force/torque requirements of $F_{\text{req,peak}} = 43$ N and $M_{\text{req}} = 3.1$ mN m. The maximum allowed power losses are $P_{\text{tot,avg,max}} = 10$ W, the maximum allowed radial load for the hydrodynamic bearing is limited to $F_{\text{rad,max}} = 25$ N and the system's mass should be minimized. As it will be shown in the following sections, these constraints introduce significant trade-offs during machine design.

3

Linear Actuator Design and Verification

The content of this chapter is also published in:

- ▶ **R. V. Giuffrida**, R. Senti, J. W. Kolar, T. Bierewirtz, K. Narayanaswamy, M. Granegger, and D. Bortis, “Design and Realization of a Highly Compact Tubular Linear Actuator for a Novel Total Artificial Heart,” *IEEE Journal of Emerging and Selected Topics in Industrial Electronics (Pioneering Work)*, vol. 4, no. 4, pp. 1010-1023, October 2023.

Chapter Abstract

This chapter presents the analysis, design and realization of the Linear Actuator (LA) part of the *ShuttlePump*, which needs to provide about 45 N of axial actuation force. Design criteria are the minimization of volume and generated power losses in the winding, which could result in excess heating and/or blood damage. The LA is implemented as a Tubular LA (TLA) to maximize the active area for linear/axial force generation. After a preliminary analysis based on first principles, the TLA is optimized in detail with the aid of FEM simulations, exploring the main design trade-off between ohmic losses and radial magnetic attraction forces. The experimental measurements conducted on the realized TLA prototype verify the FEM simulation results and confirm the suitability for the realization of the *ShuttlePump*.

3.1 Introduction

This chapter discusses in detail the analysis, design, realization and experimental verification of the Linear Actuator (LA) part of the *ShuttlePump*, which is an important interim result before continuing with the Rotary Actuator

(RA) part. In fact, as emphasized in the following section, the LA has the largest power requirements and its design is therefore prioritized. The chapter is structured as follows. **Sec. 3.2** presents the machine analysis, topology selection and dimensioning based on which the optimization of **Sec. 3.3** is conducted. This finally leads to the selection of a candidate LA design. **Sec. 3.4** introduces the realized hardware prototype of the LA and the test bench used for the experimental verification. The measurements are presented and commented in **Sec. 3.5**. Finally, **Sec. 3.6** concludes the chapter.

3.2 Machine Analysis and Dimensioning

The machine design and optimization of the LA is based on a preliminary analysis, presented in this section. The goal is to select the most suitable motor concept for the LA given the stringent constraints discussed in **Sec. 2.4** and identify the most important parameters affecting force generation, before continuing with a detailed FEM optimization.

3.2.1 LiRA Concept: Independent Actuators

The first decision taken is to realize the LiRA of the *ShuttlePump* as two independent actuators, i.e., a LA and a RA. This choice is motivated by a few important aspects. Simplicity and reliability are highly desirable features for a drive system, even more for an implantable blood pump. The higher the overall system's complexity, the higher the risk of partial failure with potentially very serious consequences for the patient. Also the practical realization of a complicated machine topology could get particularly challenging, especially under tight spatial constraints. When it comes to highly integrated LiRAs, for instance, the system's complexity can considerably increase [38–41]. Having many stator phase currents to supply and control independently is hardly advantageous. In fact, the inverter and control unit gets increasingly complicated as well and occupies a larger volume. This could be an issue, in case it is desired to implant it together with the blood pump. If that is not the case, a percutaneous driveline is needed to connect the implanted pump to the extracorporeal inverter and control unit. Even then, a large number of phase currents and control signals is not ideal, as the connecting driveline would increase in cross section. Therefore, it is highly beneficial to minimize the number of phase currents of the LiRA as much as possible. In the literature, there are interesting concepts that follow this direction. One example is the screw motor, for which the linear motion is obtained passively with a

special arrangement of the PMs [42]. By making one of the two motions passive, i.e., caused solely by reluctance forces, it is possible to only use three phase currents. Nevertheless, a solution of this kind hardly complies with the force requirements and motion profile of the *ShuttlePump*. Another aspect that motivates a separate design of the two actuators is that the required (average) mechanical output power of the LA is substantially larger than the RA. For the LA, starting from the motion profile and required force of **Fig. 2.4**, it can be calculated that $P_{\text{mech,avg,LA}} = 3.6 \text{ W}$. For the RA instead, due to the low rotational speed and torque, it is only needed to provide about $P_{\text{mech,avg,RA}} = 100 \text{ mW}$. By assuming that both actuators can be designed with the same power density, the volume share of the LA over the total LiRA volume is

$$V_{\text{share,LA}} = \frac{P_{\text{mech,avg,LA}}}{P_{\text{mech,avg,LA}} + P_{\text{mech,avg,RA}}} = 97.3 \%. \quad (3.1)$$

Therefore, it is reasonable to use as much space as possible for the LA and provide the best actuator design possible, e.g., by avoiding a combined LiRA concept that could significantly reduce the LA's efficiency. The LA is then realized as a Tubular Linear Actuator (TLA). This way, the full lateral surface of the cylindrical piston can be used for axial force generation. The TLA is implemented as a Permanent Magnet Synchronous Machine (PMSM), which is a typical choice for blood pumps [43]. In fact, PMs allow to reach high flux densities in the least volume, thus meeting the compactness requirements of such implantable devices.

3.2.2 PMSM Topology Selection for the TLA

The most suitable machine topology for the (T)LA is selected among a variety of alternatives. The first and most basic decision to take is on the poles/slots combination. With a number of stator slots $N_s = 6$ and a number of mover poles $N_p = 2$, it is possible to maximize the winding factor to $\xi = 1$. This is achieved with a distributed winding, which for a TLA can be conveniently realized with 6 individual circular coils.

For the stator, it is possible to choose either a slotted (cf. **Fig. 3.1 (a)**) or a slotless (cf. **Fig. 3.1 (b)**) design. With a slotted stator with stator teeth, the magnetic air gap length can be minimized to $d_{\text{ag,min}} = 1 \text{ mm}$, which results in a higher air gap flux density and hence a higher force constant compared to a slotless stator, where the air gap length and resulting force constant is mainly defined by the stator winding thickness (which should be maximized to minimize the winding losses). Furthermore, a slotless stator presents

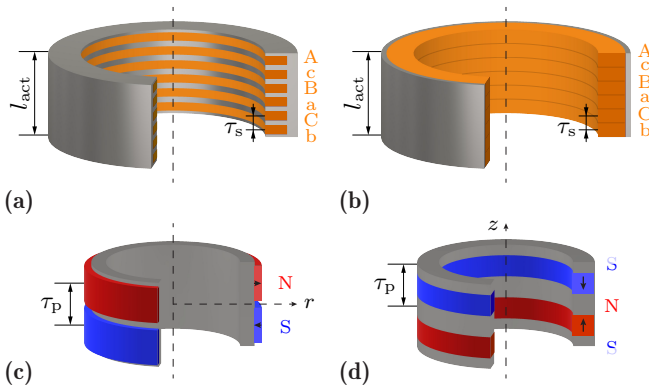


Fig. 3.1: Considered options for the stator and the mover of the TLA for the case of $N_s = 6$ stator slots and $N_p = 2$ mover poles. **(a)** Slotted stator, **(b)** slotless stator, **(c)** SPM mover with radially (r -) magnetized PMs and **(d)** IPM mover with axially (z -) magnetized PMs.

little variations in the air gap reluctance along the axial direction, which considerably mitigates cogging effects (cf. **Sec. 3.2.3**). For these reasons, both designs are considered in the subsequent FEM optimization of **Sec. 3.3**.

For what concerns the mover, the needed poles can be obtained with two different PM arrangements [44]. One option is to use Surface-mounted PMs (SPM) with a radial magnetization direction, as shown in **Fig. 3.1 (c)**. As it can be noticed, this requires a mover back iron to close the magnetic path with the minimum length. To realize this in practice, custom-made radially-magnetized PMs are required, which have extremely high manufacturing costs. Nevertheless, it is possible to obtain approximately the same result with smaller PM segments. The other option is to use Interior PMs (IPM) with an axial magnetization direction, interleaved by rings of ferromagnetic material as shown in **Fig. 3.1 (d)**. These magnets are considerably easier to produce and the mover can be assembled by stacking the ring-shaped PMs and the ferromagnetic rings together. Finally, one further option would be the Halbach array. However, due to difficult realization, this is not investigated further.

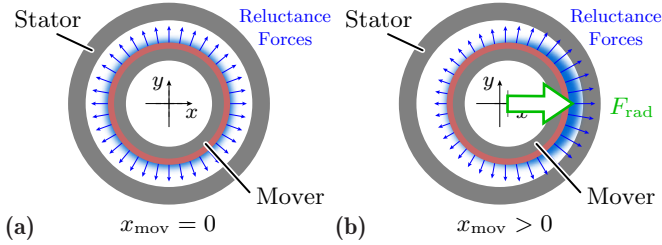


Fig. 3.2: Radial magnetic attraction force effect. (a) With a centered mover, all the radial reluctance forces are balanced, whereas (b) when the mover is displaced radially (e.g., along the x -direction), a net radial attraction force F_{rad} appears. Note that the mover is not to scale on purpose to better visualize the reluctance forces.

3.2.3 Variable Air Gap Reluctance Effects

Besides the selection of the basic machine topology, there are three important air gap reluctance effects that have to be considered to design a working TLA. These effects are much more prominent (and critical) with a small magnetic air gap length, which is the case for a slotted stator design. The first effect is the radial magnetic attraction force acting on the mover. This appears as soon as its axis is not aligned to the stator's one. In fact, it can be shown that the center of the stator is an unstable equilibrium position for the mover. As soon as this is displaced radially, the reluctance forces caused by the attraction of the PMs with the stator core are not anymore balanced, with a resulting radial magnetic pull (cf. **Fig. 3.2 (a) and (b)**). As the *ShuttlePump* has no mechanical bearing holding the mover perfectly concentric, this force can heavily disturb the hydrodynamic bearing and should hence be explicitly considered in the optimization.

The second effect is the cogging force along the axial direction, appearing for slotted stator designs. This is caused by the variable air gap reluctance profile due to the presence of the stator teeth [45]. It is known that the profile of the cogging force F_{cogg} along the axial direction z exhibits a spatial periodicity given by the least common multiple of the number of stator slots N_s and the number of mover poles N_p , i.e.,

$$F_{cogg} = \hat{F}_{cogg} \sin\left(\frac{N_{cogg} \pi}{\tau_p} z\right) \quad \text{with } N_{cogg} = \text{lcm}(N_s, N_p). \quad (3.2)$$

with $\tau_p = l_{act}/N_p$ the pole pitch and l_{act} the length of the actuator. If no counter measure is taken, the amplitude \hat{F}_{cogg} can be so large as to compromise the

operation of the TLA. The most effective way to mitigate cogging force is to use pole shoes, as they smooth out the air gap reluctance profile [46,47]. Therefore, for slotted stator designs, pole shoes will be included in the optimization as well.

The last important effect to consider is the edge effect or edge cogging force. Also this is caused by the air gap reluctance. More precisely, when the mover is displaced axially away from the center position as in **Fig. 3.3 (a)**, the total reluctance seen by the PMs sharply increases, as there is no stator in front. Consequently, there is a strong axial force $F_{ax,edge}$ that pulls the mover back towards the center position, i.e., to the condition with minimum reluctance. This can be countered by extending either the stator (**Fig. 3.3 (b)**) or the mover (**Fig. 3.3 (c)**) along the axial direction in such a way that the total reluctance is approximately constant during the whole axial motion [44]. In order to minimize the mass of the mover, the former option is preferred, i.e., the stator is extended by $2 \cdot z_{strk} = 16$ mm. Depending on the size of a stator pitch $\tau_s = l_{act}/N_s$, it would be possible to fit additional coils in the stator extensions, as e.g., visible in **Fig. 3.3 (b)**. However, energizing such coils would generate additional ohmic losses which do not fully contribute to force generation. For this reason, no further coil is added in the stator extensions. As a consequence, it is important to notice that the active length (and hence area) effectively contributing to force generation drops when the mover is displaced from the center of the actuator, i.e.,

$$l_{act,eff}(z_{mov}) = l_{act} - |z_{mov}|, \quad (3.3)$$

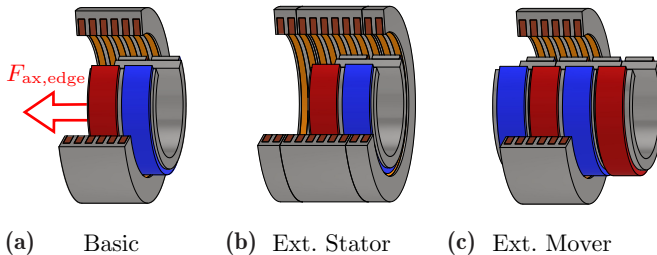


Fig. 3.3: Edge cogging force effect and possible solutions. **(a)** Basic TLA with stator and mover of equal length, for which a strong edge cogging force $F_{ax,edge}$ appears (magnetic spring) as soon as the mover is displaced from the center of the actuator. **(b)** Solution 1: TLA with extended stator. The stator extensions can optionally host additional stator coils. **(c)** Solution 2: TLA with extended mover.

where z_{mov} is the position of the mover. In future work, the stator extensions will be used to integrate the RA for a highly compact design.

3.2.4 Analysis and Dimensioning from First Principles

Before proceeding with the FEM optimization of the TLA, a short preliminary analysis based on first principles is conducted. This is useful for multiple reasons. First, it enhances the understanding and the interpretation of the subsequent optimization results. Furthermore, it allows to fix some parameters beforehand by understanding their effect, thus reducing the number of optimization variables to sweep. Last but not least, it can be used for a feasibility check, i.e., to roughly estimate whether the required force can be achieved respecting the provided constraints on power losses and dimensions.

For internal force generation in AC machines, consider the area-related force density,

$$\sigma_{\text{ax}}(z) = S(z) B_{\text{ag}}(z), \quad (3.4)$$

where $S(z)$ is the equivalent current sheet and $B_{\text{ag}}(z)$ the magnetic flux density in the air gap at the position z (assuming symmetric axisymmetric designs). The total axial force F_{ax} is obtained by integrating $\sigma_{\text{ax}}(z)$ along the active area, i.e., the (inner) lateral surface of the cylindrical TLA, hence

$$F_{\text{ax}} = 2\pi r_{\text{mov}} \int_{-l_{\text{act}}/2}^{l_{\text{act}}/2} \sigma_{\text{ax}}(z) dz. \quad (3.5)$$

With $N_p = 2$, i.e., one pole pair, only the fundamental components of $B_{\text{ag}}(z)$ and $S(z)$ contribute to force generation. Therefore, (3.5) can be rewritten as

$$F_{\text{ax}} = 2\pi r_{\text{mov}} \int_{-l_{\text{act}}/2}^{l_{\text{act}}/2} S_1(z) B_{\text{ag},1}(z) dz. \quad (3.6)$$

The fundamental component $B_{\text{ag},1}(z)$ can be written as

$$B_{\text{ag},1}(z) = -\hat{B}_{\text{ag},1} \sin\left(z \frac{2\pi}{l_{\text{act}}} + \vartheta_{\text{mov}}\right), \quad (3.7)$$

where $\vartheta_{\text{mov}} = -z_{\text{mov}} \frac{2\pi}{l_{\text{act}}}$ is the electrical angle of the mover (with respect to the stator). The amplitude $\hat{B}_{\text{ag},1}$ can be approximated from the equivalent magnetic circuit model of **Fig. 3.4 (a)**. The circuit is valid for the SPM case and it is greatly simplified. It considers only the radial field component of the main flux path, thus neglecting any leakage flux. Moreover, it assumes

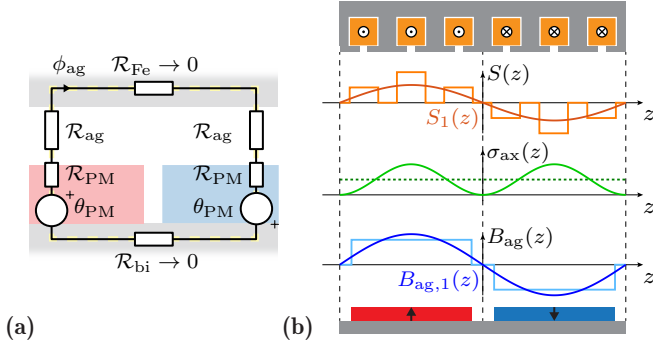


Fig. 3.4: (a) Simplified equivalent magnetic circuit at the air gap of the LA, valid for the SPM case. The field is assumed to be homogeneous in the radial direction and any leakage and fringing is neglected. It is assumed that the magnetic permeability of the cores is $\mu_{r,Fe} \rightarrow \infty$, from which $\mathcal{R}_{\{Fe,bi\}} \rightarrow 0$. (b) Exemplary machine plan for the analysis of force generation, showing the equivalent current sheet $S(z)$ and its fundamental component $S_1(z)$, the area-related force density $\sigma_{ax}(z)$ and the air gap magnetic flux density $B_{ag}(z)$ and its fundamental component $B_{ag,1}(z)$.

that the field is homogeneous and does not consider any fringing due to the large coverage of the pole shoes. With these assumptions, the peak air gap flux density is

$$\hat{B}_{ag} = \frac{\phi_{ag}}{A_{ag}} = \frac{\theta_{PM}}{\mathcal{R}_{ag,tot} A_{ag}} = \frac{H_c d_{PM} \mu_0}{d_{ag} + d_{PM}}, \quad (3.8)$$

where ϕ_{ag} is the magnetic flux in the air gap, A_{ag} the air gap cross section, θ_{PM} the magnetomotive force generated by one PM with coercivity H_c and $\mathcal{R}_{ag,tot}$ the total equivalent air gap reluctance. The amplitude of the first harmonic $\hat{B}_{ag,1}$ also depends on the PM coverage factor k_{PM} (that determines the length of and hence the gap between the PMs) and is

$$\hat{B}_{ag,1} = \frac{4}{\pi} \hat{B}_{ag} \sin\left(k_{PM} \frac{\pi}{2}\right). \quad (3.9)$$

The current sheet $S(z)$ is obtained considering the currents impressed in the distributed winding as shown in the exemplary machine plan of **Fig. 3.4 (b)**. The fundamental component $S_1(z)$ can be written as

$$S_1(z) = -\hat{S}_1 \sin\left(z \frac{2\pi}{l_{act}} + \vartheta_{stat}\right), \quad (3.10)$$

where ϑ_{stat} is the electrical angle of the stator field, which can be controlled with the inverter to be $\vartheta_{\text{stat}} = \vartheta_{\text{mov}}$ for maximum force generation (Field-Oriented Control, FOC). The amplitude \hat{S}_1 is calculated as

$$\hat{S}_1 = \frac{6 \sin\left(\left(1 - k_{\text{FeCu}}\right) \frac{\pi}{6}\right) N\hat{I}}{\left(\left(1 - k_{\text{FeCu}}\right) \frac{\pi}{6}\right) l_{\text{act}}}, \quad (3.11)$$

where $N\hat{I}$ is the peak Amperes impressed in the stator winding and the iron-to-copper ratio parameter k_{FeCu} is introduced. As in a slotted design the width of a tooth and a coil add up to a stator slot pitch $\tau_s = l_{\text{act}}/6$, it holds $l_{\text{Fe}} = k_{\text{FeCu}} \tau_s$ and $l_{\text{Cu}} = (1 - k_{\text{FeCu}}) \tau_s$. With this definition, for the special case $k_{\text{FeCu}} = 0$ a slotless stator design is obtained.

By integrating (3.6) and with the expressions for the fundamentals (3.7) and (3.11), the axial force results finally as

$$F_{\text{ax}} = \pi l_{\text{act}} r_{\text{mov}} \hat{S}_1 \hat{B}_{\text{ag},1} = \frac{1}{2} A_{\text{act}} \hat{S}_1 \hat{B}_{\text{ag},1}, \quad (3.12)$$

where $A_{\text{act}} = 2\pi r_{\text{mov}} l_{\text{act}}$ is the active area of the LA. The corresponding total ohmic losses of the stator winding are

$$P_{\text{Cu}} = 3 R_0 (N\hat{I})^2 = 3 \frac{l_{\text{w},0}}{\sigma_{\text{Cu}} k_{\text{ff}} A_{\text{Cu},0}} (N\hat{I})^2, \quad (3.13)$$

where R_0 is the single-turn resistance of a circular coil, $l_{\text{w},0}$ is the single-turn length of the coil, σ_{Cu} is the conductivity of copper, k_{ff} the fill factor and the single-turn copper cross section is

$$A_{\text{Cu},0} = d_{\text{Cu}} l_{\text{Cu}} = d_{\text{Cu}} (1 - k_{\text{FeCu}}) (l_{\text{act}}/6). \quad (3.14)$$

The derived first-principles relations offer some meaningful insights on which variables contribute to force generation and/or ohmic losses. For instance, from (3.8), (3.9) and (3.12) one can recognize the role of the air gap length d_{ag} , which should be minimized to maximize F_{ax} . In the denominator of (3.8), one can observe the effect of the series reluctance of the PMs (with thickness d_{PM}) in a SPM mover. Most importantly, from (3.13) and (3.14) it can be seen that maximizing the fill factor k_{ff} and the coil copper cross section $A_{\text{Cu},0}$ is crucial to reduce the ohmic losses. As a consequence, the available TLA volume should be maximally used. Hence it is already possible to fix $d_{\text{out}} = 70$ mm, thus maximizing d_{Cu} . Also the iron-to-copper ratio k_{FeCu} directly affects the ohmic losses for (almost) the same output force (the effect

in (3.11) is minimal) and should be ideally minimized. Nevertheless, care must be taken and further investigation is needed. In fact, very thin stator teeth are not only mechanically more fragile and difficult to manufacture, but also prone to magnetic saturation. Furthermore, recall that the simplified magnetic circuit model holds for a large shoe coverage with homogeneous field and does not include fringing and leakage effects.

Finally, (3.14) reveals that also the actuator's length l_{act} should be maximized as far as possible. Another strong motivation is given by the (effective) active length of the extended stator design found in (3.3). The larger l_{act} , the smaller the reduction of $l_{\text{act,eff}}(z_{\text{mov}})$ during the axial motion. Furthermore, recall that the thin layer of blood serving as hydrodynamic bearing can heat up very easily by absorbing the heat generated by the LiRA. If the actuator is longer, the volume of such blood layer is larger, and hence its temperature increase is smaller for the same power losses. With the chosen extended stator design the total stator length is $l_{\text{stat}} = l_{\text{act}} + 2 \cdot z_{\text{strk}}$. As the length between left and right inlets/outlets is limited to $l_{\text{mid}} = 40$ mm, the actuator's length is finally maximized to $l_{\text{act}} = 24$ mm.

The preliminary analysis is completed with one last consideration on the radial attraction force F_{rad} . Being a reluctance force, it depends linearly on the active area and quadratically on the air gap magnetic flux density, i.e.,

$$F_{\text{rad}} \propto A_{\text{act}} B_{\text{ag}}^2. \quad (3.15)$$

Recall that F_{rad} should be limited in order not to impair the hydrodynamic bearing. In contrast, for force generation (cf. (3.12)) high values of B_{ag} and A_{act} are desirable. For the same output force F_{ax} , a reduced B_{ag} would need to be compensated with increased current $N\hat{I}$ or a larger active area A_{act} . Between the two options, increasing A_{act} is more favorable, as a larger current increases quadratically the ohmic losses (cf. (3.13)). With the maximized length $l_{\text{act}} = 24$ mm and hence fixed A_{act} , the trade-off between radial attraction force F_{rad} and ohmic losses P_{Cu} becomes the main focus of the subsequent optimization, from which a Pareto-front has to be expected.

3.3 FEM Machine Optimization

This section discusses the FEM optimization conducted on a 2D parameterized model of the candidate TLA topology. The trade-offs that appear by exploring the design space are highlighted, leading to the selection of the final design.

3.3.1 2D FEM Model

A TLA can be conveniently studied with a 2D axisymmetric FEM model. However, this does not allow to investigate the radial attraction forces, as they only appear when the mover and stator axes are misaligned. Therefore, a 2D Cartesian model (i.e., with no assumed symmetry) is used instead, comprising the full cross-section of the TLA as shown in **Fig. 3.5 (a)**. This way, it is possible to obtain both the axial and radial forces acting on the mover with a single magnetostatic 2D model, avoiding to use a 3D one with considerably higher simulation effort. Nevertheless, it is necessary to verify that the results of the 2D Cartesian model approximate well the ones from the corresponding 2D axisymmetric or 3D models. Specifically, the results from the 2D Cartesian model need to be scaled correctly, as shown further, as they are returned per 1 m of length along the y -direction.

Model Definition

The model is parameterized as indicated in **Fig. 3.5 (a)**. The model parameters are summarized in **Tab. 3.1**. In order to keep the simulation effort to a minimum, the materials used in the model are simplified. The stator core

Tab. 3.1: Parameters of the FEM model. The optimization parameters are indicated with ‘Opt’ and reported in **Tab. 3.2**.

Name	Symbol	Value	Unit
Relative permeability (core)	μ_r	4000	
Mag. saturation threshold (core)	B_{sat}	2.2	T
Copper conductivity (with fill factor)	$\sigma_{\text{Cu,ff}}$	3.4	MS/m
Fill factor	k_{ff}	0.6	
PM coercitivity	H_c	1000	kA/m
Relative permeability (PM)	μ_{PM}	1.05	
Pole shoe coverage	k_{shoe}	Opt	
PM coverage	k_{PM}	Opt	
Magnetic gap length	d_{ag}	Opt	mm
PM thickness	d_{PM}	Opt	mm
Copper layer thickness	d_{Cu}	Opt	mm
Iron-copper ratio	k_{FeCu}	Opt	
Stator core thickness	d_{Fe}	Opt	mm
Back iron thickness	d_{bi}	Opt	mm

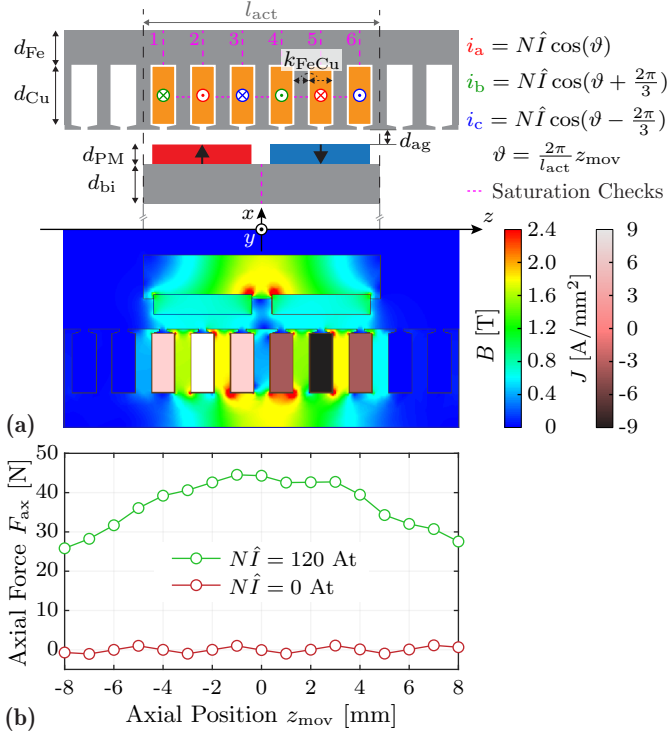


Fig. 3.5: (a) 2D FEM Cartesian model of the TLA for an exemplary design, with indicated parameters in the upper half and solved B and J fields in the bottom half (*Ansys Maxwell*). By modeling the full section of the TLA, it is possible to obtain both axial and radial forces acting on the mover with one model. (b) Exemplary axial force profiles for the cases $N\hat{I} = 120$ Atturns, giving the total axial drive force $F_{ax}(z)$ and $N\hat{I} = 0$ Atturns, giving the axial cogging force component $F_{cogg}(z)$.

and the mover back iron are made of a linear, ferromagnetic material with $\mu_r = 4000$ and negligible electrical conductivity. Consequently, the results have to be checked for potential magnetic saturation of the material, that occurs in practice for too high values of the B field (e.g., > 1.6 T for electrical steel). The coils are modeled with a solid copper cross section, i.e., with a single turn, for simplicity. In order to take into account a realistic fill factor of $k_{ff} = 0.6$, the copper material is modeled with a reduced conductivity $\sigma_{Cu,ff} = k_{ff} \sigma_{Cu} = 3.4$ MS/m. Finally, for the PMs a coercitivity $H_c = 1000$ kA/m is

assumed, which approximately corresponds to the N50 magnetization grade of commercial NdFeB PMs. As a Cartesian model is used, the magnetization direction is along the x -axis. In order to obtain the correct machine constant, the current excitations are assigned to the coils as indicated in **Fig. 3.5 (a)**. In particular, the electrical angle ϑ is tied to the axial position of the mover z_{mov} in order to generate the maximum force per ampere (MFPA) with FOC for all axial positions. This way $N\hat{I}$ corresponds effectively to the amplitude of the force-generating q -current component.

Simulation Outputs and Scaling

The outputs of the magnetostatic 2D FEM simulations needed for the subsequent machine optimization are the maximum radial attraction force $F_{\text{rad,max}}$, the axial force F_{ax} generated for the current amplitude $N\hat{I}$ (from which the machine force constant $k_m = F_{\text{ax}}/\hat{I}$ can be derived) and the corresponding ohmic losses P_{Cu} in the winding. High-frequency-copper losses are neglected since the machine will be fed by an inverter with LC -output filter, providing quasi-sinusoidal low-frequency currents. Due to the low-frequency operation, also the core losses P_{Fe} are neglected in a first step. For the maximum radial attraction force $F_{\text{rad,max}}$, the mover is displaced in the x -direction by $x_{\text{mov}} = d_{\text{bg}} = 140 \mu\text{m}$. The simulation returns a force per unit length (i.e., 1m) $F_{x,\text{sim}}$ acting on the mover along the x -direction. By comparing it with the results of the corresponding 3D FEM simulations, it is found that the total radial force is well-approximated (matching within 1.5 %) as

$$F_{\text{rad}} = (\pi r_{\text{mov}}/2) F_{x,\text{sim}}, \quad (3.16)$$

i.e., with a scaling factor equal to a quarter of the mover circumference. Similarly, the generated axial force per unit length $F_{z,\text{sim}}$ is compared to both the corresponding axisymmetric 2D and 3D FEM simulations. In this case, the scaling factor corresponds to half of the mover circumference, hence the total axial force is

$$F_{\text{ax}} = (\pi r_{\text{mov}}) F_{z,\text{sim}}, \quad (3.17)$$

which matches within 1.4 % to the results of the 2D axisymmetric model and 2.4 % for the 3D. Note that $F_{z,\text{sim}}$ is obtained for the case $x_{\text{mov}} = 0$, i.e., for a radially centered mover. The two scaling lengths used in (3.16) and (3.17) can be explained as follows. As the axial force acts in the same way over the whole mover circumference, the full 3D results are obtained by revolving the Cartesian 2D model by 180° . The radial attraction forces instead are not acting equally along the whole circumference, as already sketched in **Fig. 3.2 (b)**. It

can be approximated that the components acting along the top and bottom quarter of circumference cancel each other out and only the ones acting on the left and right sides contribute.

If the parameter z_{mov} is varied in the range $[-z_{\text{strk}}, z_{\text{strk}}]$, the axial force profile in **Fig. 3.5 (b)** is obtained. As expected from (3.3), the generated force reduces approximately linearly with $|z_{\text{mov}}|$, as the active machine length $l_{\text{act,eff}}$ reduces. For a maximally displaced mover, i.e., $|z_{\text{mov}}| = z_{\text{strk}}$, the generated force is only about $1 - |z_{\text{strk}}|/l_{\text{act}} = 2/3$ of the maximum force $F_{\text{ax,max}} = F_{\text{ax}}(z_{\text{mov}} = 0)$. For $N\hat{I} = 0$, only the cogging force component F_{cogg} appears, also reported in **Fig. 3.5 (b)**. Thanks to the pole shoes, its amplitude is small, i.e., only $\hat{F}_{\text{cogg}} \approx 1$ N.

The FEM simulation also returns the ohmic losses in the LA winding. These are obtained for the assigned currents i_a , i_b and i_c with $N\hat{I}_{\text{test}} = 120$ Aturns in this exemplary case. This is the current amplitude needed to generate the peak force $F_{\text{req,peak}} = 43$ N and is hence not needed continuously during the whole operation period. Therefore, in order to find the (instantaneous) losses profile versus time $P_{\text{Cu}}(t)$, it is necessary to combine the required force profile $F_{\text{req}}(t)$ of **Fig. 2.4** with the obtained force profile from FEM $F_{\text{ax}}(z)$ in **Fig. 3.5 (b)**. In **Fig. 3.6 (a)**, $F_{\text{ax}}(z)$ is adapted versus time as $F_{\text{ax}}(t)$ according to the motion profile $z(t)$ in **Fig. 2.4** and shown for $N\hat{I}_{\text{test}} = 120$ Aturns. This way, the required current amplitude $N\hat{I}_{\text{req}}$ is determined as

$$N\hat{I}_{\text{req}}(t) = \frac{F_{\text{req}}(t)}{F_{\text{ax}}(t)} N\hat{I}_{\text{test}}, \quad (3.18)$$

and is exemplarily shown in **Fig. 3.6 (b)**, together with the resulting phase currents. From this and with the simulated single-turn resistance R_0 , one gets the losses profile

$$P_{\text{Cu}}(t) = 3 R_0 (N\hat{I}_{\text{req}}(t))^2 \quad (3.19)$$

reported in **Fig. 3.6 (c)**, of which the average $P_{\text{Cu,avg}}$ is considered.

3.3.2 Three-Steps Optimization Procedure

The parameterized 2D FEM model can now be used to perform the machine optimization. For this purpose, the model parameters are swept as reported in **Tab. 3.2**. In order to keep the design space compact and avoid prohibitive simulation times, the parameters are divided into three groups and the optimization is performed in three steps. In a first preliminary step, the parameters k_{shoe} and k_{PM} are swept on a test design. As it will be shown, it is possible to fix them beforehand independently. In a second step, the main optimization

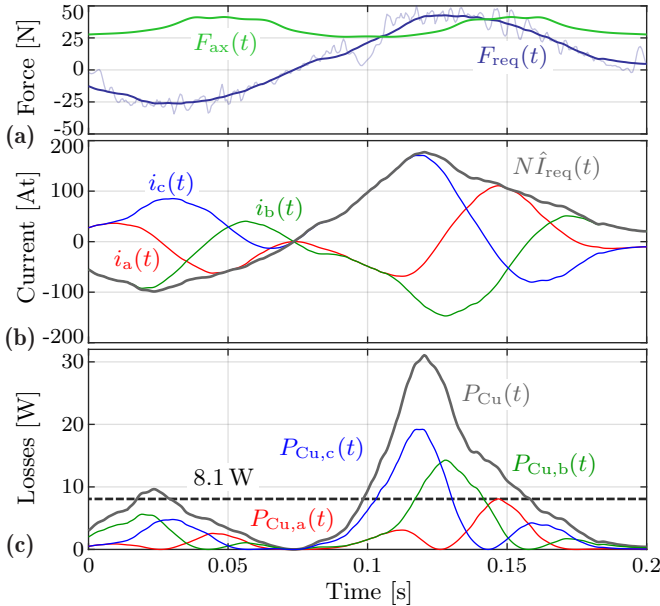


Fig. 3.6: (a) Comparison between the generated force $F_{ax}(t)$ for a fixed test current $N\hat{I}_{test} = 120$ Atturns as obtained from the FEM simulations and the required force profile from Fig. 2.4, here smoothed. (b) Required current amplitude $N\hat{I}_{req}(t)$ and resulting realistic (single-turn) phase currents $i_{\{a,b,c\}}(t)$. (c) Instantaneous ohmic losses $P_{Cu,\{a,b,c\}}(t)$ corresponding to the currents in (b) for the simulated single-turn resistance $R_0 = 330 \mu\Omega$. The continuously dissipated power is the average of the total losses $P_{Cu}(t)$.

parameters are swept. They are expected to have the most noticeable effects on the desired outputs and are hence explored in detail. Among these there is in fact the thicknesses of the permanent magnets d_{PM} , the copper layer d_{Cu} and the magnetic gap length d_{ag} , as well as the iron-to-copper ratio k_{FeCu} . Note that also the case $k_{FeCu} = 0$ is considered, which corresponds to the slotless stator designs. In a third step, i.e., after the main design space is obtained and a design is selected, the third group of parameters is adjusted. The thickness of the stator core d_{Fe} or of the mover back iron d_{bi} have a limited impact on the inspected outputs. They do not significantly change e.g., the generated force nor the reluctance forces, especially with the assumed linear magnetic material. Therefore, they are chosen only to guarantee that no

magnetic saturation occurs in the stator nor the back iron. As these two parameters do influence the resulting mover mass and actuator volume, though, in the second step they are assigned as $d_{Fe} = d_{bi} = 2 d_{PM}$. The three-steps optimization procedure can be summarized by the diagram of Fig. 3.7.

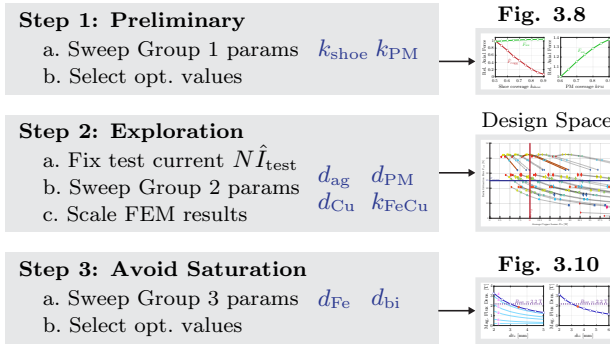


Fig. 3.7: Flow diagram showing the three-steps FEM-based optimization procedure of the TLA.

Tab. 3.2: Swept optimization parameters.

Name	Symbol	Range	Step	Unit
Group 1				
Shoe coverage	k_{shoe}	[0.5, ..., 0.9]	0.05	
PM coverage	k_{PM}	[0.6, ..., 0.9]	0.05	
Group 2 (Main)				
Magnetic gap length	d_{ag}	[1, ..., 2]	0.5	mm
PM thickness	d_{PM}	[1, ..., 3, 5]	0.5	mm
Copper layer thickness	d_{Cu}	[2, ..., 6]	1	mm
Iron-Copper ratio	k_{FeCu}	[0, ..., 0.8]	0.2	
Group 3				
Stator core thickness	d_{Fe}	[2, ..., 5]	0.5	mm
Back iron thickness	d_{bi}	[2, ..., 6]	0.5	mm

3.3.3 Optimization, Design Space and Selected Design

The results from the first (preliminary) optimization step are reported in **Fig. 3.8**. As it can be seen in **Fig. 3.8 (a)**, the shoe coverage k_{shoe} has a limited impact on the generated axial force, but a clear beneficial effect in reducing the cogging force amplitude \hat{F}_{cogg} . Therefore, k_{shoe} should be selected as large as possible. However, note that if the distance between two pole shoe edges is comparable to the air gap length d_{ag} , fringing effects start to appear, which worsen the machine constant and should hence be avoided. For this reason, it is found by inspection of the FEM fields that $k_{\text{shoe}} = 0.8$ is an adequate choice. For what concerns k_{PM} , one can observe that the impact on the axial force is much more prominent, which is expected (see (3.9), **Fig. 3.4 (b)** and the discussion thereof in **Sec. 3.2.4**). The only motivation to reduce k_{PM} is given by the very high magnetic flux density in the mover back iron, resulting if no gap is left between the PMs with opposite polarity. By inspection of the solved fields, a value around $k_{\text{PM}} = 0.8$ is reasonable. Finally, $k_{\text{PM}} = 0.83$ is chosen, as this results in a PM length of $l_{\text{PM}} = 10$ mm, which is a convenient size to manufacture and/or to find commercially.

The design space generated by the second (main) optimization step with $3 \times 6 \times 4 \times 5 = 360$ parameter configurations is explored with the aid of **Fig. 3.9**. Each design is initially simulated with a fixed test current $N\hat{I}_{\text{test}} = 120$ Aturns, which results in a certain generated maximum axial force $F_{\text{ax,max}}$. For a direct comparison, the results of each design are then scaled to the same axial force output $F_{\text{req,peak}} = 43$ N. Such force is reached for a scaled current $N\hat{I}_{\text{scal}} = (F_{\text{req,peak}}/F_{\text{ax,max}}) N\hat{I}_{\text{test}} = k_{\text{scal}} \hat{I}_{\text{test}}$, which implies that the

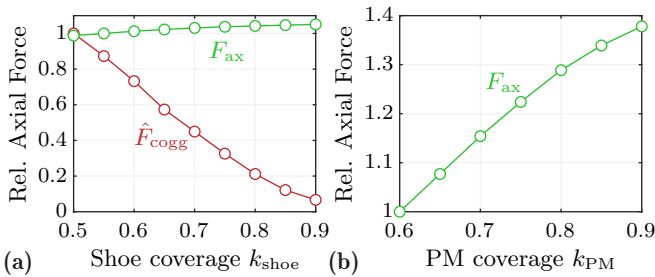


Fig. 3.8: Results of the first (preliminary) optimization step. **(a)** Effect of the shoe coverage factor k_{shoe} on the axial drive force F_{ax} and the cogging force amplitude \hat{F}_{cogg} , relatively to the case $k_{\text{shoe}} = 0.5$. **(b)** Effect of the PM coverage factor k_{PM} on the axial drive force F_{ax} , relatively to the case $k_{\text{PM}} = 0.6$.

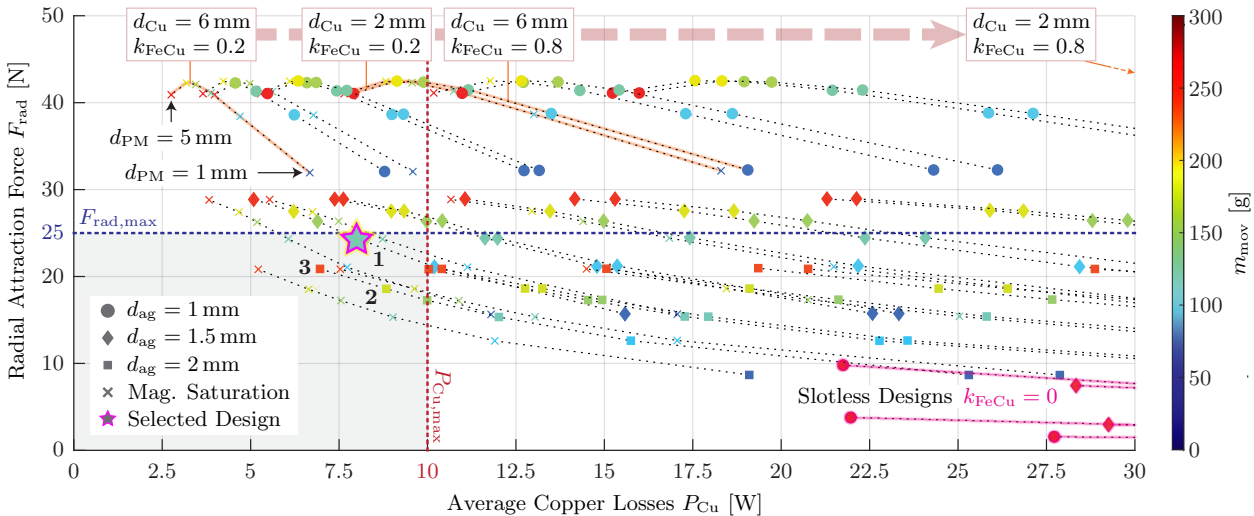


Fig. 3.9: Design space generated by the second optimization step, visualized on the P_{Cu} - F_{rad} plane. The color of each point represents the mover mass m_{mov} . The points with the same parameters configuration except for d_{PM} are connected (see e.g., the dashed lines highlighted in orange). This helps to visualize the effect of the remaining swept parameters. The considered threshold for magnetic saturation is $B_{sat} = 2.2$ T. At the bottom-right corner, the slotless designs are visible (highlighted in magenta). Moreover, the limits in losses and radial attraction force are reported, which allow to identify the feasible designs **1**, **2** and **3** listed in **Tab. 3.3**.

Tab. 3.3: Feasible LA designs under the specified constraints.

#	d_{ag}	d_{PM}	d_{Cu}	k_{FeCu}	F_{rad}	P_{Cu}	m_{mov}
1)	1.5 mm	2 mm	6 mm	0.4	24.4 N	8.0 W	129 g
2)	2 mm	3 mm	6 mm	0.4	18.6 N	8.8 W	174 g
3)	2 mm	5 mm	6 mm	0.4	20.9 N	7.0 W	241 g

average ohmic losses have to be scaled as $P_{\text{Cu,scal}} = k_{\text{scal}}^2 P_{\text{Cu}}$. In **Fig. 3.9**, the design space is visualized on the $P_{\text{Cu}}-F_{\text{rad}}$ plane, which represents the most relevant design trade-off. On this plane, it is also possible to distinguish quite clearly the effect of the swept parameters. The ‘magnetic’ parameters d_{ag} and d_{PM} have the most noticeable effect on both F_{rad} and P_{Cu} . This is expected, as they directly determine the magnetic flux density in the air gap B_{ag} (cf. (3.8)), with the consequent trade-off discussed in **Sec. 3.2.4**. The designs can be conveniently divided according to the value of d_{ag} into three groups. Furthermore, the points sharing the same parameter configuration except for d_{PM} are connected. The magnetic gap length d_{ag} affects B_{ag} as it increases the equivalent reluctance of the magnetic circuit, with the result that the magnetic flux ϕ_{ag} is lower. The extreme case is represented by the group of slotless designs, which due to the absence of stator teeth have the largest magnetic air gap. Consequently, these designs exhibit very low radial attraction force, but also comparably high losses. For instance, the best slotless design can not achieve the required force with less than $P_{\text{Cu}} = 21.8$ W and only for very thick/heavy PMs ($d_{\text{PM}} = 5$ mm). The thickness d_{PM} instead affects B_{ag} by increasing the PM’s MMF $\theta_{\text{PM}} = H_c d_{\text{PM}}$, and hence the magnetic flux ϕ_{ag} . Nevertheless, it also introduces an equivalent series reluctance comparable to air ($\mu_r \approx 1.05$), which at a certain point counterbalances the increased MMF (cf. again (3.8)). The ‘copper-related’ parameters d_{Cu} and k_{FeCu} only affect P_{Cu} instead, as they determine the copper cross section $A_{\text{Cu},0}$ (cf. (3.14)). For instance, consider a group of designs connected by a dashed line. Decreasing the value of d_{Cu} and/or increasing the value of k_{FeCu} decreases $A_{\text{Cu},0}$ and hence scales the group towards the right along the P_{Cu} -axis. Clearly, there is two limits to consider in this regard. On one hand, d_{Cu} is limited by the maximum outer diameter of the LA (and also the thickness of the stator core d_{Fe} has to be included). On the other hand, smaller values of k_{FeCu} make the stator teeth thinner, to the point that the magnetic flux density is too high and the material saturates.

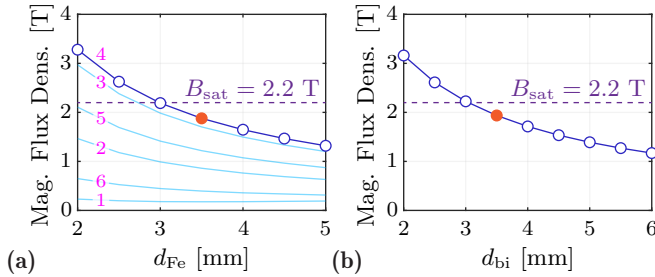


Fig. 3.10: Results of the third optimization step. **(a)** Average magnetic flux density for the six different locations in the stator core indicated in **Fig. 3.5 (a)** (above each slot) versus the thickness d_{Fe} . **(b)** Average magnetic flux density at the middle of the mover back iron versus the thickness d_{bi} .

With the limit in average losses $P_{Cu,max}$ and radial attraction force $F_{rad,max}$ and by excluding the cases with magnetic saturation, only the three feasible designs listed in **Tab. 3.3** remain. The design with the least copper losses and radial attraction force is *Design 3*. Nevertheless, the resulting mover mass is the highest. As the copper losses have to be minimized, but a radial attraction force up to the limit can be tolerated, *Design 1* is finally selected, which has almost half the mass.

With this choice, it is finally possible to complete the optimization with the third step, ensuring that no magnetic saturation occurs. The parameters d_{Fe} and d_{bi} are swept and the resulting average magnetic flux densities in the stator core (above every slot) and the mover back iron (in the middle) are shown in **Fig. 3.10**. It can be observed that it is possible to save volume and weight for both stator and mover by using a magnetic material with high saturation flux density, like e.g., *VACOFLUX50*. Considering the threshold $B_{sat} = 2.2$ T (with a little margin from it), the values $d_{Fe} = d_{bi} = 3.5$ mm are selected.

3.4 Hardware Prototype

This section describes the hardware prototype of the selected LA design and the test bench needed to conduct its experimental verification, highlighting the practical realization choices made.

3.4.1 Stator Realization

Stator Core

In order to greatly simplify the stator manufacturing and assembling, the stator core is segmented along the axial direction into multiple identical rings like the one shown in **Fig. 3.11 (b)**. As it can be seen from the reported cross section in **Fig. 3.11 (a)**, the length of each segment corresponds to a stator pitch $\tau_s = 4$ mm, spanning exactly the width of one tooth and two half slots. This way, it is possible to machine the ring down to the desired tooth thickness of $l_{\text{Fe}} = 1.6$ mm and also realize the thin pole shoe solidly together with the tooth. Furthermore, this shape allows to insert and firmly hold in place a single coil between two stator rings. The material used is the desired *VACOFLUX50*, whose magnetization curve is measured experimentally on a toroidal sample [48] and reported in **Fig. 3.11 (c)**. From this, it is possible to estimate the worst-case core losses, i.e., assuming that all the material experiences the full variation of magnetic flux density with amplitude $\Delta B = 2$ T. The encircled area on the B - H plane, multiplied by the volume of the stator core and $f_{\text{op}} = 5$ Hz results in $P_{\text{Fe}} = 3.18$ W. Nevertheless, due to the machine geometry and operation, the FEM simulations show that no part of the stator core experiences such large swing in B , but rather $\Delta B \approx 1$ T with a $B_{\text{DC}} = 0.5$ T DC bias is a more realistic average approximation. For the sake of simplicity, the DC bias is hereby neglected, otherwise a displacement factor [48] needs to be considered. According to the dependence of P_{Fe} on B^β with $2 < \beta < 3$ in the Steinmetz equation, the core losses will be at least lower than $P_{\text{Fe}} = 0.8$ W.

Coils

The coils are custom-made as well (cf. **Fig. 3.12 (b)**), with the aim of maximizing the fill factor k_{ff} of the chosen copper cross section. Importantly, the selection of the number of turns N takes into account the specifications of the inverter driving the LA. This is compactly realized based on the IC *MP6535* by *Monolithic Power Supply*. The maximum current that this module can supply is $I_{\text{inv,lim}} = 5$ A and the maximum allowed DC-link voltage is $U_{\text{DC,max}} = 26$ V. A larger N reduces the inverter current \hat{I}_{inv} and is therefore beneficial as the conduction losses of the inverter's switches are also reduced. Nevertheless, the induced voltages $u_{q,\{a,b,c\}} = N u_{q,\{a,b,c\},1}$ increase to the point that it might not be possible to impress the necessary current during operation. In fact, by simple inspection of the equivalent circuit in **Fig. 3.12 (a)** and considering that the LA is realized with two coils in series per phase, the

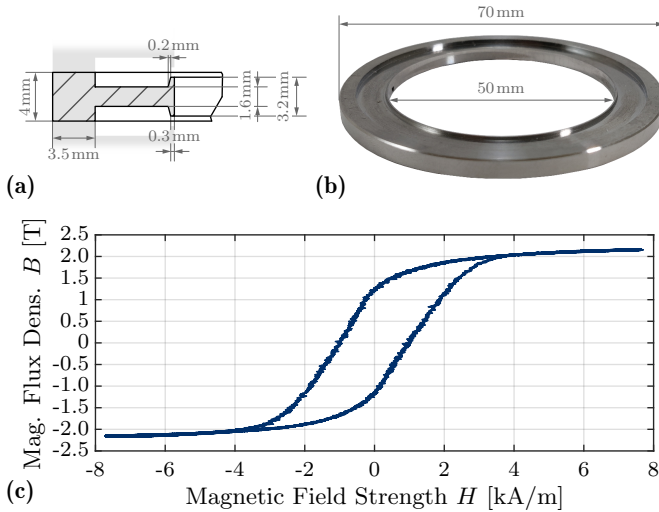


Fig. 3.11: Realized hardware prototype of the TLA. **(a)** Stator cross section with annotated dimensions. **(b)** Realized stator ring made of VACOFLUX50. **(c)** Magnetization curve of VACOFLUX50, measured on a toroidal material sample at $f_{op} = 5$ Hz with two windings. One is used to impress the sinusoidal magnetizing current and the other one to measure the induced voltage, which is then integrated and divided by the cross section of the sample.

applied phase voltages need to be $u_{\{a,b,c\}} = 2 R_c i_{\{a,b,c\}} + 2 u_{q,\{a,b,c\}}$. Note that the voltage drop on the inductance L_c is neglected due to the low operating frequency $f_{op} = 5$ Hz. The inverter can only provide a maximum voltage $U_{\{a,b,c\},max} = U_{DC,max}/2 = 13$ V. In order to check that this limit is respected, the single-turn flux linkages $\psi_{\{a,b,c\},1}(t)$ of each coil are obtained from the FEM simulations and their time derivative is considered, showing that a maximum voltage of $U_{q,1,max} = 27$ mV is induced per turn. The number of turns that can be fitted by the manufacturer with a 0.40 GiB coated wire in the given cross section is $N = 75$. The resulting fill factor is $k_{ff} = 0.53$, the inverter current is $I_{inv,max} = 2.2$ A and the maximum induced voltage is $U_{q,max} = 4.05$ V. This results in a maximum phase voltage $U_{\{a,b,c\},max} = 11.9$ V, which leaves some margin from the inverter limit. The electrical characteristics of the coil are measured and reported in **Fig. 3.12 (c)**. The DC coil resistance is $R_c = 2.16 \Omega$. The inductance is measured for three different conditions, i.e., in air and when mounted on the stator without and with mover inserted. The last case is the

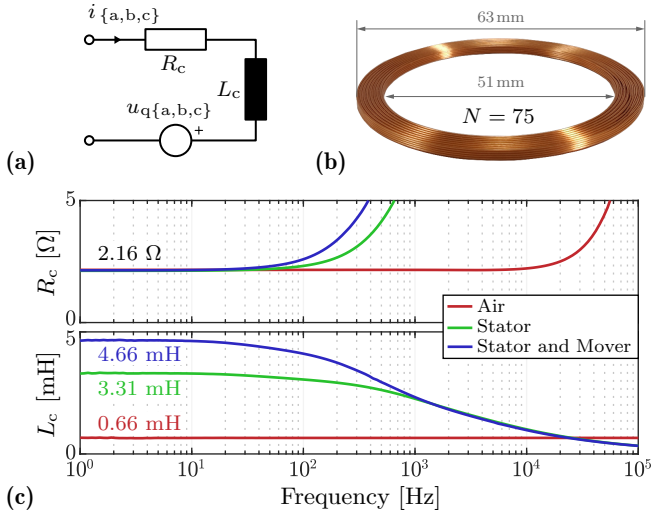


Fig. 3.12: Realized hardware prototype of the TLA. (a) Equivalent circuit of a stator coil, consisting of the resistance R_c , the inductance L_c and the induced voltage $u_{q,\{a,b,c\}}$. (b) Realized stator coil made of a 0.40 G1B coated copper wire with $N = 75$ turns. (c) Measured electrical characteristics of the realized stator coils versus frequency, using an impedance analyzer (*Omicron Lab Bode100*). Three cases are compared: in air, in stator without and with mover. The curves show that high frequency effects (eddy, skin and proximity) appear.

one to be considered to tune the current controller. The final stator assembly with the realized stator core rings and coils can be seen in **Fig. 3.13 (a)**.

3.4.2 Mover Realization

The mover consists of the back iron and the PMs. The former is also made of *VACOFLUX50* and is built from two simple rings with the dimensions indicated in **Fig. 3.13 (b)**. The radially magnetized SPMs are not only quite fragile if realized as a single ring-shaped piece, but also extremely difficult/expensive to manufacture with the correct magnetization direction. For this reason, multiple small, axially magnetized, rectangular PMs are used. They are glued on the outer surface of the back iron, one adjacent to the other as shown in **Fig. 3.13 (b)**. Their thickness is the chosen $d_{PM} = 2$ mm and their width is $w_{PM} = 4$ mm. The magnetization grade is *N50*. Such PMs are commercially

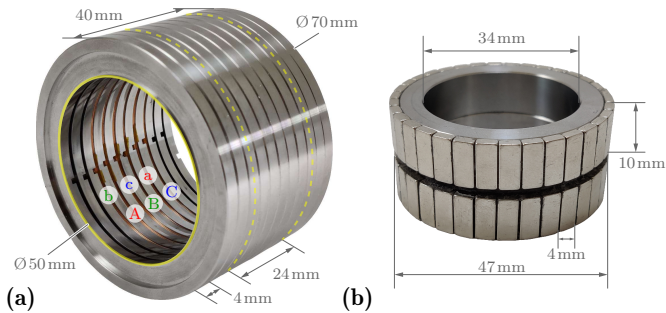


Fig. 3.13: Realized hardware prototype of the TLA. **(a)** Overall stator assembly with stacked segments equipped with coils. **(b)** Realized mover with two stacked back iron rings and segmented PMs. Each segment is $w_{PM} = 4$ mm wide and $l_{PM} = 10$ mm long.

available and rather inexpensive to purchase, and they well-approximate the desired magnetization profile. The correct polarity of each PM is verified during the gluing process with a magnetometer. The final weight of the mover is $m_{mov} = 148$ g.

3.4.3 Experimental Test Bench

In order to verify experimentally the functionality of the realized LA prototype, a custom multi-purpose test bench is built. There are two possible variants, shown in **Fig. 3.14**: one that can be used to measure axial forces and one that is specifically needed to measure the radial attraction force.

Axial Force

In order to measure the axial force, the TLA is mounted as in **Fig. 3.14 (a)**. The stator is firmly held in place with a clamp fixture directly mounted to the baseplate. The mover is mounted on a shaft and can only move along the axial direction. The shaft is supported on the two sides by teflon bearings for minimum friction. At the end of the shaft there is a linear positioning stage on which a force sensor (*Rokubi, BOTA Systems*) is mounted. To prevent the effect of unwanted backlashes coming from the linear positioning stage during measurements, the shaft and the force sensor are not connected together. Instead, the axial force is measured by energizing the TLA and pushing with the sensor against the shaft of the mover.

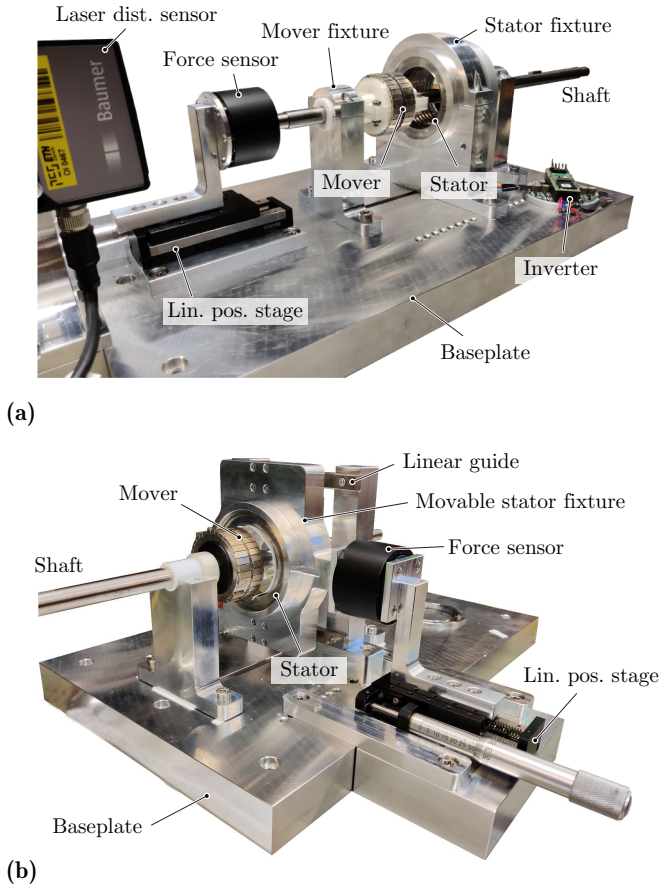


Fig. 3.14: Experimental test bench. **(a)** Variant for axial force measurements with fixed stator and movable mover along the axial direction. **(b)** Variant for radial attraction force measurements with fixed mover and movable stator along the radial (x -only) direction.

Radial Attraction Force

For this measurement, it is necessary to adjust the radial position of the mover, so it can be displaced away from the center of the machine. It is decided to fix the mover (also axially) and adjust the stator position instead. Therefore, the stator clamp is adapted as shown in **Fig. 3.14 (b)** and mounted on two linear guides, which constrain the radial movement horizontally (along the x -axis). This time, the linear positioning stage and the force sensor are placed on the side of the movable stator clamp.

3.5 Experimental Verification

The experimental measurements conducted on the hardware prototype of the LA are reported in this section. The verification includes measurements of the radial attraction force and the profile of the drive force along the axial direction. From the latter, the machine constant k_m is obtained.

3.5.1 Radial Attraction Force Measurements

In order to measure the radial attraction force, the LA is mounted on the corresponding test bench (cf. **Fig. 3.14 (b)**). It is ensured that the axis of the mover is well-aligned with the axis of the stator, especially in the y -direction. The x -position is adjusted in steps of $10\ \mu\text{m}$ and for each position the output of the force sensor is recorded for 10 s and averaged. The measurements are reported in **Fig. 3.15** for positive displacements in the x -direction. This is because the linear positioning stage can sustain a high load force only in one direction. It can be observed that the measured values are in good agreement with the simulated ones. They are obtained from a full 3D FEM simulation with the non-linear material definition for *VACOFLUX50*. It can be seen that, for the maximum displacement $x_{\text{mov}} = 140\ \mu\text{m}$, the obtained radial attraction force is $F_{\text{rad}} = 23.8\ \text{N}$, which is in agreement with what is expected from the design space.

3.5.2 Machine Constant - Axial Force Profile

The measurements of the axial force profile are carried out using the test bench of **Fig. 3.14 (a)**. The mover is initially positioned at $z_{\text{mov}} = 10\ \text{mm}$, i.e., at one end of the LA. Then, a q -current with constant amplitude $\hat{I} = 1\ \text{A}$ is impressed and controlled in the winding. The phase currents $i_{\{a,b,c\}}$ fed by the inverter are determined from the electrical angle ϑ for MFPA, hence

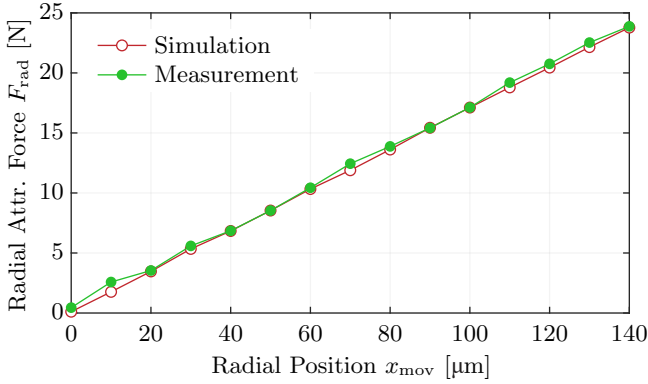


Fig. 3.15: Radial attraction force F_{rad} versus the mover's radial position x_{mov} . For comparison, the simulated forces from the corresponding 3D FEM model with realistic non-linear material definitions for *VACOFLUX50* are reported.

for each axial position of the mover z_{mov} , $\vartheta = \frac{2\pi}{l_{\text{act}}} z_{\text{mov}}$ is assigned. At this point, the mover is slowly pushed inside the LA with the help of the linear positioning stage, till it reaches $z_{\text{mov}} = -10$ mm, i.e., the other end of the actuator. During the process, the force sensor is in contact with the shaft on which the mover is mounted and measures the axial force F_{ax} pushing against it. Simultaneously, the position of the mover is measured with a laser distance sensor (*Baumer OM70-PO140*) and recorded. With this method, the points of **Fig. 3.16 (a)** are obtained. The values of the measured forces are equivalent to the machine constant k_m , as the impressed current amplitude is unitary. If the measured machine constant is compared to the results of the full non-linear 3D FEM simulations, it can be seen that they are in agreement, with an average absolute error of 3.2 % over the whole profile, with slightly higher values for the negative z_{mov} -axis (peaking at 7.7 % for $z_{\text{mov}} = -7$ mm). Also the reduction of k_m with $|z_{\text{mov}}|$ to 2/3 of its value at $z_{\text{mov}} = 0$ mm is verified. Moreover, the cogging force component is visible from the measurements and its amplitude can be estimated to be $\hat{F}_{\text{cogg}} \approx 1$ N. Most importantly, with the measured k_m it is possible to calculate the instantaneous copper losses and their average over one period of operation with the same procedure discussed in **Sec. 3.3.1** and **Fig. 3.6**. The result is a continuous copper power loss of $P_{\text{Cu,avg}} = 7.9$ W. Adding the estimated core losses $P_{\text{Fe}} = 0.8$ W and comparing to the required mechanical output power $P_{\text{mech,avg,LA}} = 3.6$ W, an efficiency of $\eta_{\text{LA}} = 41.4$ % is obtained. Finally, another aspect to verify is the

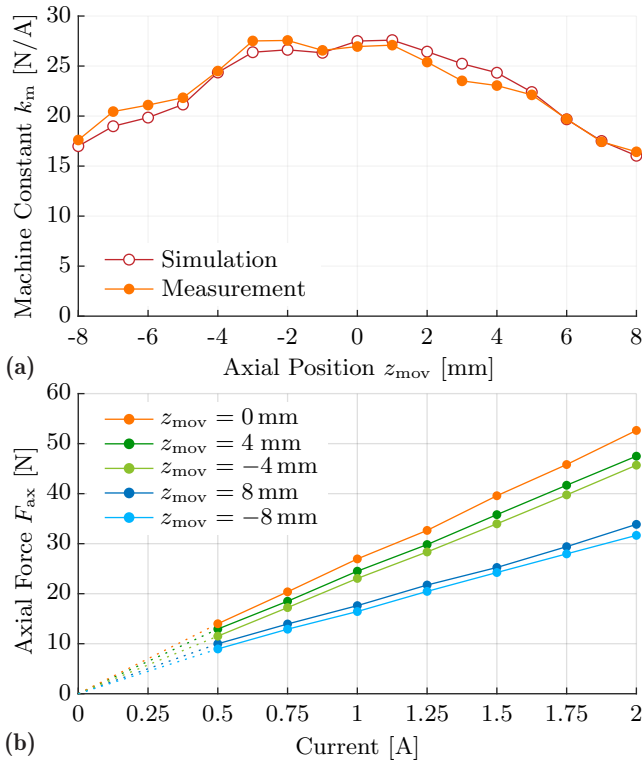


Fig. 3.16: (a) Axial force profile measured for $\hat{I} = 1$ A (corresponding to the machine constant k_m) compared to the values obtained by the non-linear 3D FEM simulation with $N\hat{I} = 75$ Aturns. (b) Linearity of the measured axial force versus the impressed current amplitude at different axial positions of the mover.

linearity of the generated axial force with respect to the current amplitude. **Fig. 3.16 (b)** shows the force measurements at different axial positions for increasing values of the current amplitude in steps of 0.25 A till $\hat{I} = 2$ A. This is the maximum value that the inverter can continuously sustain due to thermal limitations. For all measured cases, the maximum percent non-linearity does not exceed 2%.

3.6 Summary

In this chapter the analysis, design, realization and experimental verification of the LA of the *ShuttlePump* were presented. With the realized compact hardware prototype it is possible to meet the axial force requirements (up to 43 N peak) with 7.9 W of continuous power losses, which is below the specified limit of 10 W and hence prevents the risk of blood damage due to heating. Furthermore, the measured maximum radial attraction force of 23.8 N acting on the mover is within the specified allowed radial load of the hydrodynamic bearing supporting the piston during operation. The next step is the design and realization of the RA part.

4

Rotary Actuator Design and Verification

The content of this chapter is also published in:

- ▶ **R. V. Giuffrida**, R. Senti, D. Bortis, T. Bierewirtz, K. Narayanaswamy, M. Granegger, and J. W. Kolar, “Spatially Highly-Constrained Auxiliary Rotary Actuator for a Novel Total Artificial Heart,” *IEEE Open Journal of the Industrial Electronics Society*, vol. 4, pp. 732-747, December 2023.

Chapter Abstract

This chapter presents the details of the Rotary Actuator (RA) part of the *ShuttlePump*. This has considerably lower output power requirements (about 100 mW) due to the low operating torque and angular speed (3.1 mN m and up to 300 rpm, respectively). However, the RA is highly constrained spatially, as it needs to be integrated very close to the previously realized LA. This forces a Permanent Magnet Synchronous Machine (PMSM) design with a rotor only partially equipped with PMs and stators covering only half of the total circumference, which introduces a considerable cogging component to the total torque. The proposed PMSM is hence optimized using Finite Element Method (FEM) simulations to select a final design with low power losses and low cogging-induced angular speed ripple. The machine is realized as a hardware prototype, and the experimental measurements confirm that the proposed RA can meet the continuous torque requirement with 324 mW of power losses. The successful implementation of the RA (and LA) finally verifies the practical feasibility of the integrated LiRA and provides the basis for a comprehensive test of the complete *ShuttlePump* in a hydraulic test rig in the course of further research.

4.1 Introduction

This chapter moves a step further in the development of the overall LiRA and drive system by presenting the design, realization, and experimental verification of the Rotary Actuator (RA) part of the *ShuttlePump*. As the RA has the important yet auxiliary function of providing a constant rotation of the pump's piston, it needs to be accommodated in the remaining available volume close to the LA. The chapter is structured as follows: **Sec. 4.2** defines the constraints and requirements for the RA. Based on these, **Sec. 4.3** explains the proposed machine concept, and the appropriate machine topology is selected. The design is then optimized using FEM simulations in **Sec. 4.4** and the interactions with the LA are investigated. **Sec. 4.5** provides details about the realized hardware prototype of the RA, which is verified experimentally with the results of **Sec. 4.6**. Finally, **Sec. 4.7** concludes the chapter.

4.2 Spatial Constraints and Requirements for the RA

An inherent characteristic of the system is the high imbalance in the mechanical output power required from the LA and the RA. In particular, due to the high axial force required to push the blood into circulation, the LA requires $P_{\text{mech,avg,LA}} = 3.6 \text{ W}$ on average during operation. In contrast, for the RA, the continuously required axial torque, obtained from CFD simulations, is $M_{\text{req}} = 3.1 \text{ mNm}$ [26] and it is relatively low. Together with a rotational speed $\omega_{\text{op,max}} = 2\pi f_{\text{op,max}} = 31.42 \text{ rad/s}$, it results in an average mechanical output power of only $P_{\text{mech,avg,RA}} = 98 \text{ mW}$. Consequently, it was decided to design the two actuators independently, prioritizing the LA instead of selecting a combined LiRA topology [49–51]. Therefore, as can be seen by comparing together **Fig. 1.3 (b)** and **Fig. 1.3 (c)**, most of the available volume is utilized by the LA. The RA has to be accommodated in the remaining space, highlighted in **Fig. 4.1**. Both actuators consist of a fixed stator hosting the machine winding and a moving part equipped with PMs. For the sake of clarity, in this chapter, the moving part of the LA is denominated the ‘*translator*’, whereas the moving part of the RA is the ‘*rotor*’. Together, they build up the ‘*mover*’ of the LiRA, which is embedded in the moving ‘*piston*’ of the *ShuttlePump*. The term mover refers to the magnetic element that interacts with the stators of the LiRA, whereas the term piston refers to the complete mechanical/hydraulic element (i.e., including the blades). The maximum outer

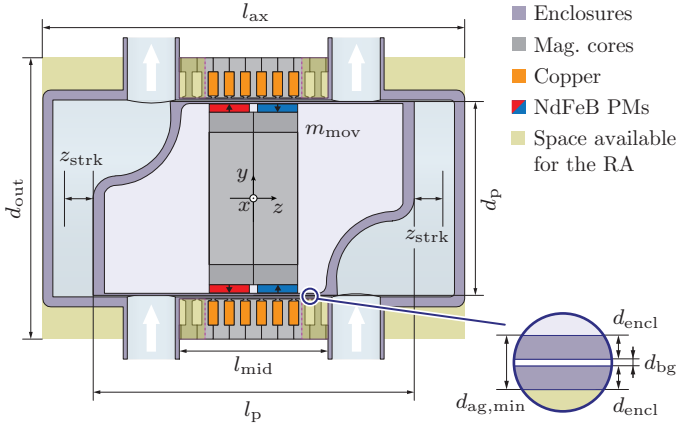


Fig. 4.1: Sectional view (yz -) of the *ShuttlePump*, showing its enclosure and specially shaped piston with annotated dimensions, reported in **Tab. 4.1**. Also the designed LA is visible, consisting of the stator (with the machine winding, around the enclosure) and the ‘translator’ (with PMs, embedded in the piston) [27]. The yellow area indicates the available space that can be used to fit the RA. Importantly, the stator extensions of the LA can also be used for this purpose.

diameter of the RA is limited as for the LA to $d_{out} = 70$ mm. Nevertheless, if possible, a design with a smaller diameter should be preferred, as it makes the overall system easier to implant. The stator of the RA will have to be placed on either side of the *ShuttlePump* or on both, within the maximum axial length of $l_{ax} = 105$ mm. Importantly, the stator extensions of the LA can also be modified for this purpose. The rotor of the RA will have to use the available surface of the piston, i.e., not already occupied by the PMs of the LA.

Compared to the LA, the requirements on the RA are less stringent altogether. Concerning the power losses, it is surely convenient to minimize them in order not to generate additional heat in the pump. However, it can be expected that the losses from the RA will only be a small share of the total. Moreover, the candidate locations for the RA are more favorable in terms of heat dissipation. In fact, unlike the thin blood layer right in the magnetic air gap of the LA, the two chambers host a large blood volume that continuously circulates through the pump, which is much more favorable for cooling. As a design guideline, a loss budget of $P_{Cu,RA,max} = 0.5$ W is defined, which

Tab. 4.1: Specifications of the *ShuttlePump*, extended from [27].

Name	Symbol	Value	Unit
Maximum axial dimensions	l_{ax}	105	mm
Maximum radial dimensions	d_{out}	70	mm
Piston axial length	l_p	78	mm
Piston outer diameter	d_p	48.72	mm
Inter- in-/outlets distance	l_{mid}	40	mm
Enclosure thickness (lateral)	d_{encl}	0.5	mm
Blood gap	d_{bg}	140	um
Magnetic gap	$d_{ag,min}$	1	mm
Axial stroke amplitude	z_{strk}	8	mm
Maximum axial force	$F_{req,peak}$	≈ 43	N
Axial torque	M_{req}	3.1	mN m
Maximum radial force	$F_{rad,max}$	25	N
Piston weight	m_{mov}	< 300	g
Piston frequency	f_{op}	1.5 - 5	Hz
Piston rotational speed	Ω_{op}	90 - 300	rpm
Maximum speed ripple	$\Delta\Omega_{op}$	< 20	%
Operating conditions		2.5 - 9	L/min
Maximum Av. Cont. Losses	$P_{Cu,avg,max}$	10	W
Blood temperature increase	ΔT_{max}	2	K

corresponds to 5 % of the maximum allowed losses $P_{Cu,avg,max}$. Analogously, eventual magnetic pull forces that act radially on the rotor and disturb the hydrodynamic bearing are not considered, as they are negligible compared to the ones already introduced by the LA. Finally, certain RA designs can introduce cogging torque components due to, e.g., a slotted stator or edge effects. This leads to a certain speed ripple $\Delta\Omega$, which, however, is uncritical as long as $M_{req} = 3.1$ mN m is provided on average. Considering further that the RA will be operated with an angular speed controller, an open-loop speed ripple up to 20 % of the operational speed Ω_{op} can be allowed. This aspect is discussed more in detail in **Sec. 4.3.3**, once the RA concept and topology are defined.

4.3 Proposed Machine Concept

This section presents the proposed machine concept for the RA, according to the considered spatial constraints. Similarly to the LA, this is also based on a PMSM with surface-mounted PMs. To keep the system's complexity as low as possible, the number of phase currents of the RA will be limited to three. Together with the three phase currents of the LA, the complete LiRA features a total of six phase currents.

4.3.1 Placement of the RA PMs and Stators

Given the tight space constraints and the geometry of the *ShuttlePump*, it is decided to realize the RA out of two modules, located on the two sides of the pump. This way, the total functional volume of the RA can be more evenly distributed around the pump compared to when a single RA module is used. Considering the presence of the pump's inlets and outlets, there are two main placement options for the two RA modules, illustrated in **Fig. 4.2**.

The first option is to place them towards the outer sides of the pump, as shown in **Fig. 4.2 (a)**. Although this way, most of the lateral surface of the two piston blades can be used to place the rotary PMs, there is one important drawback to consider. With this asymmetric design, there are two

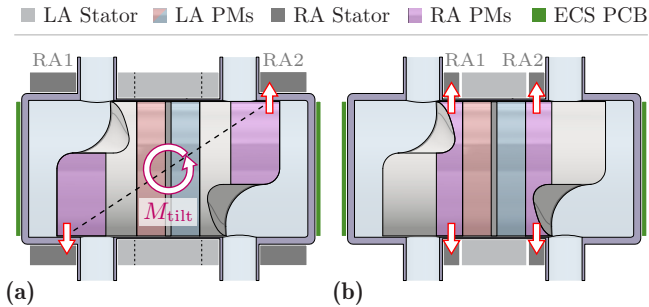


Fig. 4.2: Two possible placement options for the two RA modules. **(a)** Option 1: towards the outer sides of the *ShuttlePump*. This option introduces an undesired tilting torque M_{tilt} due to unbalanced reluctance attraction forces at the two sides of the piston. Furthermore, the RA stators could disturb the Eddy-Current Sensors (ECSs) mounted on the sides. **(b)** Option 2: towards the middle part of the *ShuttlePump*. With this option, a symmetrical design is possible, thus preventing any undesired tilting torque.

unbalanced net reluctance forces (acting between the PMs on the piston and the facing rotary stators, as indicated) along two off-set planes, which cause an undesired tilting torque M_{tilt} . For small air gaps of the RA (typically beneficial for efficient machine designs), the magnetic attraction forces are strong, to the point that M_{tilt} could compromise the pump's operation. One possible workaround would be to choose a machine design with a large magnetic air gap (e.g., slotless), which, however, would require higher ohmic losses and/or a larger stator volume for the same torque output. Finally, another aspect to consider is that the chosen location for the linear-rotary position sensors will be on the two sides of the pump [52]. Due to their eddy-current-based operating principle, no conductive material besides the piston-embedded measurement target is allowed in close proximity.

The second option overcomes the aforementioned drawbacks and is therefore the selected RA concept. As shown in **Fig. 4.2 (b)**, both modules are placed towards the middle part of the pump, i.e., right adjacent to both sides of the designed LA. The first and foremost advantage is that the stators of the RA can thus be integrated into the stator extensions of the LA. This allows to beneficially reuse the excess core material that has to be placed anyway to guarantee the functionality of the LA. The result is a highly compact LiRA design with a substantially lower total weight. The second important advantage is that this design can be made symmetric, thereby eliminating the undesired tilting torque M_{tilt} . In fact, in the middle part of the piston, it is possible to place the rotary PMs symmetrically around the lateral surface.

Considering the limitations in space seen in **Fig. 4.1**, the PMs are finally placed as shown in **Fig. 4.3 (a)**, i.e., only at four equally spaced locations around the circumference of the piston. The PM segment at location **A** is the most constrained and can only span an angle of $\alpha_{\text{PM},1} = 45^\circ$. The maximum axial length that can be fitted there sets the axial length of the rotor and is limited to $l_{\text{PM}} = 5$ mm. The PM segment at location **B**, instead, can only span an angle of $\alpha_{\text{PM},2} = 25^\circ$. The PM segments at locations **C** and **D** are symmetric with respect to the z -axis to the ones at locations **A** and **B**, respectively. As a consequence of the PM locations, the rotary stators are placed as shown in **Fig. 4.3 (b)**. As it can be noticed, most of each rotary stator is integrated into the stator extensions of the LA. To cover also the rotary magnets during the whole linear motion (and prevent unwanted axial reluctance forces), the total length of the rotary stator is $l_{\text{stat,RA}} = z_{\text{strk}} + l_{\text{PM}} = 12$ mm. Note that due to the presence of the pump's inlets and outlets, the stator cannot occupy the full circumference. As shown in **Fig. 4.3 (b)**, the angle spanned by the stator is limited to $\alpha_{\text{stat,max}} = 110^\circ$ on each side of the *ShuttlePump*.

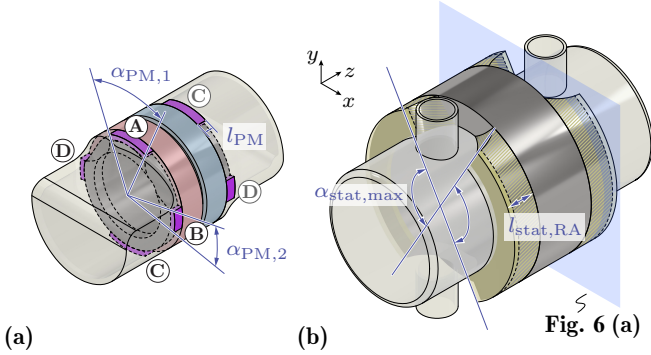


Fig. 4.3: Proposed RA concept for the *ShuttlePump*. (a) 3D view of the piston with designated locations (A to D) for the rotary PMs (purple), constrained to the limits $\alpha_{PM,1} = 45^\circ$, $\alpha_{PM,2} = 25^\circ$ and $l_{PM} = 5$ mm. (b) 3D view of the enclosure with selected locations for the rotary stator highlighted in yellow. The stators are mostly integrated in the extensions of the LA and their length along the z-direction is $l_{stat,RA} = 12$ mm. Along the circumferential direction, they are constrained to $\alpha_{stat,max} = 110^\circ$ on each side.

4.3.2 PMSM Topology Selection

In order to make the integration with the LA possible, only PMSM topologies with a slotted stator and a concentrated winding are considered for the RA. In fact, the main role of the stator extensions (and the pole shoes) used in the LA is to maintain approximately constant the total equivalent reluctance seen by the PMs of the translator while the piston shuttles along the axial direction. Without them, a strong axial reluctance pull force would appear as soon as the translator is displaced away from the center of the LA, which would compromise its operation [27]. With a slotted stator design, the RA can be integrated into the stator extensions of the LA, preserving its original air gap length $d_{gap} = 1.5$ mm. Furthermore, in order to ensure that the overall reluctance profile is unchanged, pole shoes with large coverage and sufficient thickness have to be used. For what concerns the use of a concentrated winding, it is easily understood that it would greatly simplify the realization of the RA and its coils, as well as their interconnection with minimum wire length [53].

Based on these premises, it is possible to select the pole-slot combination of the RA according to the proposed placement of the stator and the PMs in Fig. 4.2 (b) and Fig. 4.3. Three criteria guide the selection. First, given that

the stator is, in fact, split into two halves, it is reasonable to choose an even number of slots N_s . Second, N_s should not be too high in order to ensure that all the parts of the stator (teeth, pole shoes, and coils) are easy to manufacture and assemble. Third, it is necessary to accommodate the same number of coils per phase, in order to guarantee that the inverter supplying the RA is loaded symmetrically. As a result, the most suitable combination is $N_s = 12$ slots and $N_p = 8$ poles. If the defined space constraints are also considered, the standard PMSM topology has to be substantially modified, as shown in **Fig. 4.4 (a)**. In particular, the dashed contours indicate the eliminated parts, i.e., two stator sectors, as well as most of the PMs. Consequently, it can be said that the RA module consists of two identical half-machines with $N_s = 3$ slots and $N_p = 2$ poles. Each half-stator covers an angle $\alpha_{\text{stat}} = 90^\circ$ and has one coil per phase, each concentrated around a stator tooth. Motors with partial stator coverage do exist in the literature for highly spatially constrained applications [54–56]. The PMs on the rotor will all have the same (radial) magnetization direction and polarity. Although the PMs of opposite

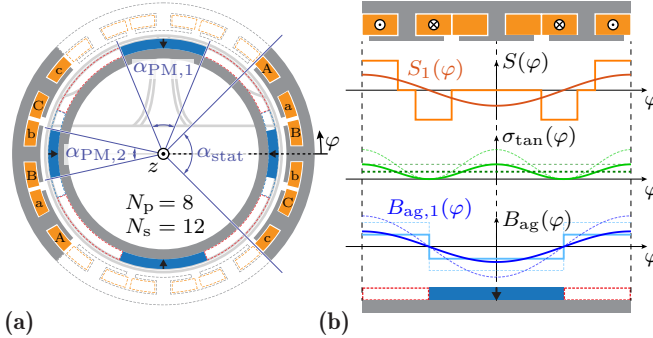


Fig. 4.4: (a) Proposed PMSM topology for the RA. The standard 8-pole, 12-slot machine is specially adapted to the space constraints of the *ShuttlePump*, with the dashed contours indicating the eliminated parts. The result is two half-stators with three slots each and a rotor equipped with four magnet segments of only one polarity. (b) Exemplary machine plan (one half-stator) demonstrating that tangential force (and hence torque) generation is still possible even if part of the PMs is removed. $S(\varphi)$ is the current sheet with its fundamental component $S_1(\varphi)$, $\sigma_{\text{tan}}(\varphi)$ is the area-related force density and $B_{\text{ag}}(\varphi)$ is the air gap magnetic flux density with its fundamental component $B_{\text{ag},1}(\varphi)$. The dashed curves correspond to the standard PMSM topology, i.e., with full PM coverage.

polarity are suppressed, it can be shown that force generation is still possible (similarly, e.g., to consequent-pole machines [57, 58]), e.g., by inspecting the half-machine plan of **Fig. 4.4 (b)**. Furthermore, it is decided to use PMs of opposite magnetization with respect to the adjacent ones of the LA. As a consequence, one RA module will have only positively r -magnetized PMs ('north') and the other module only negatively r -magnetized ones ('south') (cf. **Fig. 4.5 (a)**). This way, the spatial periodicity of the magnetic field distribution along the axial direction is respected. This measure can potentially increase the generated axial force due to the interaction between the rotary PMs and the stator of the LA. Finally, it is ensured that at least a 1 or 2 mm thick layer of core material is present in the region around the inlets and outlets that cannot be occupied by the rotary stator. These stator connectors are necessary to prevent an otherwise prohibitively strong cogging torque. However, as visible in **Fig. 4.5 (a)**, they need to have round notches (15 mm diameter) in correspondence with the inlets and outlets locations. As it will be seen in **Sec. 4.4.4** and **Fig. 4.11 (a)**, this inevitably introduces a certain cogging torque component whenever the PMs are facing the notches during linear-rotary motion.

4.3.3 Main RA Design and Integration Aspects

In order to guarantee that the proposed RA concept can work correctly and meet the design specifications, there are a couple of important aspects that need to be considered.

As the rotor is only partly and irregularly equipped with PMs, a pronounced torque ripple ΔM_{ax} has to be expected. Two main components can be distinguished. One is the typical cogging due to the interaction between the PMs and the two half stators, according to the geometry of their teeth and pole shoes. The other one, as mentioned, is introduced by the in-/outlet notches on the stator connectors during linear-rotary motion. ΔM_{ax} has to be checked, as it causes a certain angular speed ripple $\Delta\Omega$. The transfer between ΔM_{ax} and $\Delta\Omega$ (in rpm) can be very simply modeled in the Laplace domain as the first order low-pass

$$\Delta\Omega(s) = \frac{(60/2\pi)}{s \cdot J_{mov}} \Delta M_{ax}(s), \quad (4.1)$$

where s is the Laplace variable and J_{mov} is the moment of inertia of the complete mover. This implies that, according to the value of J_{mov} , ΔM_{ax} can be significantly attenuated. For instance, consider a torque ripple fundamental

$\Delta M_{\text{ax},1} = M_{\text{req}} \sin(2\pi f_{\text{rip}} t)$, i.e., with an amplitude equal to 100% of the required axial torque $M_{\text{req}} = 3.1 \text{ mN m}$. Furthermore, recall that $\Delta M_{\text{ax},1}$ exhibits $N_{\text{cogg}} = \text{lcm}(N_s, N_p) = 12$ periods per one revolution, and hence $f_{\text{rip}} = 12 f_{\text{op}}$. Already by solely considering the translator mass $m_{\text{mov}} = 130 \text{ g}$ of the previously designed LA to calculate J_{mov} , the largest angular speed ripple is obtained for $f_{\text{op},\text{min}} = 1.5 \text{ Hz}$, and its amplitude is

$$\hat{\Delta\Omega}_1 = \frac{(60/2\pi)}{2\pi (12 \cdot f_{\text{op},\text{min}}) \cdot J_{\text{mov}}} M_{\text{req}} = 4.59 \text{ rpm}, \quad (4.2)$$

which corresponds to only $\Delta\Omega\% = \hat{\Delta\Omega}_1/\Omega_{\text{op},\text{min}} = 0.051 = 5.1\%$ of the operational speed $\Omega_{\text{op},\text{min}} = 90 \text{ rpm}$. Therefore, even a pronounced torque ripple can be tolerated by the RA without compromising its operation, especially at higher angular speeds. It is then sufficient to ensure that the chosen machine design does not violate the angular speed ripple specification in **Tab. 4.1** for $f_{\text{op},\text{min}} = 1.5 \text{ Hz}$. In addition, it should be considered that (4.2) is an open-loop calculation, but in practice the RA is operated in closed-loop with an angular speed controller. Depending on the chosen control bandwidth, it can be shown that the ripple is attenuated even more. Finally, in order to set a design goal and simplify the subsequent FEM-based optimization, it is decided to neglect the ripple component introduced by the in-/outlet notches and only consider the one caused by the interactions between the PMs and the stator teeth/pole shoes (easier to model in a 2D FEM analysis). At the same time, the maximum allowed percent speed ripple is reduced to $\Delta\Omega\%_{\text{max}} = 5\%$. This way, the RA is designed for very low torque ripple in the best case for which the stator notches have no influence. In practice, it is expected that the total torque ripple will be higher but tolerable, as argued.

It is important at this point to highlight the main trade-off in the RA design. The torque ripple ΔM_{ax} is mainly caused by reluctance forces, which, as such, depend quadratically on the air gap flux density B_{ag} . Therefore, ΔM_{ax} can be mitigated by reducing B_{ag} (e.g., using weaker/thinner PMs or larger air gap lengths). Conversely, for torque generation, it holds

$$M_{\text{in}}(\varphi) \propto \sigma_{\text{tan}}(\varphi) = B_{\text{ag},1}(\varphi) \cdot S_1(\varphi) \propto B_{\text{ag}}(\varphi) \cdot I_{\text{R}}, \quad (4.3)$$

i.e., B_{ag} contributes directly, together with the equivalent current sheet $S(\varphi)$, to the (tangential) area-related force density $\sigma_{\text{tan}}(\varphi)$ (cf. **Fig. 4.4 (b)**). Therefore, to generate the same torque M_{in} with the least current I_{R} (and hence ohmic losses), B_{ag} should be large. This translates into the main design trade-off, i.e., between angular speed ripple $\Delta\Omega$ and ohmic losses P_{Cu} .

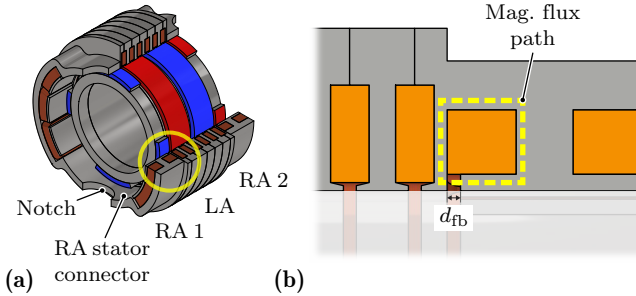


Fig. 4-5: (a) 3D view of the proposed RA concept and topology in the context of the full LiRA. The two RA modules use PMs of opposite polarity with respect to the adjacent ones of the LA. The two half-stators of each RA module are connected by two arc segments made of core material in order to prevent strong cogging effects. Due to the pump's inlets/outlets, these stator connectors need to be carved with round (\varnothing 15 mm) notches (4 in total). (b) Detailed cross-sectional view of the junction between the LA and a RA module, where a potential low-reluctance magnetic flux path can be formed. This can be avoided by introducing a flux barrier with length f_{fb} .

Another crucial aspect is the interaction between the RA and the LA. In particular, it has to be verified that the two RA modules in tandem can continuously provide the required torque M_{req} , also if the linear motion of the piston is considered. Furthermore, it has to be ensured that the axial reluctance profile of the LA is truly unaffected by the integration of the RA. Moreover, as the RA is integrated just adjacent to the LA, it must be guaranteed that both their magnetic designs are not compromised. For instance, no magnetic flux path should be created between the two (RA and LA) stators instead of through the air gap and the respective rotor/translator. With the chosen topology, a critical location is the one shown in the detail view of **Fig. 4-5 (b)**. If the bottom side of the pole shoes is in direct contact with the adjacent LA, a low-reluctance magnetic flux path through the two stators could be created. In order not to compromise torque generation, the inner side of the pole shoes is shortened, thus introducing a flux barrier with length d_{fb} .

One last aspect to consider concerns the total power losses, which need to be kept below the specified loss budget of $P_{Cu,RA,max} = 0.5$ W. Due to the low operational frequencies f_{op} , AC losses can be neglected, and hence the dominant loss component is ohmic. This can be sensibly reduced if the cross-section of the RA coils is as large as possible. It is also important to consider beforehand practical aspects of the RA realization, such as manufacturing

tolerances introducing potential unwanted air gaps or realistic reluctances along the main magnetic paths of the machine due to the used magnetic material [59, 60]. As it will be discussed in **Sec. 4.5.3**, they cause a reduction of the magnetic flux with respect to the predicted/simulated values, with a consequent increase in the required current and hence ohmic losses, to generate the same torque. In order to account for these additional components, the targeted ohmic losses for the following FEM-based optimization are $P_{\text{Cu,RA}} = 0.1 \text{ W}$ at most.

4.4 FEM Machine Optimization

This section discusses the validation and optimization of the proposed RA concept by means of parameterized 2D and 3D FEM models. For a given RA design providing the required average torque $M_{\text{req}} = 3.1 \text{ mN m}$, the optimization outputs to consider are the torque (and hence speed) ripple and the ohmic losses. Additionally, the resulting rotor mass is included. The optimization is conducted in 2D. Then, the interactions of the selected design with the LA are investigated in a 3D analysis.

4.4.1 2D FEM Model of the RA

The 2D Cartesian FEM model includes the parameterized cross-section of one of the RA modules, as shown in **Fig. 4.6 (a)**. The model parameters are summarized in **Tab. 4.2**. Due to the low operational frequencies, the model can be solved for magnetostatic conditions, which require less computational effort but neglect AC effects. As the arcs spanned by a tooth and a coil add up to a stator slot pitch, only one parameter k_{FeCu} (iron-to-copper ratio) is introduced. Furthermore, the pole shoe coverage is defined by the parameter k_{shoe} , with $k_{\text{shoe}} = 1$ indicating a fully closed slot. The modeled materials have simplified definitions. For the stator core and the rotor back iron a, linear, ferromagnetic material with $\mu_r = 4000$ and negligible conductivity is used. It is then necessary to check for potential magnetic saturations after the model is solved, ensuring that the B field is below a specified limit (e.g., 1.6 T for electrical steel). The coils are modeled with solid copper cross-sections, i.e., with a single turn. A realistic fill factor of $k_{\text{ff}} = 0.6$ is considered by modeling the copper material with a reduced conductivity $\sigma_{\text{Cu,ff}} = k_{\text{ff}} \sigma_{\text{Cu}} = 3.4 \text{ MS/m}$. Finally, the PMs are modeled with a coercitivity $H_c = 1000 \text{ kA/m}$, which approximately corresponds to the N50 magnetization grade of commercial NdFeB PMs. The magnetization direction is radial. The three phase currents

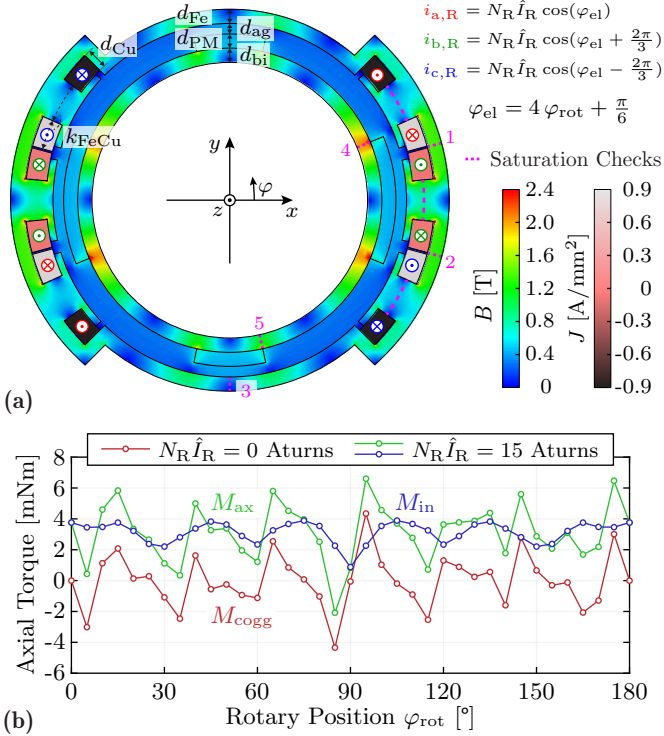


Fig. 4.6: (a) 2D FEM Cartesian model of the RA for an exemplary design, with indicated parameters and solved B and J fields (*Ansys Maxwell*). (b) Exemplary axial torque profiles for the cases $N_R \hat{I}_R = 15$ Aturns, giving the total axial drive torque $M_{ax}(\varphi_{rot})$ and $N_R \hat{I}_R = 0$ Aturns, giving the cogging torque component $M_{cogg}(\varphi_{rot})$. Their difference is the generated torque $M_{in}(\varphi_{rot})$.

are assigned to the coils as indicated in **Fig. 4.6 (a)**. The assignment yields Maximum Torque per Ampère (MTPA) using Field-Oriented Control (FOC) with the electrical angle φ_{el} .

The main simulation outputs are the torque profile $M_{ax}(\varphi_{rot})$ and the ohmic losses P_{Cu} . The 2D Cartesian model returns the torque per 1 m of length along the z -direction, so it is scaled by multiplying by the active length $l_{PM} = 5$ mm. The total torque profile $M_{ax}(\varphi_{rot})$ obtained for an exemplary design with a test current $N_R \hat{I}_R = 15$ Aturns is shown in **Fig. 4.6 (b)**. It is the sum of two components, namely the generated (internal) torque $M_{in}(\varphi_{rot})$

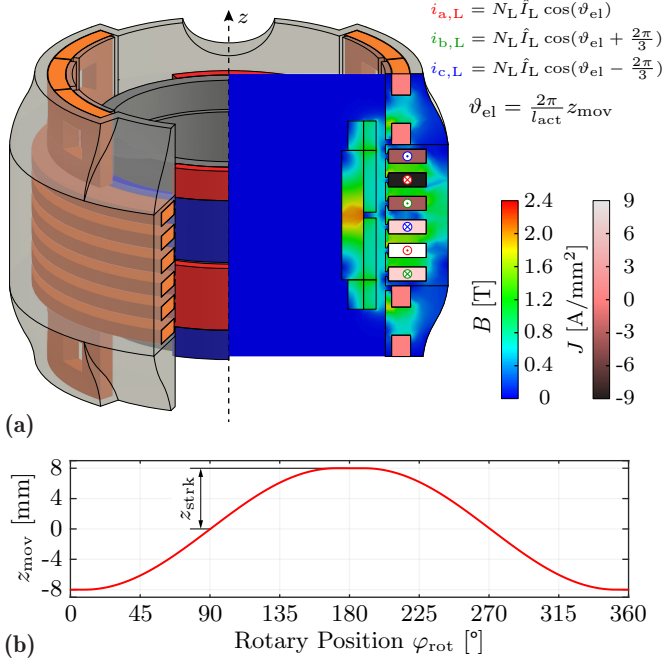


Fig. 4.7: (a) 3D FEM model of the LiRA with exemplary B and J fields on the xz -section. The currents $i_{\{a,b,c\},L}$ are impressed in the winding of the LA to generate Maximum Force per Ampère with the (linear) electrical angle ϑ_{el} [27]. (b) Linear-rotary motion profile of the *ShuttlePump*, assigned to the mover of the 3D FEM model. The linear motion follows a quasi-sinusoidal trajectory, with a stroke length $z_{strk} = 8$ mm [26].

and the cogging torque $M_{cogg}(\varphi_{rot})$. As it can be noticed, the total torque ripple $\Delta M_{ax}(\varphi_{rot})$ does not just correspond to the cogging torque $M_{cogg}(\varphi_{rot})$, but also the internal torque $M_{in}(\varphi_{rot})$ contributes to it. The ohmic losses P_{Cu} are also returned per 1 m of machine length along the z -direction. In this case, the used scaling length is not just the active length l_{PM} but the average coil length $l_{coil,avg}$. This also considers the two sides of the coil serving as return conductors and not contributing to torque generation. The resulting ohmic losses are valid for one RA module. Finally, the returned values of the B field used to check for magnetic saturations in the stator also have to be scaled. This is because the 2D model assumes that the geometry extends unchanged along the z -axis, i.e, rotor, pole shoes, and teeth have the same length, which

Tab. 4.2: Parameters of the FEM models. The optimization parameters are indicated with ‘Opt’ and reported in **Tab. 4.3**.

Name	Symbol	Value	Unit
Relative permeability (core)	μ_r	4000	
Mag. saturation threshold (core)	B_{sat}	2.2	T
Copper conductivity (with fill factor)	$\sigma_{\text{Cu,ff}}$	3.4	MS/m
Fill factor	k_{ff}	0.6	
PM coercitivity	H_c	1000	kA/m
Relative permeability (PM)	μ_{PM}	1	
Active machine length	l_{PM}	5	mm
Pole shoe coverage	k_{shoe}	0.8	
PM angle (large segment)	$\alpha_{\text{PM},1}$	45	°
PM angle (small segment)	$\alpha_{\text{PM},2}$	25	°
Magnetic gap length	d_{ag}	Opt	mm
PM thickness	d_{PM}	Opt	mm
Copper layer thickness	d_{Cu}	Opt	mm
Iron-copper ratio	k_{FeCu}	Opt	
Stator core thickness	d_{Fe}	Opt	mm
Back iron thickness	d_{bi}	Opt	mm
Axial stroke length (3D model)	z_{strk}	8	mm
Flux barrier length (3D model)	d_{fb}	Opt	mm
Average torque output	M_{req}	3.1	mNm
Max. angular speed ripple	$\Delta\Omega_{\%,\text{max}}$	5	%
Loss budget	$P_{\text{Cu,RA,max}}$	0.5	W

is not the case in practice. The scaling factor is the ratio of the tooth length l_{tooth} over the active length l_{PM} .

4.4.2 3D FEM Model of the Full LiRA

A 3D FEM model of the full LiRA is needed to check the possible interactions between the RA and the LA during the combined linear-rotary motion of the piston. Furthermore, it allows estimating the total torque ripple ΔM_{ax} also considering the effect of the round in-/outlet notches that need to be made on the rotary stators (cf. **Fig. 4.5 (a)**). Another important detail that can only be modeled and investigated in 3D is the length of the flux barrier d_{fb} between the pole shoes of the RA and the stator of the LA, introduced in **Fig. 4.5 (b)**. The

model is shown in **Fig. 4.7 (a)**. The LA part is compatible with the geometry and dimensions of the realized LA and is adapted from existing 3D models used for its analysis [27]. The RA part is parameterized analogously to its 2D counterpart. The linear-rotary position of the mover is parameterized according to the required piston motion profile of the *ShuttlePump* [26], reported in **Fig. 4.7 (b)**. The simulation returns, besides the total copper losses $P_{\text{Cu,tot}}$, also the overall profile of the axial force $F_{\text{ax}}(\varphi_{\text{rot}}, z_{\text{mov}})$ and the total torque $M_{\text{ax,tot}}(\varphi_{\text{rot}}, z_{\text{mov}}) = M_{\text{ax,1}}(\varphi_{\text{rot}}, z_{\text{mov}}) + M_{\text{ax,2}}(\varphi_{\text{rot}}, z_{\text{mov}})$ provided by the two RA modules operating together.

4.4.3 RA Optimization Procedure

The optimization of the RA is conducted on the 2D FEM model, due to the considerably higher computational effort needed to solve the 3D model repeatedly. Nevertheless, the 2D-solutions provide all the necessary information to compare the RA designs together. The optimization procedure consists of three steps.

Preliminary

Some parameters can already be fixed beforehand, thus reducing the number of designs to simulate in the 2D FEM. Besides the angles spanned by the PMs, which, as seen, are maximized to $\alpha_{\text{PM,1}} = 45^\circ$ and $\alpha_{\text{PM,2}} = 25^\circ$, the parameters of the pole shoes can also be fixed. Due to manufacturing constraints, their thickness is selected to be $d_{\text{shoe}} = 1$ mm. The shoe coverage, determined by the parameter k_{shoe} , should be as large as possible for two reasons. First, it contributes to reducing the amplitude of the cogging torque of the RA. Second, it is necessary to keep the reluctance seen by the PMs of the LA approximately constant along the axial direction. In order to prevent fringing effects, $k_{\text{shoe}} = 0.8$ is selected.

Main

The parameters that are instead swept are listed in **Tab. 4.3**. In the main optimization step, the parameters of Group 1 are varied. These parameters are expected to have the most influence on the machine design. In fact, they include both magnetic parameters ($d_{\text{ag}}, d_{\text{PM}}, k_{\text{FeCu}}$) that directly influence the air gap flux density B_{ag} and copper-related parameters ($d_{\text{Cu}}, k_{\text{FeCu}}$), which determine the cross-section of the stator coils $A_{\text{Cu},0}$ and hence have a direct impact on the ohmic losses P_{Cu} . The design space obtained with the $3 \times$

Tab. 4.3: Swept optimization parameters.

Name	Symbol	Range	Step	Unit
Group 1 (Main)				
Magnetic gap length	d_{ag}	[1, ..., 2]	0.5	mm
PM thickness	d_{PM}	[1, ..., 3, 5]	0.5	mm
Copper layer thickness	d_{Cu}	[2, ..., 6]	1	mm
Iron-copper ratio	k_{FeCu}	[0.2, ..., 0.8]	0.2	
Group 2				
Stator core thickness	d_{Fe}	[2, ..., 4]	0.5	mm
Back iron thickness	d_{bi}	[2, ..., 4]	0.5	mm

$6 \times 5 \times 4 = 360$ parameter configurations is visualized in **Fig. 4.8** on the $P_{\text{Cu}}-\Delta\Omega\%$ plane. For each design, a (total) torque profile such as the one in **Fig. 4.6 (b)** is simulated, from which the average $M_{\text{ax,avg}}$ and ripple $\Delta M_{\text{ax}}(\varphi_{\text{rot}})$ are considered. It should be noticed that for the proposed topology, the ripple on the internal (and hence total) torque depends on the amplitude of the current $N_{\text{R}}\hat{I}_{\text{R}}$. For this reason, each design is initially simulated with a test current $N_{\text{R}}\hat{I}_{\text{R,test}} = 30$ Aturns, which allows determining the scaling factor $k_{\text{scal}} = M_{\text{req}}/M_{\text{ax,test}}$, where $M_{\text{ax,test}}$ is the average total torque obtained for the test current $N_{\text{R}}\hat{I}_{\text{R,test}}$. By adjusting the current amplitude to $N_{\text{R}}\hat{I}_{\text{R,req}} = k_{\text{scal}} N_{\text{R}}\hat{I}_{\text{R,test}}$, all the designs are simulated for the same average torque output $M_{\text{req}} = 3.1$ mN m and with the correct total torque ripple $\Delta M_{\text{ax}}(\varphi_{\text{rot}})$, ensuring a fair comparison. From the $\Delta M_{\text{ax}}(\varphi_{\text{rot}})$ thus simulated, the speed ripple $\Delta\Omega$ is calculated according to the low-pass dynamics in (4.1) for the worst-case scenario, i.e. $f_{\text{op,min}} = 1.5$ Hz and expressed as a percent of the rotational speed $\Omega_{\text{op,min}}$. Finally, the single-turn average coil length $l_{\text{coil,avg}}$ (used to scale the ohmic losses P_{Cu}), as well as the mass of the rotor m_{rot} and hence the moment of inertia of the mover J_{mov} , are also specifically calculated for each design. In **Fig. 4.8 (a)-(c)** the results are grouped according to the value of d_{ag} in order to better visualize the effect of the remaining optimization parameters. As expected, a larger air gap length d_{ag} yields a smaller air gap flux density B_{ag} , which reduces the cogging torque but increases the ohmic losses, with the consequence that (for a constant output torque) the group of designs moves along a hyperbolic front on the $P_{\text{Cu}}-\Delta\Omega\%$ plane (cf. (4.3)). This can be analogously seen for different values of d_{PM} , considering, e.g., a group of designs connected by a dashed line. Both parameters influence the equivalent air gap reluctance (as the magnetic permeability of the PMs

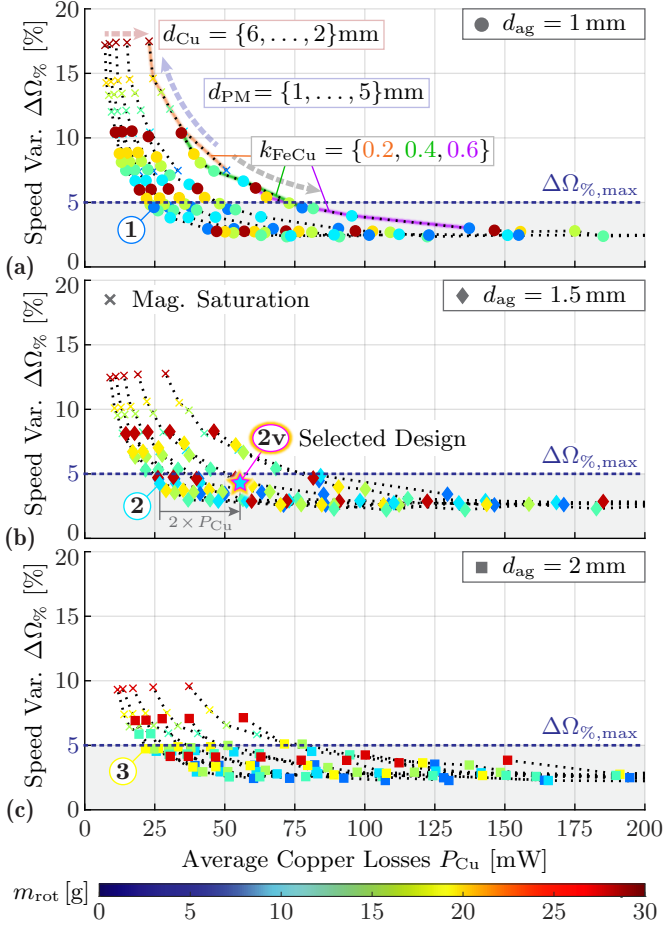


Fig. 4.8: Design space generated by the second optimization step, visualized on the P_{Cu} - $\Delta\Omega\%$ for (a) $d_{ag} = 1$ mm, (b) $d_{ag} = 1.5$ mm and (c) $d_{ag} = 2$ mm. The color of each point indicates the rotor mass m_{rot} . The points with the same parameters' configuration except for d_{PM} are connected by dashed lines. This way, the effect of the remaining swept parameters is visible, as indicated in (a). The considered threshold for magnetic saturation is $B_{sat} = 2.2$ T. The limit in speed variation is reported, which allows the identification of the feasible designs.

Tab. 4.4: Feasible RA designs under the specified constraints.

#	d_{ag}	d_{PM}	d_{Cu}	k_{FeCu}	$\Delta\Omega\%$	P_{Cu}	m_{rot}
1)	1 mm	1 mm	6 mm	0.6	4.6 %	25 mW	7.4 g
2)	1.5 mm	1.5 mm	6 mm	0.4	4.2 %	27 mW	10 g
2v)	1.5 mm	1.5 mm	3 mm	0.4	4.3 %	55 mW	10 g
3)	2 mm	3 mm	6 mm	0.4	4.7 %	22 mW	19 g

$\mu_{\text{PM}} \approx \mu_0$), but d_{PM} also defines the MMF provided by the PMs. The parameter d_{Cu} does not have a pronounced effect on $\Delta\Omega\%$, but solely on P_{Cu} . This is expected, as d_{Cu} defines the available coil cross-section $A_{\text{Cu},0}$ but does not influence the air gap flux density B_{ag} . In **Fig. 4.8 (a)-(c)**, one can observe how a group of designs scales along the P_{Cu} -axis according to the value of d_{Cu} . Therefore, for minimum ohmic losses d_{Cu} should be increased as far as possible, fully utilizing the maximum allowed outer diameter (but also considering the thickness of the stator core d_{Fe}). The parameter k_{FeCu} affects instead both $\Delta\Omega\%$ and P_{Cu} directly. In fact, by defining the thickness of the stator teeth, it still determines $A_{\text{Cu},0}$, but it additionally affects the circumferential air gap reluctance profile. A large value of k_{FeCu} gives a smoother air gap reluctance profile, which translates into reduced cogging torque (and hence $\Delta\Omega\%$). However, this way the copper cross-section $A_{\text{Cu},0}$ is also reduced, with an overall increase in P_{Cu} . As a result, the choice of k_{FeCu} is not obvious, thus providing further motivation to conduct the FEM-based optimization.

The main constraint of $\Delta\Omega_{\%,\text{max}} = 5\%$ defines the subset of feasible designs. Among these, four relevant ones are selected and reported in **Tab. 4.4**. *Design 3* is the one attaining the least losses, but it needs relatively thick PMs, resulting in the heaviest rotor. Therefore, at the cost of slightly higher losses, *Design 1* or *Design 2* shall be preferred. *Design 2* has the practical advantage of having the same air gap length $d_{\text{ag}} = 1.5$ mm as the designed LA, so the complete mover can have the same outer diameter. Furthermore, as the resulting values of P_{Cu} are way within the losses budget $P_{\text{Cu,RA,max}} = 0.5$ W (i.e., very small compared to the losses of the LA), it is decided to halve the coil thickness at the cost of doubling the ohmic losses, which corresponds to *Design 2v* (cf. **Fig. 4.8 (b)**). The important advantage is the overall rounder form factor of the LiRA, which facilitates implantation considerably. A final estimation of the total losses of the RA is provided in the next subsection, as it requires the total torque profile with both RA modules operating together, obtained from the 3D simulations.

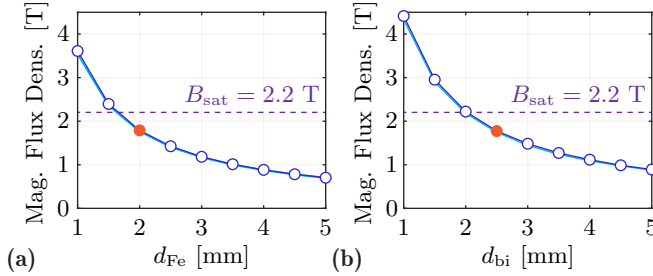


Fig. 4.9: Results of the third optimization step. (a) Average magnetic flux density at the locations 1 to 3 in the stator core indicated in Fig. 4.6 (a) versus the thickness d_{Fe} . (b) Average magnetic flux density at the locations 4 and 5 in the rotor back iron indicated in Fig. 4.6 (a) versus the thickness d_{bi} .

Avoid Saturation

As a last step, the parameters of Group 2 are swept for the selected design, i.e., the thickness of the stator core d_{Fe} and of the rotor back iron d_{bi} are optimized. In particular, both parameters should be minimized for a compact and lightweight design, but it must be ensured that no saturation of the magnetic material occurs. Fig. 4.9 (a) and (b) report the simulated average magnetic flux densities in the stator core and the rotor back iron versus d_{Fe} and d_{bi} , respectively. For each location 1 to 5 in Fig. 4.6 (a), this is calculated over all rotary positions, and only the curve with the largest values is considered. With the threshold $B_{sat} = 2.2$ T for *VACOFLUX50*, $d_{Fe} = 2$ mm and $d_{bi} = 2.5$ mm are selected.

4.4.4 Integration and Interactions with the LA

Once the 2D optimization is finalized, the selected RA design is investigated in 3D to verify its interactions with the adjacent LA. First, the length of the flux barrier d_{fb} highlighted in Fig. 4.5 (b) has to be chosen. Fig. 4.10 shows the results of a series of 3D simulations with the average axial torque obtained for different values of d_{fb} , ranging from 0 to 1 mm. For a more direct comparison with the 2D counterpart, the simulations are conducted for a fixed $z_{mov} = 4.5$ mm (i.e., with one of the rotors directly facing the RA stator teeth) and the same RA current $N_R \hat{I}_{R,req} = 15$ Aturns. The average torque is then normalized to $M_{req} = 3.1$ mN m. Furthermore, both linear and non-linear material definitions for the stator core and rotor back iron are used. The

results indicate that the absence of a flux barrier at the interface between LA and RA would be a concern in principle, but does not have a major impact on torque generation for the chosen design. With the linear material definition, for $d_{fb} = 0$ the generated torque is about 30% weaker, and, as expected, it gets to the nominal value (and even slightly above) as soon as the flux barrier is introduced. With the more realistic non-linear material definition for *VACOFLUX50*, this effect is less pronounced. This can be explained by the fact that the geometry of the pole shoe, especially due to its thickness $d_{shoe} = 1$ mm, is already offering high reluctance along the considered critical flux path. Finally, $d_{fb} = 0.8$ mm is selected.

The results of the 3D simulations of the complete LiRA with the piston following the linear-rotary motion profile of **Fig. 4.7 (b)** are reported in **Fig. 4.11**. For these simulations, only the non-linear material definition for the stator cores and mover back iron is used. In **Fig. 4.11 (a)**, the internal torque $M_{in,tot}(\varphi_{rot})$ and the total torque $M_{ax,tot}(\varphi_{rot})$ provided by both RA modules are reported and compared to their 2D counterparts. From $M_{ax,tot}(\varphi_{rot})$ it is possible to observe the expected cogging torque component introduced by the in-/outlet notches on the rotary stators. In fact, there are two doublets of opposite torque peaks right around the two rotary positions $\varphi_{rot} = 0^\circ$ and $\varphi_{rot} = 180^\circ$. As it can be understood from the linear motion profile ($z_{mov}(\varphi_{rot})$, reported from **Fig. 4.7 (b)**), those are the two conditions for which the mover reaches one of the two axial edges of the LiRA and hence the rotary PMs move in front of the notches. The additional cogging torque increases the

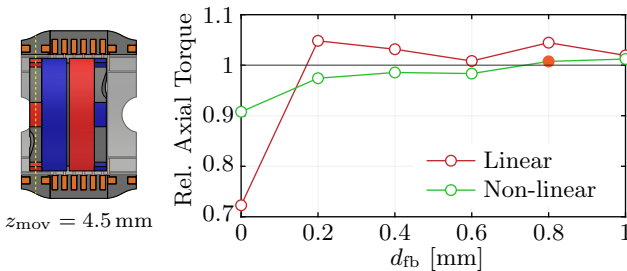


Fig. 4.10: Effect of the flux barrier at the interface between LA and RA (cf. **Fig. 4.5 (b)**). The simulated average torque is obtained for the two cases of linear ($\mu_r = 4000$) and non-linear (*VACOFLUX50*) material definitions for the stator cores and mover back iron. For the selected LiRA design, due to the thin pole shoes, the torque reduction without a flux barrier is not critical.

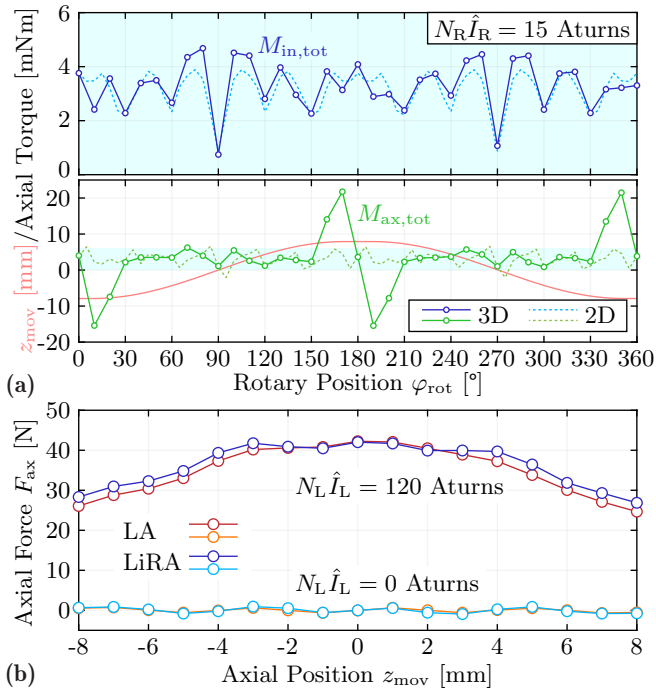


Fig. 4.11: Results of the 3D FEM simulations of the complete LiRA. **(a)** Internal and total axial torques $M_{in,tot}(\varphi_{rot})$ (zoomed range) and $M_{ax,tot}(\varphi_{rot})$ applied to the mover by both RA modules operating together, compared to their 2D counterparts. The mover follows the specified linear-rotary motion profile, reported in light red from **Fig. 4.7 (b)**. **(b)** Axial force profile $F_{ax}(z_{mov})$ for the cases $N_R \hat{J}_R = N_L \hat{J}_L = 0$ AtURNS (unenergized LiRA, giving the axial cogging force profile) and $N_R \hat{J}_R = 15$ AtURNS, $N_L \hat{J}_L = 120$ AtURNS (energized LiRA, giving the axial drive force profile). Both cases are compared to the results of the original LA design [27], verifying that the cogging force is almost unchanged, and the force generation is even slightly improved.

percent speed ripple to $\Delta\Omega\% = 14\%$, which, however, remains within the allowed range. Importantly, on average, the total internal torque is still $M_{in,tot,avg} = 3.1$ mNm. As visible from the internal torque profiles (compared in the zoomed range of **Fig. 4.11 (a)**), during the linear-rotary motion of the mover, both RA modules contribute to maintaining approximately the same internal torque profile as if only one module were acting on a single rotor. However, this also means that the required ohmic losses will be approximately

doubled. The 3D simulation returns in fact $P_{\text{Cu,tot}} = 6 R_0 (N_R \hat{I}_R)^2 = 102 \text{ mW}$. **Fig. 4.11 (b)** shows instead the profile of the axial force $F_{\text{ax}}(z_{\text{mov}})$ acting on the mover. Two cases are considered, namely when the LiRA is not energized and when it is, and compared to the corresponding results that are valid for the original design of the LA with its stator extensions [27]. In the first case, it is possible to verify that the axial reluctance profile of the original LA is maintained, and hence no large axial cogging forces are introduced. In the second case, it can be observed that adding the RA modules not only does not impair axial force generation, but even improves it due to the chosen arrangement of the PMs of the RA. It can be calculated that this increase in the machine constant of the LA contributes to an overall reduction in ohmic losses with respect to the original design amounting to 4%.

4.5 Hardware Prototype

This section describes the hardware prototype of the selected RA design and provides insight into a specific type of mechanical assembly tolerance. Furthermore, the test bench used for the experimental measurements is presented.

4.5.1 Stator Realization

Stator Core

The realized stator core is shown in **Fig. 4.12 (a)**. The material used is the same as for the LA, i.e., the *VACOFLUX50*. Due to the low operational frequencies, the material is not laminated. As visible from the sectional view in **Fig. 4.12 (b)**, half of a LA stator ring is integrated as a single piece with the rotary stator core. This facilitates the manufacturing of the half-ring and ensures a solid buildup. Furthermore, the sectional view shows the solution chosen for the realization of the stator teeth and pole shoes, which ensures an easy mounting of the coils. As depicted in **Fig. 4.12 (c)**, each stator tooth with its large pole shoe is realized as a separate part, made up of two pieces glued together. This way, the tooth can be inserted through a single coil and screwed to the stator core. Two pins with a diameter of 1 mm are used to connect all the parts (pole shoe, tooth, and stator) together and align them correctly. All six coils can thus be held firmly in place.

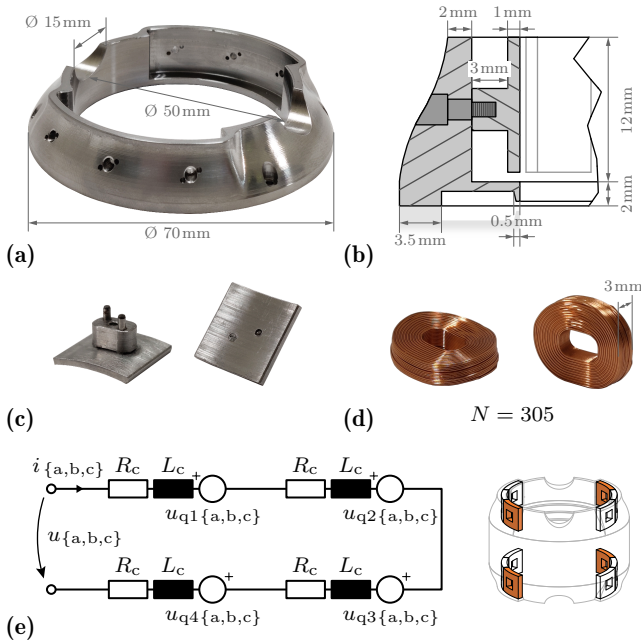


Fig. 4.12: Realized hardware prototype of the RA. (a) Realized stator core made of VACOFLUX50. (b) Stator section at the coils side (xz -) with annotated dimensions. (c) Realized demountable stator teeth with large-coverage pole shoes. (d) Realized stator coil with a special bent shape, made of a 0.18 G1B coated copper wire with $N_R = 305$ turns. (e) Interconnection diagram valid for each phase $\{a, b, c\}$ of the RA, including the equivalent circuits of each stator coil with the resistance R_c , the inductance L_c and the induced voltages $u_{q\{1,2,3,4\}\{a,b,c\}}$.

Coils

As shown in **Fig. 4.12 (d)**, the coils are specially manufactured with a bent shape to maximize the fill factor k_{ff} . It is advantageous to select a large number of turns N_R so that smaller currents have to be supplied by the inverter, thus reducing its conduction losses. At the same time, N_R should not be too large, as it can be difficult to precisely control the phase currents to very small values due to, e.g., noise on the current measurement signals. Furthermore, the induced voltages in each phase $u_{q,\{a,b,c\}}(t)$ also have to be taken into account in order to guarantee that the currents can be impressed until the maximum operational speed. In fact, the three-phase inverter module

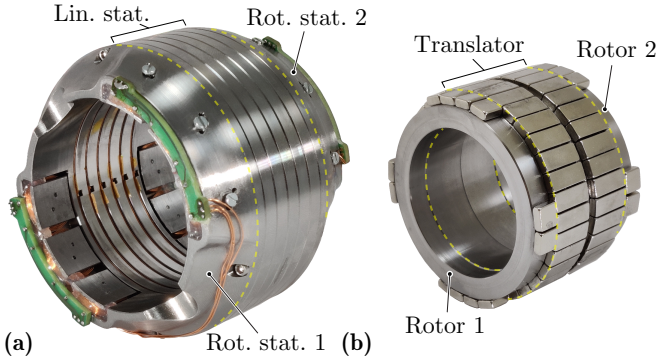


Fig. 4.13: Realized hardware prototype of the RA. **(a)** Complete stator assembly equipped with coils, side interconnection PCBs and mounted together with the LA. **(b)** Realized complete mover with back iron rings and multiple NdFeB PMs. It consists of the previously realized translator of the LA plus the two rotors of the RA on the sides. The mover will be finally integrated into the piston (cf. Fig. 4.3 (a)).

(MP6535 by *Monolithic Power Supply*, already used to supply the LA [27]) can be operated with a maximum DC-link voltage of $U_{DC,lim} = 26 \text{ V}$, which gives $U_{\{a,b,c\},lim} = U_{DC,lim}/2 = 13 \text{ V}$. The selected compromise value for the number of turns is $N_R = 305$ that can be fitted in the given cross-section $A_{Cu,0}$ with a 0.18 G1B coated copper wire. The resulting fill factor is $k_{ff} = 0.61$, and the inverter current amplitude for nominal torque is $I_{inv} = 49.2 \text{ mA}$. The measured electrical characteristics of a manufactured coil, namely the DC coil resistance and inductance, are $R_c = 6.4 \Omega$ and $L_c = 6.9 \text{ mH}$ (mounted in the stator). The maximum induced voltage is checked, considering the maximum induced voltage per turn for each coil and their interconnection in the two RA modules. All the coils are energized at the same time and hence supplied by a single three-phase inverter module. Therefore, this is loaded with four coils in series per phase, as depicted in the interconnection diagram (equivalent circuit) of Fig. 4.12 (e). The induced voltages per turn $u_{q,\{a,b,c\},1}(t)$ are found for each phase by taking the time derivatives of the single-turn flux linkages $\psi_{\{a,b,c\},1}(t)$ obtained from the 3D FEM simulations. The maximum induced voltage found (over all phases) is $U_{q,max} = 3.28 \text{ V}$. Neglecting the voltage drop on the inductance L_c due to the low operating frequency $f_{op} = 5 \text{ Hz}$, the required phase voltages are $u_{\{a,b,c\}}(t) = 4 R_c i_{\{a,b,c\},R}(t) + u_{q,\{a,b,c\}}(t)$, which is at most $U_{max} = 4.35 \text{ V} < U_{\{a,b,c\},lim}$. For the final assembly, as shown in Fig. 4.13 (a), the coils are fixed to the stator core, and their terminals are

guided to small PCBs placed on the outer side of the RA, in order to facilitate their interconnection.

4.5.2 Rotor Realization

Fig. 4.13 (b) shows the complete mover to be embedded in the piston, i.e. the translator of the LA plus the two rotors of the RA at its two axial ends. Each rotor is very simply built using a back iron ring made of *VACOFLUX50* and small NdFeB PMs glued on the outer surface. Their thickness is the chosen $d_{\text{PM}} = 1.5$ mm, and their magnetization grade is N48. According to the chosen RA concept, all the magnets of one rotor are oriented in the same direction (i.e., with their magnetization axis pointing radially inwards or outwards of it), whereas the magnets of the other rotor have opposite polarity. The weight of a single rotor is $m_{\text{rot}} = 48$ g. Together with the mass of the translator of the LA $m_{\text{mov}} = 148$ g, the total mover mass is $m_{\text{tot}} = 244$ g.

4.5.3 Effect of the Stator Assembly Tolerances

An important aspect to consider for the realized prototype is the effect of mechanical tolerances in the assembly of the RA stators [59,60]. This can lead to a considerable reduction in the generated torque, which corresponds to an increase in the required ohmic losses. This is the reason why, in **Sec. 4.3.3** a rather conservative margin within the available losses budget (0.1 W out of the allowed $P_{\text{Cu,RA,max}} = 0.5$ W) was defined for the RA optimization. The most critical manufacturing tolerances concern the mounting of the stator teeth to the rest of the stator core according to **Fig. 4.12 (b)**. In fact, if the two contact surfaces are not perfectly matched, at the interface between each tooth and the rest of the stator a certain undesired air gap is introduced, to which the magnetic design of the RA results very sensitive.

For a qualitative understanding, consider the magnetic circuit in **Fig. 4.14 (a)**, defined by the main magnetic flux paths in the RA. This is substantially simplified by assuming a planar, homogeneous field in the radial direction and neglecting fringing effects. Furthermore, under the assumption $\mu_{\text{PM}} \approx \mu_0$, the reluctance of the PM is included in the total air gap reluctance \mathcal{R}_{ag} . Each undesired tolerance air gap with length d_{tol} (here assumed to be all equal for simplicity) adds a reluctance $\mathcal{R}_{\text{tol,+}} = \frac{d_{\text{tol}}}{\mu_0 A_{\text{tooth}}}$ to the magnetic circuit, where A_{tooth} is the equivalent cross-section of the flux path at the back of the tooth. At the same time, as illustrated in **Fig. 4.14 (b)**, the total air gap length $d_{\text{ag}} + d_{\text{PM}}$ is reduced by d_{tol} . Therefore, the total air gap reluctance \mathcal{R}_{ag}

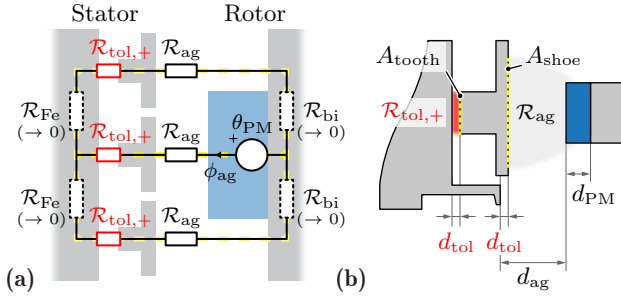


Fig. 4.14: (a) Simplified equivalent magnetic circuit of the RA. The air gaps introduced between each tooth and the stator core due to tolerances in the stator assembly add the undesired reluctances $\mathcal{R}_{tol,+}$. The relative dimensions of the individual parts are intentionally not to scale. (b) Stator section with a protruding tooth. The reduction in the main air gap reluctance \mathcal{R}_{ag} does not compensate for the introduced $\mathcal{R}_{tol,+}$ due to the different equivalent cross-sections of the flux path at the tooth side (A_{tooth}) and pole shoe side (A_{shoe}).

is reduced by $\mathcal{R}_{tol,-} = \frac{d_{tol}}{\mu_0 A_{shoe}}$, where A_{shoe} is the equivalent cross-section of the flux path in front of the pole shoe. If the equivalent cross-sections A_{tooth} and A_{shoe} were the same, the total reluctance

$$\mathcal{R}_{ag,tot} = 1.5 (\mathcal{R}_{ag} + \mathcal{R}_{tol,+} - \mathcal{R}_{tol,-}) \quad (4.4)$$

would be unchanged, as $\mathcal{R}_{tol,+} = \mathcal{R}_{tol,-}$ (note that the factor 1.5 is obtained considering the two parallel branches of the equivalent circuit). In that case, the magnetic design would be insensitive to the assembly tolerances of the stator teeth. Nevertheless, as $A_{tooth} < A_{shoe}$, then $\mathcal{R}_{tol,+} > \mathcal{R}_{tol,-}$, so the total reluctance $\mathcal{R}_{ag,tot}$ can considerably increase. In more detail, (4.4) can be written as

$$\mathcal{R}_{ag,tot} = 1.5 \left(\frac{d_g + d_{PM}}{\mu_0 A_{shoe}} + \frac{d_{tol}}{\mu_0 A_{tooth}} - \frac{d_{tol}}{\mu_0 A_{shoe}} \right). \quad (4.5)$$

By introducing the ratio $k_A = A_{shoe}/A_{tooth}$, all the reluctances in (4.5) can be expressed with respect to A_{shoe} , obtaining

$$\mathcal{R}_{ag,eq} = 1.5 \frac{d_g + d_{PM} + (k_A - 1) d_{tol}}{\mu_0 A_{shoe}}, \quad (4.6)$$

which shows that the equivalent air gap is increased by $(k_A - 1) d_{tol}$, i.e., that the contribution of d_{tol} is amplified by the ratio of the cross sections k_A .

For the realized prototype, the effect of the undesired d_{tol} is investigated more accurately with the aid of the 3D FEM model. Already for $d_{\text{tol}} = 0.1 \text{ mm}$, estimated in **Appendix A**, the internal torque M_{in} is reduced by 40 %. Consequently, the RA will require about 3 times the predicted ohmic losses to generate the nominal torque (i.e., $3 \cdot 0.1 \text{ W} = 0.3 \text{ W}$), which is still within the available losses budget. It is therefore clear that a trade-off between manufacturing complexity and required ohmic losses exists. For the case at hand, the chosen stator construction is relatively simple to realize, and the additional losses it introduces are not critical as they are negligible compared to the total losses of the LiRA. For future designs or a different system where losses minimization could be a serious concern, a different stator construction solution shall be preferred, e.g., with extended teeth to be inserted in the stator core.

4.5.4 Experimental Test Bench

The experimental test bench shown in **Fig. 4.15** is adapted from the one already used for the commissioning of the LA [27]. The torque sensor used is the *Rokubi* from *BOTA Systems*, which provides 6-axis force/torque measurements and was already used to commission the LA [27]. Its measurement principle is based on resistive strain gauges, and about its z -axis, it can measure up

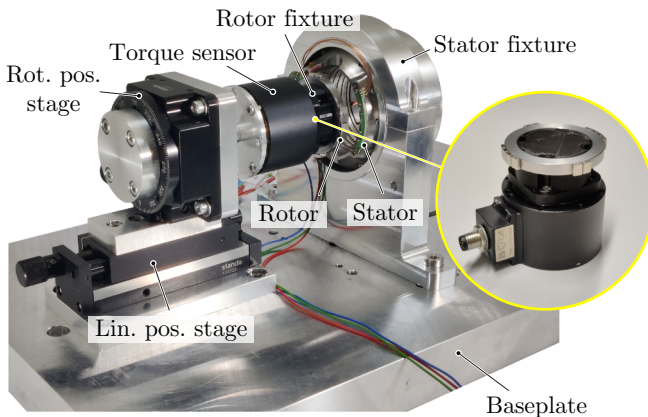


Fig. 4.15: Experimental test bench used for the commissioning (torque measurement) of the RA. The closeup view shows how the single rotor is directly mounted to the sensor with a rigid plastic fixture.

to 12 N m with a signal noise level of 0.5 mN m. The torque to be measured for the experimental verification of the RA is in the 10 mN m range, which is relatively low. If the complete mover is rigidly coupled to the sensor, a shaft and rotary bearings would be needed. However, as verified by preliminary tests, these would introduce parasitic axial torques due to friction, especially in the presence of strong radial attraction forces that exist between mover and stator [27]. A reasonable alternative is to measure the torque applied to a single rotor. As seen from **Fig. 4.11 (a)**, this is equivalent to the total internal torque $M_{\text{in,tot}}(\varphi_{\text{rot}})$ (i.e., applied to the complete mover), as long as the single rotor is axially aligned with the teeth of a rotary stator. A single rotor can be directly mounted to the torque sensor, with a very good transmission of the generated torque to it. On the test bench, as visible in the closeup of **Fig. 4.15**, this is done by gluing the rotor to a rigid plastic fixture, which is then tightly screwed to the sensor. Coupled to the sensor, a rotary positioning stage is used to precisely position the rotor down to a 0.1° resolution. Finally, a linear positioning stage is also used in order to adjust the rotor's position along the axial direction. The test bench can thus be used to measure the generated axial torque exerted by the fixed stator on the single rotor for different angular positions φ_{rot} .

4.6 Experimental Verification

The experimental measurements conducted on the hardware prototype of the RA assembled into the complete LiRA are reported in this section. The verification includes measurements of the profile of the internal torque along the circumferential direction from which the (average) machine constant k_m is obtained. For the presented measurements, the test bench in **Fig. 4.15** is used. The axial position of the rotor is fixed such that it aligns with the middle of the stator teeth. This corresponds to the condition $z_{\text{mov}} = 4.5$ mm. As can e.g. be seen from the illustration in **Fig. 4.10**, for this axial position of the mover, the total torque is almost totally provided by one rotary stator. This way, as mentioned, the internal torque generated and applied to the single rotor is approximately equivalent to the total $M_{\text{in,tot}}(\varphi_{\text{rot}})$ that would be generated and applied to the complete mover (i.e., with two rotors). In order to obtain the average internal torque $M_{\text{in,avg}}$, the angular position of the rotor φ_{rot} is adjusted in steps of 5° from 0° to 180° . This is sufficient, as $M_{\text{in}}(\varphi_{\text{rot}})$ has a period of 180° due to the machine geometry, as seen, e.g., from **Fig. 4.11 (a)**. For each angular position φ_{rot} , the torque sensor is calibrated after the rotor is positioned in order to cancel any parasitic torque and measure exclusively

the internal one. Then, as visible from the exemplary measurements in **Fig. 4.16 (a)**, a slowly rotating stator field is generated by impressing the currents $i_{\{a,b,c\},R}$ in the RA winding with a fixed amplitude \hat{I}_{rf} and a low frequency $f_{rf} = 0.04$ Hz. This way, a sinusoidally varying torque $M_{rf}(t)$ is applied to the fixed rotor and measured by the torque sensor. The amplitude \hat{I}_{rf} is chosen such that the peak-to-peak amplitude of $M_{rf}(t)$ is at least 5 times larger than the declared noise-free resolution of the torque sensor, which is specified as $M_{sens,nfr} = 3$ mN m. With $\hat{I}_{rf} = 0.2$ A, a peak-to-peak amplitude of $2\hat{M}_{rf,02} \approx 20$ mN m $> 5M_{sens,nfr}$ is expected. The amplitude of the measured torque wave $\hat{M}_{rf,02}$ is reported in **Fig. 4.16 (b)** for each angular position and compared to the results of the corresponding 3D FEM simulations. As it can be

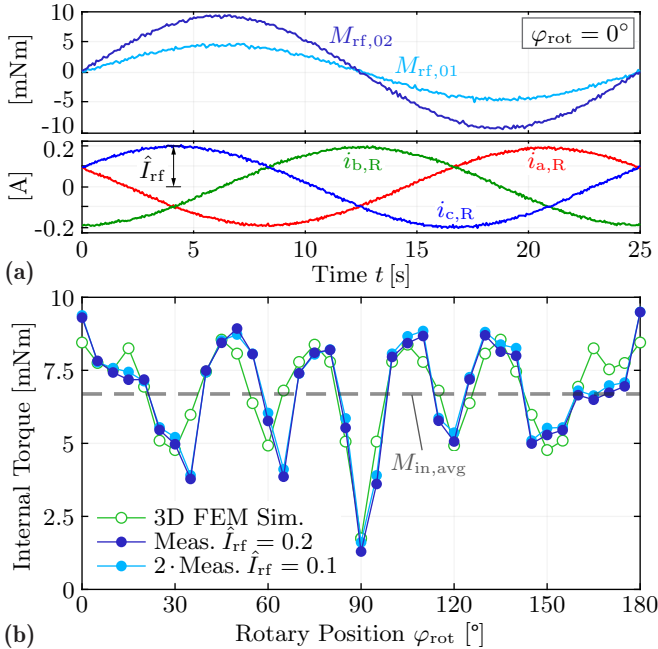


Fig. 4.16: (a) Exemplary measured torque profiles $M_{rf,\{02,01\}}(t)$ for the case $\varphi_{rot} = 0^\circ$, generated by the slowly varying phase currents $i_{\{a,b,c\},R}$ with amplitude $\hat{I}_{rf} = \{0.2, 0.1\}$ A. (b) Internal axial torque profile for a single RA module, compared to the results of the 3D FEM simulation with $N_R \hat{I}_R = 61$ Atturns. The results for $\hat{I}_{rf} = 0.1$ A are doubled for a direct comparison and verification of the torque linearity.

observed, the results are in good agreement with the simulation. The special shape of the torque profile due to the machine geometry with missing PMs is validated. Furthermore, in order to verify the linearity of the generated torque with respect to the impressed current, the measurements are also repeated with $\hat{I}_{\text{rf}} = 0.1 \text{ A}$. The average absolute error of 11 % is the result of mismatches in the torque profile at certain angular positions (e.g., $\varphi_{\text{rot}} = 35^\circ$ or 65°) that can be attributed to slight imperfections in the gluing of the PMs. Nevertheless, the average internal torque $M_{\text{in,avg}} = 6.75 \text{ mN m}$ matches the simulated value, with an absolute error as low as 1.5 %. From this result, the machine constant $k_{\text{m}} = M_{\text{in,avg}}/\hat{I}_{\text{rf}} = 33.75 \text{ mN m/A}$ is obtained. The (continuous) ohmic losses are then found as $P_{\text{Cu}} = 6 R_{\text{c}} (M_{\text{req}}/k_{\text{m}})^2 = 324 \text{ mW}$.

4.7 Summary

In this chapter, the analysis, design, realization, and experimental verification of the Rotary Actuator (RA) of the *ShuttlePump* are presented. The experimental measurements verify that the proposed integrated RA concept is practically feasible and allows meeting the torque requirement of 3.1 mN m with 324 mW of continuous power losses. Together with the estimated 8.7 W for the LA, this results in a total of 9 W for the whole LiRA. With the two building blocks of the LiRA designed and experimentally verified, the next step targets the operation of the complete drive system with full linear-rotary closed-loop position control. This requires first the realization of the appropriate linear-rotary position sensors, to be interfaced with a dedicated power electronics supply and control unit.

5

Integrated Linear-Rotary Eddy-Current Sensors

The content of this chapter is also published in:

- ▶ **R. V. Giuffrida**, J. W. Kolar, and D. Bortis, “Eddy-Current Linear-Rotary Position Sensor for an Implantable Total Artificial Heart,” in *Proc. of the 25th International Conference on Electrical Machines and Systems (ICEMS)*, Chiang Mai, Thailand, November 2022.

Chapter Abstract

This chapter presents an eddy-current linear-rotary position sensor for the *ShuttlePump*. The sensor is obtained by extending a commercially available rotary position sensor with appropriate post-processing to also capture the information about the linear position. In fact, the commercial IC serving as the interface for the rotary sensor provides sine and cosine voltage outputs, whose amplitude changes with the linear distance of the target. Furthermore, the interface adjusts its excitation frequency due to the changing coupling between the sensor and the linearly moving target. Hence, there are two options to additionally measure the linear position, which are analyzed theoretically with Finite Element Method (FEM) simulations, validated experimentally, and compared in terms of achievable sensitivity, bandwidth, and linearity. Both options allow reaching z -resolutions below the required $100\ \mu\text{m}$ and a φ -accuracy in the 5° range while meeting the specified 100 Hz bandwidth requirement, and can hence be used for feedback position control of the *ShuttlePump*.

5.1 Introduction

Contactless position measurement of a moving target following a linear and/or rotary motion is essential to ensure the correct operation of many actuators in different applications [61–65]. Among contactless position sensors, magnetic sensors (such as e.g., Hall-effect or magneto-resistive sensors) or Eddy-Current Sensors (ECSs) are the preferred choice and offer position resolutions even down to the nm range [66]. In the case of Linear-Rotary Actuators (LiRAs), it is necessary to measure accurately both linear and rotary positions of the *mover*, i.e., the movable part carrying/serving as the end-effector. The simplest approach is to use two sensors to capture linear and rotary motion independently. However, for applications that require a high level of integration, a combined solution is needed. This is the case for the *ShuttlePump*, which requires accurate measurements of the linear and rotary positions of its piston to control its motion and ensure correct operation. The required linear and rotary position measurement resolutions are in the range of 100-250 μm and 1-5°, with a targeted bandwidth of at least 50 Hz (i.e., 10 times larger than the operational motion frequency $f_{\text{op}} = 5$ Hz). All the specifications of the application are also reported in **Tab. 5.1**. Another challenge in the design of the sensor is the very limited accessibility of the piston surface, since the lateral surface of the pump is largely occupied by the stators of the LiRA. Therefore, there is no space inside the stator for the linear and rotary position sensors, which have to be placed at the two axial ends of the housing. As a consequence, the main challenge is represented by the large air gap δ between the sensor plane and the measurement target, which increases up to $\delta_{\text{max}} = 16$ mm during the linear motion of the piston. This condition makes, e.g., Hall sensors not suitable for this application, as the magnetic field coming from a permanent magnet target would be very weak and easily disturbed by external magnetic fields. On the other hand, ECSs are still an option, as they offer better immunity to external noise and there exist off-the-shelf solutions that can be used to measure absolute linear or rotary positions [67, 68]. However, due to the tight space constraints of the *Shut-*

Tab. 5.1: Sensor specifications for the *ShuttlePump*.

	Linear Position (z)	Rotary Position (φ)
Measurement range	0 ... 16 mm	0 ... 360 °
Measurement resolution	100 - 250 μm	1 - 5 °
Measurement bandwidth	50 - 100 Hz	50 - 100 Hz

tlePump, it is desirable to use only one ECS to capture both motions. Hence, this chapter discusses the design and realization of a highly-integrated eddy-current-based linear-rotary position sensor for the *ShuttlePump*, obtained by extending a commercial “single-axis” ECS with additional post-processing. In **Sec. 5.2**, the general operating principle of the sensor is explained and the proposed sensor concept is presented. **Sec. 5.3** discusses two post-processing options to extend a commercial rotary ECS into a full linear-rotary position sensor and compares them in terms of sensitivity, achievable resolution and bandwidth. In **Sec. 5.4**, the design and realization of the PCB-embedded sensor prototype are presented. **Sec. 5.5** verifies with experimental measurements the proposed linear-rotary position sensor and discusses the results evaluating the sensitivities obtained with both concepts. Finally, **Sec. 5.6** concludes the chapter.

5.2 Linear Sensor's Operating Principle

An ECS exploits the variation of magnetic coupling existing between an excitation coil carrying a high frequency current and the secondary magnetic field generated by the induced eddy currents circulating in a nearby conductive target. As depicted in **Fig. 5.1**, the excitation coil is usually placed with its axis perpendicular to the target, such that the maximum amount of primary magnetic flux is linked by it, and therefore larger eddy currents are induced. Typically, an ECS measures variations of the air gap length $\delta(t)$ between the excitation coil and the target, as this directly affects the amount of total

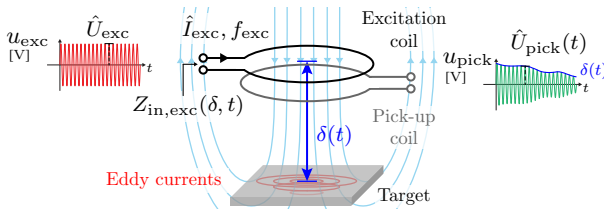


Fig. 5.1: Basic operating principle of a conventional ECS, consisting of an excitation coil, a conductive target and (eventually) a pick-up coil. The variable air gap length $\delta(t)$ can be measured either from the excitation coil's equivalent input impedance $Z_{in,exc}(\delta, t)$ or from the induced voltage $u_{pick}(\delta, t)$ in the pick-up coil.

magnetic flux that is linked by one turn of the excitation coil, i.e.,

$$\Phi_{\text{exc}}(\delta, t) = \iint_{\mathcal{S}} B(\delta, t) \, dS, \quad (5.1)$$

where $B(\delta, t)$ is the flux density and \mathcal{S} the excitation coil's (integration) area. As a result, the equivalent input impedance of the excitation coil $Z_{\text{in,exc}}(\delta, t)$ varies and it can be used to measure $\delta(t)$. As an alternative, the total magnetic flux can also be linked by a separate pick-up coil placed nearby, at whose terminals an induced voltage $u_{\text{pick}}(t)$ appears, according to Faraday's law of induction

$$u_{\text{pick}}(\delta, t) = -N_{\text{pick}} \frac{d\Phi_{\text{pick}}(\delta, t)}{dt}, \quad \Phi_{\text{pick}}(\delta, t) = \iint_{\mathcal{P}} B(\delta, t) \, dP, \quad (5.2)$$

where N_{pick} is the number of turns of the pick-up coil (here assumed to be all identical), $\Phi_{\text{pick}}(\delta, t)$ the magnetic flux of the pick-up coil and \mathcal{P} its (integration) area.

Consequently, as it can be noticed from (5.1) and (5.2), the total magnetic flux of the excitation or pick-up coils also depends on their coil area, \mathcal{S} or \mathcal{P} . This offers another realization option for the ECS, namely if the coils are shaped in a special way with respect to the target, e.g., along a certain direction $x(t)$, it is possible to obtain a variable $Z_{\text{in,exc}}(x, t)$ or $u_{\text{pick}}(x, t)$ even with a fixed air gap length δ . An example of this realization is the inductive position sensor proposed and commercially available by *Renesas* [68–70] as shown in **Fig. 5.2**. This ECS can be designed to measure either linear (cf. **Fig. 5.2 (a)**) or rotary (cf. **Fig. 5.2 (b)**) positions by utilizing special sinusoidally-shaped pick-up coils that can be conveniently realized on a PCB. In particular, the induced voltage u_{pick} appearing at the terminals of the pick-up coil is sinusoidally modulated in amplitude by the position of the target along the linear x or rotary φ direction. In order to gain unique position information, 90° spatially displaced coils are used to obtain sine- and cosine-modulated signals $u_{\text{pick,sin}}$ and $u_{\text{pick,cos}}$, which can be used after demodulation to calculate x or φ as the argument $\{x, \varphi\}(t) = \text{atan2}(u_{\text{sin}}, u_{\text{cos}})$ as typically done for, e.g., a resolver. As for conventional ECS, a sensor interface is needed in order to drive the excitation coil and demodulate plus eventually post-process the measurement signal(s). For this purpose fully-integrated solutions exist, like the *Renesas IPS2550* [68], which specifically offers two demodulation channels for the discussed inductive position sensor (cf. **Fig. 5.2 (c)**). For such ECS realization with variable-shape pick-up coils, an air gap variation is typically a problem, because if the amplitude of $u_{\text{pick,sin}}$ and $u_{\text{pick,cos}}$ reduces,

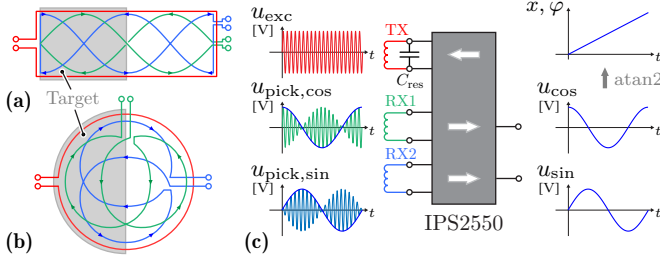


Fig. 5.2: Inductive position sensor from *Renesas*, a fixed-air-gap-length variable-coil-shape ECS with excitation coil (red) and two 90° spatially displaced pick-up coils (green and blue) to uniquely determine the target position. **(a)** Linear position sensor realization and **(b)** rotary position sensor realization. **(c)** Integrated sensor interface *IPS2550* with a transmitter and two receivers with coherent demodulators, providing either the linear position (x) or rotary position (φ) of the target.

the achievable resolution of φ , calculated from u_{\sin} and u_{\cos} after sampling and quantization with an ADC, is also worsened. In order to prevent this, the effect of a variable air gap can be eliminated/compensated with appropriate post-processing or, in the case of the *IPS2550*, with an automatic adjustment of the receivers' amplifiers gain (Automatic Gain Control, AGC) [68]. Nevertheless, this issue can be turned into a feature when it comes to a full linear-rotary ECS realization, since along the axial direction this configuration still corresponds to the variable air gap length type ECS of **Fig. 5.1**. Therefore, instead of compensating the air gap length variations, it is possible to use them to measure the linear/axial position $z(t)$. The proposed sensor concept consists then of a variable-coil-shape rotary ECS as the one of **Fig. 5.2 (b)**, extended to a full linear-rotary position sensor by also measuring the variable air gap length with appropriate post-processing. As illustrated in **Fig. 5.3**, the semi-circular conductive target is embedded in both piston's axial surfaces and one sensor PCB per side is used in a *differential sensor configuration*. This way, it is necessary to measure with high sensitivity only till half the distance, i.e., $\delta_{\max}/2 = 8$ mm instead of $\delta_{\max} = 16$ mm. This allows accurate position control each time the piston is closest to either ECS, in order to avoid any collision with the enclosure along the axial direction.

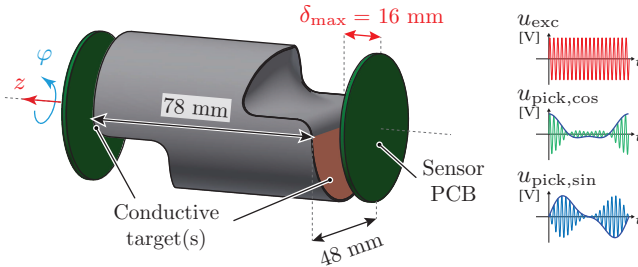


Fig. 5.3: The piston of the *ShuttlePump* with a thin 0.5 mm highly conductive target (made of, e.g., copper) embedded below its outer axial surface. The multi-layer-PCB-embedded linear-rotary ECS prototype, described in detail in [Sec. 5.4](#), is placed right in front. A second identical sensor and target can be placed at the opposite axial surface to realize a differential sensor.

5.3 Extension to a Linear-Rotary Sensor

In order to extend the commercial rotary ECS from *Renesas* into a full linear-rotary ECS, it is necessary to extract information about the mover's axial position $z(t)$. This can be done in two possible ways, discussed in the following.

5.3.1 Option 1: Magnitude and Argument

As mentioned, for a fixed air gap length the demodulated voltages u_{\sin} and u_{\cos} are used to calculate the rotary position $\varphi(t)$. If the air gap length $\delta(t)$ (from now on equivalent to the linear/axial position $z(t)$) is varied, the magnetic coupling and hence the mutual inductance between the eddy currents' circulation paths in the target and the pick-up coil(s) changes. As a result, the amplitude of both induced voltages changes. This can be easily calculated from the magnitude of the two demodulated signals as

$$u_{\text{mag}} = \sqrt{u_{\sin}^2 + u_{\cos}^2}, \quad (5.3)$$

which is known to be independent from $\varphi(t)$ and therefore is a good option to obtain $z(t)$. In the specific case of the *Renesas IPS2550*, this is actually the calculation used in the IC to correct air gap variations with the AGC [68]. Consequently, in order to also measure the linear distance by means of the amplitude variation, the ACG must be disabled and the IC must be 90

operated with constant gain. The main drawback of this option lies in the noticeable sensitivity degradation for increasing linear position z , which also leads to reduced angle resolution, especially without AGC. This is because the magnetic coupling between the excitation coil and the target decreases exponentially with increasing distance, a well-known fact in ECS design [71]. The dependence of the voltage amplitude on the distance can be verified by a simple 3D FEM simulation (cf. Fig. 5.4), where the amplitude of the induced voltage in the pick-up coil is recorded for increasing values of z from 0 mm

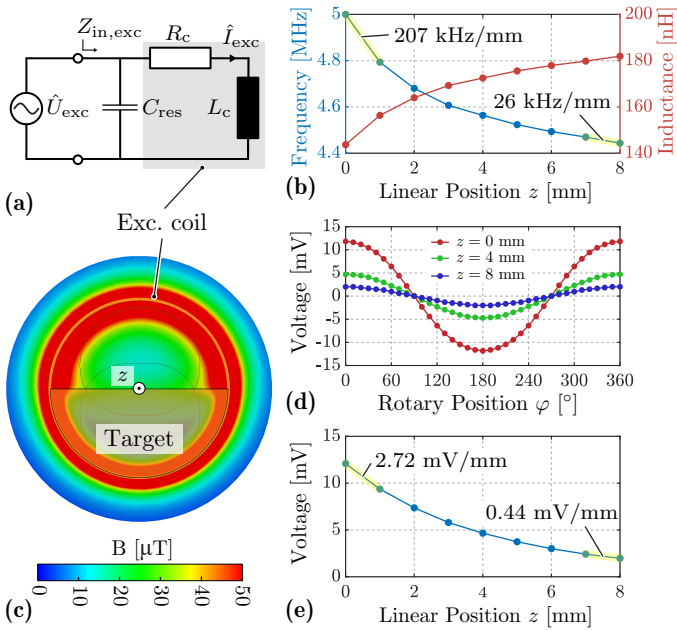


Fig. 5.4: 3D FEM simulation results (ANSYS Maxwell) to verify the magnitude-based measurement *Option 1*. (a) Driving stage of the Renesas IPS2550, i.e., an oscillator with parallel resonance. (b) Simulated excitation coil inductance profile $L_{in,exc}(z)$, from which the resonant frequency $f_{res}(z)$ is calculated with a reference capacitor $C_{res} = 7.05$ nF. The best- and worst-case frequency sensitivities are indicated. (c) Simulated distribution of the B field for $z = 1$ mm with $f_{exc,ref} = 5$ MHz and $\hat{I}_{exc,ref} = 1$ Aturns. (d) Amplitude $\hat{U}_{pick}(\varphi, z)$ of the induced voltage in one of the pick-up coils $u_{pick(,cos)}(\varphi, z) = \hat{U}_{pick}(\varphi, z) \sin(2\pi f_{exc} t)$ for $z = \{0, 4, 8\}$ mm. (e) Magnitude from the demodulated u_{sin} and u_{cos} versus the linear position z , with indicated best- and worst-case amplitude sensitivities.

to 8 mm. The simulation is performed for the reference case with $\hat{I}_{\text{exc,ref}} = 1$ Aturns and $f_{\text{exc,ref}} = 5$ MHz. In order to obtain realistic results, it should be observed that the *IPS2550* can drive the excitation coil only in resonance with a parallel capacitor C_{res} (cf. **Fig. 5.4 (a)**). Moreover, remember that although not used for measurement, the equivalent input impedance of the excitation coil $Z_{\text{in,exc}}$ still changes with z . Specifically, if the inductance $L_{\text{in,exc}}(z)$ varies, the *IPS2550* adjusts its excitation frequency f_{exc} to the resonance frequency $f_{\text{res}}(z) = \frac{1}{2\pi\sqrt{L_{\text{in,exc}}(z)C_{\text{res}}}}$. In **Fig. 5.4 (b)**, the simulated $L_{\text{in,exc}}(z)$ is shown and used to calculate the corresponding $f_{\text{res}}(z)$. As a reference case, the value of C_{res} is selected such that $f_{\text{res}}(z = 0 \text{ mm}) = f_{\text{exc,ref}} = 5$ MHz. Another consequence of the variable $f_{\text{res}}(z)$ is that also the amplitude of the current $\hat{I}_{\text{exc}}(z)$ resonating between C_{res} and the excitation coil depends on z and has to be considered. For a fixed unity driving voltage $\hat{U}_{\text{exc}} = 1$ V, this is obtained as $\hat{I}_{\text{exc}}(z) = \hat{U}_{\text{exc}} \omega_{\text{res}}(z) C_{\text{res}}$, with $\omega_{\text{res}}(z) = 2\pi f_{\text{res}}(z)$. The simulated B field distribution, an example of which is shown in **Fig. 5.4 (c)**, is integrated in the pick-up coil area to obtain the amplitude of the flux $\hat{\Phi}_{\text{pick}}(\varphi, z)$ for each value of z and φ . Finally, the amplitude of the induced voltage is

$$\hat{U}_{\text{pick}}(\varphi, z) = -N_{\text{pick}} \omega_{\text{res}}(z) \hat{\Phi}_{\text{pick}}(\varphi, z) \begin{pmatrix} \hat{I}_{\text{exc}}(z) \\ \hat{I}_{\text{exc,ref}} \end{pmatrix}. \quad (5.4)$$

For the given coil dimensions, induced peak voltages of about 12 mV per turn can be expected for the reference case, as shown in **Fig. 5.4 (d)** and **Fig. 5.4 (e)**, where the simulated pick-up voltage is given as a function of rotary and linear position, respectively. Over an axial distance of 8 mm, $u_{\text{pick,mag}}$ reduces by about 85% and hence the z -sensitivity decreases significantly. In order to limit this effect, $\hat{U}_{\text{pick}}(\varphi, z)$ should be maximized with three possible options. As it appears from (5.4), one option is to maximize the excitation frequency f_{exc} , which for the *IPS2550* is limited to 5.6 MHz. In practice, though, there is also an upper limit due to the unavoidable parasitic capacitance C_{p} that results in practical coil realizations. In fact, this leads to a certain Self-Resonant-Frequency (SRF) $f_{\text{SRF}} = \frac{1}{2\pi\sqrt{L_{\text{pick}}C_{\text{p}}}}$ of the pick-up coil, above which it exhibits predominantly a capacitive behavior. As a rule of thumb, it is advisable to select $f_{\text{exc}} \ll f_{\text{SRF}}$, separating the two by, e.g., a factor 5 to 10. The second option appearing from (5.4) is to increase the number of turns of the pick-up coil N_{pick} . As shown in **Sec. 5.4**, special care must be taken in the design, as multiple turns also increase the parasitic capacitance C_{p} (e.g., if multiple PCB layers are used), with the result that f_{SRF} is decreased. Finally, the (fixed) internal gain of the IC receivers can be maximized. The *IPS2550* has a

maximum output voltage swing of 3 V_{pp} for 5 V operation, so the internal gain is programmed in such a way that at $z = 0\text{ mm}$ this swing is achieved. This way, the z -sensitivity becomes 338 mV/mm at $z = 0\text{ mm}$ and 54.8 mV/mm at $z = 8\text{ mm}$. The final z -resolution is defined by the number of bits of the ADC used to sample u_{sin} and u_{cos} : 10 bits, for example, allow to resolve $5\text{ V}/2^{10} = 4.8\text{ mV}$, corresponding to $14.5\text{ }\mu\text{m}$ at $z = 0\text{ mm}$ and to $89\text{ }\mu\text{m}$ at $z = 8\text{ mm}$.

5.3.2 Option 2: Frequency and Argument

A second way to measure the linear position z is deduced from the frequency variation shown in Fig. 5.4 (b), where it can be observed that the excitation frequency f_{exc} selected by the *IPS2550* depends on the linear position z , since the self-inductance is changing with the axial distance of the target and the IC always tracks the *LC* resonance frequency. According to the FEM simulation, a maximum sensitivity of 207 kHz/mm at $z = 0\text{ mm}$, reducing to 26 kHz/mm at $z = 8\text{ mm}$ is to be expected. There are two main advantages when utilizing f_{exc} to measure z . The first one is that the *IPS2550* can be operated with the AGC enabled and in this way the demodulated u_{sin} and u_{cos} retain a constant amplitude even for increased distances z . As a consequence, the measurement accuracy of the calculated φ is improved and decoupled from z . The second one is that the z measurement resolution can be increased by trading-off measurement bandwidth. This is because the resolution of frequency counters implemented digitally on an MCU depends directly on the duration of the counting time interval [72]. If f_{count} is the counter's frequency,

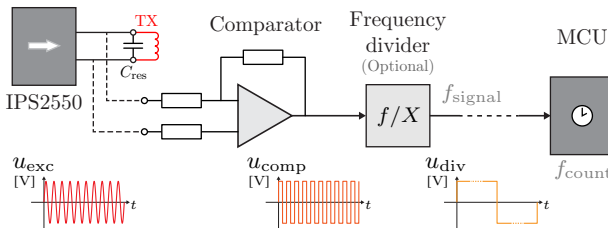


Fig. 5.5: Schematic of the frequency-based measurement *Option 2*. The high frequency excitation signal u_{exc} is converted into a square wave signal u_{comp} with a high-speed comparator for further logic counting with an MCU, running with clock frequency f_{count} . In case the distance between comparator and MCU is not negligible, a frequency divider stage can be optionally included to mitigate electromagnetic noise emissions.

$f_{\text{signal}} = f_{\text{exc}}$ the frequency to be measured and P the number of counted periods of f_{signal} , it can be shown that the frequency resolution is

$$\Delta f \approx \frac{f_{\text{signal}}^2}{f_{\text{count}}} \frac{1}{P}, \quad (5.5)$$

i.e., it can be enhanced by acquiring multiple periods P of f_{signal} . Clearly, this reduces the measurement bandwidth since it increases the latency, as a measurement is complete only when and shortly after the counter is stopped. The measurement bandwidth is then approximately

$$f_{\text{BW}} \approx f_{\text{signal}} \frac{1}{P}. \quad (5.6)$$

For a measurement bandwidth of, e.g., 100 Hz and $f_{\text{signal}} = f_{\text{exc}} = 5$ MHz, it results $P = 50000$. Therefore, with a MCU clock frequency of $f_{\text{count}} = 100$ MHz, the frequency resolution is $\Delta f = 5$ Hz at $z = 0$ mm and $\Delta f = 3.94$ Hz at $z = 8$ mm. This corresponds to a z -resolution of 24.2 nm and 151.9 nm, respectively. A schematic representation of the chosen hardware implementation for this frequency-based measurement option is shown in **Fig. 5.5**.

5.4 Hardware Prototype

The presented linear-rotary ECS is realized as an integrated PCB hardware prototype, shown in **Fig. 5.6 (b)**. It consists of a *sensor head* (excitation and pick-up coils) and a *sensor interface* for demodulation and frequency detection.

5.4.1 Measurement Requirements

The sensor is realized taking into account the measurement requirements defined by the application (cf. **Tab. 5.1**), i.e., by the *ShuttlePump*'s geometry and operation. During the linear motion, it is possible that the piston tilts slightly, as the hydrodynamic bearing supporting it is realized with a 140 μm gap. Given the piston's dimensions, this leads to a maximum error of $2 \cdot 90 \mu\text{m}$ in the linear position z . It is therefore not reasonable to target a z -accuracy below 200 μm . Nevertheless, another important requirement is that the piston does not collide with the enclosure when maximally displaced to one side. The z -accuracy must hence be below, e.g., 0.5 mm. Finally, opening and closing of the inlets/outlets imposes a requirement on the maximum φ measurement

error. Considering that the piston's shape allows for a maximum error of 2 mm along the circumferential direction, with the piston's diameter of 48 mm a φ measurement error no larger than 5° can be allowed.

5.4.2 PCB-Embedded Realization

The outer diameter of the PCB prototype is maximized to 48 mm, chosen according to the *ShuttlePump*'s geometry, i.e., of its piston and enclosure. The circular excitation coil has a diameter of 46.8 mm and covers the largest possible area with the primary magnetic field. The sine- and cosine-shaped pick-up coils cover most of the PCB area between the inner and outer diameters of 17 mm and 42.4 mm, respectively. The inner radius is chosen such that enough space is left to place the *Renesas IPS2550* sensor interface. The PCB is realized with 6 layers that are all spanned by both the excitation and

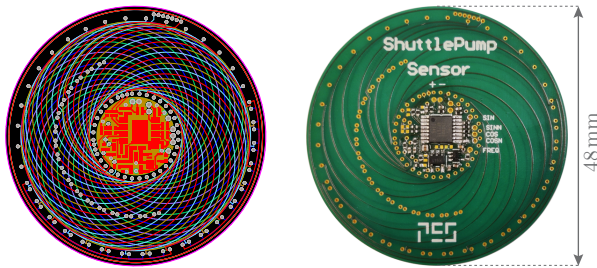


Fig. 5.6: Multi-layer-PCB-embedded linear-rotary ECS. (a) Layout details (*Altium Designer*) with distributed shifted turns and (b) realized hardware prototype.

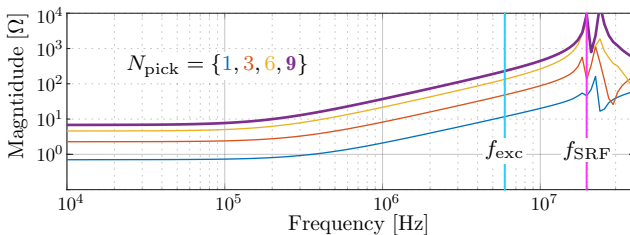


Fig. 5.7: Impedance magnitude of one of the pick-up coils, measured on the realized prototype for different number of turns N_{pick} . Due to the distributed layout with shifted turns, it can be verified that f_{SRF} remains around 20 MHz and a high $f_{\text{exc}} = 5$ MHz can be safely selected.

pick-up coils. Therefore, the number of turns of the excitation coil is $N_{\text{exc}} = 6$. For the pick-up coils, the number of turns is instead $N_{\text{pick}} = 9$ and can only be reached with the special PCB layout shown in **Fig. 5.6 (a)**. As it can be noticed, the coil is distributed in multiple layers and each turn is shifted along the φ -direction with respect to the previous one. Although this way more turns can be fit in less layers, it should be noticed that the *effective* number of turns $N_{\text{pick,eff}}$ is lower than N , as each turn links more or less magnetic flux according to the relative position to the target. Another advantage of shifting the turns is that the total parasitic capacitance C_p is smaller with respect to the case of perfectly overlapped turns, thus allowing to select f_{exc} as high as possible. In **Fig. 5.7**, showing the measured impedance magnitude of one of the realized pick-up coils, it can be observed that f_{SRF} stays around 20 MHz even with $N_{\text{pick}} = 9$. Consequently, to maximize the induced voltage in the pick-up coils $f_{\text{exc}} = f_{\text{SRF}}/4 = 5$ MHz can be selected, which is close to the maximum possible excitation frequency that the *IPS2550* can provide. Finally, in order to implement *Option 2*, a comparator is included, which generates the digital signal u_{comp} used for frequency detection. In addition, since the MCU unit of the *ShuttlePump* is placed outside the body and the signals have to be transmitted via a percutaneous drive line of ≈ 1 m length, a flip-flop-based frequency divider with $X = 1024$ stages is included to decrease the sensor frequency without degrading the sensitivity.

5.5 Measurements and Results

In order to verify the sensor's functionality, the realized PCB-embedded prototype is mounted on the custom test bench shown in **Fig. 5.8**. The target thickness should be selected larger than the skin depth, which is $30 \mu\text{m}$ for copper at $f_{\text{exc}} = 5$ MHz. Due to mechanical stability and only for this set of measurements, 3 mm is chosen. The final target thickness will instead be reduced to 0.5 mm. The test bench features two precision linear and rotary positioning stages, which allow to accurately adjust the target's linear and rotary positions down to the μm range and fractions of $^\circ$.

5.5.1 Option 1: Magnitude and Argument

For *Option 1*, the AGC of the *IPS2550* is disabled, such that the magnitude variations of the received signals are not compensated. The measurements are reported in **Fig. 5.9 (a.i, b.i, c.i)**. For each value of the linear position $z = \{0, 4, 8\}$ mm, the rotary position is increased in steps of 10° from 0° to 96

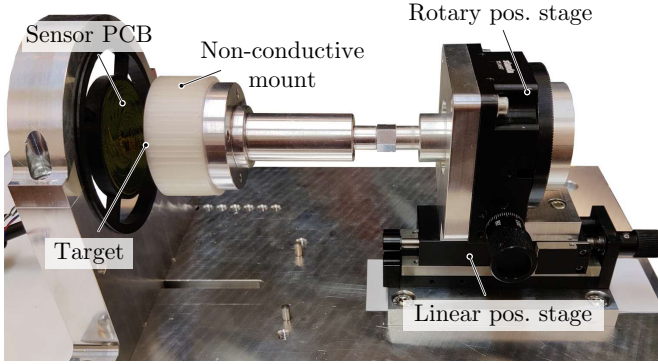


Fig. 5.8: Test bench used for the experimental sensor characterization. The sensor PCB is fixed to the base plate and the semi-circular conductive target is mounted on a non-conductive support. The target's position can be accurately adjusted with a linear and a rotary stage.

360°. Even though the amplitude of the induced voltages noticeably reduces for increasing z , the demodulated voltages of **Fig. 5.9 (a.i)** can still be used to calculate φ pretty accurately. The argument shown in **Fig. 5.9 (b.i)** is calculated taking into account that the measured u_{\sin} and u_{\cos} are sampled with a 10-bits ADC and are hence quantized in 1024 levels. This influences the final φ -error, which is shown right below the calculated argument. The worst case occurs for the largest distance $z = 8$ mm, as u_{\sin} and u_{\cos} have the smallest amplitude then and hence their quantization is more coarse. As a result, the maximum φ -error is $\varphi_{\text{err,max}} = 7^\circ$, which results in a worst-case percentage non-linearity of 1.94%. For what concerns the linear position z , from the results of **Fig. 5.9 (c.i)** it is possible to calculate the best- and worst-case z -sensitivities, which are 1.42 V/mm at $z = 0$ mm and 0.16 V/mm

Tab. 5.2: Linear-Rotary ECS measurement results.

	<i>Option 1</i>	<i>Option 2</i>
z -sensitivity	1.42 - 0.16 V/mm	750 - 46.4 kHz/mm
z -resolution	3.39 - 30 μm	6.75 - 90.5 nm
z -bandwidth	10 kHz	100 Hz
φ -error (max)	3.75 - 7 $^\circ$	3.84 - 4.58 $^\circ$
φ -bandwidth	10 kHz	10 kHz

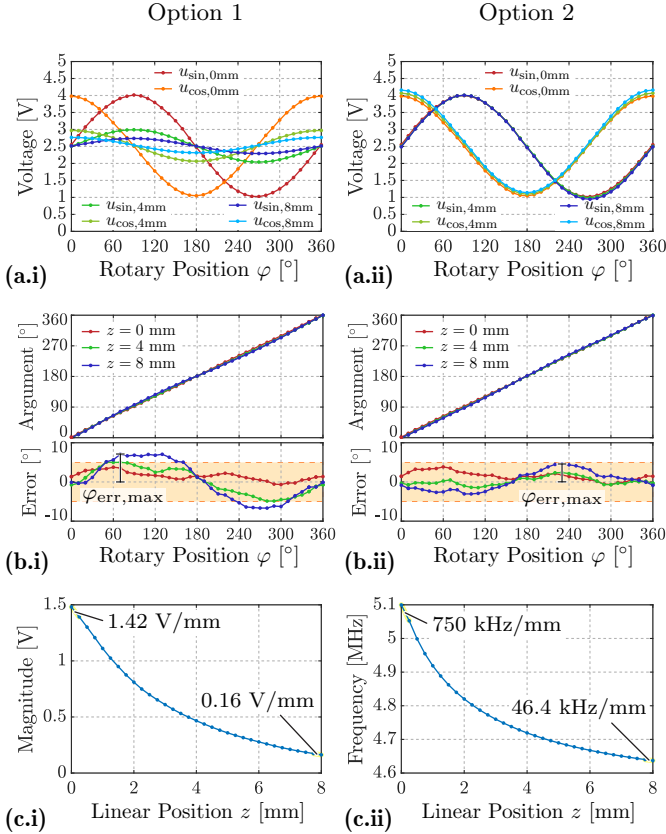


Fig. 5.9: Experimental measurements for the linear-rotary ECS for both z measurement options. **(a.i, a.ii)** Measured voltages u_{\sin} and u_{\cos} at the output of the *IPS2550* without (*Option 1*) or with (*Option 2*) AGC for $z = \{0, 4, 8\}$ mm. **(b.i, b.ii)** Calculated argument from u_{\sin} and u_{\cos} and resulting φ measurement error for $z = \{0, 4, 8\}$ mm. **(c.i)** Measured magnitude of u_{\sin} and u_{\cos} versus the linear position z , with indicated best- and worst-case amplitude sensitivities. **(c.ii)** Measured excitation frequency f_{exc} versus the linear position z , with indicated best- and worst-case frequency sensitivities.

at $z = 8$ mm, respectively. Consequently, with a 10-bits ADC, the final z -resolution is $3.39 \mu\text{m}$ at $z = 0$ mm and $30 \mu\text{m}$ at $z = 8$ mm. Finally, the measurement bandwidth for both z and φ is in this case defined by the cutoff frequency of the internal low-pass filter used for demodulation, which for the

IPS2550 is 10 kHz [68]. An alternative worth mentioning for *Option 1*, although not implemented, would be to keep the AGC enabled and read periodically the internal gain used by the AGC via the I2C interface used to program the IC. This allows to obtain magnitude information while retaining the full amplitude for u_{\sin} and u_{\cos} .

5.5.2 Option 2: Frequency and Argument

For *Option 2*, the AGC of the *IPS2550* is enabled instead, as the linear position is measured from the excitation frequency f_{exc} . The measurements are then repeated and shown in **Fig. 5.9 (a.ii, b.ii, c.ii)**. Due to the AGC, the amplitude of the induced voltages in **Fig. 5.9 (a.ii)** does not reduce for increasing z . Therefore, u_{\sin} and u_{\cos} are always quantized into the same number of levels, which with the argument calculation of **Fig. 5.9 (b.ii)** translates into a lower φ -error for the worst-case of $z = 8$ mm. This time, in fact, the maximum error is $\varphi_{\text{err,max}} = 4.58^\circ$, which results in a percentage non-linearity of 1.27%. From the results of **Fig. 5.9 (c.ii)**, showing this time how f_{exc} varies versus z , the best- and worst-case z -sensitivities are 750 kHz/mm at $z = 0$ mm and 46.4 kHz/mm at $z = 8$ mm, respectively. As discussed in **Sec. 5.3.2**, in this case the measurement resolution is defined according to (5.5). The MCU clock is $f_{\text{count}} = 100$ MHz and due to the frequency divider $f_{\text{signal}} = f_{\text{exc}}/1024 = 4.98$ kHz at $z = 0$ mm and $f_{\text{signal}} = f_{\text{exc}}/1024 = 4.53$ kHz at $z = 8$ mm. Consequently, for a 100 Hz measurement bandwidth $P = 50$ and $\Delta f(z = 0 \text{ mm}) = 0.005$ Hz and $\Delta f(z = 8 \text{ mm}) = 0.004$ Hz, hence the achievable z -resolution is 6.75 nm at $z = 0$ mm and 90.5 nm at $z = 8$ mm.

5.5.3 Comparison and Discussion

The achieved ECS specifications for both options are summarized in **Tab. 5.2**. As mentioned, the effect of the AGC on the measured φ can be seen by comparing the φ -error for both cases. As it can be seen, *Option 2* benefits from it, with $\varphi_{\text{err,max}}$ always below the maximum allowed 5° . Although for *Option 1* $\varphi_{\text{err,max}} > 5^\circ$ for the worst-case distance $z = 8$ mm, it should be observed that opening/closing of the *ShuttlePump*'s inlets/outlets occurs when the piston is close to the enclosure's sides. In that case (i.e., $z = 0$ mm), both options are usable and offer comparable φ -accuracy with errors below 5° . For the linear position z , the frequency-based *Option 2* considerably increases the z -resolution by trading-off measurement bandwidth. Nevertheless, for the targeted application, also *Option 1* offers sufficient z -resolution. Finally, it should be mentioned that *Option 1* only requires two measurement signals

(u_{\sin} and u_{\cos}), whereas *Option 2* additionally requires the excitation voltage u_{exc} (processed into u_{div}) to measure f_{exc} .

5.5.4 Real Mission Profile - Dynamic Operation

Starting from the measurements of **Fig. 5.9**, it is finally possible to predict the actual sensor outputs during the dynamic operation of the *ShuttlePump*. For this, the linear-rotary mission profile for one period in **Fig. 5.10 (a)** and **Fig. 5.10 (b)** is used. The linear motion follows a sinusoidal trajectory from one side of the enclosure to the other and back, while continuously rotating with constant speed, all at $f_{\text{op}} = 5$ Hz. **Fig. 5.10 (c)** and **Fig. 5.10 (d)** show the resulting 2.5 V-offset-free u_{\sin} and u_{\cos} for *Option 1* and are generated interpolating the results of **Fig. 5.9 (c.i)**. The outputs are generated also for a second

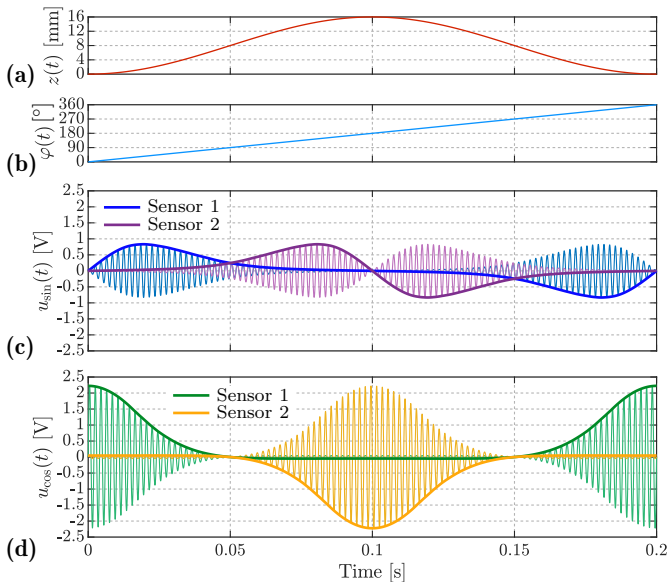


Fig. 5.10: Dynamic operation of the *ShuttlePump* with the actual mission profiles for (a) linear position $z(t)$ and (b) rotary position $\varphi(t)$. The offset-free linear-rotary ECSs outputs for *Sensor 1* (at $z = 0$ mm) and *Sensor 2* (at $z = 16$ mm) are shown in (c) for the sine output u_{\sin} and (d) for the cosine output u_{\cos} . The frequency of the modulation carrier is not to scale and only reported for conceptual purposes.

sensor placed on the opposite axial surface at $z = 16$ mm, thus emphasizing the advantage of using the differential measurement configuration.

5.6 Summary

In this chapter, a compact integrated eddy-current linear-rotary position sensor for the *ShuttlePump* was proposed. The ECS was obtained by extending a commercial rotary ECS into a full linear-rotary one by appropriate post-processing with two linear position measurement options. The experimental results showed that both are usable for the targeted application, with linear and rotary position accuracies below the required $100\ \mu\text{m}$ and 5° and largely sufficient measurement bandwidths ≥ 100 Hz. Therefore, as a next step, the proposed ECS can be used for feedback position control of the *ShuttlePump*'s piston.

6

Linear-Rotary Position Control

The content of this chapter is also published in:

- ▶ **R. V. Giuffrida**, A. Horat, D. Bortis, T. Bierewirtz, K. Narayanaswamy, M. Granegger, and J. W. Kolar, “Linear-Rotary Position Control System with Enhanced Disturbance Rejection for a Novel Total Artificial Heart,” *IEEE Open Journal of the Industrial Electronics Society*, vol. 5, pp. 359-375, April 2024.

Chapter Abstract

Closed-loop speed and/or position control of electromechanical blood pumps used in circulatory assist devices is essential to guarantee their functionality. This is especially important for the *ShuttlePump*, to guarantee that the specified linear-rotary motion is tracked while providing the necessary hydraulic force and torque. This chapter provides the details of the closed-loop linear-rotary position control system required to operate the *ShuttlePump*. The design of the position control system targets tight reference tracking (± 8 mm linear stroke and continuous rotation) up to an operational frequency of 5 Hz, under the heavy disturbance introduced by the axial hydraulic load force, as high as 45 N. The experimental measurements show successful linear-rotary position tracking under the specified axial load, with a maximum error of 1 mm and 5° .

6.1 Introduction

Electro-mechanically actuated blood pumps inevitably need feedback control to operate. For instance, for rotary blood pumps the angular speed of the impeller needs to be controlled to guarantee a specified flow rate [73, 74]. Similarly, some positive displacement blood pumps make use of a controlled

linear motion to push the blood into circulation [75, 76]. Finally, the most advanced blood pumps featuring active magnetic bearings strictly rely on stable position control of the levitated impeller [77, 78]. Also the *ShuttlePump* is an eloquent example of the importance of feedback control in enabling blood pumping operation. This chapter represents a point of arrival in the development of the complete *ShuttlePump* drive system. The realized LiRA prototype is complemented with its inverter and control unit, on which the closed-loop linear-rotary position control system is implemented. This way, it is possible to show simultaneous linear-rotary position control and test the LiRA under the required axial load. The chapter is structured as follows. **Sec. 6.2** recapitulates the characteristics of the realized LiRA that are relevant for system modeling and control, and defines the motion control requirements. In **Sec. 6.3**, the derivation of an electro-mechanical dynamical model for the LiRA of *ShuttlePump* is presented. This is used in **Sec. 6.4** to design the cascaded current and linear-rotary position control systems. The hardware implementation of the entire system is then discussed in **Sec. 6.5**. The experimental verification with the LiRA operated in closed-loop follows in **Sec. 6.6**. Finally, **Sec. 6.7** concludes the chapter.

6.2 ShuttlePump LiRA and Motion Control Requirements

This section reports the parameters of the designed LiRA discussed in the previous chapters, and that are relevant for system modeling and control. Furthermore, the motion control requirements (motion profile, required force/torque) are defined.

6.2.1 Parameters of the LiRA and Linear-Rotary Position Sensors

The final design of the LiRA looks like in **Fig. 6.1**, with the dimensions of **Tab. 4.1**, here reported in **Tab. 6.1**. The parameters that are relevant for the subsequent electro-mechanical system modeling and feedback control are instead collected in **Tab. 6.2**. The winding of the LA consists of 6 circular coils with resistance $R_{c,lin} = 2.2 \Omega$ and inductance $L_{c,lin} = 4.7 \text{ mH}$. For each phase, 2 coils are connected in antiserries. Therefore, in the following sections, the total phase resistances $R_{lin} = 2 \cdot R_{c,lin}$ and inductance $L_{lin} = 2 \cdot L_{c,lin}$ are considered for the LA. The winding of the RA instead consists of 12 concentrated coils

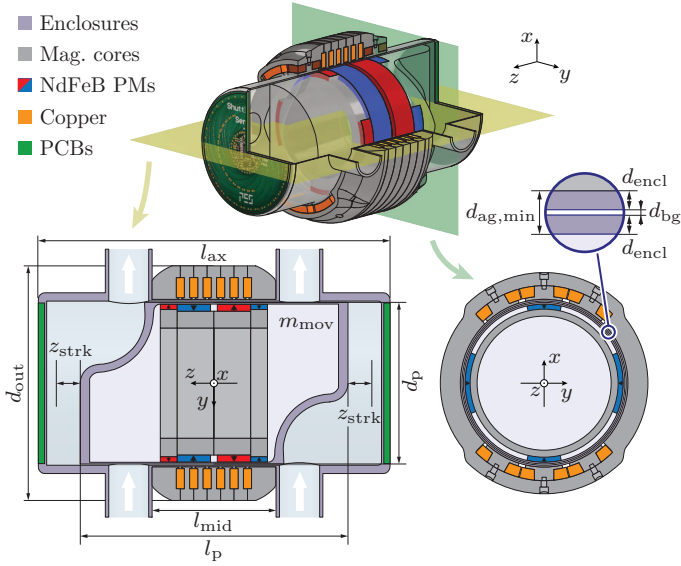


Fig. 6.1: Sectional (xy - and yz -) views of the *ShuttlePump*, showing its enclosure and specially-shaped piston with annotated dimensions, reported in **Tab. 2.2**. Also the designed LiRA is visible, consisting of linear and rotary stators (around the enclosure) and the moving part with NdFeB permanent magnets, i.e., the *mover*, which is embedded in the piston [27, 28].

with resistance $R_{c,rot} = 6.4 \Omega$ and inductance $L_{c,rot} = 6.9 \text{ mH}$. With 4 coils per phase, $R_{rot} = 4 \cdot R_{c,rot}$ and $L_{rot} = 4 \cdot L_{c,rot}$ are considered. The measured machine constants (cf. **Fig. 3.16 (a)** and **Fig. 4.16 (b)**) are reported here for convenience in **Fig. 6.2**. On average, the force and torque constants are $k_{LA} = 22.9 \text{ N/A}$ and $k_{RA} = 33.3 \text{ mNm/A}$, respectively. The phase flux linkages $\psi_{\{a,b,c\},\{\text{lin},\text{rot}\}}$ for the LA and the RA are extracted from FEM simulations and reported in **Fig. 6.3**.

For what concerns the sensors, two of the realized linear-rotary eddy-current position sensors are used, placed on the two sides of the enclosure. From the demodulated voltage output signals, the rotary position measurements are obtained as

$$\varphi_{\{S1,S2\}} = \text{atan2}(u_{\sin,\{S1,S2\}}, u_{\cos,\{S1,S2\}}), \quad (6.1)$$

Tab. 6.1: Specifications of the *ShuttlePump* (cf. **Fig. 6.1**), reported from **Tab. 4.1**.

Name	Symbol	Value	Unit
Maximum axial dimensions	l_{ax}	105	mm
Maximum radial dimensions	d_{out}	70	mm
Piston axial length	l_{p}	78	mm
Piston outer diameter	d_{p}	48.72	mm
Inter- in-/outlets distance	l_{mid}	40	mm
Inlet/outlet diameter	d_{io}	12	mm
Enclosure thickness (lateral)	d_{encl}	0.5	mm
Blood gap	d_{bg}	140	um
Magnetic gap	$d_{\text{ag,min}}$	1	mm
Axial stroke amplitude	z_{strk}	8	mm
Maximum axial force	$F_{\text{req,peak}}$	≈ 43	N
Axial torque	M_{req}	3.1	mNm
Maximum radial force	$F_{\text{rad,max}}$	25	N
Piston frequency	f_{op}	1.5 - 5	Hz
Piston rotational speed	Ω_{op}	90 - 300	rpm
Max. speed ripple (open loop)	$\Delta\Omega_{\text{op,max}}$	20	%
Operating conditions		2.5 - 9	L/min
Max. average cont. losses	$P_{\text{Cu,avg,max}}$	10	W
Blood temperature increase	ΔT_{max}	2	K

whereas the linear position is calculated from the magnitude as

$$z_{\{S1,S2\}} = f_{\text{fit}} \left(\sqrt{u_{\text{sin},\{S1,S2\}}^2 + u_{\text{cos},\{S1,S2\}}^2} \right), \quad (6.2)$$

where f is the inverse of a fitted exponential calibration function. The measured sensor signals are post-processed with a linear weighting according to the axial position of the piston, as further explained in **Appendix B**. This is done to use the information from the sensor that is closer to its target, for which the measurement signals have better quality (higher sensitivity, less noise). The measurement bandwidth is $f_{\text{sens}} = 10$ kHz, which is largely sufficient and hence does not introduce significant delays to be considered during the design of the controller.

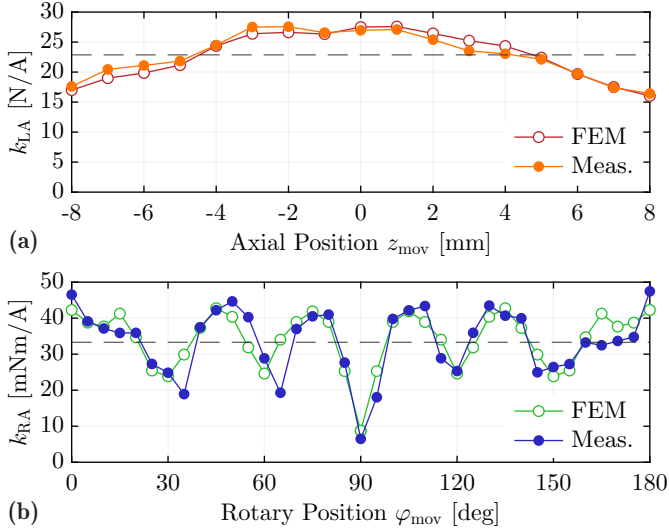


Fig. 6.2: Measured machine constants, compared to the simulated values from FEM, for (a) the LA and (b) the RA. Both exhibit a position dependency due to the motor characteristics [27, 28]. On average, $k_{LA} = 22.9$ N/A and $k_{RA} = 33.3$ mNm/A.

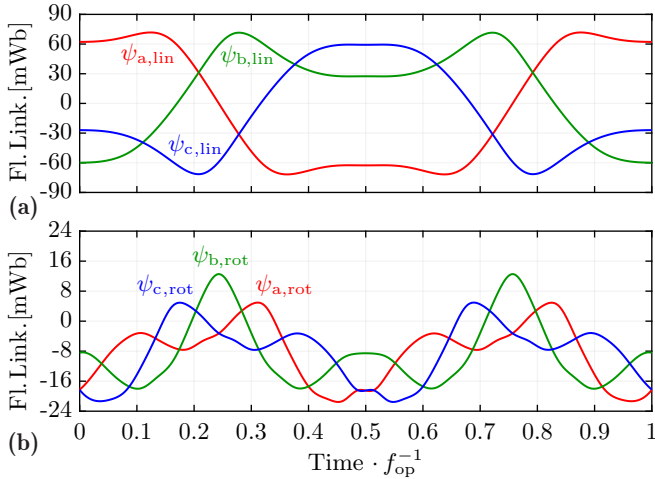


Fig. 6.3: Simulated phase flux linkages $\psi_{\{a,b,c\},\{lin,rot\}}$ for (a) the LA and (b) the RA for a cycle of operation with frequency $f_{op} = \{1.5, \dots, 5\}$ Hz.

Tab. 6.2: Control-oriented parameters of the realized *ShuttlePump* LiRA.

Name	Symbol	Value	Unit
Mover mass	m_{mov}	0.248	kg
Linear friction coefficient	b_{lin}	1	N s/m
Mover moment of inertia	J_{mov}	70	kg m ²
Rotary friction coefficient	b_{rot}	10^{-4}	N m s/rad
Phase resistance (LA)	R_{lin}	$2 \cdot 2.2$	Ω
Phase inductance (LA)	L_{lin}	$2 \cdot 4.7$	mH
Phase resistance (RA)	R_{rot}	$4 \cdot 6.4$	Ω
Phase inductance (RA)	L_{rot}	$4 \cdot 6.9$	mH
Force constant	k_{LA}	Fig. 6.2 (a)	N/A
Torque constant	k_{RA}	Fig. 6.2 (b)	mNm/A
Pole pitch (LA)	τ_{pp}	24	mm
Pole pairs (RA)	P	4	
Peak flux linkage (LA)	$\hat{\Psi}_{\text{PM,lin}}$	70	mWb
Peak flux linkage (RA)	$\hat{\Psi}_{\text{PM,rot}}$	7.3	mWb
LC filter inductance	L_f	22	μH
LC filter capacitance	C_f	10	μF
LC filter damping resistance	R_f	2	Ω

6.2.2 Motion Control Requirements for the LiRA

It is now important to briefly pinpoint the motion control requirements that guide the following linear-rotary position control design. The specified motion profile for the piston is shown in **Fig. 6.5**. Synchronization of the axial/linear position z_{mov} with the angular/rotary position φ_{mov} is essential. In fact, the pump operates correctly if the blood is pushed out of one chamber only when its inlet is closed and its outlet opened. To guarantee that this condition is respected with the given piston and enclosure geometry, the piston holds its axial position for a short time interval t_{hold} at the two edge positions $z_{\text{mov}} = \pm z_{\text{strk}}$, while the rotation continues (cf. **Fig. 6.5**). The duration of the hold interval depends on the operational frequency as

$$t_{\text{hold}} = \frac{\varphi_{\text{hold}}}{360^\circ} \frac{1}{f_{\text{op}}}, \quad (6.3)$$

where φ_{hold} is the rotary angle to be traveled during the hold phase, which is strictly linked to the rotary positioning accuracy.

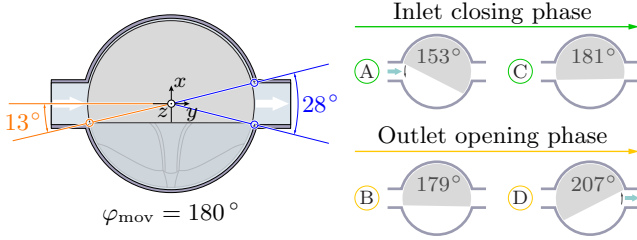


Fig. 6.4: Sectional view of the *ShuttlePump* for the case $\varphi_{mov} = 180^\circ$. According to the given geometry of the piston and the highlighted angles, the inlet closing phase and the outlet opening phase are defined.

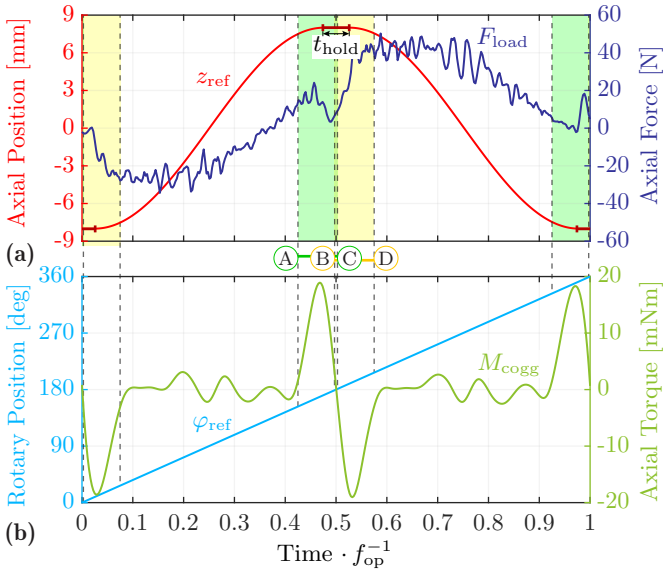


Fig. 6.5: Specified linear (a) and rotary (b) motion profile of the *ShuttlePump*, with force and torque requirements. Both motions have to be synchronized and tracked in the operational range $f_{op} = \{1.5, \dots, 5\}$ Hz. The hydraulic load force F_{load} and the cogging torque M_{cogg} are the main disturbances to be rejected by the position control system. The inlet closing phase and the outlet opening phase are highlighted in green and yellow, respectively.

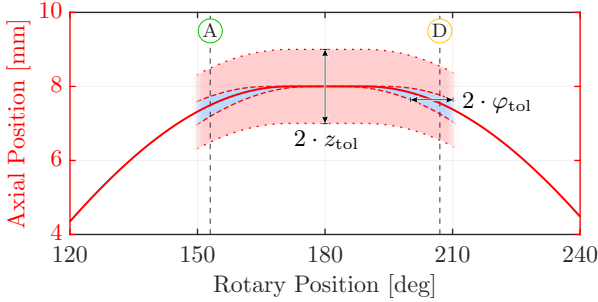


Fig. 6.6: Axial-rotary position diagram with highlighted tolerance bands. The control error boundaries $z_{tol} = 1$ mm and $\varphi_{tol} = 5^\circ$ should be respected tightly in the range $\varphi_{mov} = [153^\circ, 207^\circ]$.

To understand how φ_{hold} can be selected, consider the sectional view of **Fig. 6.4**. With a diameter of $d_{io} = 12$ mm, a single inlet/outlet spans 28° along the inner circumference of the enclosure. When the piston blade lies horizontally, i.e., for $\varphi_{mov} = \{0, 180\}^\circ$, it occludes an angle of 27° in front of both the inlet and the outlet, as the angle to the flat edge of the blade is 13° . For the sake of simplicity, consider only the case $\varphi_{mov} = 180^\circ$ illustrated in **Fig. 6.4** (the case $\varphi_{mov} = 0^\circ$ is analogous). With the given geometry and angles, it is possible to define the *inlet closing phase* over the range $\varphi_{mov} = [153^\circ, 181^\circ]$, and the *outlet opening phase* over the range $\varphi_{mov} = [179^\circ, 207^\circ]$. With $\varphi_{hold} = 2 \cdot 10^\circ$, i.e., with a symmetric plateau in the axial position over 18° of rotation in the range $\varphi_{mov} = [170^\circ, 190^\circ]$, a maximum rotary position lead/lag (or maximum absolute rotary position error) of $\varphi_{err,max} = 9^\circ$ can be tolerated. This way, the outlet opening phase can start as late as at $\varphi_{mov} = 188^\circ$ (lag case) or the inlet closing phase can end as early as at $\varphi_{mov} = 172^\circ$ (lead case), with 2° of margin for both cases, hence without compromising the pumping operation.

It should be further considered that $\varphi_{err,max}$ consists of two components, namely a control component $\varphi_{err,contr} = \varphi_{ref} - \varphi_{meas}$ due to the tracking performance of the rotary position controller and a measurement component $\varphi_{err,meas} = \varphi_{meas} - \varphi_{mov}$ given by the sensor accuracy. In total, $\varphi_{err,max} = |\varphi_{err,contr,max}| + |\varphi_{err,meas,max}|$ in the worst case. Considering that the sensor introduces already $|\varphi_{err,meas,max}| = 4^\circ$ [52], the specification on the tracking error for the rotary position controller is set to $\varphi_{tol} = |\varphi_{err,contr,max}| = 5^\circ$. As indicated in **Fig. 6.6**, this specification should be respected tightly in the

ranges $\varphi_{\text{mov}} = [153^\circ, 207^\circ]$ and $\varphi_{\text{mov}} = [0^\circ, 27^\circ] \cup [333^\circ, 360^\circ]$, i.e., from the beginning of the inlet closing phase till the end of the outlet opening phase. Finally, it should be observed that, if necessary, it is always possible to extend the duration of t_{hold} to accommodate for larger rotary positioning inaccuracies. However, this results in a sharper linear motion profile with higher acceleration, which requires higher current and hence ohmic losses in the LA.

For the linear motion, the main requirement on the tracking of the quasi-sinusoidal motion profile is that the piston does not hit the axial ends of the enclosure. As a safety margin of 3 mm between piston and enclosure at the two edge positions $z_{\text{mov}} = \pm z_{\text{strk}}$ is already considered in the dimensions of the *ShuttlePump*, the maximum tracking error for the linear position controller is set to $z_{\text{tol}} = |z_{\text{err,contr,max}}| = 1$ mm. This specification should be met particularly around the plateau phase (cf. Fig. 6.5).

6.3 Electro-Mechanical System Modeling

This section introduces the electro-mechanical model [79–81] of the *ShuttlePump* LiRA. First, the mechanical linear and rotary dynamic subsystems are derived and linearized. The radial dynamics of the piston is not considered, as it is stabilized by the hydrodynamic journal bearing. Then, the electrical subsystem describing the phase currents of the LiRA in the mover-oriented frame is introduced. Note that in the following, in order to keep the notation simple, the dependency on time t is not explicitly indicated.

6.3.1 Linear/Axial Position Dynamics

In order to describe its axial z -motion, the piston of the *ShuttlePump* is modeled as a rigid body with mass m_{mov} , for which the force balance

$$\frac{d^2z}{dt^2} = \frac{1}{m_{\text{mov}}} F_{\text{tot}} = \frac{1}{m_{\text{mov}}} (F_z + F_{\text{cogg}} - F_{\text{fric}} - F_{\text{load}}) \quad (6.4)$$

is written. In detail:

- ▶ F_z is the electro-mechanical internal axial force generated and exerted by the stator of the LA on the mover. It is the input of the system.
- ▶ F_{cogg} is the cogging force of the LA. Due to its small amplitude (by design, [27]), it can be neglected and eventually modeled as an input disturbance.

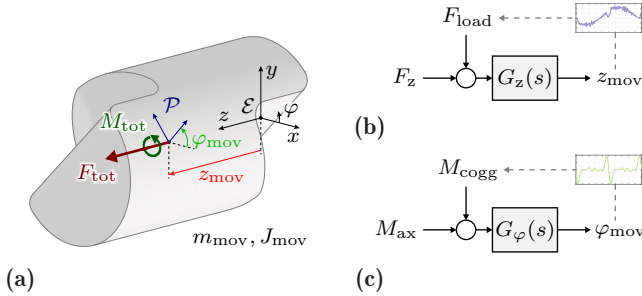


Fig. 6.7: (a) Free-body diagram of the piston of the *ShuttlePump*, with enclosure (\mathcal{E}) and piston (\mathcal{P}) reference frames. The piston linear-rotary motion is described with respect to the frame \mathcal{E} with the axial position z_{mov} and the angular position φ_{mov} . (b) Open loop block diagram for the linear/axial z -dynamics with input disturbance F_{load} . (c) Open loop block diagram for the rotary/angular φ -dynamics with input disturbance M_{cogg} .

- ▶ F_{fric} is the friction force, modeled as a viscous friction $F_{fric} = b_{lin} \frac{dz}{dt}$ with the coefficient b_{lin} representing the viscosity of blood.
- ▶ F_{load} is the required hydrodynamic load force of **Fig. 6.5 (b)**. Although this actually depends on the axial position z_{mov} , it is not included in the plant, but modeled as an external input disturbance.

The equilibrium points of the dynamics in (6.4) are found imposing $\frac{d^2z}{dt^2} = 0$. This is satisfied for $z = z_{ss} = \text{const}$, with $z_{ss} \in [-z_{strk}, z_{strk}]$, and with the steady-state input force $F_{z,ss} = F_{load}$. The plant in the Laplace domain becomes

$$G_z(s) = \frac{Z(s)}{F_z(s)} = \frac{1}{m_{mov} s^2 + b_{lin} s}, \quad (6.5)$$

which is valid $\forall z_{ss} \in [-z_{strk}, z_{strk}]$. G_z has one pole in the origin ($\lambda_{z,1} = 0$) and one pole in the left-half plane ($\lambda_{z,2} = -b_{lin}/m_{mov}$), so it is only *marginally stable* in open loop. The modeled plant for the axial dynamics is finally represented by the block diagram in **Fig. 6.7 (b)**.

6.3.2 Rotary/Angular Position Dynamics

For what concerns the rotational φ -dynamics, the piston is analogously modeled as a rigid body with a moment of inertia J_{mov} and the torque balance

$$\frac{d^2\varphi}{dt^2} = \frac{1}{J_{\text{mov}}} M_{\text{tot}} = \frac{1}{J_{\text{mov}}} (M_{\text{ax}} + M_{\text{cogg}} - M_{\text{fric}} - M_{\text{load}}) \quad (6.6)$$

is written. Similarly:

- ▶ M_{ax} is the electro-mechanical internal torque generated and applied by the RA to the mover. It is the input of the system.
- ▶ M_{cogg} is the cogging force of the RA, reported in **Fig. 6.5 (c)**. Also in this case, although it exhibits a dependency on the rotary position φ_{mov} , it is modeled as an external input disturbance to the system.
- ▶ $M_{\text{fric}} = b_{\text{rot}} \frac{d\varphi}{dt}$ is the viscous friction torque, modeled with the coefficient b_{rot} representing the blood viscosity for the rotary motion.
- ▶ M_{load} is the required hydrodynamic load torque.

The equilibrium points of (6.6) are found for $\frac{d^2\varphi}{dt^2} = 0$, which is satisfied for $\varphi = \varphi_{\text{ss}} = \text{const}$, with $\varphi_{\text{ss}} \in [0, 2\pi]$, and with the steady-state input torque $M_{\text{ax,ss}} = -M_{\text{cogg}} + M_{\text{load}}$. The plant in the Laplace domain becomes

$$G_{\varphi}(s) = \frac{\Phi(s)}{M_{\text{ax}}(s)} = \frac{1}{J_{\text{mov}} s^2 + b_{\text{rot}} s}. \quad (6.7)$$

Analogously to (6.5), this has the poles $\lambda_{\varphi,1} = 0$ and $\lambda_{\varphi,2} = -b_{\text{rot}}/J_{\text{mov}}$. The modeled plant for the rotary dynamics is represented by the block diagram in **Fig. 6.7 (c)**.

6.3.3 Electrical Dynamics in the Mover-Oriented Frame

The dynamic model of the electrical subsystem describes the transient behavior of each phase current of the LiRA. As known, this is captured by the *stator equation*, which can be written for both the LA or the RA by simple analysis of the equivalent circuit model of **Fig. 6.8 (a)**. The *stator equation* is

$$u_{s,\{a,b,c\}} = R_{\{a,b,c\}} i_{s,\{a,b,c\}} + L_{\{a,b,c\}} \frac{di_{s,\{a,b,c\}}}{dt} + u_{q,\{a,b,c\}}, \quad (6.8)$$

where

- ▶ $u_{s,\{a,b,c\}}$ and $i_{s,\{a,b,c\}}$ are the phase voltage and current, respectively,
- ▶ $R_{\{a,b,c\}}$ and $L_{\{a,b,c\}}$ are the phase resistance and inductance, respectively,
- ▶ $u_{q,\{a,b,c\}} = \frac{d\psi_{\{a,b,c\}}}{dt}$ is the induced voltage caused by the changing magnetic flux linkage with the stator coils $\psi_{\{a,b,c\}}$ (reported in **Fig. 6.3**) due to the mover's linear and/or rotary motion.

By orienting the stator field (Field-Oriented Control) correctly with respect to the mover field, the necessary electromechanical force F_z or torque M_{ax} is generated. In particular, field orientation requires the electrical angle

$$\theta_{el} = \begin{cases} \vartheta_{el} = \frac{2\pi}{\tau_{pp}} z_{mov} & \text{for the LA} \\ \varphi_{el} = P \varphi_{mov} & \text{for the RA} \end{cases}, \quad (6.9)$$

where τ_{pp} is the pole pitch of the LA and P the number of pole pairs of the RA. Transforming the stator equation (6.8) into the mover-oriented dq -frame (cf. **Fig. 6.8 (c-d)**), one obtains

$$u_{s,\{d,q\}} = R_{\{d,q\}} i_{s,\{d,q\}} + L_{\{d,q\}} \frac{di_{s,\{d,q\}}}{dt} + \underbrace{\mp \frac{d\theta_{el}}{dt} L_{\{d,q\}} i_{s,\{q,d\}} + \frac{d\psi_{\{d,q\}}}{dt} - \frac{d\theta_{el}}{dt} \psi_{\{q,d\}}}_{u_{ff,\{d,q\}}}. \quad (6.10)$$

As both the LA and RA have a non-salient pole translator/rotor,

$$(R_d, L_d) = (R_q, L_q) = \begin{cases} (R_{lin}, L_{lin}) & \text{for the LA} \\ (R_{rot}, L_{rot}) & \text{for the RA} \end{cases}, \quad (6.11)$$

whereas for the flux linkage due to field-orientation it holds

$$(\psi_d, \psi_q) = \begin{cases} (\hat{\Psi}_{PM,lin}, 0) & \text{for the LA} \\ (\hat{\Psi}_{PM,rot}, 0) & \text{for the RA} \end{cases}, \quad (6.12)$$

which can also be verified by transforming the phase flux linkages $\psi_{\{a,b,c\}}$ in **Fig. 6.3** to the dq -frame. The dq -transformation of the time derivatives introduces cross-coupling terms that are compensated as feedforward voltages $u_{ff,\{d,q\}}$. This way, the d - and q -dynamics are correctly decoupled and can hence be controlled independently. The resulting open loop plants are

$$G_{c,\{d,q\}}(s) = \frac{1}{L_{\{d,q\}} s + R_{\{d,q\}}}, \quad (6.13)$$

as shown in the block diagram of **Fig. 6.8 (b)**.

For completeness, the electrical subsystem is complemented with a simple model of the inverter used to supply the LiRA. This consists of the delay element introduced by the power electronics and the foreseen LC output filter (cf. **Sec. 6.5**). For the former, a first order approximation is sufficient, i.e.,

$$G_{PE}(s) = \frac{1}{T_{PE} s + 1}, \quad (6.14)$$

where T_{PE} is the sum of the switching period and the controller update period. For the latter, the transfer function has the well-known second-order form

$$G_{LC}(s) = \frac{1}{L_f C_f s^2 + \frac{L_f}{R_f} s + 1}, \quad (6.15)$$

where L_f and C_f are the filter capacitance and inductance and R_f is the resistance of the damping resistor.

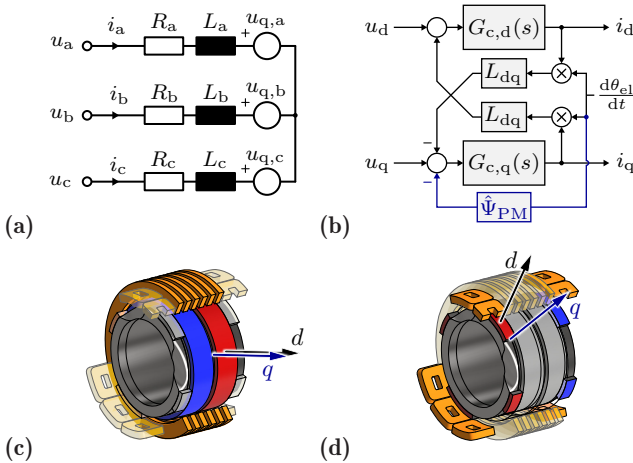


Fig. 6.8: (a) PMSM equivalent circuit with phase resistances, inductances and induced voltages, valid either for the LA or the RA. (b) Open loop block diagram of the electrical subsystem in the mover-oriented frame with voltage cross-coupling terms introduced by the dq -transformation. The diagram is valid either for the LA or the RA with the generic electrical angle θ_{el} in (6.9). (c) LA part of the *ShuttlePump*, with indicated mover-oriented frame. (d) RA part of the *ShuttlePump*, with indicated mover-oriented frame.

6.4 Control System Design

This section covers the design of the linear-rotary position control system of the *ShuttlePump* LiRA.

6.4.1 Control Structure and Specifications

Position or speed control of PMSMs typically makes use of the well-established technique of cascaded control. As the mechanical linear and rotary dynamics are well decoupled, they are controlled by independent single-input-single-

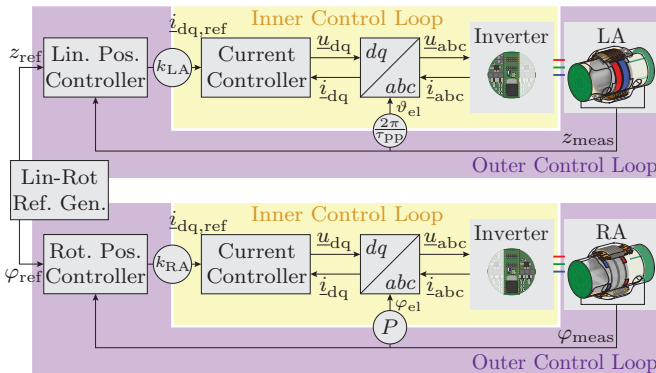


Fig. 6.9: Overall control diagram of the *ShuttlePump* LiRA. The two independent cascaded loops consist of an outer linear or rotary position control loop and an inner dq -current control loop. The two loops get synchronized linear and rotary position references from the reference generator.

Tab. 6.3: LiRA control specifications for the *ShuttlePump*.

	LA dq -Current	RA dq -Current
Max tracking error	$i_{\{d,q\},err} = 0.05 \text{ A}$	$i_{\{d,q\},err} = 0.05 \text{ A}$
Control BW	$\omega_c = 2\pi 600 \text{ rad/s}$	$\omega_c = 2\pi 600 \text{ rad/s}$
Input sat. limit	$u_{\{d,q\},lim} = \pm 13 \text{ V}$	$u_{\{d,q\},lim} = \pm 13 \text{ V}$
	Linear Position z	Rotary Position φ
Max tracking error	$z_{err,max} = 1 \text{ mm}$	$\varphi_{err,max} = 5^\circ$
Control BW	$\omega_z = 2\pi 150 \text{ rad/s}$	$\omega_\varphi = 2\pi 80 \text{ rad/s}$
Input sat. limit	$F_{lim} = \pm k_{LA} 2.7 \text{ A}$	$M_{lim} = \pm k_{RA} 0.5 \text{ A}$

output (SISO) controllers. Therefore, as illustrated in the diagram of **Fig. 6.9**, there is two independent cascaded controllers, each consisting of an outer control loop for the (slower) mechanical linear or rotary dynamics and an inner control loop for the (faster) electrical dynamics. For these to work properly, it is necessary to guarantee that the dynamics of the two loops are decoupled. Specifically, the inner electrical loop is expected to regulate the required force- or torque-generating current components ‘almost instantly’ from the point of view of the outer mechanical loop. In the frequency domain, this means that the closed-loop bandwidth of the inner loop should be much larger (e.g., by a factor 10) than the one of outer loop. This leads to the definition of the control specifications in **Tab. 6.3**. The motion control requirements previously defined in **Sec. 6.2.2** are complemented with frequency-domain specifications on the control bandwidths and the input saturation limits. As all the controllers need to be implemented digitally, the design is first conducted in continuous time and the discretization is performed in a second step.

6.4.2 Current Controller Design

For the dq -current controllers, a simple PI controller of the type

$$K_{\text{PI},c}(s) = k_{\text{p},c} + k_{\text{i},c} \frac{1}{s} \quad (6.16)$$

is sufficient, implemented as in **Fig. 6.10 (a)**. This can, e.g., be tuned with classical *loop shaping* methods [82]. The electrical plant considered is $G_{\text{c,tot}}(s) \approx G_{\text{c}}(s)$, i.e., the influence of the LC output filter and of the delays introduced by the power electronics are neglected. This is allowed, as for frequencies up to the targeted $\omega_{\text{c}} = 2\pi 600$ rad/s, $G_{\text{LC}}(s)$ and $G_{\text{PE}}(s)$ are both approximately equal to 1. As shown in the bode diagram of **Fig. 6.10 (b)**, the crossover frequency of the loop gain $L_{\text{c}}(s) = G_{\text{c}}(s) K_{\text{PI},c}(s)$ is set to the desired closed-loop bandwidth $\omega_{\text{c}} = 2\pi 600$ rad/s. The specified phase margin is $\phi_{\text{c}} = 50^\circ$ to guarantee a fast response, even at the cost of a slightly under-damped behavior, that is nevertheless tolerable by the system. The necessary PI gains for this design are reported in **Tab. 6.4**, both for the LA and the RA case.

The designed controller $K_{\text{PI},c}(s)$ is tested in simulation on an accurate model of the LiRA built in the software PLECS [83]. The results of the simulation are reported in **Fig. 6.11**. The assigned references are representative of typical operation: for the q -current a sine with amplitude $i_{\text{q,nom}} = 2$ A and frequency $f_{\text{op,max}} = 5$ Hz, whereas for the d -current a constant $i_{\text{d,ref}} = 0$ A. Note that while the q -current is correctly tracked, the d -current is not disturbed

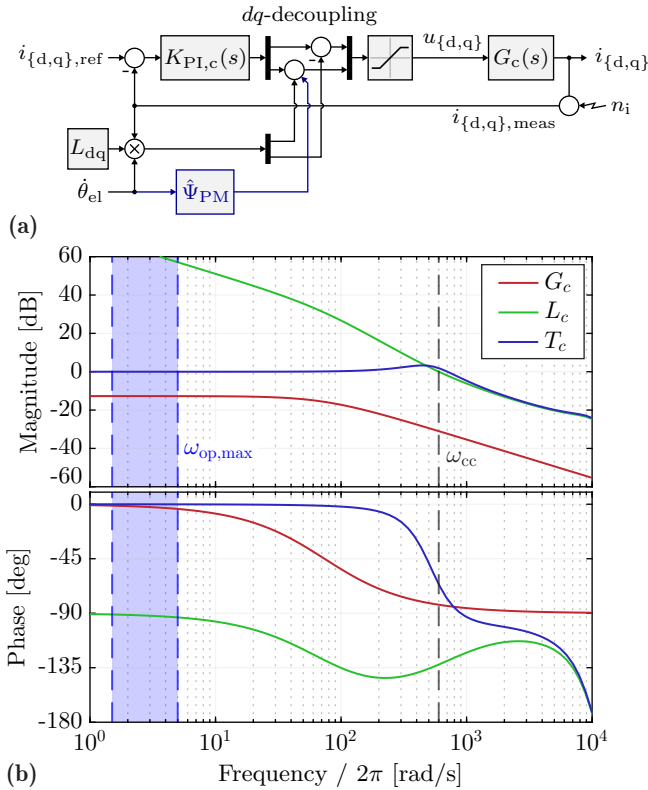


Fig. 6.10: (a) Closed-loop dq -current control block diagram, valid either for the LA or the RA electrical subsystems in the mover-oriented frame. The d - and q -voltages commanded by the PI controller $K_{PI,c}(s)$ are corrected with feed-forward components for proper decoupling of the d - and q - dynamics (cf. Fig. 6.8 (b)). (b) Bode plots of the current control loop (LA case): plant $G_c(s)$, loop gain $L_c(s)$ and complementary sensitivity $T_c(s)$.

and successfully kept to 0 A due to proper decoupling of the two current components. Furthermore, it can be seen that the q -voltage stays within the saturation limits $u_{\{d,q\},lim} = \pm 13$ V. To account for eventual voltage saturations, the integrator of the PI controller is implemented with an anti-windup scheme, using conditional integration [84].

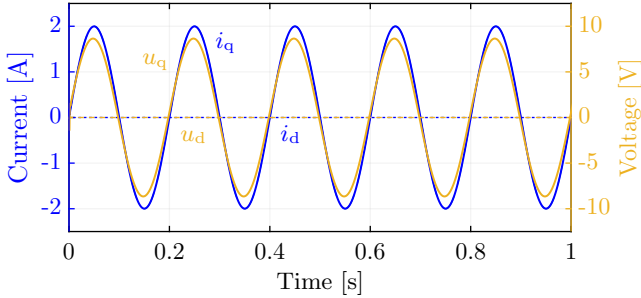


Fig. 6.11: dq -current control: simulated tracking response (PLECS [83], LA case) for the references $i_{q,\text{ref}} = 2 \text{ A} \sin(2\pi 5 t)$ and $i_{d,\text{ref}} = 0$, together with voltage commands $u_{\{d,q\}}$.

6.4.3 Linear/Axial Position Controller Design

For the z -position controller, derivative action is also needed to reach the targeted closed-loop bandwidth ω_z without prohibitively large gains. The PID controller is typically implemented in the form

$$K_{\text{PID},z}(s) = k_{p,z} + k_{i,z} \frac{1}{s} + k_{d,z} \frac{s}{\frac{1}{k_{f,z}} s + 1}, \quad (6.17)$$

i.e., with a first-order filter on the derivative term. This makes the derivative term proper and hence practically realizable. Furthermore, it beneficially reduces high-frequency noise introduced, e.g., by the measurement signals. Another option is to implement a *state observer*, which provides a smooth estimate of the axial translational speed \dot{z}_{est} to be used for the derivative action. Note that the dot notation ($\dot{\star}$) is used to indicate the time-derivative $d(\star)/dt$. The state observer can also provide a smooth estimate of the axial position z_{est} , which is used for control as well. As shown in the block diagram of **Fig. 6.12 (a)**, the control action (or force command) is then computed as

$$F_z = k_{p,z}(z_{\text{ref}} - z_{\text{est}}) + k_{i,z} \int (z_{\text{ref}} - z_{\text{est}}) dt + k_{d,z} (\dot{z}_{\text{ref}} - \dot{z}_{\text{est}}), \quad (6.18)$$

where z_{ref} is the reference position and \dot{z}_{ref} its time-derivative (that can be, e.g., pre-computed). The chosen state observer is a Luenberger observer, shown in the diagram of **Fig. 6.12 (b)** [85, 86]. In order to use the estimates z_{est} and \dot{z}_{est} for closed-loop control, they have to converge to the estimated values

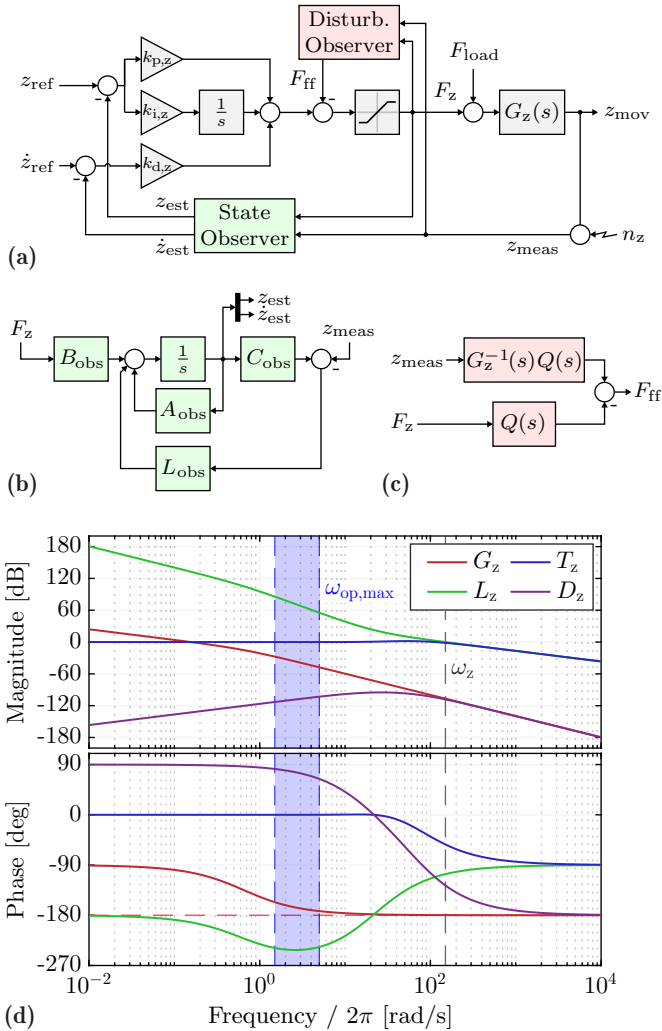


Fig. 6.12: (a) Closed-loop z-position control block diagram, employing a state observer and a disturbance observer. (b) Implemented Luemberger observer, estimating the linear position z_{mov} and speed \dot{z}_{mov} from the measured position z_{meas} and the force command F_z . (c) Implementation of the disturbance observer with the filter $Q(s)$ to perform the plant inversion of $G_z(s)$. (d) Bode plots of the linear position control loop: plant $G_z(s)$, loop gain $L_z(s)$, complementary sensitivity $T_z(s)$, and disturbance transfer $D_z(s)$.

reasonably fast with respect to the targeted bandwidth of the z -controller ω_z . Therefore, the poles of the observer should be placed on the left-half plane with a real (negative) part equal to or greater than about $5 \cdot \omega_z$.

The targeted control bandwidth $\omega_z = 2\pi 150$ rad/s is chosen to provide good reference tracking up to $\omega_{z,\text{ref}} = 2\pi 5$ rad/s (recall that the maximum operational frequency of the *ShuttlePump* is 5 Hz). For this purpose, $\omega_z/3 = 10 \cdot \omega_{z,\text{ref}} = 2\pi 50$ rad/s would already be sufficient. However, it is necessary to consider also the load force F_{load} , acting as a heavy input disturbance to the system. As visible from **Fig. 6.5 (b)**, this has a fundamental component with frequency $\omega_{z,\text{dist}} = \omega_{z,\text{ref}}$ (i.e., the same as the reference), but a rather large amplitude $\tilde{F}_{\text{load}} = 33$ N. The larger the control bandwidth, the better the disturbance due to F_{load} is rejected. Therefore, the PID z -controller is tuned with $\omega_z = 2\pi 150$ rad/s and a phase margin $\phi_z = 30^\circ$ using the `pidtune` command in MATLAB, with the gains indicated in **Tab. 6.4**. The corresponding Bode plots are shown in **Fig. 6.12 (d)**. In particular, the disturbance transfer

$$D_z(s) = \frac{G_z(s)}{1 + G_z(s) \tilde{K}_{\text{PID},z}(s)} \quad (6.19)$$

can be used to study the disturbance rejection capabilities of the control loop. Assuming the load force consists solely of its fundamental component, i.e., $F_{\text{load}} = \tilde{F}_{\text{load}} \sin(2\pi \omega_{z,\text{dist}} t)$, the disturbance response would have an amplitude $z_{\text{dist}} = |D_z(j \omega_{z,\text{ref}})| \cdot \tilde{F}_{\text{load}} = 0.21$ mm, which is adequately small.

The disturbance rejection can be further enhanced with a feed-forward component F_{ff} on the force command that compensates F_{load} . One option is to preprogram $F_{\text{ff}} \approx F_{\text{load}}$ according to, e.g., the results of the CFD simulations. Ideally, if F_{load} was perfectly predicted, it could be completely compensated. Nevertheless, this is hardly the case due to the nature of the hydrodynamic forces acting on the piston. If F_{ff} is substantially incorrect, it could lead to even worse reference tracking results compared to the case when it is not added at all. This can happen under certain circumstances and operating conditions, like, e.g., for a reduced/increased head pressure, and hence load force. A more advanced option is to implement a *disturbance observer* (DOB) [87–89]. Similarly to the state observer, this exploits the model of the plant $G_z(s)$ to calculate an estimate F_{dob} of the load force F_{load} . The disturbance observer is implemented as in **Fig. 6.12 (c)**. In order to invert the plant $G_z(s)$, it is necessary to introduce a filter term

$$Q(s) = \left(\frac{\omega_{\text{dob}}}{s + \omega_{\text{dob}}} \right)^q \quad (6.20)$$

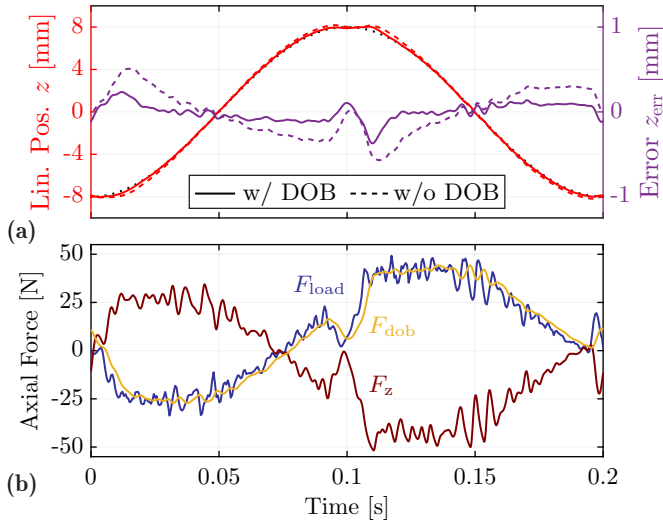


Fig. 6.13: (a) Linear position control, simulated reference tracking (PLECS): response and tracking error with (solid line) and without (dashed line) disturbance observer feedforward. (b) Linear position control, simulated reference tracking (PLECS): corresponding load/disturbance force F_{load} , force command F_z , and observed force F_{dob} .

with order q , chosen such that $G_z^{-1}(s)Q(s)$ is proper. For the case at hand, $q = 2$. The cutoff frequency ω_{dob} should be on one hand large enough to provide good tracking of the disturbance F_{load} , but, on the other hand, not too large to avoid introducing noise in the feedback loop. In the case at hand, $\omega_{dob} = 2\pi 100$ rad/s is selected.

The controller is tested in the PLECS model and the simulation results are shown in **Fig. 6.13 (a)** and **(b)**. To better visualize the details, only one period of the 5 Hz operation is shown. **Fig. 6.13 (a)** shows successful tracking of the sinusoidal reference with amplitude $z_{strk} = 8$ mm, and the corresponding tracking error z_{err} . Two cases are simulated, namely with and without disturbance observer used as feedforward compensation. Without disturbance observer, z_{err} is already below the specified boundaries, with a maximum absolute error $z_{err,max} = \max(|z_{err}|) = 0.57$ mm. The disturbance observer helps reduce the tracking error to an absolute maximum of $z_{err,max} = 0.37$ mm. The corresponding force command F_z is reported in **Fig. 6.13 (b)**, and it is

compared to the disturbance load force F_{load} . To effectively compensate it, the force command F_z uses the force F_{dob} estimated by the disturbance observer, which closely captures F_{load} .

6.4.4 Rotary/Angular Position Controller Design

For the φ -position controller, it is possible to follow analogous design considerations as for the presented z -position controller. The block diagram of the control loop is shown in **Fig. 6.14 (a)**. Also in this case a derivative term is needed and provided by a Luenberger state observer for the rotary dynamics, in the same form seen in **Fig. 6.12 (b)**. The targeted bandwidth is $\omega_\varphi = 2\pi 80$ rad/s, chosen to track the ramp reference φ_{ref} with a slope of $2\pi 5$ rad/s. The controller is again tuned with the aid of the `pidtune` command in MATLAB, the selected phase margin is $\phi_\varphi = 40^\circ$ and the necessary gains can be found in **Tab. 6.4**. The corresponding Bode plots are shown in **Fig. 6.14 (b)**. This time, the main disturbance to the system is the cogging torque M_{cogg} . Its effect is not as severe as the load force disturbing the z -controller. Therefore, with the chosen bandwidth, M_{cogg} is already largely attenuated, and no special disturbance rejection measure is taken. Optionally, it would be possible to introduce a preprogrammed feed-forward torque component $M_{\text{ff}} \approx M_{\text{cogg}}$ [90, 91]. In fact, the profile of the cogging torque is well-known from the Finite Element Method (FEM) simulations of the RA (more accurately than what CFD simulations would predict for F_{load}).

The results of a PLECS simulation are shown in **Fig. 6.15 (a)** and **(b)**. As expected from the *system type* of the loop gain (that contains one integrator), the ramp reference φ_{ref} can be tracked very tightly (ideally with zero steady-state error). The tracking error φ_{err} in **Fig. 6.14 (c)**, not larger than $\varphi_{\text{err,max}} = \max(|\varphi_{\text{err}}|) = 0.57^\circ$, is then caused by the disturbance M_{cogg} . In particular, **Fig. 6.15 (b)** shows how the torque command M_z counters the cogging torque M_{cogg} , but reaches its saturation limits. During the intervals while the control action is saturated, the tracking error is the largest. Nevertheless, this is not of concern, as φ_{err} is way within the specified boundaries (cf. **Tab. 6.3**).

6.4.5 Controller Discretization

Once the design in continuous time is completed, the controllers need to be discretized for digital implementation. The execution frequency (or reciprocally time) of each controller $f_{\text{ex}} = 1/T_{\text{ex}}$ is indicated in **Tab. 6.4**. Given that the execution frequencies are much larger than the chosen control bandwidths,

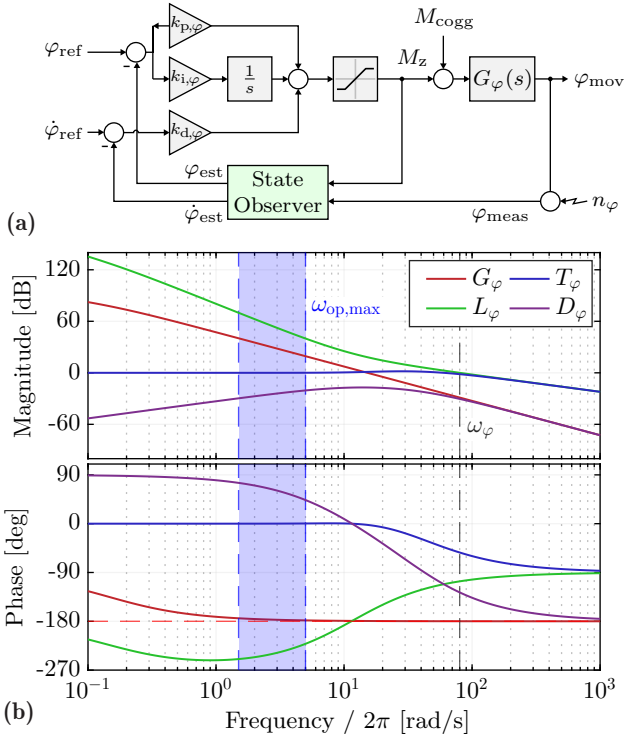


Fig. 6.14: (a) Closed-loop φ -position control block diagram, employing a state observer. (b) Bode plots of the rotary position control loop: plant $G_\varphi(s)$, loop gain $L_\varphi(s)$, complementary sensitivity $T_\varphi(s)$, and disturbance transfer $D_\varphi(s)$. (c) Simulated reference tracking (PLECS): response and tracking error. (d) Simulated reference tracking (PLECS): corresponding cogging/disturbance torque M_{cogg} and torque command M_z .

the mapping used is the *Forward-Euler*, for which the gains are adapted as $k_{p,\text{disc}} = k_{p,\text{cont}}$, $k_{i,\text{disc}} = k_{i,\text{cont}} \cdot T_{\text{ex}}$, and $k_{d,\text{disc}} = k_{d,\text{cont}} \cdot f_{\text{ex}}$.

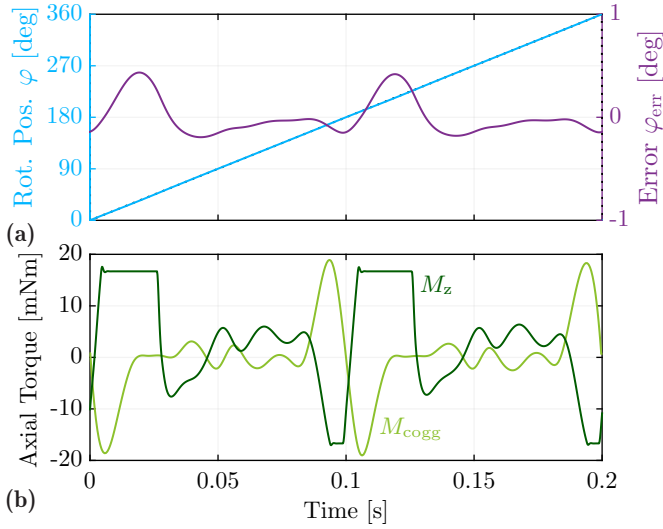


Fig. 6.15: (a) Rotary position control, simulated reference tracking (PLECS): response and tracking error. (b) Rotary position control, simulated reference tracking (PLECS): corresponding cogging/disturbance torque M_{cogg} and torque command M_z .

Tab. 6.4: Chosen controller gains/parameters and execution frequencies.

	Linear Position z		Rotary Position φ	
k_p	$6.18 \cdot 10^4$	N/m	7.80	N m/rad
k_i	$4.24 \cdot 10^6$	N/(m s)	$2.83 \cdot 10^2$	N m/(rad s)
k_d	$2.25 \cdot 10^2$	N s/m	$5.37 \cdot 10^{-2}$	N m s/rad
l_{11}	$9.89 \cdot 10^3$	1/s	$5.28 \cdot 10^3$	1/s
l_{12}	$2.44 \cdot 10^7$	1/s ²	$6.94 \cdot 10^6$	1/s ²
f_{ex}	10	kHz	10	kHz
	LA dq -Current		RA dq -Current	
k_p	$2.41 \cdot 10^1$	V/A	$3.16 \cdot 10^1$	V/A
k_i	$9.76 \cdot 10^4$	V/(A s)	$1.63 \cdot 10^5$	V/(A s)
f_{ex}	20	kHz	20	kHz

6.5 Hardware Implementation

This section presents the hardware PCB prototype of the inverter and control unit on which the designed and discretized controller is implemented. Furthermore, the experimental assembly of the LiRA and the custom test bench used for measurements are described.

6.5.1 Inverter and Control Unit

The six-phase inverter unit and the digital control unit are implemented together on a single, compact PCB (\varnothing 54 mm), shown in **Fig. 6.16 (b)**. The inverter unit consists of two identical parts, each based on the *MP6536* integrated inverter module from *Monolithic Power Systems*. This is selected as it conveniently offers a three-phase inverter of adequate power level together with integrated gate drivers in a single 5-by-5 mm chip. The IC can be operated with a DC-link voltage up to $U_{\text{DC,max}} = 26$ V, which is the finally selected value U_{DC} . The maximum phase current is 5 A and the on-state resistance of the power MOSFETS is $R_{\text{ds,on}} = 240$ m Ω . For the first animal tests, the inverter and control unit will be extracorporeal. Therefore, as illustrated by **Fig. 6.16 (a)**, a long (approx. 2 m) percutaneous driveline is needed to realize the connection with the implanted *ShuttlePump*. In order to prevent signal reflections along the driveline and unwanted disturbances to the sensors due to the inverter's switching frequency, it is necessary to utilize *LC* filters at the output of the inverter modules. The value of the filter inductor L_f is selected together with the switching frequency f_{sw} to guarantee a certain worst-case peak-to-peak inductor current ripple

$$\Delta i_{L_f,\text{max}} = \frac{U_{\text{DC}}}{4 f_{\text{sw}} L_f} < 0.3 \text{ A.} \quad (6.21)$$

As the inductor volume scales with L_f , for a compact realization the highest possible f_{sw} is used, which for the *MP6536* is $f_{\text{sw}} = 1$ MHz. The needed inductance is then $L_f = 22$ μ H. The cutoff frequency of the *LC* filter is accordingly placed two decades lower, i.e., $f_{\text{LC}} = 10^{-2} \cdot f_{\text{sw}} = 10$ kHz, by using $C_f = 10$ μ F. The damping resistor is $R_f = 2$ Ω . For current control, two in-line phase current measurements per module are used. These are based on the voltage drop u_{sh} over a $R_{\text{sh}} = 30$ m Ω shunt resistor, which is then amplified by a current sense amplifier with gain $H_{\text{csa}} = 20$ V/V (*MAX40056TAUA+*). The amplified voltage is sampled by an ADC with 10 bits and 5 V analog input

range, giving a current measurement resolution

$$i_{\text{res}} = \frac{1}{R_{\text{sh}} H_{\text{csa}}} \frac{5 \text{ V}}{2^{10}} = 8.1 \text{ mA}. \quad (6.22)$$

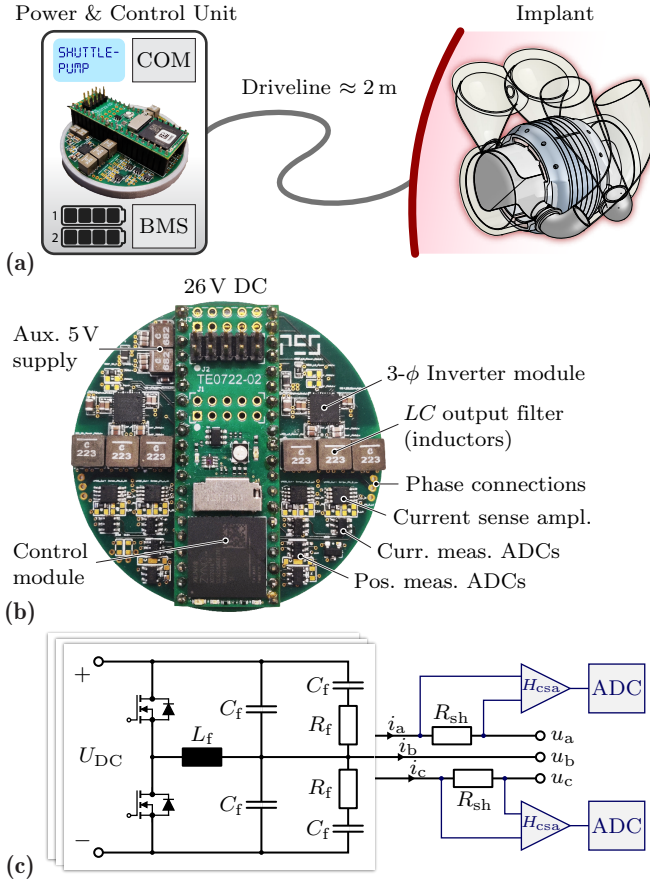


Fig. 6.16: (a) Overall *ShuttlePump* TAH system. The power and control unit hosting the inverter, the battery pack and the communication interface is connected to the implanted pump via a percutaneous driveline. (b) Realized inverter board and its components. The diameter of the PCB is 54 mm. (c) Circuit schematic of one phase of the three-phase inverter with LC output filter and in-line current measurements with shunt resistors on two phases.

The same ADCs are also used for the position sensor signals and are placed on the bottom part of the board. Finally, the core of the control unit is the *TE-0722* module by *Trenz Electronic*, with the *AMD/Xilinx Zynq 7010* system on chip. The current and position controllers are executed by the processing unit, whereas the low-level hardware I/O interfaces (PWM modulator, ADCs, etc.) are implemented in the FPGA.

6.5.2 Experimental Test Bench

Fig. 6.17 (a) shows the custom experimental test bench used to verify the functionality of the designed linear-rotary position controller. On the left side of the test bench, there is the complete test assembly of the *ShuttlePump* LiRA. As visible from the sectional view of **Fig. 6.17 (b)**, the piston of the *ShuttlePump* is replaced with a simplified structure holding together the mover of the LiRA and the semi-circular copper sensor targets through an aluminum shaft. At each side of the stator of the LiRA, there is a round lid made of POM with a center hole, through which the aluminum shaft can be inserted and slid with low friction. This way, the mover is held radially centered with respect to the stator and can still perform linear-rotary motion. This bearing system is a simplified mechanical alternative to the foreseen hydrodynamic journal bearing. In addition, the aluminum shaft facilitates the mechanical coupling of the LiRA with an external axial load. For this purpose, also a special version of the sensor is realized, with a 12 mm hole at the center of the PCB, visible in **Fig. 6.17 (c)**.

On the right side of the test bench, there is a linear test motor (*LinMot P501-23x80-HP* [92]) that can be used as a controllable axial load. The linear test motor is mounted on a vertical positioning stage to adjust its alignment with the LiRA. As the slider of the linear test motor can be freely rotated inside its stator without affecting its operation/linear force generation, it could be directly coupled to the mover of the LiRA. However, to rotate both elements and overcome the additional friction the RA would be overloaded. Therefore, a custom linear coupling is realized, which allows free rotation of the mover while transmitting the axial force generated by the linear motor. As visible from **Fig. 6.17 (c)** (dismounted coupling), this features a rotary ball bearing to minimize the frictional torque. The chosen driver for the test linear motor (*LinMot B1100-VF* [93]) allows force(/current) control operation with an external custom reference, which can, e.g., be programmed to emulate the realistic CFD load force profile of **Fig. 6.5 (b)**.

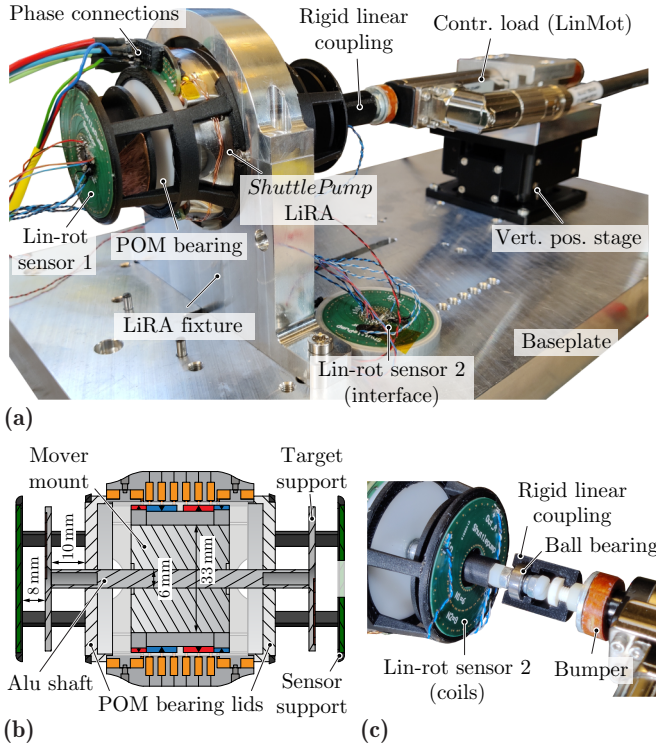


Fig. 6.17: (a) Experimental test bench used to commission the linear-rotary position controller of the *ShuttlePump* LiRA. This is coupled with a custom linear coupling to a linear motor (*LinMot* [92]), used as a controllable axial load. (b) Cross-sectional view of the *ShuttlePump* LiRA with a simplified mechanical bearing system. The mover is fixed to an aluminum shaft, which is held by two side bearing lids made of POM. (c) Replacement version of the sensor with a 12 mm hole, to allow coupling the mover of the *ShuttlePump* to the controllable axial load. The realized custom linear coupling integrates a rotary ball bearing.

6.6 Experimental Measurements and Verification

This section presents the experimental measurements demonstrating the operation of the complete LiRA system of the *ShuttlePump*, with simultaneous linear-rotary position control. The linear and rotary position signals, as well as the q -currents and q -voltages are recorded internally by the control unit after a preliminary calibration round for each quantity. In particular, the calibration of the linear position sensor is performed with the aid of the linear motor (in servo-mode).

6.6.1 Linear-Rotary Position Control: Tracking with No Load

The measurements for no load operation are reported in **Fig. 6.18**. Note that in this case the *ShuttlePump* is mechanically decoupled from the controllable load. As expected, the linear position z_{mov} tracks the specified reference z_{ref} closely (cf. **Fig. 6.18 (a)**), with a maximum absolute error as low as $z_{\text{err,max}} = 0.38$ mm. For this case, a relatively small force F_z is commanded, as it can be seen from the q -current $i_{q,z}$ in **Fig. 6.18 (b)**. The distinguishable positive and negative q -voltage and q -current peaks occur in correspondence of the linear position zero-crossings, i.e., around $z_{\text{mov}} = 0$. It should be noted that, around those instants, there is the transition from the measurement signal of one sensor to the other to calculate z_{mov} (cf. **Appendix C**). It could be observed experimentally that this transition is delicate, and introduces a slight measurement disturbance in both linear and rotary position measurements. Simultaneously, the rotary position φ_{mov} tracks its reference φ_{ref} with a maximum absolute error $\varphi_{\text{err,avg}} = 4.7^\circ$. Therefore, φ_{err} is always kept within the $\pm 5^\circ$ error tolerance band, especially during the inlet/outlet opening/closing phases, highlighted with shaded boxes in **Fig. 6.18 (c)**. The torque-generating current $i_{q,\varphi}$ exhibits a ripple indicating that the cogging torque is being compensated. Part of this ripple is caused by the measurement disturbance introduced by the aforementioned post-processing sensor transition. The average of the current is $i_{q,\varphi,\text{avg}} = 0.22$ A, which corresponds to about 7.4 mNm. This is the residual friction that is still present after careful manufacturing of the contacting parts. However, in the actual application, this is substantially lower. Therefore, the fact that it is possible to keep φ_{err} within the specified boundaries even for such high friction is a remarkable result.

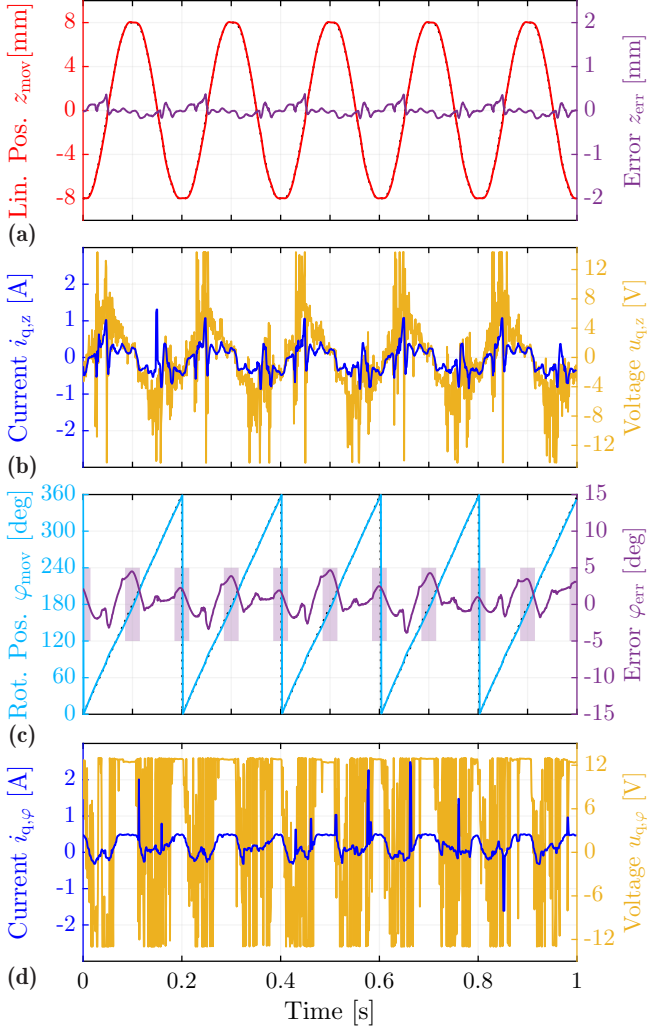


Fig. 6.18: Linear-rotary position tracking measurements with no load, for $f_{\text{op}} = 5$ Hz. **(a)** Linear position z_{mov} and tracking error z_{err} . **(b)** Linear q -current $i_{q,z}$, with the corresponding voltage command $u_{q,z}$. **(c)** Rotary position φ_{mov} and tracking error φ_{err} . The $\pm 5^\circ$ error tolerance band during the inlet/outlet opening/closing phases is indicated with shaded boxes. **(d)** Rotary q -current $i_{q,\varphi}$, with the corresponding voltage command $u_{q,\varphi}$.

6.6.2 Linear-Rotary Position Control: Tracking with Axial Load

For this set of measurements, the *ShuttlePump* is coupled to the controllable load via the custom linear coupling (cf. **Fig. 6.17 (c)**). The force reference for the test motor F_{comm} is programmed to be exactly the same as the force F_{load} of **Fig. 6.5 (b)**, obtained from the CFD simulations. To guarantee the correct synchronization between the linear-rotary position controller commands and the controllable load, F_{comm} is sent from the inverter board to the *LinMot* driver. Before proceeding with measurements, it is verified that the force delivered by the controllable load is correct, i.e., that it tracks the reference F_{comm} . For this purpose, a force sensor is mounted at the coupling location between the *ShuttlePump* LiRA and the linear test motor. The used sensor is the miniature tension/compression load cell *Burster 8417*. Its voltage output is amplified with an instrumentation amplifier to facilitate reading on the oscilloscope. The measured force F_{meas} is compared to the force reference F_{comm} in **Fig. 6.19**, where it can be seen that they are in good agreement. The sensor is subsequently removed to shorten the length of the coupling between the LiRA and the test motor.

The measurements for linear-rotary position tracking with axial load are reported in **Fig. 6.20**. In this first case, the disturbance observer is disabled. The linear position reference is still adequately tracked under the heavy load disturbance (cf. **Fig. 6.20 (a)**). Clearly, this time the tracking error z_{err} is larger with respect to the no-load case, up to a maximum of $z_{\text{err,max}} = 1.96$ mm. This peak, however, does not occur during the critical plateau phase. The reaction of the controller countering the disturbance force is

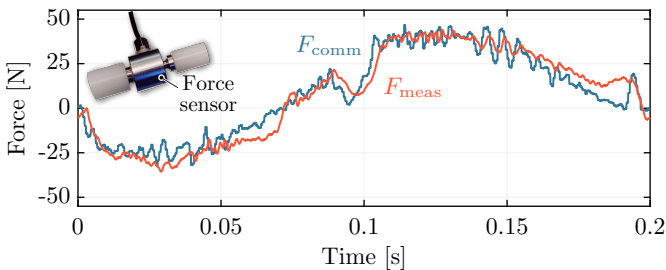


Fig. 6.19: Verification of the force delivered by the controllable load. The force F_{meas} , measured by the load cell placed at coupling between the two motors, is compatible with the commanded force F_{comm} .

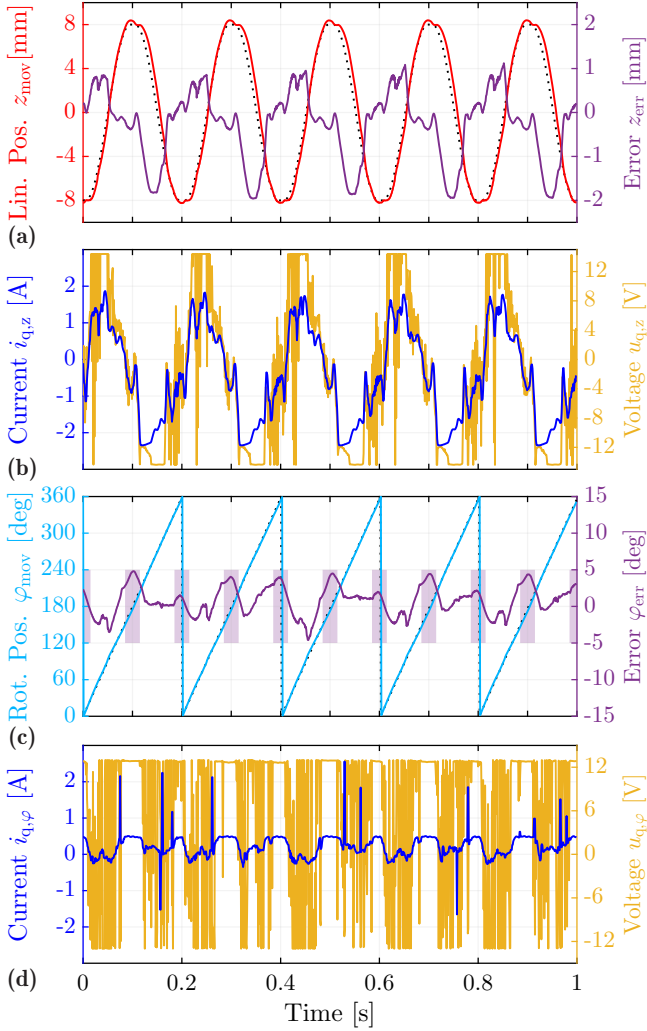


Fig. 6.20: Linear-rotary position tracking measurements with full axial load and no disturbance observer in feedforward, for $f_{\text{op}} = 5$ Hz. **(a)** Linear position z_{mov} and tracking error z_{err} . **(b)** Linear q -current $i_{q,z}$, with the corresponding voltage command $u_{q,z}$. **(c)** Rotary position φ_{mov} and tracking error φ_{err} . The $\pm 5^\circ$ error tolerance band during the inlet/outlet opening/closing phases is indicated with shaded boxes. **(d)** Rotary q -current $i_{q,\varphi}$, with the corresponding voltage command $u_{q,\varphi}$.

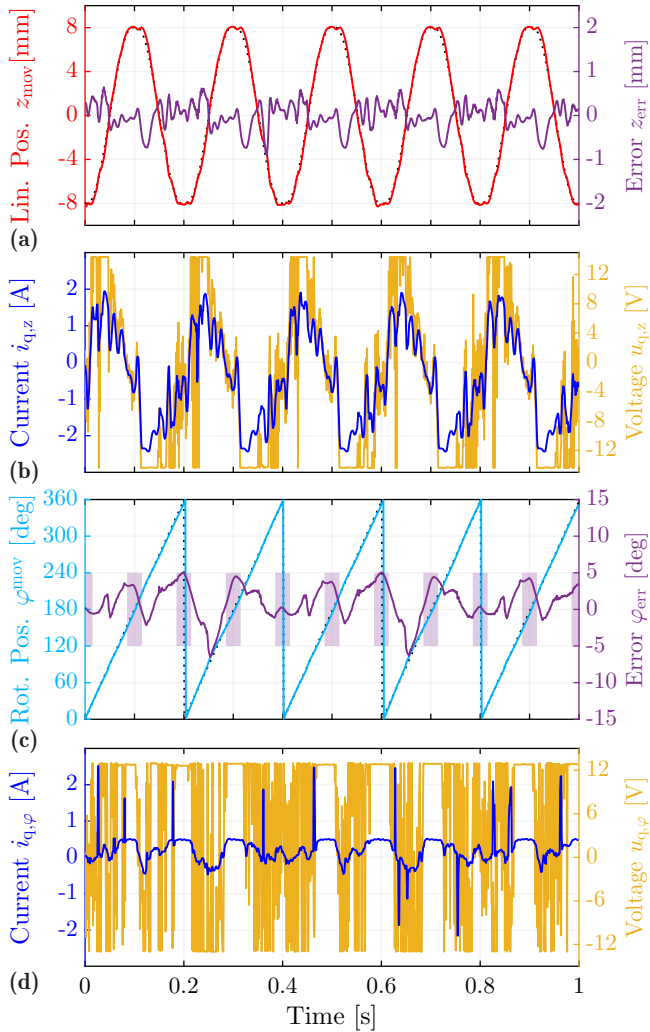


Fig. 6.21: Linear-rotary position tracking measurements with full axial load and disturbance observer enabled in feedforward, for $f_{op} = 5$ Hz. **(a)** Linear position z_{mov} and tracking error z_{err} . **(b)** Linear q -current $i_{q,z}$, with the corresponding voltage command $u_{q,z}$. **(c)** Rotary position φ_{mov} and tracking error φ_{err} . The $\pm 5^\circ$ error tolerance band during the inlet/outlet opening/closing phases is indicated with shaded boxes. **(d)** Rotary q -current $i_{q,\varphi}$, with the corresponding voltage command $u_{q,\varphi}$.

reflected in the commanded q -current $i_{q,z}$, which reaches peaks around ± 2 A (cf. **Fig. 6.20 (b)**), corresponding to about 46 N. The rotary position tracking is substantially unchanged, and the error φ_{err} is kept within the targeted $\pm 5^\circ$ band.

Finally, with the disturbance observer enabled, the measurements of **Fig. 6.21** are obtained. The main advantage is that the maximum linear tracking error is now reduced to $z_{\text{err,max}} = 0.89$ mm, and hence the $z_{\text{err,max}} = 1$ mm specification is always met.

6.7 Summary

The operation of the blood pumps used as (left) ventricular assist devices or Total Artificial Hearts (TAHs) substantially relies on feedback control of their impeller's speed and/or position. For the novel implantable TAH *ShuttlePump*, this is especially the case due to its operating principle, which requires synchronized linear-rotary position control of its specially-shaped piston. The control system designed in this chapter on a detailed electromagnetic model of the Linear-Rotary Actuator (LiRA), and subsequently implemented in a hardware demonstrator system is suitable to operate the *ShuttlePump*. The experimental results demonstrate that the specified linear-rotary motion profile can be tracked with an accuracy below 1 mm and 5° up until 5 Hz of operation even under the heavy axial load disturbance (45 N peak) introduced by the required hydraulic forces for pumping operation. The complete drive system can hence be reliably used in further experiments *in vitro* (i.e., with a dedicated hydraulic test bench) and *in vivo* (i.e., with implantation in animal models) to validate the predicted fluid-dynamic and clinical characteristics of the blood pump.

7

Eddy-Current Position Sensor Through Conductive Barriers

The content of this chapter is also published in:

- ▶ **R. V. Giuffrida**, S. Mirić, J. W. Kolar, and D. Bortis, “Highly Dynamic Eddy-Current-Based Sealed Magnetic Bearing Position Measurement with Temperature Drift Correction - “Seeing Through Conductive Walls”,” *IEEE Open Journal of the Industrial Electronics Society*, vol. 3, pp. 252-264, April 2022.
- ▶ **R. V. Giuffrida**, S. Mirić, D. Bortis, and J. W. Kolar, “Looking Through Walls – Actuator Position Measurement Through a Conductive Wall,” in *Proc. of the 23rd International Conference on Electrical Machines and Systems (ICEMS)*, Hamamatsu, Japan, November 2020.

Chapter Abstract

This chapter investigates the design of an Eddy-Current Sensor (ECS) for position measurement of a moving conductive target located behind a fixed conductive shielding surface. Such a sensor can, e.g., be used in completely sealed actuators with magnetically levitated rotor or mover for high purity applications. Starting from the analysis of the sensor’s operating principle, the design of the excitation coil, the achievable sensitivity and bandwidth as well as the temperature stability of the sensor are investigated. Subsequently, a suitable sensor interface, consisting of the driving and signal conditioning electronics, is selected. With this it is possible to distinguish between position and temperature variations, for which the optimal operational frequencies are identified. The results are finally verified with measurements on a hardware sensor prototype, showing that the ECS can achieve a sensitivity of 1 mV/ μm , a position resolution of 1 μm , with a measurement bandwidth of 30 kHz and can hence be used to capture the mover’s position in an active magnetic bearing feedback control structure.

7.1 Introduction

In many industrial applications, contactless position sensing of an object is of primary importance. In the case of a conductive object, a popular choice is Eddy-Current Sensors (ECSs), which, due to their non-contact nature, offer a clear advantage over, e.g., resistive or capacitive sensors [94, 95]. Moreover, ECSs can also operate under harsh conditions, dirty environments or in vacuum, which makes them applicable for Magnetic Bearings (MBs) of magnetically levitated actuator systems [80, 96–98], where the ECSs located on the stator are used to capture the position of the levitated mover (cf. **Fig. 7.1 (a)**). ECSs are also extensively used in Non-Destructive Testing (NDT) for inspection of damages on the surface of conductive materials [99]. There are also applications where the moving conductive target is located behind another conductive material. For example, in entirely sealed actuator systems used for high purity food, medical, or chemical applications, the stator and the magnetically levitated mover are fully encapsulated with, e.g., a stainless steel housing (cf. **Fig. 7.1 (b)**). Consequently, the ECS located on the stator has to measure the mover position through the stator housing, which due to its conductivity highly degrades the magnetic coupling between excitation and/or pick-up coil and the mover, and in turn leads to a reduction of the measurement sensitivity, i.e., the mover's position accuracy. As a further challenge, the sensor is expected to operate under different temperature conditions, as high as 100 °C due to ohmic losses in the stator. Therefore, it is important to study the sensor's stability with respect to temperature sensitivity, to prevent the magnetic bearings from failing due to thermal drift of the measured mover's position. In contrast to other magnetic sensors as, e.g., Hall effect sensors, which can also be used to estimate the mover's position through the stator's housing exploiting the magnetic field of the mover's permanent magnets, ECSs typically provide higher resolution, thermal stability and immunity to external disturbing magnetic fields [95, 96]. In the literature [100], such an ECS measuring through a conductive wall is, e.g., used for periodical inspections of nuclear power plants by measuring the distance between two conductive tubes. There, a commercial ECS is used, with excitation frequencies up to 16 kHz, which for stationary applications are clearly sufficient. However, for highly dynamic position measurements in entirely sealed MBs, this could result in a too low measurement bandwidth. For instance, in very-high-speed magnetically levitated machines, position control bandwidths up to 1 kHz are needed [101]. Consequently, sensor measurement bandwidths of at least 10 kHz have to be achieved [80, 96], which in

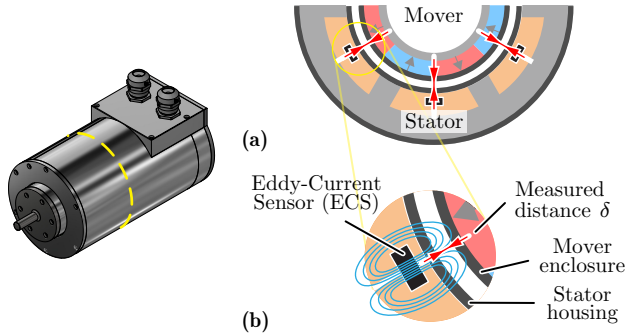


Fig. 7.1: 3D-view of a magnetically levitated rotary-linear actuator system with (a) corresponding cross section showing the placement of the Eddy-Current Sensors (ECSs) inside a sealed stator. (b) Detail of the sealed actuator with the used ECS, which has to measure the mover's position through the conductive stator housing.

Tab. 7.1: ECS specifications defined by the underlying application.

Parameter	Value	Unit
Measurable Distance δ	0 ...2	[mm]
Sensor Resolution	1 ...10	[μm]
Sensor Bandwidth f_{bw}	> 10	[kHz]
Max. ECS Coil Diameter d_c	11.5	[mm]
Enclosure Thickness (Stator and Mover)	0.2 ...0.5	[mm]
Enclosure Material (Stator and Mover)	Stainless Steel	

turn leads to roughly 10 times higher excitation frequencies of about 100 kHz. Importantly, however, it has also to be considered that above a certain excitation frequency, defined by the material properties and dimensions of the conductive wall, the skin and proximity effects of this intermediate layer start to play an important role, leading in the worst case to a complete loss of any mover position information. Consequently, the ECS's excitation frequency has to be selected properly, such that on one hand a sufficient position sensor bandwidth is achieved and, on the other hand, the position sensitivity is not compromised too much by the intermediate conductive layer.

This chapter presents and discusses the design of an ECS capable of measuring through conductive walls. In particular, the ECS is used as a position sensor for entirely sealed actuator systems with a magnetically levitated

mover, targeting the specifications of **Tab. 7.1**. In the first part of the chapter, the operating principle of the conventional ECS is briefly summarized in **Sec. 7.2** and used to analyze the ECS measuring through the walls in **Sec. 7.3**. The analysis not only aims to provide an understanding of the proposed ECS concept but also to offer design guidelines and an optimal design procedure for the excitation coil, i.e., the sensor head. For this purpose, an equivalent transformer model is introduced, whose circuit elements (impedances) are calculated analytically depending on the coil geometry and material properties. Furthermore, the model is validated by comparison with FEM simulations and measurements on the optimally-designed excitation coil. Afterwards, in **Sec. 7.4** the temperature's influence on the coil impedance is investigated and quantified, in order to propose a method to measure and/or compensate it. In the second part of the chapter, the practical problem of selecting a sensor interface with appropriate signal conditioning, which finally provides a measurable voltage signal, is addressed. This explicitly takes into account the influence of temperature on the sensor's output, finally providing a way of measuring both position and temperature, as described in detail in **Sec. 7.5**. The concept is verified in **Sec. 7.6** with a hardware sensor prototype (head and interface) on which experimental measurements are performed. Finally, **Sec. 7.7** concludes the chapter.

7.2 Operating Principle of the Conventional ECS

In general, as shown in **Fig. 7.2 (a)** for a simplified planar structure, a single-coil ECS consists of a *stationary excitation coil* which is placed at a certain distance δ from a *moving target* with specific conductivity σ_t , relative permeability $\mu_{r,t}$ and thickness d_t . Since in many applications a paramagnetic material, e.g., stainless steel, copper, or aluminum, is selected for the target, in the following a permeability of $\mu_{r,t} \approx 1$ is assumed. The coil is excited with a high-frequency AC current, generating a surrounding magnetic field H_c which also penetrates the moving target. The high-frequency magnetic flux is linked by the target and induces a voltage in it, causing eddy currents to circulate due to the target's conductivity σ_t . In turn, the eddy currents generate a secondary magnetic field H_t counteracting the primary magnetic field of the coil. For a fixed excitation frequency and given material properties of the target, the intensity of this interaction, i.e., the magnetic coupling between coil and target, depends solely on the distance δ . For a single-coil

ECS configuration, this finally reflects into a measurable change of the coil's input impedance $Z_{c,\text{in}}(\omega, \delta)$. Hence, by knowing the relation between δ and the variation of the coil's input resistance and/or inductance, the position of the target is accurately measurable. Instead of using $Z_{c,\text{in}}(\omega, \delta)$, in a dual-coil ECS configuration a second stationary *pickup coil* is used, where a distance-dependent induced voltage is measured. The presented analysis is conducted only for the single-coil ECS configuration. The findings are directly applicable to the dual-coil case, since the induced voltage variation is directly related to the inductance variation.

7.2.1 Equivalent Transformer Model

For a conventional ECS (*without* intermediate shield), a convenient way of describing the variations of $Z_{c,\text{in}}(\omega, \delta) = R_{c,\text{in}}(\omega, \delta) + j\omega L_{c,\text{in}}(\omega, \delta)$ is the *transformer model* in **Fig. 7.2 (b)**, where R_c and L_c are the (DC) resistance and inductance of the excitation coil, R_t and L_t are the resistance and inductance of the target, ω is the angular excitation frequency and $M_{ct} = k_{ct}\sqrt{L_c L_t}$ the mutual inductance between coil (*c*) and target (*t*), with the coupling factor $k_{ct}(\omega, \delta)$. Note that both the mutual inductance $M_{ct}(\omega, \delta)$ and the coupling factor $k_{ct}(\omega, \delta)$ depend on the angular frequency ω and the distance δ . The measurement sensitivity is proportional to the variation of the coil's input impedance $Z_{c,\text{in}}$, which can be split into an equivalent input resistance $R_{c,\text{in}}$ and inductance $L_{c,\text{in}}$, which according to the equivalent model are expressed as

$$R_{c,\text{in}}(\omega, \delta) = R_c + \frac{\omega^2 M_{ct}^2}{R_t^2 + \omega^2 L_t^2} R_t = R_c + R_{c,\text{var}}(\omega, \delta), \quad (7.1)$$

$$L_{c,\text{in}}(\omega, \delta) = L_c - \frac{\omega^2 M_{ct}^2}{R_t^2 + \omega^2 L_t^2} L_t = L_c + L_{c,\text{var}}(\omega, \delta). \quad (7.2)$$

For low angular frequencies ω , the variable parts $R_{c,\text{var}}(\omega, \delta)$ and $L_{c,\text{var}}(\omega, \delta)$ vanish, and a distance-independent impedance $Z_{c,\text{in}} = R_c + j\omega L_c$ given by the coil's resistance and self-inductance is measured. In order to obtain significant variations in $R_{c,\text{in}}$ and $L_{c,\text{in}}$ with the air gap length δ , the excitation frequency has to be selected above a *coupling-independent* angular cutoff frequency

$$\omega_{\text{co}} = 2\pi f_{\text{co}} = \frac{R_t}{L_t}, \quad (7.3)$$

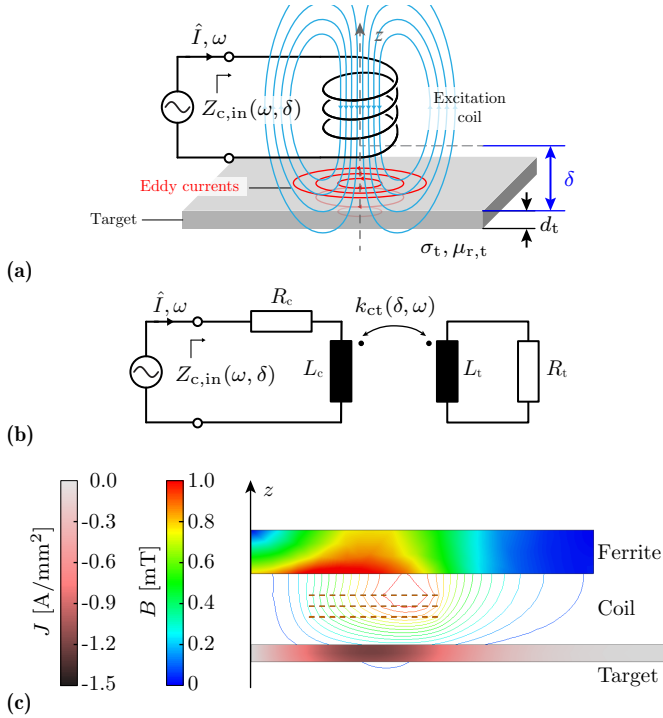


Fig. 7.2: (a) Structure of a conventional planar single-coil ECS to measure the distance δ between the stationary excitation coil and the moveable target. (b) Transformer equivalent circuit for the conventional ECS (without intermediate shield) with coil and target self-inductances L_c and L_t as well as the frequency- and distance-dependent coupling factor $k_{ct}(\omega, \delta)$. (c) ECS arrangement used for the axisymmetrical 2D FEM simulations (ANSYS Maxwell) with exemplary field and current distribution for a 0.5 mm stainless steel target at an excitation frequency of $f_{exc} = 430$ kHz.

which can be found as the frequency for which $R_{c,in}$ and $L_{c,in}$ experience half of their total variations

$$R_{c,var}(\omega \rightarrow \infty, \delta) = \left(\frac{M_{ct}}{L_t} \right)^2 R_t = k_{ct}(\omega, \delta)^2 L_c \omega_{co}, \quad (7.4)$$

$$L_{c,var}(\omega \rightarrow \infty, \delta) = - \left(\frac{M_{ct}}{L_t} \right)^2 L_t = -k_{ct}(\omega, \delta)^2 L_c. \quad (7.5)$$

Accordingly, for a selected excitation frequency f_{exc} around or above f_{co} , the resistance and/or the inductance variation can be used to measure the distance δ between target and coil. In this case, the coupling factor $k(f_{\text{exc}}, \delta)$ only depends on δ and thus for larger δ , i.e., lower coupling $k(f_{\text{exc}}, \delta)$, the measured resistance $R_{\text{c,in}}$ decreases, while the measured inductance $L_{\text{c,in}}$ increases. Furthermore, it is interesting to note that ω_{co} can be modified by the target material and thickness, i.e., the target resistance R_t , and the dimensions of the ECS, since L_t scales proportionally to the coil's self-inductance L_c . Consequently, for a given ECS geometry, a target material with higher conductivity σ_t or larger thickness d_t shifts ω_{co} to lower frequencies and in cases where the inductance variation is measured, either a lower f_{exc} could be selected or a higher sensitivity can be achieved. In case of resistance variation, however, a lower R_t also means lower sensitivity.

7.2.2 Impedance Variations from FEM Simulations

Fig. 7.3 verifies the derived relationships between the cutoff frequency f_{co} and the resistance and inductance variations $R_{\text{c,var}}(\omega, \delta)$ and $L_{\text{c,var}}(\omega, \delta)$ for a fixed target thickness of 0.5 mm and two different materials, i.e., stainless steel and aluminum. The distance δ is gradually increased between 0 mm (min.

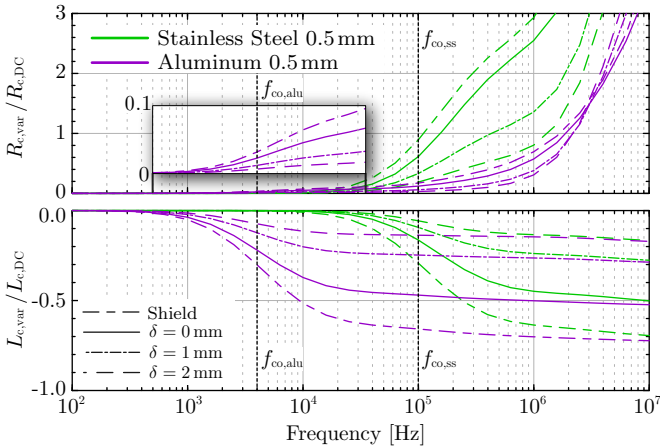


Fig. 7.3: Normalized variable parts $R_{\text{c,var}}(\omega, \delta)$ and $L_{\text{c,var}}(\omega, \delta)$ versus frequency for stainless steel and aluminum target ($d_t = 0.5$ mm) at $\delta = 0$ mm, 1 mm and 2 mm, obtained from FEM simulations (cf. **Fig. 7.2 (c)**).

position), 1 mm (nom. position) and 2 mm (max. position). Note that for the conventional ECS without intermediate conductive layer an offset of 0.5 mm is added (for a more direct comparison with the following case), which means that for $\delta = 0$ mm the effective distance between coil and target is 0.5 mm. The impedance curves of **Fig. 7.3** are obtained from axisymmetrical 2D FEM simulations (*ANSYS Maxwell*) for the ECS geometry shown in **Fig. 7.2 (c)**, whose excitation coil design is discussed in **Sec. 7.3.4**.

As can be noticed from **Fig. 7.3**, since aluminum has an approximately 26 times higher conductivity than stainless steel, its cutoff frequency $f_{\text{co,alu}}$ as well as its resistance sensitivity $R_{\text{c,alu}}(\omega, \delta)$ are lowered by the same amount with respect to $f_{\text{co,ss}}$ and $R_{\text{c,ss}}(\omega, \delta)$. The inductance variation instead stays constant for both materials, i.e., $L_{\text{c,alu}}(\omega \rightarrow \infty, \delta) = L_{\text{c,ss}}(\omega \rightarrow \infty, \delta)$. It should be added that in contrast to the simple transformer equivalent model, the FEM simulations also consider the AC resistance of the targets, which is the reason why the resistances are not settling to the aforementioned values for high frequencies. For materials with high conductivity, this effect is more pronounced, which means it results in a larger scaling $R_{\text{AC}}/R_{\text{DC}}$ at a given frequency. Furthermore, above a certain frequency this also negatively affects the resistance variation. In general, as a rule of thumb, it can be stated that for the conventional ECS the target material and thickness should be selected such that f_{co} is located at least one decade below the desired excitation frequency f_{exc} , e.g., defined by the needed sensor bandwidth, in order to obtain the highest position sensitivity.

7.3 Analysis of the ECS Measuring Through Walls

Consider now the configuration of **Fig. 7.4 (a)**, where, based on the underlying application, the excitation coil is located inside the sealed stator, i.e., behind a *stationary shield* with conductivity σ_s and relative permeability $\mu_{r,s}$. The distance δ between the shield and the moving target has to be measured. As for the target, in the following a relative permeability of $\mu_{r,s} \approx 1$ is assumed for the shield. Since now the excitation coil is almost directly attached to the conductive shield, the magnetic coupling between coil and shield is much higher than between coil and target, especially if the target is located at a large distance δ . Therefore, the eddy currents induced in the intermediate conductive shield significantly affect the variations of $Z_{\text{c,in}}(\omega, \delta)$, i.e., the position sensitivity.

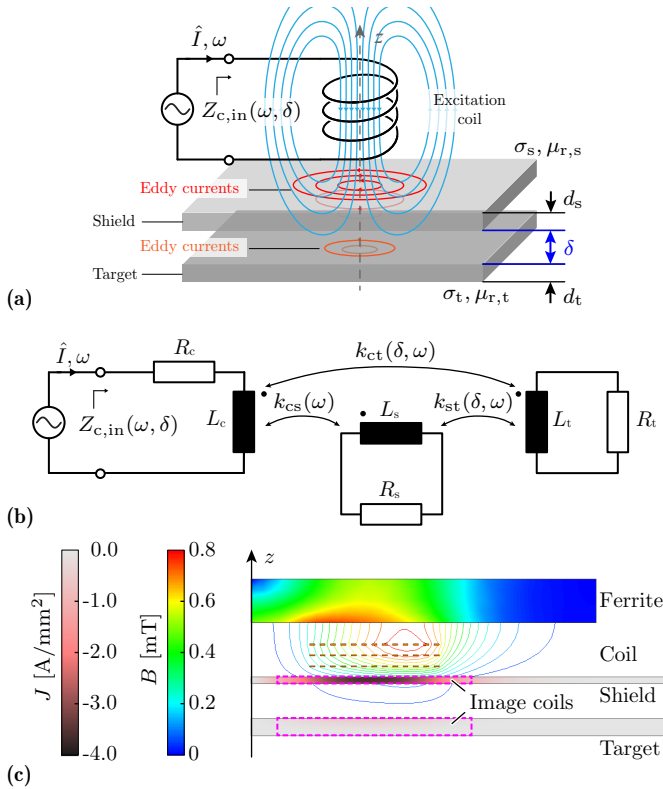


Fig. 7.4: (a) Planar single-coil ECS measuring the distance δ between the stationary intermediate conductive shield and the moveable conductive target. (b) Extended transformer model with a secondary and a tertiary side modeling the equivalent input impedance $Z_{c,in}(\omega, \delta)$ of the excitation coil of the ECS measuring through conductive walls. The electric behavior of shield and target is described by the lumped secondary parameters $R_{\{s,t\}}$ and $L_{\{s,t\}}$ and the magnetic coupling between excitation coil, shield and target are considered by the three coupling factors k_{cs} , k_{ct} and k_{st} . (c) Axisymmetrical 2D FEM simulation (ANSYS Maxwell) with exemplary field and current distribution for a 0.2 mm stainless steel shield and 0.5 mm stainless steel target combination at an excitation frequency of $f_{exc} = 1.25$ MHz. The shield and target image coils are highlighted in purple. A ferrite disk is added on top of the excitation coil to increase its self-inductance L_c .

A general understanding of how $Z_{c,in}(\omega, \delta)$ varies for this new scenario can be gained as follows. Considering the case where $\delta \rightarrow \infty$, i.e., when the target is far away. This corresponds to the conventional ECS with the shield in place of the target, and hence the same considerations as before apply, but now the cutoff frequency $\omega_{co,s} = 2\pi f_{co,s} = R_s/L_s$ is defined by the shield. When the target approaches the shield, it offers a parallel circulation path for the eddy currents, thus reducing the original R_s of the shield alone. The secondary-side resistance can be substituted by an equivalent resistance R_{eq} , which can be seen as some special target at some equivalent position having mixed material properties of shield and target. The resulting R_{eq} is smaller than R_s and continuously reduces with the target approaching the shield. Consequently, also the cutoff frequency $\omega_{co,s}$ shifts to lower frequencies. For the extreme case with $\delta = 0$ mm, assuming that shield and target have the same coupling to the coil, the minimum cutoff frequency is roughly given by the parallel connection of R_s and R_t as

$$\omega_{co,min} = 2\pi f_{co,min} = \frac{R_s R_t}{(R_s + R_t) L_s}. \quad (7.6)$$

Consequently, in cases where the target has a much higher conductivity than the shield, $\omega_{co,min}$ is much lower than $\omega_{co,s}$, while for equal shield and target resistances, $\omega_{co,min}$ is roughly $\omega_{co,s}/2$.

7.3.1 Impedance Variations from FEM Simulations and Optimal Excitation Frequencies

The air gap-dependent shift of the cutoff frequency affects the variations of resistance $R_{c,var}$ and inductance $L_{c,var}$ as shown in the exemplary curves of **Fig. 7.5**. They are obtained from FEM simulations, using the geometry of **Fig. 7.4 (c)**. Four different material and thickness combinations are considered, reported in **Tab. 7.2**. The cases $\delta = 0$ mm, 1 mm, 2 mm, and $\delta \rightarrow \infty$ (i.e., only the shield) are simulated. For the designs **D1** and **D2**, with an aluminum target much more conductive than the stainless steel shield, a large impedance variation is obtained (cf. **Fig. 7.5 (a-b)**). In particular, the low $R_{t,alu}$ leads to a wide shift of $f_{co,s}$ to $f_{co,min}$ and thus to a large inductance variation. The cutoff frequency shift also reflects into a progressively smaller total resistance variation in the frequency range above $f_{co,s}$, compatibly with (7.4). Nevertheless, above a certain frequency, the skin and proximity effects of the shield become dominant and hinder the magnetic field from passing through the shield layer, thus losing sensitivity to the target's position. Therefore,

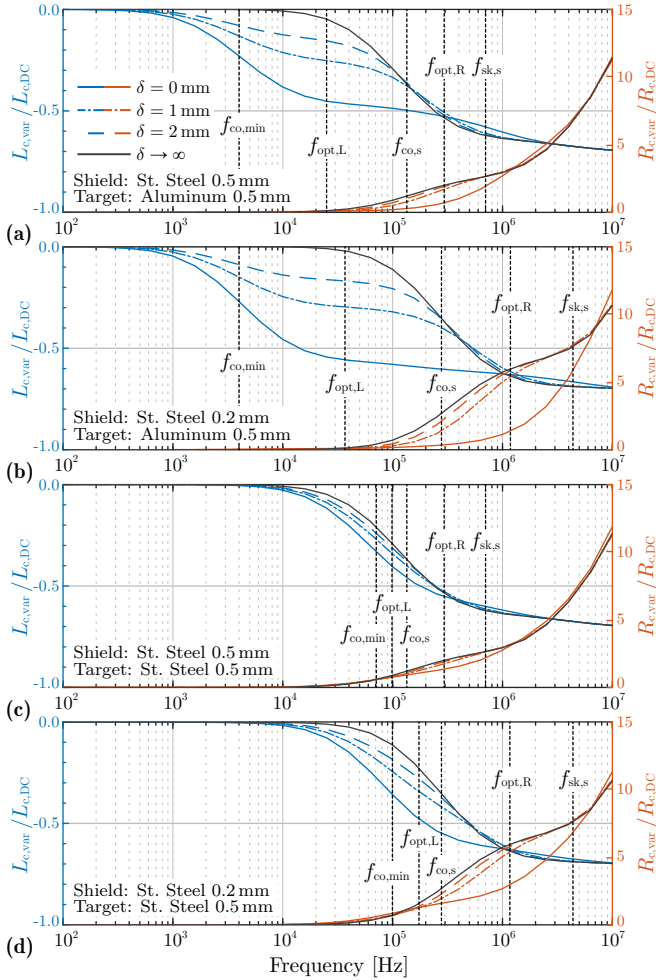


Fig. 7.5: Normalized $R_{c,var}(\omega, \delta)$ and $L_{c,var}(\omega, \delta)$ versus frequency for the designs listed in **Tab. 7.2** at $\delta = 0$ mm, 1 mm, 2 mm and $\delta \rightarrow \infty$ (i.e., only shield), as obtained from FEM simulations. In this exemplary case, the resulting DC coil parameters are $R_c = 2.8 \Omega$ and $L_c = 13.9 \mu\text{H}$. The cutoff frequency f_{co} , the skin depth related frequency of the shield $f_{sk,s}$ and the optimal excitation frequencies $f_{exc,opt,R}$ and $f_{exc,opt,L}$ are also indicated (cf. **Tab. 7.3**).

Tab. 7.2: Considered material and thickness combinations.

Design Name	Shield Material	Shield Thickness	Target Material	Target Thickness
D1	Stainless Steel	0.5 mm	Aluminum	0.5 mm
D2	Stainless Steel	0.2 mm	Aluminum	0.5 mm
D3	Stainless Steel	0.5 mm	Stainless Steel	0.5 mm
D4	Stainless Steel	0.2 mm	Stainless Steel	0.5 mm

the excitation frequency f_{exc} must be kept below a certain *skin-depth-related* frequency $f_{\text{sk},s}$ of the shield. This can be deduced from the skin depth $\delta_{\text{sk},s}$, imposing $\delta_{\text{sk},s} = d_s$, i.e.,

$$\delta_{\text{sk},s} = \sqrt{\frac{2}{\pi\mu_0\mu_{r,s}\sigma_s f}} \Rightarrow f_{\text{sk},s} = \frac{2}{\pi\mu_0\mu_{r,s}\sigma_s d_s^2}. \quad (7.7)$$

In this work, only non-magnetic materials ($\mu_{r,\{s,t\}} = 1$) are considered. As it appears from (7.7), ferromagnetic materials (such as ferritic stainless steel) would reduce the penetration depth of the excitation field, resulting in lower sensitivity. With these considerations it can be more easily understood why the position sensitivity is enhanced for the design **D2**. In fact, due to a 2.5 times thinner shield, $R_{s,ss}$ and hence $f_{\text{co},s}$ increase by the same amount, while $f_{\text{sk},s}$ increases by a factor 2.5^2 . As a result, the frequency ranges offering usable position sensitivity are larger, and the resistance variation is more pronounced (cf. (7.4)). On the other hand $f_{\text{co},\text{min}}$, which is mainly defined by the target with $R_{t,\text{alu}}$, stays unchanged. In design **D3** (cf. **Fig. 7.5 (c)**), with shield and target made of the same material and thickness, the frequency shift from $f_{\text{co},s}$ to $f_{\text{co},\text{min}} \approx f_{\text{co},s}/2$ is smaller, thus the inductance variation is limited. This is also reflected in the much smaller resistance variation. Again, similar to design **D2**, also in case of equal materials a shield thickness reduction improves the position sensitivity (cf. design **D4** with the results in **Fig. 7.5 (d)**).

Generalizing, for all the studied cases in **Tab. 7.2** and **Fig. 7.5**, the maximum resistance variation $\Delta R_{\text{c,var}}(f_{\text{exc,opt,R}}, \delta)$ and inductance variation $\Delta L_{\text{c,var}}(f_{\text{exc,opt,L}}, \delta)$ occur in two distinct frequency ranges and thus two distinct optimal excitation frequencies $f_{\text{exc,opt,R}}$ and $f_{\text{exc,opt,L}}$ can be defined. In particular, $L_{\text{c,var}}$ is mostly sensitive to variations of the air gap δ in the frequency range between $f_{\text{co},\text{min}}$ and $f_{\text{co},s}$. The optimal excitation frequency $f_{\text{opt,L}}$ that maximizes the position sensitivity of $L_{\text{c,var}}$ lies approximately in

the center of this interval, i.e., the geometric mean of the two boundary frequencies

$$f_{\text{opt,L}} \approx \sqrt{f_{\text{co,min}} \cdot f_{\text{co,s}}} \quad (7.8)$$

The frequency range for which $R_{\text{c,var}}$ is mostly sensitive to variations of δ lies above $f_{\text{co,s}}$, but beyond $f_{\text{sk,s}}$ no sensitivity can be achieved. Thus, the optimal excitation frequency $f_{\text{opt,R}}$, lies approx. in the center between $f_{\text{co,s}}$ and $f_{\text{sk,s}}$, i.e., again the geometric mean

$$f_{\text{opt,R}} \approx \sqrt{f_{\text{sk,s}} \cdot f_{\text{co,s}}} \quad (7.9)$$

7.3.2 General ECS Design Guidelines

In summary, from the FEM results and the considerations of **Sec. 7.3.1**, it is possible to provide the following design guidelines for the ECS measuring through conductive walls:

- ▶ In order to achieve a high measurement sensitivity, for both resistance and inductance variation, the shield resistance R_s should be much larger than the target resistance R_t , which is either obtained by selecting different materials or by using different thicknesses.
- ▶ A large shield resistance R_s increases both the cutoff frequency $f_{\text{co,s}}$ and the skin depth related frequency $f_{\text{sk,s}}$, resulting in a larger measurement bandwidth.
- ▶ The resistance variation starts around $f_{\text{co,s}}$ and ends around $f_{\text{sk,s}}$, which are both defined by only the shield layer.
- ▶ The range of inductance variation is defined by $f_{\text{co,min}}$ and $f_{\text{co,s}}$.
- ▶ The optimal excitation frequency is roughly calculated with (7.8) or (7.9), i.e., with the geometric mean of the frequency boundaries.

7.3.3 Extended Equivalent Transformer Model

So far, only the relations between $R_{\text{c,var}}(\omega, \delta)$, $L_{\text{c,var}}(\omega, \delta)$ and the optimal excitation frequencies are defined, but it is still not possible to calculate $f_{\text{ext,opt,L}}$ and $f_{\text{ext,opt,R}}$ for a given ECS configuration based on its electrical and geometrical parameters. For this, expressions for all the terms used in (7.3) and (7.6) are needed. If the values of the optimal frequencies are found, it possible to optimally design the excitation coil of the ECS measuring

through conductive walls and immediately estimate the position sensitivity. The impedance variations of the excitation coil can be modeled analytically with an extended three-windings transformer model. In order to account for the additional shield layer, the transformer model previously introduced in **Fig. 7.2 (b)** for the conventional ECS is modified as shown in **Fig. 7.4 (b)**, i.e., with a secondary side consisting of the series connection of the lumped shield resistance and inductance R_s and L_s and a tertiary side with the lumped target parameters R_t and L_t . Consequently, also the mutual inductances $M_{cs} = k_{cs} \sqrt{L_c L_s}$ and $M_{st} = k_{st} \sqrt{L_s L_t}$ are introduced, where $k_{cs} = k_{cs}(\omega, \delta)$ and $k_{st} = k_{st}(\omega, \delta)$ are the coil-shield and shield-target coupling factors. It can be observed that k_{cs} is always larger than k_{ct} . By circuital analysis, an expression for the input impedance of the excitation coil $Z_{c,in}(\omega, \delta)$ can be provided. This is slightly more complicated with respect to the conventional ECS case, cf. (7.1) and (7.2), and is hence reported in the **Appendix C**. The description of $Z_{c,in}$ provided by the transformer model is completed with the analytical expressions for all its parameters, as derived in the following.

Excitation Coil (Primary-Side) Parameters

Expressions for the coil resistance R_c and inductance L_c can usually be found in the literature for different coil geometries [102, 103]. A common choice for ECSs is a PCB-integrated *planar spiral coil*, as it allows obtaining a relatively large inductance already with a single-layer coil. This way, the inter-layer parasitic capacitance of the coil is minimized, thus allowing to use higher excitation frequencies. Minimizing the parasitic capacitance $C_{c,par}$ is needed to guarantee that the coil's Self-Resonant Frequency (SRF) is well above the chosen excitation frequency. This is a stringent requirement for the correct operation of the ECS and the validity of the introduced transformer model. For the scope of this analysis it is sufficient to consider at least the following relations linking the coil geometry to its electrical properties. For the coil's DC resistance

$$R_c \propto \frac{d_{c,avg} N}{\sigma_{cu}}, \quad (7.10)$$

whereas for the inductance, in general

$$L_c \propto \mu_0 d_{c,avg} N^2 \quad (7.11)$$

where $d_{c,avg}$ is the average diameter of the excitation coil.

Shield/Target (Secondary-Side) Parameters

Providing expressions for the lumped shield or target resistance $R_{\{s,t\}}$ and inductance $L_{\{s,t\}}$ requires some preliminary consideration on the geometry of the eddy current circulation paths. Following the work of Vyroubal [104], for a circular excitation coil the volume of the target carrying significant eddy currents (the *effective* volume) can be segmented into a certain number K of concentric rings. Each of them can be considered insulated with respect to the other, as it can be shown that the current density vector field \vec{j} inside the target, expressed in polar coordinates, has no radial component. The simplest approximation, corresponding to $K = 1$, is to describe the effective volume with a circular single-turn *image coil* of rectangular cross section, with inner and outer radii r_{in} and r_{out} , as indicated in purple in **Fig. 7.4 (c)**. The thickness of such image coil can be assumed to be equal to the shield or target thickness $d_{\{s,t\}}$, as long as the eddy currents penetrate the material completely. However, for higher frequencies, the penetration depth reduces due to aforementioned skin effect, according to the expression for the skin depth

$$\delta_{\text{sk},\{s,t\}}(\omega) = \sqrt{\frac{2}{\mu_0 \mu_{r,\{s,t\}} \sigma_{\{s,t\}} \omega}}. \quad (7.12)$$

When eventually $\delta_{\text{sk},\{s,t\}}$ becomes smaller than $d_{\{s,t\}}$, the eddy currents are distributed only in a portion of the total shield or target thickness. Consequently, the effective height of the image coil is

$$h_{\{s,t\}}(\omega) = \begin{cases} d_{\{s,t\}}, & \text{for } \delta_{\text{sk},\{s,t\}}(\omega) \geq d_{\{s,t\}} \\ \delta_{\text{sk},\{s,t\}}(\omega), & \text{otherwise} \end{cases}, \quad (7.13)$$

which decreases for higher frequencies. However, a reduction of the penetration depth is only allowed for the target. The excitation frequency f_{exc} should always be lower than the skin-depth frequency of the shield. Consequently, as previously seen, the thickness and the selected material of the shield immediately limit the excitation frequency range and the analysis thereof.

This way, $R_{\{s,t\}}$ and $L_{\{s,t\}}$ can be found as the resistance and the self-inductance of the respective equivalent image coils. For the resistance $R_{\{s,t\}}$, it is sufficient to integrate the resistance of an infinitely thin loop in the volume of the image coil, obtaining

$$R_{\{s,t\}}(\omega) = \frac{2\pi}{\sigma_{\{s,t\}} h_{\{s,t\}}(\omega) \ln\left(\frac{r_{\text{out}}}{r_{\text{in}}}\right)}. \quad (7.14)$$

For the inductance $L_{\{s,t\}}$, instead, the empirical formula from [105] for a circular coil of rectangular cross section can be used

$$L_{\{s,t\}} [\mu\text{H}] \approx \frac{40 r_{\text{avg}}^2}{8 r_{\text{avg}} + 11 (r_{\text{out}} - r_{\text{in}})}, \quad (7.15)$$

where $r_{\text{avg}} = (r_{\text{out}} + r_{\text{in}})/2$ is the average radius of the image coil. In a first approximation, r_{in} and r_{out} can coincide with the inner and outer radii of the excitation coil, and hence $r_{\text{avg}} = d_{\text{c,avg}}/2$. In this case, FEM simulations reveal that 80 % of the eddy currents are induced in this volume for both shield and target. The volume enclosed by an image coil with the same average radius r_{avg} but a 50 % wider cross section (i.e., $1.5 \cdot (r_{\text{out}} - r_{\text{in}})$), as the ones represented in **Fig. 7.4 (b)** would instead consider up to 95 % of the total eddy currents.

Coupling Factors

Finally, the coupling factors can be obtained from the mutual inductances M_{cs} , M_{st} and M_{ct} according to the formula $k_{12} = M_{12}/\sqrt{L_1 L_2}$. With the introduced image coils, it is possible to use formulas for the mutual inductance of coaxial disk coils that can be found in the literature [106, 107]. As the model is highly sensitive to these three parameters, it is recommended to obtain or verify them with a FEM simulation.

7-3-4 Optimal PCB-Embedded Coil Design Considerations

Once the transformer model and all the expressions for its parameters are introduced, they can be used to optimally design the excitation coil. As mentioned, this is typically realized as a PCB- or flex-PCB-embedded spiral coil, hence there are only a few main parameters to be determined, i.e., the coil diameter d_c and the number of turns N , which can be distributed in m layers. The optimal design procedure is summarized with the flow diagram of **Fig. 7.6**. The specified shield material with its conductivity σ_s and thickness d_s defines the skin-depth related frequency $f_{\text{sk},s}$ (cf. (7.7)). From the required controller bandwidth, the needed excitation frequency f_{exc} is defined, which coincides with $f_{\text{opt,R}}$. Based on (7.9), it is hence possible to calculate the shield crossover frequency $f_{\text{co},s}$, which gives the ratio between R_s and L_s (cf. (7.3)). These two electrical parameters allow to select the dimensions of the image coil (average, inner and outer radii r_{avg} , r_{in} and r_{out} , cf. (7.14) and (7.15)) and, consequently, of the excitation coil. With the maximum diameter d_c ,

the maximum number of turns N of the excitation coil can be calculated, which gives a high excitation coil's self-inductance L_c and, in turn, a high position sensitivity (cf. (7.4) and (7.5)). The number of turns N can be further increased by using multiple PCB layers, but special care must be taken, as this particularly increases the parasitic capacitance $C_{c,par}$, thus lowering the coil's SRF. Another way of further increasing L_c , compatibly with the available space in the stator, is to place a layer of ferromagnetic material on top of the excitation coil. As an additional benefit, this provides shielding against external disturbing magnetic fields.

Therefore, for the given case, the excitation coil's diameter is maximized to the available $d_c = 11.5$ mm, which with the minimum track width and distance of $150 \mu\text{m}$ yields a maximum number of turns per layer of $N = 13$. A picture of the realized PCB-embedded excitation coil is shown in **Fig. 7.7 (a)**. In order to ensure that the coil's SRF is above 10 MHz, (i.e., well above the range of the considered excitation frequencies), the number of PCB layers is limited to $m = 3$. In addition, a high-frequency ferrite core is added on top of the coil (cf. **Fig. 7.7 (b)**) to further increase L_c , resulting in a total $L_c = 13 \mu\text{H}$.

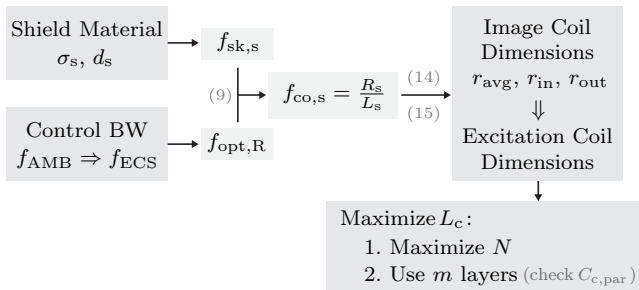


Fig. 7.6: Flow diagram illustrating the optimal PCB-embedded coil design. From the specified shield material and control bandwidth, it is possible to define the characteristic frequencies, which are linked to the coil's geometry through the secondary-side parameters R_s and L_s . Once the coil's dimensions are obtained, its self-inductance L_c is maximized.

7.3.5 Experimental Impedance Measurements and Model Verification

The impedance variations of the ECS measuring through conductive walls are verified with the realized PCB-embedded excitation coil in the studied planar geometry of **Fig. 7.4 (a)**. This is realized with a collection of square samples of aluminum and stainless steel (304, IE 1.4301, austenitic) with thicknesses 0.5 mm and 0.2 mm, to be used as shield or target (cf. **Fig. 7.7 (c)**). The air gap between the two samples is fixed with spacers, realized with a non-conductive, temperature-resistant material (PTFE) and different thicknesses. This way, it is possible to fix the air gap in steps of 0.25 mm, which is the thickness of the thinnest spacer. The selected shield sample, spacer(s) and target sample are stacked up, with the excitation coil PCB on top, as shown in **Fig. 7.7 (d)**. All layers are also pressed together, thus reducing the bending of the metallic samples or the spacers. This measure is important to ensure correct results,

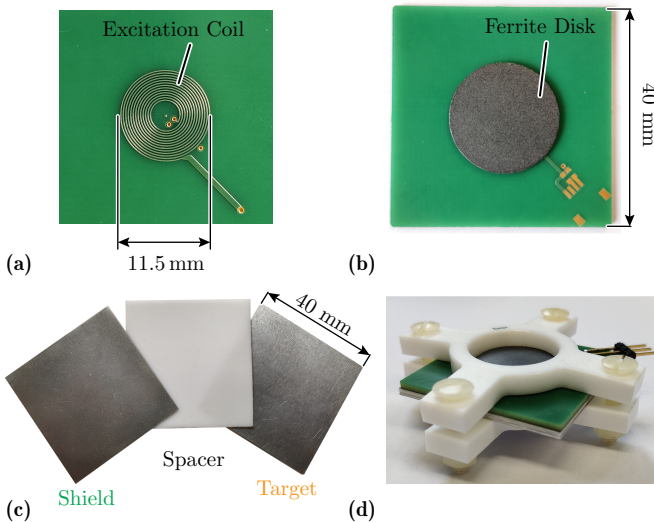


Fig. 7.7: (a) Realized PCB-embedded excitation coil. (b) On top of the excitation coil, a high-frequency ferrite disk is added to increase the self-inductance L_c . (c) Realized exemplary shield/target and spacer samples, made of stainless steel or aluminum and PTFE, respectively. (d) PCB coil buildup implementing the studied planar geometry, held together by a PTFE fixture.

Tab. 7.3: Comparison of the optimal excitation frequencies.

	Fig. 7.8 (a)		Fig. 7.8 (b)		Unit
	$f_{opt,L}$	$f_{opt,R}$	$f_{opt,L}$	$f_{opt,R}$	
Measured	178	1189	56	1259	[kHz]
FEM	178	1122	47	1334	[kHz]
Analytical	175	1195	40	1195	[kHz]

especially considering the high sensitivity and the targeted resolution in the μm range.

The measurements are performed with the *Omicron Lab Bode100* impedance analyzer for the 0.2 mm thick stainless steel shield and 0.5 mm thick stainless steel target configuration and for the 0.2 mm thick stainless steel shield and 0.5 mm thick aluminum target configuration. The results are compared to the corresponding FEM simulations in **Fig. 7.8**, showing good agreement between the two. In particular, the optimal frequencies reported in **Tab. 7.3** match closely. Also the values calculated with the analytical transformer model are reported and matching. The model allows obtaining the complete impedance curves, which however were found to be in agreement only until around $f_{sk,s}$. For the sake of this analysis and the optimal coil design, calculating the characteristic frequencies is sufficient, and therefore the impedance curves are not reported.

7.4 Influence of the Temperature on the Sensor's Output

An important aspect to investigate for many sensors and particularly for the studied ECS is its behavior under different operating temperatures. Ideally, for a constant position, the sensor output has to stay constant throughout the entire range of operating temperatures. In the considered case, this problem is of particular interest. In fact, the temperature inside the sealed stator (where the ECS is located) varies in the range of 25 °C to 100 °C, since the actuator's winding, located inside the stator, heats up during operation. Consequently, a thermal drift of the sensor's output in active magnetic bearings would translate in a certain offset in the controlled position of the levitated mover with respect to the geometric center of the machine, which can lead in the worst case to failure of the levitation control. For these reasons, it is important

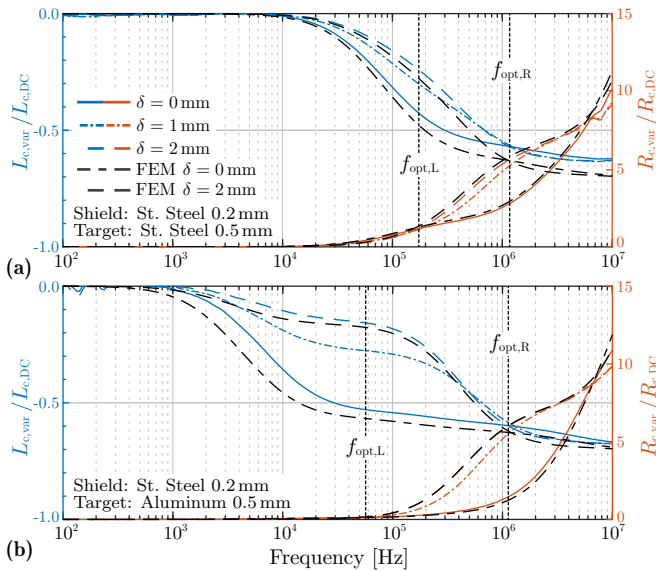


Fig. 7.8: Normalized $R_{c,var}(\omega, \delta)$ and $L_{c,var}(\omega, \delta)$ versus frequency for **(a)** 0.2 mm thick stainless steel shield and 0.5 mm thick stainless steel target configuration and **(b)** 0.2 mm thick stainless steel shield and 0.5 mm thick aluminum target configuration at $\delta = 0$ mm, 1 mm and 2 mm, as obtained from impedance measurements. For a direct comparison, also the FEM results for the cases $\delta = 0$ mm, 2 mm are reported (black dashed lines) and the optimal frequencies are indicated and reported in **Tab. 7.3**.

to quantify the effect of temperature on the sensor's output and, possibly, take specific actions to limit or compensate it.

As a starting point for this investigation, it should be considered that the conductivity σ exhibits a temperature dependency. Another effect is thermal expansion, which however is not expected to be prominent in this case for thin shields or targets and is therefore neglected. As a consequence of the

Tab. 7.4: Conductivity and Temperature Coefficient of the considered materials.

Material	Conductivity at 25 °C σ_0	Temperature Coeff. (C_T)
Copper	59.6 MS	3900 ppm/°C
Aluminum	37.7 MS	3800 ppm/°C
Stainless Steel	1.37 MS	850 ppm/°C

dependency on the conductivity σ , it has to be expected that the electrical properties of all the elements in the studied ECS configuration, i.e., coil, shield and target, are affected by temperature. The temperature dependency is usually given for the resistivity $\rho = \sigma^{-1}$ with the approximated linear relationship

$$\rho(T) = \rho_0 [1 + C_T (T - T_0)], \quad (7.16)$$

where T is the temperature, ρ_0 is the resistivity of the material at the reference temperature T_0 (e.g., 25 °C) and C_T is the *temperature coefficient* of the material, expressed in 1/°C. The values of ρ_0 and C_T for copper, aluminum and stainless steel are reported in **Tab. 7.4**. For the considered operating temperature range of 75 °C, the resistivity of copper increases by about 30 %.

Based on the analytical model previously introduced in **Sec. 7.3**, it is already possible to predict qualitatively how the temperature influences $Z_{c,in}$. The most prominent effect, given the high C_T of copper, is the increase of R_c (cf. (7.10)), which offsets the total $R_{c,var}$ with respect to the nominal DC resistance at 25 °C $R_{c,DC[25^\circ C]}$. Secondly, also R_s and R_t increase with temperature (cf. (7.14)), according to their materials' properties. This reflects into an increase of the cutoff frequencies $f_{co,s}$ (cf. (7.3)) and $f_{co,min}$ (cf. (7.6)), which can affect the final sensitivity (cf. (7.4)) and alters the optimal excitation frequencies. Some influence has also to be expected for higher frequencies, as the skin depth $\delta_{sk,s}$ depends on σ_s as well. On the contrary, no relevant effect has to be expected on L_c (cf. (7.11)) nor on $L_{c,var}$ (cf. (7.5)). This is the main reason why conventional ECSs rely on $L_{c,var}$ to measure δ and disregard $R_{c,var}$ [108].

These considerations are verified by measuring the impedance of the realized PCB-integrated excitation coil at 25 °C and 100 °C. The measurements are conducted for the shield/target combination with 0.2 mm thick stainless steel shield and 0.5 mm thick stainless steel target, as well as 0.2 mm thick stainless steel shield and 0.5 mm thick aluminum target. The latter are shown in **Fig. 7.9**. With these results, it is possible to observe and quantify the influence of temperature on the equivalent input impedance of the excitation coil. As expected, this is much more prominent on $R_{c,in}$, with variations of about 30 % of the value of $R_{c,DC[25^\circ C]}$ at the optimal excitation frequencies, compared to $L_{c,in}$, which differs by less than 6 % of the value of $L_{c,DC[25^\circ C]}$ and is hence negligible. In particular, the increased DC resistance of the sensing coil R_c represents the main difference component of $R_{c,var}$, which is about 30 % larger for all frequencies (cf. **Fig. 7.9 (b)**). Additionally, the crossover frequencies $f_{co,min}$ and $f_{co,s}$ are shifted slightly towards higher frequencies as a result of the increased R_s and R_t , causing the largest differences in $L_{c,var}$ in **Fig. 7.9 (b)**. The prominent effect of temperature on $R_{c,var}$ leads to an

error in the measured position, which can be visualized in Fig. 7.9 (c) for different values of the air gap δ when exciting the coil at, e.g., $f_{\text{opt,R}}$. If the sensor is calibrated for $T = 25^\circ\text{C}$, in the extreme case of $T = 100^\circ\text{C}$ the error δ_{err} on the measured position can be as large as 1.1 mm. This is quite concerning for the stability of the magnetic bearings and needs to be explicitly corrected. On the other hand, if the same is checked for $L_{\text{c,var}}$ at the optimal

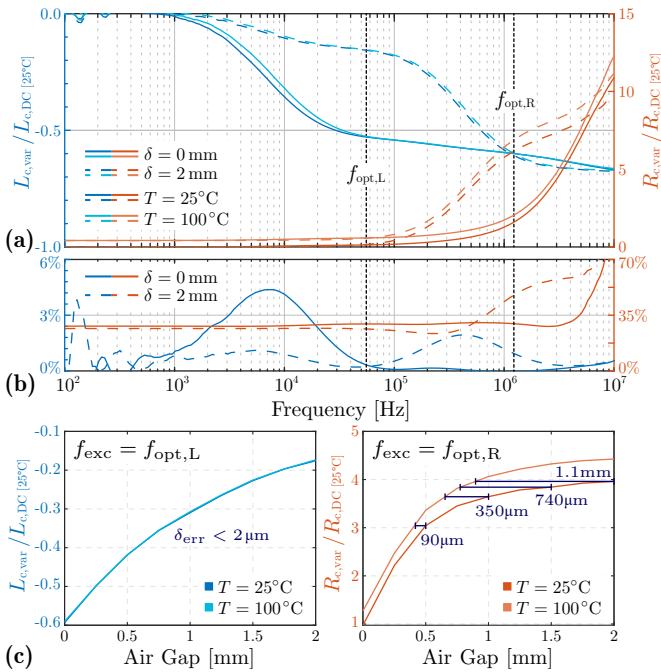


Fig. 7.9: (a) Normalized $R_{\text{c,var}}(\omega, \delta)$ and $L_{\text{c,var}}(\omega, \delta)$ versus frequency for the 0.2 mm thick stainless steel shield and 0.5 mm thick aluminum target configuration at $\delta = 0$ mm and 2 mm and $T = 25^\circ\text{C}$ and 100°C , as measured from the realized excitation coil. All values are normalized to its DC resistance and inductance at 25°C . (b) Differences between the normalized $R_{\text{c,var}}(\omega, \delta)$ and $L_{\text{c,var}}(\omega, \delta)$ at $T = 25^\circ\text{C}$ and 100°C , for both $\delta = 0$ mm and 2 mm. The values represent the percent difference in $R_{\text{c,var}}(\omega, \delta)$ and $L_{\text{c,var}}(\omega, \delta)$ over $\Delta T = 75^\circ\text{C}$. (c) Values of $R_{\text{c,var}}$ and $L_{\text{c,var}}$ versus air gap δ for $T = 25^\circ\text{C}$ and 100°C , measured for the optimal inductance and resistance excitation frequencies. The position error δ_{err} due to the temperature variation $\Delta T = 75^\circ\text{C}$ is indicated.

excitation frequency $f_{\text{opt,L}}$, δ_{err} results smaller than $2\ \mu\text{m}$, i.e., temperature does not have a significant influence on the measured position. However, it has to be considered that $f_{\text{opt,L}}$ is smaller than $f_{\text{opt,R}}$, even by an order of magnitude in the case of **Fig. 7.9 (a)**, and it might not be sufficient for highly dynamic applications as, e.g., very-high-speed magnetically levitated machines. In such a case, it is therefore necessary to be able to distinguish between impedance variations caused by position or temperature variations. This is only possible if full knowledge about the impedance $Z_{\text{c,in}}$ is gained, which means that not only $R_{\text{c,in}}$ or $L_{\text{c,in}}$ but both values have to be determined. In order to achieve this, an appropriate sensor interface is needed, as discussed in the next section. There it is shown that in this way, the ECS measuring through conductive walls allows measuring accurately the air gap δ , since variations in temperature T are compensated.

7.5 Sensor Interface and Signal Conditioning

Once the sensor concept is analyzed, it is possible to understand its operating principle and which quantities contain information on the measurand. The next problem to address is how to extract such information and convert it into a usable signal. For this purpose, a *measurement circuit* (or *sensor interface*) is needed, which has three main functions. First, it has to provide an appropriate AC excitation signal to the sensor coil. Secondly, it has to transduce its impedance variations into measurable voltage or current signals. Finally, the obtained signals have to be further conditioned to be easily measured, e.g., to be digitized and acquired by a MCU and to be translated into a position. As mentioned, in the considered case an important requirement is the possibility of gaining full information on the excitation coil's impedance variation $\Delta Z_{\text{c,in}}(\delta, T, \omega)$, in order to be able to distinguish and measure both variations of the air gap δ and of the temperature T .

7.5.1 Overview of the Proposed Measurement Circuit

An overview of the proposed measurement circuit is given in **Fig. 7.10**. It consists of three main parts, which implement the three aforementioned functions.

The excitation frequency $\omega_{\text{exc}} = 2\pi f_{\text{exc}}$ directly determines the sensor's position (and temperature) sensitivity, as it affects the penetration depth of the primary magnetic field in the shield-target combination. Therefore, it is reasonable to select a measurement circuit which operates with a *fixed*

excitation frequency. Consequently, measurement circuits that perform an impedance-to-frequency conversion, commonly used for conventional ECS [109], have to be excluded. With a fixed excitation frequency, $\Delta Z_{c,in}$ can then be converted into an amplitude variation ΔU or ΔI .

The most suitable candidate circuit performing such conversion is the AC Wheatstone bridge, often found in the literature as an ECS interface [110]. The bridge is excited by a sinusoidal voltage signal U_{exc} with frequency f_{exc} and its output is the voltage $U_{br,out}$. This circuit is particularly well suited to measure unbalances between the impedances of its two legs. Therefore, in many cases, the excitation coil of the ECS is included in the bridge together with a replica, purposely manufactured and used as a *reference coil*, kept in nominal conditions (e.g. at the nominal distance from the target). This solution is used for high precision sensors, capable, e.g., to measure in the subnanometer range [66]. An additional advantage, in fact, is that any changes which are common to both coils (like, e.g., the offset in R_c due to temperature found in Fig. 7.9), are canceled. In the considered application, due to the axial symmetry of the machine, it is advantageous to implement the ECS as a *differential sensor*, which is obtained by placing two identical copies of the excitation coil ECS_+ and ECS_- at the two opposite sides of the levitated

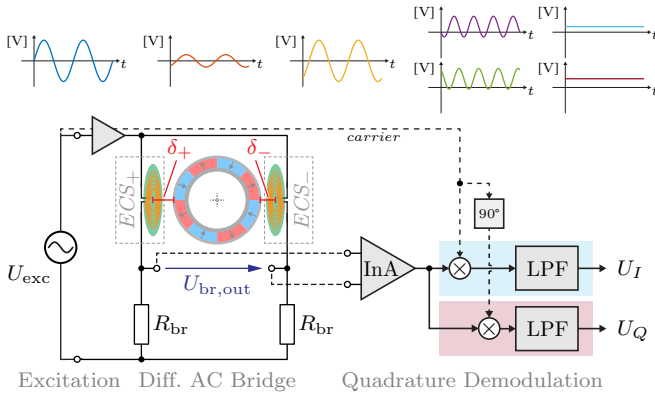


Fig. 7.10: Schematic of the proposed measurement circuit, comprising excitation stage, differential AC Wheatstone bridge, amplification and demodulation stages. Differential sensing is realized by using two copies of the designed PCB-integrated excitation coil. In order to implement quadrature demodulation, two channels consisting each of a multiplier followed by a low-pass filter (LPF) are needed, together with a 90° carrier phase-shifter. Exemplary intermediate signals are also reported.

rotor. By including both sensing coils in the AC Wheatstone bridge, it can be shown that the output voltage $U_{\text{br,out}}$ depends of the differential impedance $Z_{\text{diff}} = Z_{\text{c+,in}} - Z_{\text{c-,in}}$, which finally gives a measurement of the *differential position* $\delta_{\text{diff}} = \delta_+ - \delta_-$. It can be proved that differential sensing improves the sensitivity and the linearity of the sensor's output, even though the original variations of the measurand are not linear [111].

As a result of the variations of both the air gap δ and temperature T , the output voltage $U_{\text{br,out}}$ is finally an attenuated and phase-shifted version of the excitation voltage U_{exc} . More specifically, the variable air gap $\delta_{\text{diff}}(t)$ *modulates in amplitude and phase* $U_{\text{br,out}}$. Therefore, in order to recover $\delta_{\text{diff}}(t)$ and simultaneously gain full information (real and imaginary parts) on $U_{\text{br,out}}$ (and hence on the impedance Z_{diff}) *quadrature demodulation* is used. In case only $\delta_{\text{diff}}(t)$ is of interest, with, e.g., minimal influence of T , it is sufficient to use only one demodulation channel.

7.5.2 Analysis and Selection of the AC Wheatstone Bridge Configuration

The AC Wheatstone bridge can be configured in many different ways: for example, the two excitation coils can be placed either in the same bridge leg or in two different legs. Additionally, it is possible to add a capacitor C_{res} in series to the excitation coil to compensate its inductive reactance at a specific resonant frequency. In this case, it would also be possible to excite the bridge with a square wave voltage, which is much simpler to realize in practice.

Three configurations of most interest are analyzed. In configuration **B1** (Fig. 7.11 (a.i)), the two excitation coils make part of two different bridge legs. This is the most basic configuration, and the value of the bridge resistors R_{br} is optimized to yield the largest magnitude of $U_{\text{br,out}}$. In configuration **B2** (Fig. 7.11 (b.i)), a capacitor C_{res} is added in series to each coil, and chosen to resonate with the value of $L_{\text{c,in}}$ for $\delta = 1$ mm, which is the nominal air gap. The resonant frequency is also optimized, together with the value of R_{br} , to yield the largest magnitude of $U_{\text{br,out}}$. Finally, configuration **B3** (Fig. 7.11 (c.i)) is a variant of **B2** realized with only one capacitor in series with both bridge legs. Bridge configurations where both the excitation coils are in the same leg were studied as well, but provide in general slightly worse sensitivity to δ_{diff} , hence they are not reported. In order to select the most appropriate bridge circuit, together with the corresponding optimal excitation frequency f_{opt} , each configuration is investigated analytically. By simple AC circuital analysis, the transfer function $G(s)$ from the input voltage U_{exc} to the output voltage

$U_{br,out}$ is derived. With this, it is possible to obtain $U_{br,out} = G(s) U_{exc}$ as a complex-valued phasor for a given array of frequencies and differential positions, starting from the measured impedance of the realized PCB-embedded coil. The influence of temperature discussed in **Sec. 7.4** can also be easily included in this analysis. The values of $R_{c,in}$ and $L_{c,in}$ used are the ones measured for the most sensitive shield/target combination, i.e., 0.2 mm thick stainless steel shield and 0.5 mm thick aluminum target. In **Fig. 7.11**, for each bridge configuration, $U_{br,out}$ is visualized on the complex plane for different frequencies, values of the differential position δ_{diff} and temperatures $T = 25^\circ\text{C}$ and 100°C .

The studied configurations are compared according to a few selection criteria. The most important requirement is high sensitivity to the differential position δ_{diff} , which translates in the largest magnitude of the phasor $U_{br,out}$. The second aspect to take into consideration is the sensitivity to the temperature T . As mentioned, the designer can choose whether measuring T is of interest, or whether it is more important to minimize its influence on the δ_{diff} measurement. The normalized sensitivity curves in **Fig. 7.12** are extracted from the data in **Fig. 7.11** for the exemplary configuration **B1**. The δ_{diff} -sensitivity curve is given by the magnitude of $U_{br,out}$ for the largest $\delta_{diff} = 1\text{ mm}$ versus frequency and normalized to its maximum. For the T -sensitivity curve, instead, the magnitude of the difference vector $U_{br,out,100^\circ\text{C}} - U_{br,out,25^\circ\text{C}}$ versus frequency is considered, again for $\delta_{diff} = 1\text{ mm}$ and normalized to its maximum. With the sensitivity curves two optimal frequencies can be identified, for two scenarios:

1. in case *combined sensitivity* to δ_{diff} and T is desired, the optimal frequency $f_{opt,comb}$ can be found, which corresponds to the peak of the product sensitivity curve shown in **Fig. 7.12**, which in case of configuration **B1** leads to an optimal frequency $f_{opt,comb} = 299\text{ kHz}$. The corresponding $U_{br,out}$ obtained at this frequency on the complex plane is highlighted in blue in **Fig. 7.11 (a.ii)**;
2. in case only δ_{diff} is of interest, it is possible to select the frequency $f_{opt,\delta}$, which offers the optimal compromise between sensitivity to δ_{diff} and to T . This corresponds to the condition for which the sensitivity to δ_{diff} dominates the most with respect to the sensitivity T , i.e., to the peak of the ratio sensitivity curve as shown in **Fig. 7.12**. In case of configuration **B1** this leads to an optimal excitation frequency $f_{opt,\delta} = 563\text{ kHz}$. The corresponding $U_{br,out}$ obtained at this frequency on the complex plane is highlighted in orange in **Fig. 7.11 (a.ii)**.

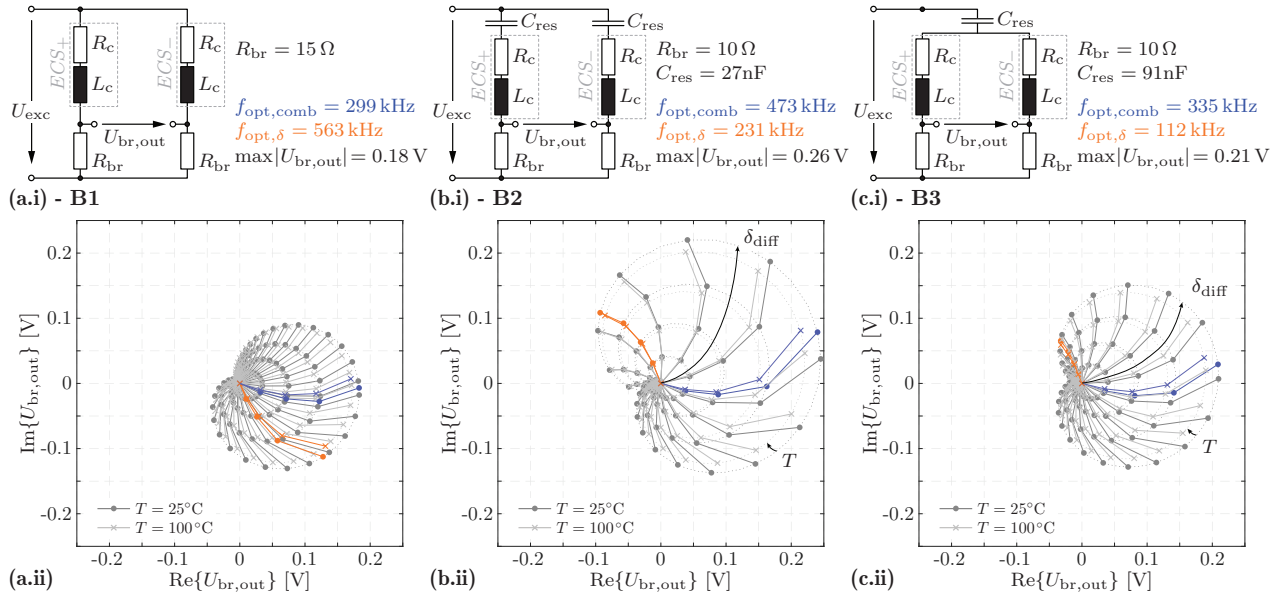


Fig. 7.11: Analysis of three differential AC Wheatstone bridge configurations with **(a.i)** no resonant series capacitor, **(b.i)** a series resonant capacitor per coil and **(c.i)** only one series resonant capacitor shared for the two coils. For each case, the bridge output voltage phasor $U_{br,out}$ resulting for a unitary U_{exc} is visualized on the complex plane in **(a.ii)**, **(b.ii)** and **(c.ii)**. $U_{br,out}$ is calculated for values of $f = 2\pi\omega$ logarithmically evenly spaced between 100 Hz and 10 MHz with 40 points per decade, $\delta_{diff} = \{0, 0.25, 0.5, 0.75, 1\}$ mm and $T = 25^\circ\text{C}$ and 100°C . In order to improve visibility, only positive values of δ_{diff} are shown, as all curves are symmetric with respect to the origin. The indicated values of R_{br} and C_{res} are optimized to yield the largest magnitude of $U_{br,out}$. The highlighted curves correspond to the optimal excitation frequencies $f_{opt,comb}$ (combined δ_{diff} and T sensitivity) and $f_{opt,\delta}$ (least influence of T on δ_{diff} sensitivity) identified in **Fig. 7.12**.

Besides sensitivity, another important requirement is the measurement bandwidth of the sensor, which has to be sufficiently high. This is directly related (approx. one decade before) to the selected f_{exc} . Finally, linearity has the least priority, as the non-linear sensor readout can eventually be corrected (e.g., in firmware).

With the results of **Fig. 7.11**, the analyzed bridge configurations can be compared and some trade-offs outlined. The sensitivity to δ_{diff} is higher for the alternatives with a resonant capacitor C_{res} . For **B2** (max 0.26 V/mm) it is up to 40 % larger than **B1**. The enhanced sensitivity comes at the cost of a visibly higher non-linearity. For **B3**, instead, it is only 20 % larger than **B1**. As mentioned, the value of C_{res} is optimized together with the resonant frequency to yield the largest possible $U_{br,out}$. Interestingly, during the analysis it was found that resonance yields a sensitivity above 0.2 V/mm for a large range of frequencies, from 100 kHz to 1.4 MHz for **B2** and from 150 kHz to 600 kHz for **B3**. Therefore, these configurations give the freedom of adjusting f_{exc} according to the designer's preferences, also allowing to obtain larger bandwidths. Nevertheless, in **B2** the two resonant capacitors have to be precisely matched for good results, which can be impaired by the components' tolerances and that would require cumbersome capacitive trimming. In this sense, the advantage of **B1** is that no additional component is required. Furthermore, this simple configuration still offers a sensitivity comparable to, e.g., **B3** and it allows using higher excitation frequencies.

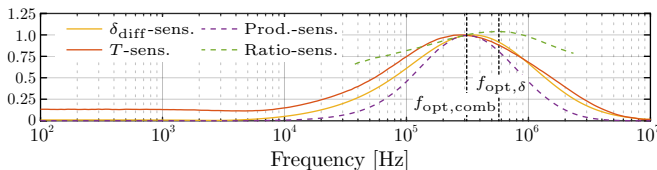


Fig. 7.12: Sensitivity curves extracted from the data of **Fig. 7.11** for the configuration **B1**. Each curve is normalized to its maximum. With the product curve and the ratio curve it is possible to identify the optimal excitation frequencies for combined or δ_{diff} -only sensitivity. The ratio curve is calculated only for values of the δ_{diff} -sensitivity curve > 0.25 .

7.5.3 Amplification and Demodulation Stage

Before processing $U_{\text{br,out}}$ further, a difference amplifier is employed at the output of the bridge. Typically an instrumentation amplifier is used, due to its high input impedance and common mode rejection ratio. The amplified signal is then demodulated with *coherent demodulation*, in order to preserve information on its sign. Coherent demodulation is realized by multiplying $U_{\text{br,out}}$ with the excitation signal U_{exc} (the carrier). Finally, the resulting $2 \cdot f_{\text{exc}}$ components in the multiplied signal are removed by a low-pass filter $H(s)$, with a cutoff frequency chosen, e.g., a decade before f_{exc} . This way, only the low frequency information about $\delta_{\text{diff}}(t)$ is retained. Importantly, provided that all the previous stages are designed to achieve a sufficiently high bandwidth (e.g., at least one decade larger than f_{exc}), the final measurement bandwidth of the ECS is only defined by the cutoff frequency of the low-pass filter. Quadrature demodulation is realized with an additional channel, which employs a 90° phase-shifted version of the carrier. With the combined information from the *in-phase* (I -) and *quadrature* (Q -) channels, the modulating signal can be fully recovered. In fact, it can be easily verified that the I - and Q - voltages U_I and U_Q correspond to the real and imaginary components of the complex phasor $U_{\text{br,out}}$ scaled by a factor 0.5 and hence

$$\delta_{\text{diff}}(t) \propto |U_{\text{br,out}}|(t) = 2 \sqrt{U_I^2(t) + U_Q^2(t)}. \quad (7.17)$$

Finally, the demodulated U_I and U_Q are the signals that have to be measured or sampled by an ADC. If the gain of the instrumentation amplifier is adjusted to fully utilize the input range of the ADC, the final resolution of the ECS is defined by the number of bits of the ADC. Clearly, bridge configurations that offer a large sensitivity will result in a better signal-to-noise ratio.

7.5.4 Realized Measurement/Evaluation Board

The proposed measurement circuit is implemented with a hardware evaluation board prototype, shown in **Fig. 7.13**. The excitation stage consists of a stimulus generator followed by a driving stage, which can supply the bridge with sufficient current. In order to allow for the maximum flexibility during commissioning of the ECS, the stimulus generator is the Direct Digital Synthesizer *AD9833* by *Analog Devices*. This IC is very simple to use and it can be programmed via SPI to generate sine, square or triangular voltage waveforms with frequencies up to 12.5 MHz and a resolution of 0.1 Hz. The

generated signal is pre-processed with a RC high-pass filter (15 Hz cutoff) for DC removal, and then pre-amplified to an amplitude of 1 V, which matches the input specifications of the analog multiplier. In fact, this is the signal used later as demodulation carrier. The 90° phase-shifted carrier for the Q -channel is also generated exactly in the same way, with a second $AD9833$. The driving amplifier is configured with a gain of 2.5, thus outputting the excitation voltage U_{exc} with an amplitude of 2.5 V. The AC differential Wheatstone bridge follows, implemented in such a way that all the possible bridge configurations (cf. **Fig. 7.11**) can be realized. Although monolithic solutions exist, the instrumentation amplifier is realized with three op-amps in order to guarantee high bandwidth (above 10 MHz). The gain of the instrumentation amplifier is adjustable with a 2 k Ω precision trimmer resistor, in order to match the input voltage levels of the analog multiplier (± 1 V) for the largest $\delta_{\text{diff}} = \pm 1$ mm. For each of the two demodulation channels, the analog multiplier takes the amplified version of $U_{\text{br,out}}$ and the pre-amplified U_{exc} as inputs. Each product signal is then filtered with an active 4th order lowpass filter in a *Multi-Feedback* configuration [112]. The chosen cutoff frequency is 30 kHz. Additionally, this stage features a gain of 2 to compensate the 0.5 factor in-

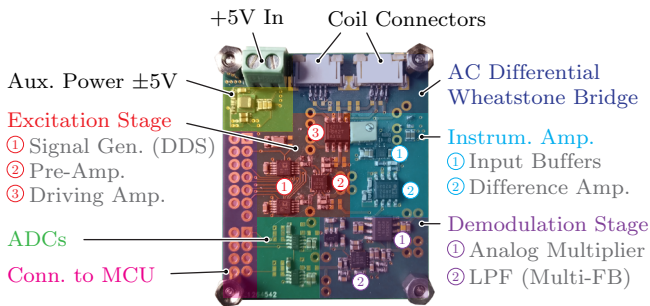


Fig. 7.13: Realized PCB prototype of the measurement/evaluation board. The board is provided with a single $U_{\text{DC}} = 5$ V power supply, from which a dual ± 5 V power supply is generated by the auxiliary power stage ($LMZ21701$ and $TPS63700$, Texas Instruments). The excitation stage uses a $LTC6227$ (Analog Devices) for pre-amplification and a $THS4211$ (Texas Instruments) to drive the coils. The instrumentation amplifier is realized with two $LTC6228$ as input buffers and a $AD8099$ for the difference amplifier (very good CMRR, -105 dB up to 1 MHz). The demodulation stage uses the $AD835$ (Analog Devices) four-quadrant analog multiplier and another $LTC6227$ for the active lowpass filter.

troduced by demodulation and a 2.5 V level shift to obtain a positive output signal. This way, the two demodulated I - and Q - voltages can be sampled with the 12-bit ADC $LTC2313$, which has an input voltage range from 0 V to 4.096 V. Therefore, with the gain of the instrumentation amplifier adjusted to get a ± 1 V output for $\delta_{\text{diff}} = \pm 1$ mm, the final sensitivity is $1 \text{ mV}/\mu\text{m}$, which with the given 12-bits quantization and input range of the $LTC2313$ results in a displacement resolution of $1 \mu\text{m}$.

7.6 Measurements and Results

The impedance variations were verified with the realized PCB-embedded excitation coil in **Sec. 7.3** for different values of the air gap δ . In this section, the proposed measurement circuit, implemented with the realized evaluation board, is verified instead.

7.6.1 Measurement Circuit Verification

The functionality of the measurement circuit is verified with both *static* and *dynamic* measurements.

Static Measurements for Different Temperatures

As the name suggests, the static measurements are realized for fixed values of the differential position δ_{diff} . By sweeping the excitation frequency and plotting on the complex plane the measured values of U_I and U_Q , it is possible to obtain the experimental version of the bridge output plots of **Fig. 7.11**, scaled by the constant gain of the instrumentation amplifier. Also the temperature T is varied from 25°C to 100°C . With the following set of measurements, the functionality of the measurement circuit (excitation, differential bridge configuration, demodulation) is verified completely.

First of all, multiple sample buildups are prepared as described in **Sec. 7.3** for the differential positions $\delta_{\text{diff}} = \{0.5, 0.75, 1\}$ mm and placed in an oven with controllable temperature. They are connected through a hole in the wall of the oven to the evaluation board, which is placed outside of the oven as close as possible. For each measurement, all the sample buildups are first heated up to the desired temperature. Then, a pair of sample buildups is connected to the evaluation board and a frequency sweep from 10 kHz to 10 MHz and 40 points per decade is automatically performed. This is done by commanding the desired frequency to the signal generators and then

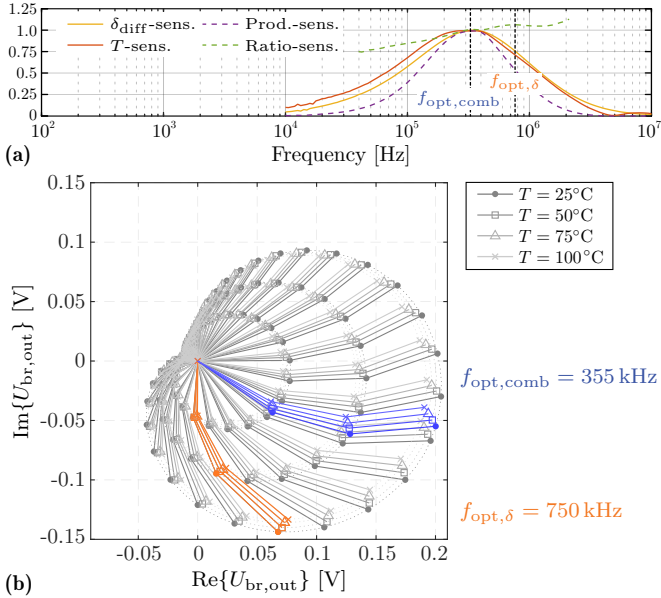


Fig. 7.14: Experimental verification of the evaluation board implementing the bridge configuration **B1**. **(a)** Sensitivity curves (δ_{diff} -, T -, product and ratio) extracted from the measurements, each normalized to its maximum. The optimal excitation frequencies for combined or δ_{diff} -only sensitivity are indicated. **(b)** Complex plane with the gain of the instrumentation amplifier to reconstruct the bridge output voltage phasor $U_{\text{br,out}}$. The measurements are performed automatically for values of $f = \omega/2\pi$ logarithmically evenly spaced between 10 kHz and 10 MHz with 40 points per decade, $\delta_{\text{diff}} = \{0.5, 0.75, 1\}$ mm and $T = \{25, 50, 75, 100\}$ °C.

acquiring 100 samples with both I - and Q - channels ADCs, which are then averaged. In the process, some intermediate signals, like, e.g., U_{exc} and the output of the instrumentation amplifier are monitored with an oscilloscope. When the measurement is completed, the next pair of sample buildups is connected, a certain time is waited in order for their temperature to settle again to the desired value and finally the routine is restarted. The results are visualized in **Fig. 7.14** for the prototypical case with 0.2 mm thick stainless steel shield and 0.5 mm thick aluminum target and the bridge configuration **B1**. The 2.5 V level shift introduced by the low-pass stage is removed by measuring the ADC readings for no excitation and removing such offset from 168

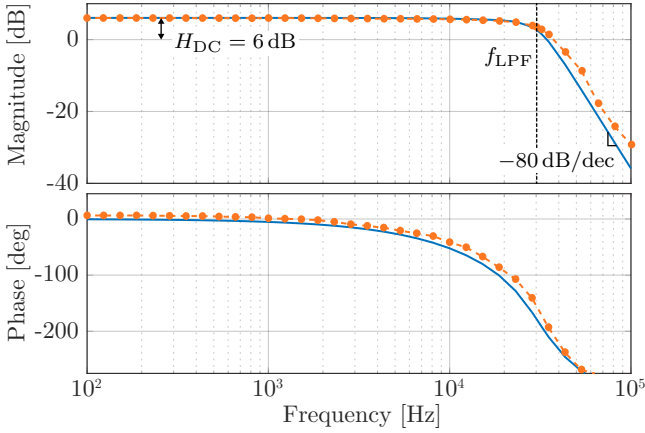


Fig. 7.15: Experimental Bode plot verifying the transfer function $H(s)$ of the low-pass stage used after the analog multiplier for amplitude demodulation. The blue line is obtained from the analytic transfer function. The measurements confirm the expected DC gain, cutoff frequency and a fourth-order low-pass characteristic.

the measured data. Additionally, in order to recover the original $U_{br,out}$ and allow a more direct comparison with **Fig. 7.11 (a.ii)**, the measurements are scaled down by the gain of instrumentation amplifier, which is measured experimentally for a test excitation and is equal to $G_{InA} = 1.5 \text{ V/V}$ in this case, and by a factor 2.5 because of the $\pm 2.5 \text{ V } U_{exc}$. **Fig. 7.14 (a)** shows the sensitivity curves introduced in **Fig. 7.12**, which are extracted from the measured data plotted on the complex plane in **Fig. 7.14 (b)**. The optimal excitation frequency $f_{opt,comb} = 355 \text{ kHz}$ is close to the expected value of 299 kHz . However, $f_{opt,\delta} = 750 \text{ kHz}$ is about 33 % off. This can be explained by the fact that the ratio-sensitivity curve in **Fig. 7.14 (a)** is relatively flat, and hence its maximum can deviate strongly from the predicted one in **Fig. 7.12**. Also the temperature's influence is visible and measurable if two demodulation channels are used. With the additional points for 50°C and 75°C , it can also be verified that the voltage varies smoothly within the two boundary curves.

Dynamic Measurements and Bandwidth Verification

As a final step, the measurement bandwidth of the realized ECS is verified with an experimental Bode plot. As mentioned, the low-pass filter of the demodulation stage is the one defining the final ECS bandwidth. For this reason,

this verification can be conducted electrically with a signal generator. In particular, the $U_{br,out}$ resulting from a target moving sinusoidally can be emulated by a sinusoidal carrier at the frequency f_{exc} with double-sideband amplitude modulation (DSB-AM). The carrier's frequency is fixed to $f_{exc} = 300$ kHz and its amplitude is 0.4 V, chosen together with the gain of the instrumentation amplifier $G_{InA} = 2.5$ V/V to get a ± 1 V output. The frequency of the modulating sine wave is swept from 100 Hz to 100 kHz with 11 points per decade. The ± 1 V carrier used for demodulation by the multiplier is provided by the same external generator, in order to guarantee synchronization between the signals. The output of the low-pass filter is a sine wave with the same frequency as the modulating signal, as expected. For each frequency, its amplitude is measured (which, compared to the unitary voltage input directly gives the gain of $H(s)$), together with the phase-shift with respect to the DSB-AM modulating signal. **Fig. 7.15** shows the obtained experimental Bode plot. The analytic transfer function for the Multi-Feedback active filter configuration is given in [112]. Two of such second-order filter stages are cascaded, with the values of the passive components selected to yield a DC gain $H_{DC} = 6$ dB, a cutoff frequency of $f_{LPF} = 30$ kHz and an overall fourth-order low-pass characteristic with -80 dB slope beyond f_{LPF} . All these characteristics are verified by the measurements. Consequently, the final ECS measurement bandwidth lies approx. one decade before f_{LPF} , i.e., $f_{ECS} \approx 3$ kHz.

7.7 Summary

This chapter discusses the design of an Eddy-Current Sensor (ECS) measuring the position of a moving conductive target located behind another fixed conductive shield. The analysis previously started with the aid of FEM simulations in [113] is now extended and completed with a full analytical transformer model, which describes the impedance variations of the sensor's excitation coil for varying frequency and air gap and allows calculating the optimal excitation frequencies, thus allowing to design optimally the excitation coil to maximize, e.g., position sensitivity. Then an investigation on the temperature's influence on the sensor's output is conducted, which is a relevant problem given the underlying application. Temperature particularly affects the resistive part of the impedance variations, so it has to be taken into account also while selecting a sensor interface. The most suitable measurement circuit is a differential AC Wheatstone bridge, which is analyzed thoroughly to find the optimal excitation frequencies which result in the maximum output voltage. Finally, a measurement setup consisting of a hardware prototype of

the evaluation board, the excitation coil and various thin metallic samples is realized. The results verify the functionality of the measurement circuit, of the sensor concept itself and its achievable bandwidth. With a 30 kHz measurement bandwidth, a sensitivity of $1 \text{ mV}/\mu\text{m}$ and $1 \mu\text{m}$ resolution, the studied ECS is applicable as a highly-dynamic position measurement system for entirely sealed MBs. In future work, stable operation of AMBs using the proposed ECS can be demonstrated experimentally with a hardware prototype of a sealed actuator. In this context, the exact number of sensors required and their placement will be analyzed. Such experimental setup would also allow to investigate the impact of disturbing magnetic fields coming from the stator's winding on the proposed ECS.



Conclusion and Outlook

NEXT-generation Total Artificial Hearts (TAHs) need novel pumping principles and designs that could improve their durability, reliability, and hemocompatibility, paving the way to full implantation. The novel TAH *ShuttlePump* is a promising example, but, as seen, it comes at the cost of a more advanced and highly integrated Linear Rotary Actuator (LiRA) drive system. This work addressed its design and experimental verification, overcoming numerous challenges to satisfy all the stringent constraints and requirements imposed by the application.

8.1 Summary and Findings

The content of this thesis is briefly summarized in the following, highlighting the most significant results.

The requirements identified in the course of the preliminary feasibility studies by the project partners at *Charité Berlin* and the *Medical University of Vienna* were discussed in **Chapter 2**. The most relevant ones for the subsequent machine design were:

1. The required motion profile, with quasi-sinusoidal 8 mm-stroke linear motion, synchronized to continuous rotation at 90-300 rpm (i.e., 1.5-5 Hz operation). The targeted linear and rotary tracking accuracies were 1 mm and 5°, respectively;
2. The required axial force profile, peaking at 43 N, and the required continuous torque of 3.1 mNm;
3. The maximum 40 N radial load capability of the hydrodynamic bearing;

4. The limits in power losses (10 W), volume (maximum outer dimensions $\varnothing 70 \text{ mm} \times 105 \text{ mm}$), and mass (900 g).

From these requirements, the mechanical output power for the LA (3.6 W) and the RA (0.1 W) were obtained, which led to the decision to prioritize the design of the LA over the RA.

- ▶ The design of the LA was presented in **Chapter 3**. To maximize the active area for force generation, the chosen Permanent Magnet Synchronous Machine (PMSM) topology was a tubular LA. The Finite Element Method (FEM) optimization explored the crucial trade-off between ohmic power losses and radial magnetic attraction force. The final design was selected with the primary target of minimizing the ohmic losses within the maximum radial pull design limit of 25 N. The results of the experimental verification confirmed the predicted machine constant profile, with a peak of 27.5 N/A. Over a period of operation, the resulting average ohmic losses amount to 7.9 W. The radial attraction force measured at 140 μm displacement is 23.8 N.
- ▶ The design of the RA was discussed in **Chapter 4**. This was split in two modules placed at the two sides of the designed LA. Due to the tight spatial constraints, a PMSM configuration with only a partial coverage of both the rotor PMs and the stators had to be chosen. This introduces a significant cogging torque component. FEM simulations were used to ensure that the RA can generate the required 3.1 mN m torque on average and to investigate the trade-off between cogging-induced speed ripple and ohmic losses. Furthermore, the 3D FEM simulations of the complete LiRA confirmed that the RA does not have any negative effect (increased axial cogging or reduced force generation) on the LA. The experimental measurements on the RA prototype closely verified the torque profile predicted by FEM. The required torque can be provided with 324 mW of power losses.
- ▶ The design of the linear-rotary ECS was the topic of **Chapter 5**. The sensor was obtained by extending a commercially available rotary sensor with two post-processing options to extract also the linear position information. The amplitude-based option is simple to implement and uses the same measurement signals as for the rotary position. The frequency-based option instead allows trading off bandwidth for measurement accuracy. The realized ECS prototype offers position accuracies below 100 μm and around 5°, with adequately large bandwidth up to 10 kHz.

- ▶ Simultaneous linear-rotary motion control of the LiRA was finally demonstrated in **Chapter 6**. The current and position controllers were designed based on the derived electromechanical dynamic model of the LiRA and implemented digitally in the realized inverter and control unit. The achieved linear positioning accuracies were of 0.38 mm for no load operation, and 0.89 mm (advantageously making use of a disturbance observer) for nominal operation under strong axial disturbance, provided by the controllable load. Simultaneously, the rotary position is kept within the specified tolerance band of $\pm 5^\circ$.
- ▶ **Chapter 7** complemented the work with a focus on contactless sensing, presenting an ECS measuring through a conductive barrier. Based on the described impedance variations of the sensor's excitation coil, design rules for the ECS were provided, as well as a procedure to design the coil to maximize position sensitivity. The influence of temperature on the sensor's output was investigated, showing that it could cause a large measurement error. With the selected differential AC Wheatstone bridge, it is possible to distinguish between position and temperature variations. It was possible to distinguish two optimal excitation frequencies: one for which temperature variations have the least effect, and one for which both variations can be captured. The results verified the functionality of the measurement circuit, the sensor concept itself, and the achievable bandwidth. The considered design offers a 30 kHz measurement bandwidth, a sensitivity of 1 mV/mm and 1 μ m resolution. Hence, the studied ECS can be used not just for the *ShuttlePump* in presence of a metallic enclosure, but also for stabilization of entirely sealed active magnetic bearings.

8.2 Outlook and Future Research

The obtained results clearly indicate that the designed LiRA drive system is adequate to enable the pumping operation of the *ShuttlePump*. Clearly, this is a first design iteration that leaves space for improvements. Some of these, together with further ideas and observations on the overall *ShuttlePump* concept are collected in the following list.

- ▶ The most delicate aspect of the *ShuttlePump* may be the radial load capabilities of its hydrodynamic bearing. The predicted limit of 40 N needs to be thoroughly verified with experimental measurements for nominal

operation and most importantly with the realized LiRA. The radial magnetic attraction force that this introduces, and that was analyzed during the LA design, was in fact intentionally kept to a conservative limit of 25 N for the maximum radial displacement of 140 μm . An unexpected hydraulic radial force disturbance might destabilize the hydrodynamic bearing, with a potential damage of the pump's inner surfaces due to contact between the piston and the enclosure. In this context, especially challenging can be the startup phase from a standstill piston, when the bearing still needs to be established. An interesting option could be the design of an auxiliary active magnetic bearing helping to counteract strong piston eccentricities.

- ▶ As known from scaling laws for electric machines, also appearing in the first principle derivations of **Chapter 3**, there is a direct proportionality between generated force and volume. Therefore, it might be reasonable to consider a different balance between operational frequency (linear/axial speed) and required force for the same mechanical output power. If slightly higher operational frequencies can be allowed, with limited impact to blood damage due to the increased shear rates, the volume of the *ShuttlePump* can be reduced. A smaller LiRA would be lighter and more compact, making the device suitable for a larger patients population or even for pediatric use. Furthermore, the radial attraction forces introduced by the LiRA would also be reduced, improving the stability of the hydrodynamic bearing. The price to pay due to the higher operational frequencies would be increased AC losses (requiring, e.g., lamination of the stator cores to limit the effect of eddy currents) and larger bandwidths for position and current control.
- ▶ For the first animal tests, the power supply and the inverter and control units will be extracorporeal, with a drive line connecting to the implanted pump. However, for the final version of the *ShuttlePump*, a transcutaneous energy transfer system can be foreseen. This should be designed together with the battery management system and a new version of the inverter and control unit. In particular, aiming for an overall miniaturization, the control unit needs to be replaced with a simpler and more compact alternative.
- ▶ As discussed for the RA design in **Chapter 4**, the undesirable tolerance air gap at the bottom of the stator teeth yields a drastic reduction in magnetic flux and hence generated torque. A different construction of the rotary stator would be highly beneficial. For instance, each

tooth could be inserted in the stator yoke through a matching cavity. This measure would more move the tolerance air gap in a less critical location.

- ▶ To simplify its realization, the back iron of the mover was built out of multiple simple rings. However, following the distribution of the magnetic flux density, it is certainly possible to shape its thickness to be large only where strictly needed (e.g., at the center of the mover, between the two LA magnet arrays). This way, a large amount of magnetic material can be removed, and the total weight of the piston can be sensibly reduced. Furthermore, other mover realizations, e.g., using Interior Permanent Magnets (IPM), can be considered. In that case, custom PMs would be required.
- ▶ For the linear-rotary ECS, although the alternative frequency-based option to measure the linear position was proposed and studied, it was finally not used for control. It would be of interest to look further into this option and compare the tracking results.
- ▶ The primary optimization objective of the LiRA was not efficiency, and it is anyway a common challenge to attain high values for linear motors. Nevertheless, this could be improved, also given that the system is battery-powered.
- ▶ During the early stage of this work, i.e., while exploring suitable LiRA concepts, the possibility of making one of the two motions passive was explored. This might be done exploiting reluctance forces with a special magnetic design. For the case at hand, this option was excluded, but its potential to halve the number of phases should be considered for future or alternative designs, e.g. with lower axial force requirements.

Extending the outlook beyond the scope of the *ShuttlePump*, a few further considerations on the design process of MCS devices with electromechanical actuation can be made. As exemplified by this work, the multi-disciplinary collaboration behind the *ShuttlePump* was essential to combine the expertise coming from so diverse research fields. In this context and learning from the experience of this project, it might be beneficial to establish the co-design process of the system in a different way. In particular, more space could be given to the electrical engineer to think of and negotiate the motor requirements early stage, already during the definition of the pumping concept.

In conclusion, the pursuit of heart replacement solutions is ceaseless. Recently, two xenotransplantations involving hearts from different species were performed successfully. However, despite the success of the procedures, the patients' lives could not be saved. In comparison, the decades of research and experience supporting the development of TAH and MCS technologies have accelerated their maturity. This is evident in the numerous successful implantations of LVADs as a notable example. The hope of tackling the ever-growing public health problem of heart failure with improved long-term treatment remains strong.

Appendices

A

Measurements of the Undesired Air Gaps in the RA

In the following, the measurements of the undesired assembly tolerance air gap lengths, discussed in **Sec. 4.5.3**, are reported. The air gap lengths are measured with two methods: a direct one (mechanical) and an indirect one (magnetic). For the first method, the inner radius of the tested RA module is measured at several locations, as indicated in **Fig. A.1 (a)**. This is done using the measurement probe of the 5-axis CNC machine *DMU 40 monoBlock* from *Deckel Maho*, which offers an accuracy of $5\ \mu\text{m}$. The difference with

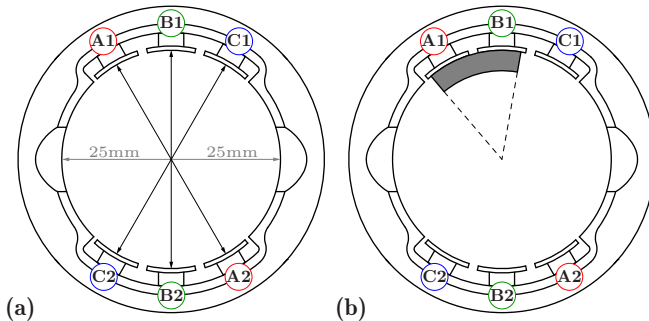


Fig. A.1: (a) Measured inner radii of the RA to find the length of the introduced tolerance air gaps. (b) Indirect (magnetic) method to estimate the length of the introduced tolerance air gaps. Two teeth are magnetically shorted together with an arc-shaped piece of magnetic material, and the inductance of one of the coils in the magnetic circuit is measured.

respect to the nominal $r_{\text{in}} = 25$ mm corresponds to the introduced tolerance air gap length d_{tol} . The measurements are reported in **Tab. A.1**. For the second method, each tooth is made part of a magnetic circuit, where the tolerance gap is the main air gap. This is done by magnetically shorting two teeth against each other with a small piece of magnetic material, as shown in **Fig. A.1 (b)**. This way, by measuring the inductance of a stator coil $L_{\text{meas},i}$, the tolerance air gap length can be calculated as

$$d_{\text{tol},i} = \frac{\mu_0 N_{\text{R}}^2 A_{\text{tooth}}}{2 L_{\text{meas},i}}. \quad (\text{A.1})$$

The measurements obtained with this method are reported in **Tab. A.2**. Finally, an average value of $d_{\text{tol}} = 0.1$ mm is considered for **Sec. 4.5.3** and **Sec. 4.6**.

Tab. A.1: Measured assembly tolerance air gap lengths (direct method).

Tooth	r_{in} [mm]	d_{tol} [mm]	Tooth	r_{in} [mm]	d_{tol} [mm]
A1	24.809	0.191	A2	24.863	0.137
B1	24.739	0.261	B2	24.911	0.089
C1	24.839	0.161	C2	24.877	0.123

Tab. A.2: Estimated assembly tolerance air gap lengths (indirect method). The underlined tooth indicates that the coil mounted on it is measured.

Connection	L [mH]	d_{tol} [mm]	Connection	L [mH]	d_{tol} [mm]
<u>A1</u> to B1	10.02	0.107	<u>A2</u> to B2	11.03	0.097
<u>B1</u> to A1	9.89	0.109	<u>B2</u> to A2	10.73	0.100
<u>B1</u> to C1	10.08	0.107	<u>B2</u> to C2	10.56	0.102
<u>C1</u> to B1	12.34	0.087	<u>C2</u> to B2	11.73	0.092

B

Post-Processing of the Linear-Rotary Measurement Signals

The measured signals from the two ECSs of the *ShuttlePump* are combined to obtain a final measurement of the linear position z_{meas} and the rotary position φ_{meas} . To always use the higher quality signals measured by the sensor with the closest target, the simplest approach is to use a linear weighting of the form

$$z_{\text{meas}} = (8 \text{ mm} - z_{\text{S1}})(1 - w_z) - (8 \text{ mm} + z_{\text{S2}}) w_z, \quad (\text{B.1})$$

with the weight w_z depending on the (previous-step) axial position defined as

$$w_z = \begin{cases} 1, & \text{for } z_{\text{meas}} \leq -z_{\text{comb}} \\ \frac{z_{\text{comb}} - z_{\text{meas}}}{2 z_{\text{comb}}}, & \text{for } -z_{\text{comb}} < z_{\text{meas}} < z_{\text{comb}} \\ 0 & \text{for } z_{\text{meas}} \geq z_{\text{comb}} \end{cases}, \quad (\text{B.2})$$

where z_{comb} defines the axial position range $[-z_{\text{comb}}, z_{\text{comb}}]$ for which the sensors measurements are linearly combined. In the presented results, $z_{\text{comb}} = 6 \text{ mm}$ is used, and the resulting weight w_z is shown in **Fig. B.1**. As mentioned in **Sec. 6.6**, this post-processing method could introduce measurement disturbances especially around the zero-crossings of the linear position, which can be significant if the calibration is not performed correctly.

For what concerns the rotary angle φ_{meas} , the output angles $\varphi_{\{S1, S2\}}$ calculated by (6.1) are in the range $[-\pi, \pi]$, so they are first conditioned to $[0, 2\pi]$. Then, the same weighting method as for z_{meas} is used, hence

$$\varphi_{\text{meas}} = (1 - w_\varphi) \cdot \varphi_{\text{S1}} + w_\varphi \cdot (\varphi_{\text{S2}} - \varphi_{\text{mis}}), \quad (\text{B.3})$$

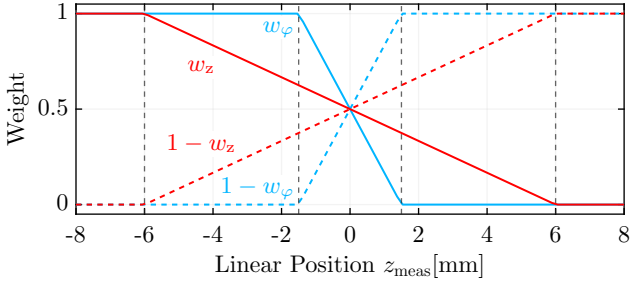
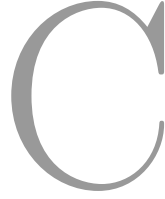


Fig. B.1: Weights w_z and w_φ , as well as the curves $(1 - w_z)$ and $(1 - w_\varphi)$, used to linearly combine the sensors signals $z_{\{S1,S2\}}$ in (6.2) and $\varphi_{\{S1,S2\}}$ in (6.1). The weights w_z and w_φ are calculated according to (B.2) with $z_{\text{comb}} = 6$ mm and $z_{\text{comb}} = 1.5$ mm, respectively.

with w_φ calculated according to (B.2) with $z_{\text{comb}} = 1.5$ mm as visible in **Fig. B.1**. This value proved to yield the best results experimentally. Finally, the misalignment correction offset φ_{mis} is also a crucial parameter, as the sensors might still provide a slightly different reading even though care is taken during mounting to adjust their relative position. If this is not carefully selected, a pronounced measurement disturbance appears in the measured rotary angle φ_{meas} , corresponding to the difference $\varphi_{S1} - \varphi_{S2}$.



Input Impedance of the Excitation Coil for the ECS Through the Walls

The complete analytical expression of the excitation coil's input impedance $Z_{c,in}(\omega, \delta)$ obtained from the equivalent transformer model in **Sec. 7.3.3** is reported:

$$Z_{c,in}(\omega, \delta) = \frac{Z_{\text{NUM}}(\omega, \delta)}{Z_{\text{DEN}}(\omega, \delta)}, \quad (\text{C.1})$$

where

$$\begin{aligned} Z_{\text{NUM}}(\omega, \delta) = & R_1 R_2 R_3 + j(L_1 R_2 R_3 + L_2 R_1 R_3 + L_3 R_1 R_2) \omega + \dots \\ & - (L_1 L_2 R_3 + L_1 L_3 R_2 + L_2 L_3 R_1 - L_1 L_2 R_3 k_{12}^2 - L_1 L_3 R_2 k_{13}^2 - L_2 L_3 R_1 k_{23}^2) \omega^2 + \dots \\ & - (L_1 L_2 L_3 - j L_1 L_2 L_3 k_{12}^2 - j L_1 L_2 L_3 k_{23}^2 - j L_1 L_2 L_3 k_{13}^2 + 2j L_1 L_2 L_3 k_{12} k_{13} k_{23}) \omega^3, \end{aligned} \quad (\text{C.2})$$

and

$$Z_{\text{DEN}}(\omega, \delta) = R_2 R_3 + j(L_2 R_3 + L_3 R_2) \omega + L_2 L_3 (k_{23}^2 - 1) \omega^2. \quad (\text{C.3})$$

Bibliography

- [1] P. Ponikowski, S. D. Anker, K. F. AlHabib, M. R. Cowie, T. L. Force, S. Hu, T. Jaarsma, H. Krum, V. Rastogi, L. E. Rohde, U. C. Samal, H. Shimokawa, B. Budi Siswanto, K. Sliwa, and G. Filippatos, “Heart Failure: Preventing Disease and Death Worldwide,” *ESC Heart Failure*, vol. 1, no. 1, pp. 4–25, 2014, DOI: [10.1002/ehf2.12005](https://doi.org/10.1002/ehf2.12005).
- [2] G. Savarese and L. H. Lund, “Global Public Health Burden of Heart Failure,” *Cardiac Failure Review*, vol. 3, no. 1, pp. 7–11, 2017, DOI: [10.15420/cfr.2016:25:2](https://doi.org/10.15420/cfr.2016:25:2).
- [3] N. Conrad, A. Judge, J. Tran, H. Mohseni, D. Hedgecott, A. P. Crespillo, M. Allison, H. Hemingway, J. G. Cleland, J. J. V. McMurray, and K. Rahimi, “Temporal Trends and Patterns in Heart Failure Incidence: a Population-Based Study of 4 Million Individuals,” *The Lancet*, vol. 391, no. 10120, pp. 572–580, 2018, DOI: [10.1016/S0140-6736\(17\)32520-5](https://doi.org/10.1016/S0140-6736(17)32520-5).
- [4] J. Stehlik, J. Kobashigawa, S. A. Hunt, H. Reichenspurner, and J. K. Kirklin, “Honoring 50 Years of Clinical Heart Transplantation in Circulation: In-Depth State-of-the-Art Review,” *Circulation*, vol. 137, no. 1, pp. 71–87, 2018, DOI: [10.1161/CIRCULATIONAHA.117.029753](https://doi.org/10.1161/CIRCULATIONAHA.117.029753).
- [5] L. H. Lund, K. K. Khush, W. S. Cherikh, S. Goldfarb, A. Y. Kucheryavaya, B. J. Levvey, B. Meiser, J. W. Rossano, D. C. Chambers, R. D. Yusen, and J. Stehlik, “The Registry of the International Society for Heart and Lung Transplantation: Thirty-Fourth Adult Heart Transplantation Report—2017; Focus Theme: Allograft Ischemic Time,” *The Journal of Heart and Lung Transplantation*, vol. 36, no. 10, pp. 1037–1046, 2017, DOI: [10.1016/j.healun.2017.07.019](https://doi.org/10.1016/j.healun.2017.07.019).
- [6] M. Fuchs, D. Schibilsky, W. Zeh, M. Berchtold-Herz, F. Beyersdorf, and M. Siepe, “Does the Heart Transplant Have a Future?” *European Journal of Cardio-Thoracic Surgery : Official Journal of the European Association for Cardio-Thoracic Surgery*, vol. 55, no. Suppl 1, pp. i38–i48, 2019, DOI: [10.1093/ejcts/ezz107](https://doi.org/10.1093/ejcts/ezz107).
- [7] K. S. Shah, M. M. Kittleson, and J. A. Kobashigawa, “Updates on Heart Transplantation,” *Current Heart Failure Reports*, vol. 16, no. 5, pp. 150–156, 2019, DOI: [10.1007/s11897-019-00432-3](https://doi.org/10.1007/s11897-019-00432-3).

- [8] M. C. Alraies and P. Eckman, "Adult Heart Transplant: Indications and Outcomes," *Journal of Thoracic Disease*, vol. 6, no. 8, pp. 1120–1128, 2014, DOI: [10.3978/j.issn.2072-1439.2014.06.44](https://doi.org/10.3978/j.issn.2072-1439.2014.06.44).
- [9] J. L. Vieira, H. O. Ventura, and M. R. Mehra, "Mechanical Circulatory Support Devices in Advanced Heart Failure: 2020 and Beyond," *Progress in Cardiovascular Diseases*, vol. 63, no. 5, pp. 630–639, 2020, DOI: [10.1016/j.pcad.2020.09.003](https://doi.org/10.1016/j.pcad.2020.09.003).
- [10] T. D. Ryan, J. L. Jefferies, F. Zafar, A. Lorts, and D. L. S. Morales, "The Evolving Role of the Total Artificial Heart in the Management of End-Stage Congenital Heart Disease and Adolescents," *ASAIO Journal*, vol. 61, no. 1, p. 8, 2015, DOI: [10.1097/MAT.000000000000156](https://doi.org/10.1097/MAT.000000000000156).
- [11] H. Hoshi, T. Shinshi, and S. Takatani, "Third-Generation Blood Pumps With Mechanical Noncontact Magnetic Bearings," *Artificial Organs*, vol. 30, no. 5, pp. 324–338, 2006, DOI: [10.1111/j.1525-1594.2006.00222.x](https://doi.org/10.1111/j.1525-1594.2006.00222.x).
- [12] J. A. Cook, K. B. Shah, M. A. Quader, R. H. Cooke, V. Kasirajan, K. K. Rao, M. C. Smallfield, I. Tchoukina, and D. G. Tang, "The Total Artificial Heart," *Journal of Thoracic Disease*, vol. 7, no. 12, 2015, DOI: [10.3978/j.issn.2072-1439.2015.10.70](https://doi.org/10.3978/j.issn.2072-1439.2015.10.70).
- [13] M. Samak, J. Fatullayev, A. Sabashnikov, M. Zeridouh, P. B. Rahmanian, Y.-H. Choi, J. Wippermann, T. Wahlers, B. Schmack, A. Ruhparwar, P. M. Dohmen, M. Karck, A.-F. Popov, A. R. Simon, and A. Weymann, "Past and Present of Total Artificial Heart Therapy: A Success Story," *Medical Science Monitor Basic Research*, vol. 21, pp. 183–190, 2015, DOI: [10.12659/MSMBR.895418](https://doi.org/10.12659/MSMBR.895418).
- [14] G. Sunagawa, D. J. Horvath, J. H. Karimov, N. Moazami, and K. Fukumachi, "Future Prospects for the Total Artificial Heart," *Expert Review of Medical Devices*, vol. 13, no. 2, pp. 191–201, 2016, DOI: [10.1586/17434440.2016.1136212](https://doi.org/10.1586/17434440.2016.1136212).
- [15] B. P. Griffith, R. L. Hardesty, R. L. Kormos, A. Trento, H. S. Borovetz, M. E. Thompson, and H. T. Bahnson, "Temporary Use of the Jarvik-7 Total Artificial Heart Before Transplantation," *New England Journal of Medicine*, vol. 316, no. 3, pp. 130–134, 1987, DOI: [10.1056/NEJM198701153160303](https://doi.org/10.1056/NEJM198701153160303).
- [16] P. Mohacsi and P. Leprince, "The Carmat Total Artificial Heart," *European Journal of Cardio-Thoracic Surgery: Official Journal of the European*

- Association for Cardio-Thoracic Surgery*, vol. 46, no. 6, pp. 933–934, 2014, DOI: [10.1093/ejcts/ezu333](https://doi.org/10.1093/ejcts/ezu333).
- [17] K. Valeske, C. Yerebakan, M. Mueller, and H. Akintuerk, “Urgent Implantation of the Berlin Heart Excor Biventricular Assist Device as a Total Artificial Heart in a Patient with Single Ventricle Circulation,” *The Journal of Thoracic and Cardiovascular Surgery*, vol. 147, no. 5, pp. 1712–1714, 2014, DOI: [10.1016/j.jtcvs.2014.01.012](https://doi.org/10.1016/j.jtcvs.2014.01.012).
- [18] G. Torregrossa, A. Anyanwu, F. Zucchetta, and G. Gerosa, “SynCardia: the Total Artificial Heart,” *Annals of Cardiothoracic Surgery*, vol. 3, no. 6, pp. 61 220–61 620, 2014, DOI: [10.3978/j.issn.2225-319X.2014.11.07](https://doi.org/10.3978/j.issn.2225-319X.2014.11.07).
- [19] B. Pelletier, S. Spiliopoulos, T. Finocchiaro, F. Graef, K. Kuipers, M. Laumen, D. Guersoy, U. Steinseifer, R. Koerfer, and G. Tenderich, “System Overview of the Fully Implantable Destination Therapy – ReinHeart - Total Artificial Heart,” *European Journal of Cardio-Thoracic Surgery*, vol. 47, no. 1, pp. 80–86, 2015, DOI: [10.1093/ejcts/ezu321](https://doi.org/10.1093/ejcts/ezu321).
- [20] R. D. Dowling, L. A. Gray, S. W. Etoch, H. Laks, D. Marelli, L. Samuels, J. Entwistle, G. Couper, G. J. Vlahakes, and O. H. Frazier, “The AbioCor Implantable Replacement Heart,” *The Annals of Thoracic Surgery*, vol. 75, no. 6, Supplement, pp. S93–S99, 2003, DOI: [10.1016/S0003-4975\(03\)00484-3](https://doi.org/10.1016/S0003-4975(03)00484-3).
- [21] D. Timms, J. Fraser, M. Hayne, J. Dunning, K. McNeil, and M. Percy, “The BiVACOR Rotary Biventricular Assist Device: Concept and In Vitro Investigation,” *Artificial Organs*, vol. 32, no. 10, pp. 816–819, 2008, DOI: [10.1111/j.1525-1594.2008.00633.x](https://doi.org/10.1111/j.1525-1594.2008.00633.x).
- [22] J. Glynn, H. Song, B. Hull, S. Withers, J. Gelow, J. Mudd, A. Starr, and R. Wampler, “The OregonHeart Total Artificial Heart: Design and Performance on a Mock Circulatory Loop,” *Artificial Organs*, vol. 41, no. 10, pp. 904–910, 2017, DOI: [10.1111/aor.12959](https://doi.org/10.1111/aor.12959).
- [23] F. A. Arabia, R. S. Cantor, D. A. Koehl, V. Kasirajan, I. Gregoric, J. D. Moriguchi, F. Esmailian, D. Ramzy, J. S. Chung, L. S. Czer, J. A. Kobashigawa, R. G. Smith, and J. K. Kirklin, “Interagency Registry for Mechanically Assisted Circulatory Support Report on the Total Artificial Heart,” *The Journal of Heart and Lung Transplantation*, vol. 37, no. 11, pp. 1304–1312, 2018, DOI: [10.1016/j.healun.2018.04.004](https://doi.org/10.1016/j.healun.2018.04.004).

- [24] F. D. Pagani, “Clinical Implications of the Total Artificial Heart: Adversity and Progress,” *The Journal of Heart and Lung Transplantation*, vol. 37, no. 11, pp. 1298–1300, 2018, DOI: [10.1016/j.healun.2018.07.019](https://doi.org/10.1016/j.healun.2018.07.019).
- [25] M. Granegger, T. Bierewirtz, M. Nicolai, and U. Kertzscher, “Blood Pump,” EU Patent WO/2022/049166, Mar 10, 2022.
- [26] T. Bierewirtz, K. Narayanaswamy, R. V. Giuffrida, T. Rese, D. Bortis, D. Zimpfer, J. W. Kolar, U. Kertzscher, and M. Granegger, “A Novel Pumping Principle for a Total Artificial Heart,” *IEEE Transactions on Biomedical Engineering*, pp. 1–10, 2023, DOI: [10.1109/TBME.2023.3306888](https://doi.org/10.1109/TBME.2023.3306888).
- [27] R. V. Giuffrida, R. Senti, J. W. Kolar, T. Bierewirtz, K. Narayanaswamy, M. Granegger, and D. Bortis, “Design and Realization of a Highly Compact Tubular Linear Actuator for a Novel Total Artificial Heart,” *IEEE Journal of Emerging and Selected Topics in Industrial Electronics*, vol. 4, no. 4, pp. 1010–1023, 2023, DOI: [10.1109/JESTIE.2023.3305939](https://doi.org/10.1109/JESTIE.2023.3305939).
- [28] R. V. Giuffrida, R. Senti, D. Bortis, T. Bierewirtz, K. Narayanaswamy, M. Granegger, and J. W. Kolar, “Spatially Highly Constrained Auxiliary Rotary Actuator for a Novel Total Artificial Heart,” *IEEE Open Journal of the Industrial Electronics Society*, vol. 4, pp. 732–747, 2023, DOI: [10.1109/OJIES.2023.3339838](https://doi.org/10.1109/OJIES.2023.3339838).
- [29] A. Oliveros, A. Guiseppi-Elie, and S. E. Sadow, “Silicon Carbide: A Versatile Material for Biosensor Applications,” *Biomedical Microdevices*, vol. 15, no. 2, pp. 353–368, 2013, DOI: [10.1007/s10544-013-9742-3](https://doi.org/10.1007/s10544-013-9742-3).
- [30] M. J. Chen, G. A. Pappas, D. Massella, A. Schlothauer, S. E. Motta, V. Falk, N. Cesarovic, and P. Ermanni, “Tailoring Crystallinity for Hemocompatible and Durable Peek Cardiovascular Implants,” *Biomaterials Advances*, vol. 146, p. 213288, 2023, DOI: [10.1016/j.bioadv.2023.213288](https://doi.org/10.1016/j.bioadv.2023.213288).
- [31] N. K. Ranganath, M. Rashidi, J. F. Antaki, K. G. Phillips, Z. N. Kon, D. E. Smith, A. Reyentovich, and N. Moazami, “Mechanical Blood-Immersed Bearings in Continuous-Flow Rotary Blood Pumps,” *ASAIO Journal*, vol. 66, no. 4, p. 343, 2020, DOI: [10.1097/MAT.0000000000000994](https://doi.org/10.1097/MAT.0000000000000994).
- [32] E. Potapov, F. Kaufmann, A. M. Scandroglio, and M. Pieri, “Pump Thrombosis,” in *Mechanical Circulatory Support in End-Stage Heart Failure: A Practical Manual*, A. Montalto, A. Loforte, F. Musumeci, T. Krabatsch,

- and M. S. Slaughter, Eds. Cham: Springer International Publishing, 2017, pp. 495–512.
- [33] J. K. Kirklin, D. C. Naftel, R. L. Kormos, F. D. Pagani, S. L. Myers, L. W. Stevenson, M. A. Acker, D. L. Goldstein, S. C. Silvestry, C. A. Milano, J. T. Baldwin, S. Pinney, J. Eduardo Rame, and M. A. Miller, “Interagency Registry for Mechanically Assisted Circulatory Support (intermacs) Analysis of Pump Thrombosis in the Heartmate II Left Ventricular Assist Device,” *The Journal of Heart and Lung Transplantation: The Official Publication of the International Society for Heart Transplantation*, vol. 33, no. 1, pp. 12–22, 2014, DOI: [10.1016/j.healun.2013.11.001](https://doi.org/10.1016/j.healun.2013.11.001).
- [34] *Implants for Surgery - Active Implantable Medical Devices - Part 1: General Requirements for Safety, Marking and for Information to be Provided by the Manufacturer*, ISO Std. 14708-1:2000, 2014.
- [35] J. X. Wang, J. R. Smith, and P. Bonde, “Energy Transmission and Power Sources for Mechanical Circulatory Support Devices to Achieve Total Implantability,” *The Annals of Thoracic Surgery*, vol. 97, no. 4, pp. 1467–1474, 2014, DOI: [10.1016/j.athoracsur.2013.10.107](https://doi.org/10.1016/j.athoracsur.2013.10.107).
- [36] O. Knecht, R. Bosshard, and J. W. Kolar, “High-Efficiency Transcutaneous Energy Transfer for Implantable Mechanical Heart Support Systems,” *IEEE Transactions on Power Electronics*, vol. 30, no. 11, pp. 6221–6236, 2015, DOI: [10.1109/TPEL.2015.2396194](https://doi.org/10.1109/TPEL.2015.2396194).
- [37] F. Boehning, D. Timms, P.-L. Hsu, T. Schmitz-Rode, and U. Steinseifer, “Experimental and Analytical Performance Evaluation of Short Circular Hydrodynamic Journal Bearings Used in Rotary Blood Pumps,” *Artificial Organs*, vol. 37, no. 10, pp. 913–920, 2013, DOI: [10.1111/aor.12076](https://doi.org/10.1111/aor.12076).
- [38] S. Mirić, R. Giuffrida, G. Rohner, D. Bortis, and J. W. Kolar, “Design and Experimental Analysis of a Selfbearing Double-Stator Linear-Rotary Actuator,” in *Proc. of the IEEE International Electric Machines & Drives Conference (IEMDC)*, 2021, pp. 1–8, DOI: [10.1109/IEMDC47953.2021.9449501](https://doi.org/10.1109/IEMDC47953.2021.9449501).
- [39] L. Xie, J. Si, Y. Hu, H. Feng, and K. Ni, “Characteristics Analysis of the Motions of the Two-Degree-of-Freedom Direct Drive Induction Motor,” *IEEE Transactions on Industrial Electronics*, vol. 67, no. 2, pp. 931–941, 2020, DOI: [10.1109/TIE.2019.2898590](https://doi.org/10.1109/TIE.2019.2898590).

- [40] A. Z. Shukor and Y. Fujimoto, "Direct-Drive Position Control of a Spiral Motor as a Monoarticular Actuator," *IEEE Transactions on Industrial Electronics*, vol. 61, no. 2, pp. 1063–1071, 2014, DOI: [10.1109/TIE.2013.2262757](https://doi.org/10.1109/TIE.2013.2262757).
- [41] P. Jin, H. Lin, S. Fang, and S. L. Ho, "Decoupling Control of Linear and Rotary Permanent Magnet Actuator Using Two-Directional dq Transformation," *IEEE Transactions on Magnetics*, vol. 48, no. 10, pp. 2585–2591, 2012, DOI: [10.1109/TMAG.2012.2202321](https://doi.org/10.1109/TMAG.2012.2202321).
- [42] Z. Ling, J. Ji, J. Wang, and W. Zhao, "Design Optimization and Test of a Radially Magnetized Magnetic Screw with Discretized PMs," *IEEE Transactions on Industrial Electronics*, vol. 65, no. 9, pp. 7536–7547, 2018, DOI: [10.1109/TIE.2017.2740820](https://doi.org/10.1109/TIE.2017.2740820).
- [43] D. Timms, "A Review of Clinical Ventricular Assist Devices," *Medical Engineering & Physics*, vol. 33, no. 9, pp. 1041–1047, 2011, DOI: [10.1016/j.medengphy.2011.04.010](https://doi.org/10.1016/j.medengphy.2011.04.010).
- [44] N. Bianchi, S. Bolognani, D. Dalla Corte, and F. Tonel, "Tubular Linear Permanent Magnet Motors: An Overall Comparison," in *Record of the 37th IEEE Industry Applications Society Annual Meeting (IAS)*, vol. 2, 2002, pp. 1266–1273, DOI: [10.1109/IAS.2002.1042721](https://doi.org/10.1109/IAS.2002.1042721).
- [45] H. Hu, J. Zhao, X. Liu, Y. Guo, and J. Zhu, "No-Load Magnetic Field and Cogging Force Calculation in Linear Permanent-Magnet Synchronous Machines with Semiclosed Slots," *IEEE Transactions on Industrial Electronics*, vol. 64, no. 7, pp. 5564–5575, 2017, DOI: [10.1109/TIE.2016.2645509](https://doi.org/10.1109/TIE.2016.2645509).
- [46] A. Souissi, I. Abdennadher, and A. Masmoudi, "An Approach to Reduce the Cogging Force in Tubular Linear PM Synchronous Machines," in *Proc. of the 10th International Conference on Ecological Vehicles and Renewable Energies (EVER)*, 2015, pp. 1–7, DOI: [10.1109/EVER.2015.7112998](https://doi.org/10.1109/EVER.2015.7112998).
- [47] T. Jahns and W. Soong, "Pulsating Torque Minimization Techniques for Permanent Magnet AC Motor Drives - A Review," *IEEE Transactions on Industrial Electronics*, vol. 43, no. 2, pp. 321–330, 1996, DOI: [10.1109/41.491356](https://doi.org/10.1109/41.491356).
- [48] G. Niedermeier and M. Esguerra, "Measurement of Power Losses with DC-Bias – The Displacement Factor," in *Proc. of the 41st International Conference on Power Conversion and Intelligent Motion (PCIM)*, 2000.

-
- [49] T. T. Overboom, J. W. Jansen, E. A. Lomonova, and F. J. F. Tacke, "Design and Optimization of a Rotary Actuator for a Two-Degree-of-Freedom $z\phi$ -Module," *IEEE Transactions on Industry Applications*, vol. 46, no. 6, pp. 2401–2409, 2010, DOI: [10.1109/TIA.2010.2073430](https://doi.org/10.1109/TIA.2010.2073430).
- [50] J. Si, H. Feng, L. Ai, Y. Hu, and W. Cao, "Design and Analysis of a 2-DoF Split-Stator Induction Motor," *IEEE Transactions on Energy Conversion*, vol. 30, no. 3, pp. 1200–1208, 2015, DOI: [10.1109/TEC.2015.2418578](https://doi.org/10.1109/TEC.2015.2418578).
- [51] K. Guo and Y. Guo, "Design Optimization of Linear-Rotary Motion Permanent Magnet Generator With E-Shaped Stator," *IEEE Transactions on Applied Superconductivity*, vol. 31, no. 8, pp. 1–5, 2021, DOI: [10.1109/TASC.2021.3089121](https://doi.org/10.1109/TASC.2021.3089121).
- [52] R. V. Giuffrida, J. W. Kolar, and D. Bortis, "Eddy-Current Linear-Rotary Position Sensor for an Implantable Total Artificial Heart," in *Proc. of the 25th International Conference on Electrical Machines and Systems (ICEMS)*, 2022, pp. 1–6, DOI: [10.1109/ICEMS56177.2022.9982894](https://doi.org/10.1109/ICEMS56177.2022.9982894).
- [53] J. Cros and P. Viarouge, "Synthesis of High Performance PM Motors with Concentrated Windings," *IEEE Transactions on Energy Conversion*, vol. 17, no. 2, pp. 248–253, 2002, DOI: [10.1109/TEC.2002.1009476](https://doi.org/10.1109/TEC.2002.1009476).
- [54] A. Tüysüz, C. Zwyssig, and J. W. Kolar, "A Novel Motor Topology for High-Speed Micro-Machining Applications," *IEEE Transactions on Industrial Electronics*, vol. 61, no. 6, pp. 2960–2968, 2014, DOI: [10.1109/TIE.2013.2273481](https://doi.org/10.1109/TIE.2013.2273481).
- [55] T. Taufer and L. Billet, "Compact BLDC & Stepper Motor Technology for Ultra-Slim Actuators," in *Proc. of the 10th ETG/GMM Symposium on Innovative Small Drives and Micro-Motor Systems (IKMT)*, 2015, pp. 1–6.
- [56] M. Flankl, L. de Oliveira Baumann, A. Tüysüz, and J. W. Kolar, "Energy Harvesting With Single-Sided Linear Induction Machines Featuring Secondary Conductive Coating," *IEEE Transactions on Industrial Electronics*, vol. 66, no. 6, pp. 4880–4890, 2019, DOI: [10.1109/TIE.2018.2821637](https://doi.org/10.1109/TIE.2018.2821637).
- [57] K. Wang, J. Li, S. S. Zhu, and C. Liu, "Novel Hybrid-Pole Rotors for Consequent-Pole PM Machines Without Unipolar Leakage Flux," *IEEE Transactions on Industrial Electronics*, vol. 66, no. 9, pp. 6811–6823, 2019, DOI: [10.1109/TIE.2018.2877165](https://doi.org/10.1109/TIE.2018.2877165).

- [58] J. Li, K. Wang, and H. Zhang, "Flux-Focusing Permanent Magnet Machines With Modular Consequent-Pole Rotor," *IEEE Transactions on Industrial Electronics*, vol. 67, no. 5, pp. 3374–3385, 2020, DOI: [10.1109/TIE.2019.2922922](https://doi.org/10.1109/TIE.2019.2922922).
- [59] Z. Q. Zhu, Z. Azar, and G. Ombach, "Influence of Additional Air Gaps Between Stator Segments on Cogging Torque of Permanent-Magnet Machines Having Modular Stators," *IEEE Transactions on Magnetics*, vol. 48, no. 6, pp. 2049–2055, 2012, DOI: [10.1109/TMAG.2011.2179667](https://doi.org/10.1109/TMAG.2011.2179667).
- [60] N. Leboeuf, T. Boileau, B. Nahid-Mobarakeh, N. Takorabet, F. Meibody-Tabar, and G. Clerc, "Effects of Imperfect Manufacturing Process on Electromagnetic Performance and Online Interturn Fault Detection in PMSMs," *IEEE Transactions on Industrial Electronics*, vol. 62, no. 6, pp. 3388–3398, 2015, DOI: [10.1109/TIE.2014.2387338](https://doi.org/10.1109/TIE.2014.2387338).
- [61] S. Fericean and R. Droxler, "New Noncontacting Inductive Analog Proximity and Inductive Linear Displacement Sensors for Industrial Automation," *IEEE Sensors Journal*, vol. 7, no. 11, pp. 1538–1545, 2007, DOI: [10.1109/JSEN.2007.908232](https://doi.org/10.1109/JSEN.2007.908232).
- [62] C. Ding, J. L. G. Janssen, A. A. H. Damen, P. P. J. van den Bosch, J. J. H. Paulides, and E. Lomonova, "Modeling and Realization of a 6-DoF Contactless Electromagnetic Anti-Vibration System and Verification of its Static Behavior," in *Proc. of the IEEE/ASME International Conference on Advanced Intelligent Mechatronics (AIM)*, 2012, pp. 149–154, DOI: [10.1109/AIM.2012.6265880](https://doi.org/10.1109/AIM.2012.6265880).
- [63] A. Arcire and G. Mihalache, "Position Control of a Bidirectional Moving Magnet Actuator Based on Contactless Hall-Effect Transducer," in *Proc. of the 9th International Symposium on Advanced Topics in Electrical Engineering (ATEE)*, 2015, pp. 417–421, DOI: [10.1109/ATEE.2015.7133840](https://doi.org/10.1109/ATEE.2015.7133840).
- [64] K. Wang, L. Zhang, S. Zheng, J. Zhou, and X. Liu, "Analysis and Experiment of Self-Differential Eddy-Current Sensor for High-Speed Magnetic Suspension Electric Machine," *IEEE Transactions on Industry Applications*, vol. 55, no. 3, pp. 2538–2547, 2019, DOI: [10.1109/TIA.2018.2890032](https://doi.org/10.1109/TIA.2018.2890032).
- [65] R. Hooijschuur, N. Saikumar, S. H. HosseinNia, and R. A. J. van Ostayen, "Air-Based Contactless Wafer Precision Positioning System," *Applied Sciences*, vol. 11, no. 16, p. 7588, 2021, DOI: [10.3390/app11167588](https://doi.org/10.3390/app11167588).

- [66] V. Chaturvedi, J. G. Vogel, K. A. A. Makinwa, and S. Nihtianov, "A 19.8-mW Eddy-Current Displacement Sensor Interface with Sub-Nanometer Resolution," *IEEE Journal of Solid-State Circuits*, vol. 53, no. 8, pp. 2273–2283, 2018, DOI: [10.1109/JSSC.2018.2832168](https://doi.org/10.1109/JSSC.2018.2832168).
- [67] Texas Instruments, "LDC Device Selection Guide," Tech. Rep. SNOA954D, June 2021. [Online]. Available: <https://www.ti.com/lit/an/snoa954d/snoa954d.pdf>
- [68] Renesas Electronics Corporation, "IPS2550 Datasheet," 2022. [Online]. Available: <https://www.renesas.com/us/en/document/dst/ips2550-datasheet>
- [69] Q. Gentjan, M. Passarotto, and R. Specogna, "Sensor Coil Optimization," US Patent 10,690,517 B2, Jun 23, 2020.
- [70] A. Hoxha, M. Passarotto, G. Qama, and R. Specogna, "Design Optimization of PCB-Based Rotary-Inductive Position Sensors," *Sensors*, vol. 22, no. 13, p. 4683, 2022, DOI: [10.3390/s22134683](https://doi.org/10.3390/s22134683).
- [71] S. D. Roach, "Designing and Building an Eddy Current Position Sensor," *Sensors - The Journal of Applied Sensing Technology*, vol. 15, no. 9, pp. 56–74, 1998. [Online]. Available: <https://www.fierceelectronics.com/components/designing-and-building-eddy-current-position-sensor>
- [72] S. Theobald, "High-Resolution Frequency Counter," *Electronics & Wireless World*, 1989.
- [73] A.-H. H. AlOmari, A. V. Savkin, M. Stevens, D. G. Mason, D. L. Timms, R. F. Salamonsen, and N. H. Lovell, "Developments in Control Systems for Rotary Left Ventricular Assist Devices for Heart Failure Patients: A Review," *Physiological Measurement*, vol. 34, no. 1, p. R1, 2012, DOI: [10.1088/0967-3334/34/1/R1](https://doi.org/10.1088/0967-3334/34/1/R1).
- [74] K. Ohuchi, D. Kikugawa, K. Takahashi, M. Uemura, M. Nakamura, T. Murakami, T. Sakamoto, and S. Takatani, "Control Strategy for Rotary Blood Pumps," *Artificial Organs*, vol. 25, no. 5, pp. 366–370, 2001, DOI: [10.1046/j.1525-1594.2001.025005366.x](https://doi.org/10.1046/j.1525-1594.2001.025005366.x).
- [75] J.-F. Llibre, N. Martinez, P. Leprince, and B. Nogarede, "Analysis and Modeling of Linear-Switched Reluctance for Medical Application," *Actuators*, vol. 2, no. 2, pp. 27–44, 2013, DOI: [10.3390/act2020027](https://doi.org/10.3390/act2020027).

- [76] K. Fukunaga, A. Homma, A. Funakubo, E. Tatsumi, Y. Taenaka, S. Kitamura, and Y. Fukui, "Pulsatile Blood Pump with a Linear Drive Actuator," *Journal of Artificial Organs*, vol. 10, no. 2, pp. 77–84, 2007, DOI: [10.1007/s10047-007-0375-2](https://doi.org/10.1007/s10047-007-0375-2).
- [77] H. S. Zad, T. I. Khan, and I. Lazoglu, "Design and Analysis of a Novel Bearingless Motor for a Miniature Axial Flow Blood Pump," *IEEE Transactions on Industrial Electronics*, vol. 65, no. 5, pp. 4006–4016, 2018, DOI: [10.1109/TIE.2017.2762626](https://doi.org/10.1109/TIE.2017.2762626).
- [78] J. J. Lee, C. B. Ahn, J. Choi, J. W. Park, S.-J. Song, and K. Sun, "Development of Magnetic Bearing System for a New Third-Generation Blood Pump," *Artificial Organs*, vol. 35, no. 11, pp. 1082–1094, 2011, DOI: [10.1111/j.1525-1594.2011.01376.x](https://doi.org/10.1111/j.1525-1594.2011.01376.x).
- [79] R. V. Giuffrida, S. Mirić, A. Horat, D. Bortis, and J. W. Kolar, "Control System Design and Experimental Verification of a Self-Bearing Double-Stator Linear-Rotary Actuator," in *Proc. of the 13th International Symposium on Linear Drives for Industry Applications (LDIA)*, 2021, pp. 1–6, DOI: [10.1109/LDIA49489.2021.9505865](https://doi.org/10.1109/LDIA49489.2021.9505865).
- [80] S. Mirić, R. Giuffrida, D. Bortis, and J. W. Kolar, "Dynamic Electromechanical Model and Position Controller Design of a New High-Precision Self-Bearing Linear Actuator," *IEEE Transactions on Industrial Electronics*, vol. 68, no. 1, pp. 744–755, 2021, DOI: [10.1109/TIE.2020.2992943](https://doi.org/10.1109/TIE.2020.2992943).
- [81] Z. Ping, T. Wang, Y. Huang, H. Wang, J.-G. Lu, and Y. Li, "Internal Model Control of PMSM Position Servo System: Theory and Experimental Results," *IEEE Transactions on Industrial Informatics*, vol. 16, no. 4, pp. 2202–2211, 2020, DOI: [10.1109/TII.2019.2935248](https://doi.org/10.1109/TII.2019.2935248).
- [82] S. Skogestad and I. Postlethwaite, *Multivariable Feedback Control: Analysis and Design*. Wiley New York, 2007, vol. 2.
- [83] Plexim GmbH, *PLECS Standalone*, Plexim GmbH, 2023, version 4.7.1. [Online]. Available: https://www.plexim.com/products/plecs/plecs_standalone
- [84] A. Visioli, "Anti-Windup Strategies," in *Practical PID Control*, ser. Advances in Industrial Control. London: Springer, 2006, pp. 35–60.
- [85] A. Lagrioui and H. Mahmoudi, "Speed and Current Control for the PMSM Using a Luenberger Observer," in *Proc. of the International*

- Conference on Multimedia Computing and Systems*, 2011, pp. 1–6, DOI: [10.1109/ICMCS.2011.5945721](https://doi.org/10.1109/ICMCS.2011.5945721).
- [86] D. Luenberger, “Observers for Multivariable Systems,” *IEEE Transactions on Automatic Control*, vol. 11, no. 2, pp. 190–197, 1966, DOI: [10.1109/TAC.1966.1098323](https://doi.org/10.1109/TAC.1966.1098323).
- [87] L. Xiaoquan, L. Heyun, and H. Junlin, “Load Disturbance Observer-Based Control Method for Sensorless PMSM Drive,” *IET Electric Power Applications*, vol. 10, no. 8, pp. 735–743, 2016, DOI: [10.1049/iet-epa.2015.0550](https://doi.org/10.1049/iet-epa.2015.0550).
- [88] W.-H. Chen, J. Yang, L. Guo, and S. Li, “Disturbance-Observer-Based Control and Related Methods — An Overview,” *IEEE Transactions on Industrial Electronics*, vol. 63, no. 2, pp. 1083–1095, 2016, DOI: [10.1109/TIE.2015.2478397](https://doi.org/10.1109/TIE.2015.2478397).
- [89] W.-H. Chen, “Disturbance Observer Based Control for Nonlinear Systems,” *IEEE/ASME Transactions on Mechatronics*, vol. 9, no. 4, pp. 706–710, 2004, DOI: [10.1109/TMECH.2004.839034](https://doi.org/10.1109/TMECH.2004.839034).
- [90] L. Xin, Z. Dong, Z. Pei, and W. Rui, “The Current Feedforward Compensation Method for the Cogging Torque of Permanent Magnet Synchronous Motors,” in *Proc. of the IEEE 9th Annual International Conference on CYBER Technology in Automation, Control, and Intelligent Systems (CYBER)*, 2019, pp. 1091–1095, DOI: [10.1109/CYBER46603.2019.9066631](https://doi.org/10.1109/CYBER46603.2019.9066631).
- [91] K. C. Yeo, G. Heins, F. De Boer, and B. Saunders, “Adaptive Feedforward Control to Compensate Cogging Torque and Current Measurement Errors for PMSMs,” in *Proc. of the IEEE International Electric Machines & Drives Conference (IEMDC)*, 2011, pp. 942–947, DOI: [10.1109/IEMDC.2011.5994942](https://doi.org/10.1109/IEMDC.2011.5994942).
- [92] LinMot, “Linear Motors P01-23X80,” Datasheet. [Online]. Available: https://shop.linmot.com/data/import/Dokumente/0185-1000-E_1V1_DS_Linear_Motors_P01-23x80.pdf
- [93] LinMot, “Servo Drive B1100,” Datasheet. [Online]. Available: https://shop.linmot.com/data/import/Dokumente/0185-1019-E_16V3_DS_Drive_Series_B1100.pdf

- [94] A. J. Fleming, "A Review of Nanometer Resolution Position Sensors: Operation and Performance," *Sensors and Actuators A: Physical*, vol. 190, pp. 106–126, 2013, DOI: [10.1016/j.sna.2012.10.016](https://doi.org/10.1016/j.sna.2012.10.016).
- [95] B. George, Z. Tan, and S. Nihtianov, "Advances in Capacitive, Eddy Current, and Magnetic Displacement Sensors and Corresponding Interfaces," *IEEE Transactions on Industrial Electronics*, vol. 64, no. 12, pp. 9595–9607, 2017, DOI: [10.1109/TIE.2017.2726982](https://doi.org/10.1109/TIE.2017.2726982).
- [96] J. Boehm, R. Gerber, and N. Kiley, "Sensors for Magnetic Bearings," *IEEE Transactions on Magnetics*, vol. 29, no. 6, pp. 2962–2964, 1993, DOI: [10.1109/20.280903](https://doi.org/10.1109/20.280903).
- [97] L. Xi'nan, W. Fengxiang, and W. Baoguo, "Application of Eddy-Current Sensor for Air Gap Detection in Magnetic Suspension Motors," in *Proc. of the IEEE 5th International Conference on Electrical Machines and Systems (ICEMS)*, vol. 1, 2001, pp. 326–329 vol.1, DOI: [10.1109/ICEMS.2001.970678](https://doi.org/10.1109/ICEMS.2001.970678).
- [98] T. Wellerdieck, "Die lagerlose Pumpe für hohe Fluidtemperaturen (in German)," Ph.D. dissertation, ETH Zurich, 2017.
- [99] A. Sophian, G. Tian, and M. Fan, "Pulsed Eddy Current Non-Destructive Testing and Evaluation: A Review," *Chinese Journal of Mechanical Engineering*, vol. 30, no. 3, pp. 500–514, 2017, DOI: [10.1007/s10033-017-0122-4](https://doi.org/10.1007/s10033-017-0122-4).
- [100] S. Shokralla, S. Sullivan, J. Morelli, and T. W. Krause, "Modelling and Validation of Eddy Current Response to Changes in Factors Affecting Pressure Tube to Calandria Tube Gap Measurement," *NDT & E International*, vol. 73, pp. 15–21, 2015, DOI: [10.1016/j.ndteint.2015.02.005](https://doi.org/10.1016/j.ndteint.2015.02.005).
- [101] T. Baumgartner, R. M. Burkart, and J. W. Kolar, "Analysis and Design of a 300-W 500 000-r/min Slotless Self-Bearing Permanent-Magnet Motor," *IEEE Transactions on Industrial Electronics*, vol. 61, no. 8, pp. 4326–4336, 2014, DOI: [10.1109/TIE.2013.2284159](https://doi.org/10.1109/TIE.2013.2284159).
- [102] S. Mohan, M. del Mar Hershenson, S. Boyd, and T. Lee, "Simple Accurate Expressions for Planar Spiral Inductances," *IEEE Journal of Solid-State Circuits*, vol. 34, no. 10, pp. 1419–1424, 1999, DOI: [10.1109/4.792620](https://doi.org/10.1109/4.792620).
- [103] J. Zhao, "A New Calculation for Designing Multilayer Planar Spiral Inductors," *EDN (Electrical Design News)*, vol. 55,

- pp. 37–40, 2010. [Online]. Available: <https://www.edn.com/a-new-calculation-for-designing-multilayer-planar-spiral-inductors>
- [104] D. Vyroubal, “Impedance of the Eddy-Current Displacement Probe: The Transformer Model,” *IEEE Transactions on Instrumentation and Measurement*, vol. 53, no. 2, pp. 384–391, 2004, DOI: [10.1109/TIM.2003.822705](https://doi.org/10.1109/TIM.2003.822705).
- [105] H. Wheeler, “Simple Inductance Formulas for Radio Coils,” *Proc. of the Institute of Radio Engineers*, vol. 16, no. 10, pp. 1398–1400, 1928, DOI: [10.1109/JRPROC.1928.221309](https://doi.org/10.1109/JRPROC.1928.221309).
- [106] C. Akyel, S. Babic, and S. Kincic, “New and Fast Procedures for Calculating the Mutual Inductance of Coaxial Circular Coils (Circular Coil - Disk Coil),” *IEEE Transactions on Magnetics*, vol. 38, no. 5, pp. 2367–2369, 2002, DOI: [10.1109/TMAG.2002.803576](https://doi.org/10.1109/TMAG.2002.803576).
- [107] W. G. Hurley, M. C. Duffy, J. Zhang, I. Lope, B. Kunz, and W. H. Wölfle, “A Unified Approach to the Calculation of Self- and Mutual-Inductance for Coaxial Coils in Air,” *IEEE Transactions on Power Electronics*, vol. 30, no. 11, pp. 6155–6162, 2015, DOI: [10.1109/TPEL.2015.2413493](https://doi.org/10.1109/TPEL.2015.2413493).
- [108] M. R. Nabavi and S. N. Nihtianov, “Design Strategies for Eddy-Current Displacement Sensor Systems: Review and Recommendations,” *IEEE Sensors Journal*, vol. 12, no. 12, pp. 3346–3355, 2012, DOI: [10.1109/JSEN.2012.2204321](https://doi.org/10.1109/JSEN.2012.2204321).
- [109] P. Kejík, C. Kluser, R. Bischofberger, and R. S. Popovic, “A Low-Cost Inductive Proximity Sensor for Industrial Applications,” *Sensors and Actuators A: Physical*, vol. 110, no. 1, pp. 93–97, 2004, DOI: [10.1016/j.sna.2003.07.007](https://doi.org/10.1016/j.sna.2003.07.007).
- [110] G. Zhao, J. Yin, L. Wu, and Z. Feng, “Ultrastable and Low-Noise Self-Compensation Method for Circuit Thermal Drift of Eddy Current Sensors Based on Analog Multiplier,” *IEEE Transactions on Industrial Electronics*, vol. 67, no. 10, pp. 8851–8859, 2020, DOI: [10.1109/TIE.2019.2949511](https://doi.org/10.1109/TIE.2019.2949511).
- [111] R. Pallás-Areny and J. G. Webster, *Sensors and Signal Conditioning*, 2nd ed. New York: Wiley, 2001.
- [112] J. Karki, “Active Low-Pass Filter Design,” Texas Instruments, Tech. Rep. SLOA049B, September 2002. [Online]. Available: <https://www.ti.com/lit/an/sloa049d/sloa049d.pdf>

- [113] R. V. Giuffrida, S. Mirić, D. Bortis, and J. W. Kolar, ““Looking Through Walls” – Actuator Position Measurement Through a Conductive Wall,” in *Proc. of the 23rd International Conference on Electrical Machines and Systems (ICEMS)*, 2020, pp. 1649–1654, DOI: [10.23919/ICEMS50442.2020.9291020](https://doi.org/10.23919/ICEMS50442.2020.9291020).

Curriculum Vitae

Personal Information

Name Rosario Vincenzo Giuffrida
Date of birth August 27, 1994
Nationality Italian, European
Citizen of Catania, Italy
Contact giuffrida@lem.ee.ethz.ch



Education

2019 – 2024 Doctorate, ETH Zurich
Power Electronic Systems Laboratory (PES)
2016 – 2019 MSc ETH, ETH Zurich
Robotics, Systems and Control
2013 – 2016 BSc, Università degli Studi di Catania
Ingegneria Elettronica
2008 – 2013 High School, Catania
Liceo Scientifico

Work Experience

2019 – 2024 Research Assistant, ETH Zurich
Power Electronic Systems Laboratory (PES)
2017 – 2018 Internship at maxon motor ag, Sachseln